ISSN 1344-6320

2012

PHOTON FACTORY ACTIVITY REPORT

PART A : HIGHLIGHT AND FACILITY REPORT #30

KEK Progress Report 2013-6

KEK Reports are available from:

Library and Archives
High Energy Accelerator Research Organization (KEK)
1-1 Oho, Tsukuba, Ibaraki, 305-0801
JAPAN

E-mail: irdlib@mail.kek.jp
URL: http://www.kek.jp/

#30

PHOTON FACTORY ACTIVITY REPORT

2012

April 2012 to March 2013

1 O. Konstantinova
2 A. Toyoshima
3 M. Tanaka
4 H. Miyamoto
5 R. Kumai
6 N. Sakabe
7 S. Adachi
8 Y. Murakami
9 K. Ito
10 Y. Kobayashi
11 H. Kawata
12 T. Senda
13 M. Sakamaki
14 M. Kitamura
15 N. Usami
16 H. Tanaka
17 W. Hishinuma
18 T. Uchiyama
19 F. Mori
20 H. Toyama
21 Y. Watanabe
22 H. Makio
23 T. Aoki
24 T. Ohta
25 T. Nogami
26 N. Matsugaki
27 K. Inoue
28 S. Naito
29 S. Watanabe
30 K. Sasajima
31 T. Miyajima
32 M. Shimada
33 T. Zeniya
34 A. Unjo
35 A. Hirata
36 T. Obina
37 N. Nakamura
38 Y. Uchida
39 S. Nozawa
40 T. Honda
41 J. Adachi
42 H. Sagehashi
43 T. Kikuchi
44 Y. Wu
45 I. Mochizuki
46 K. Horiba
47 T. Hyodo
48 J. Okamoto
49 K. Wada
50 F. Gallat
51 Y. Lo
52 N. Kuwabara
53 N. Nagata
54 H. Abe
55 M. Senda
56 Y. Misumi
57 G. Ishikawa
58 R. Sukegawa
59 A. Kikuchi
60 H. Ohshima
61 M. Mochida
62 T. Kosuge
63 S. Kishimoto
64 S. Nagahashi
65 W. Watanabe
66 H. Nitani
67 K. Mase
68 T. Yamasaki
69 A. Harada
70 Y. Sato
71 Yo. Takahashi
72 R. Takai
73 N. Inami
74 R. Kato
75 Y. Yamasaki
76 T. Sudayama
77 A. Kamijo
78 N. Shimizu
79 K. Hyodo
80 L. Chavas
81 A. Ueda
82 Y. Tanimoto
83 A. Koyama
84 T. Koide
85 N. Igarashi
86 T. Sasaki
87 F. Yumoto
88 M. Kawasaki
89 Y. Kitajima
90 T. Ueno
91 Yu. Takahashi
92 K. Saito
93 K. Amemiya
94 K. Kishida
95 N. Adachi
96 Y. Akai
97 A. Tomita
98 T. Sato
99 N. Suzuki

Editorial

This is the 30th edition of the Photon Factory (PF) Activity Report, and covers scientific activities for the Japanese fiscal year 2012 (April 2012 to March 2013). The report is divided into two parts. PART A summarizes scientific highlights achieved by users, newly developed experimental facilities including beamlines and experimental apparatuses, topical in-house research activities, research and development of storage rings and an energy recovery linac based future light source, reports of public events, and an outline of the organization of the PF. PART B presents a number of users' short reports and a list of research proposals.

For the past several editions we have encouraged the electronic distribution of the PF Activity Report. Accordingly, the List of Awards, Theses and Publications in the Appendices of PART A and the entire content including PART B are published on the PF's website at *http://pfwww.kek.jp/pfacr/index.html*.

Finally, we would like to express our sincere gratitude to all of those who have contributed to this volume.

Shunsuke Nozawa, Editor-in-Chief

CONTENTS

Awards, Theses and Publication List are available on the PF's website(*http://pfwww.kek.jp/pfacr/*).

Introduction

Youichi Murakami

On behalf of the staff of the Photon Factory (PF) we are pleased to present Photon Factory Activity Report 2012. This report covers the research activities carried out in the fiscal year 2012 (April 2012 - March 2013), which is my first year as the Director of the PF. The PF leadership has partially changed: Prof. Reiji Kumai (from April 2013), Prof. Shinichi Adachi (from April 2012) and Prof. Toshiya Senda (from January 2013) join us as Heads of Division 1 & 2 of Synchrotron Radiation (SR) Science and as Head of the Structural Biology Research Center, respectively.

Organization of the Photon Factory

The organization of the SR Science Division 1 & 2 was changed in order to carry out inter-university research efficiently and to enhance the SR research with limited budget and manpower. The divisions consist of three group layers: the beamline group layer, engineering and administration group layer, and working group layer (http://pfwww.kek.jp/orgchart/indexe.html). The beamline group layer has five scientific groups (Gs): electronic structure G, condensed matter G, material chemistry G, life science G, and slow positron G. These groups operate and maintain their respective beamlines. The engineering and administration group layer has two groups: one group responsible for beamline engineering, technical service and safety, and the other group responsible for user support and publicity work. The working group (WG) layer has two groups at this stage: ultrafast dynamics WG and advanced detector R&D WG; the WGs have definite goals and are time-limited. In the future some new WGs such as coherent X-ray WG, nano-beam WG, and inelastic X-ray scattering WG will be proposed to underpin the developments in the PF.

KEK roadmap and future light source

Inter-University Research Institute Corporation of the High Energy Accelerator Research Organization (KEK) published a draft of the KEK roadmap at the end of August 2012 and solicited the opinions of user communities. The Photon Factory User Association (PF-UA) and the Japanese Society for Synchrotron Radiation Research (JSSRR) expressed their opinions concerning photon science in the KEK roadmap. The communities also made specific proposals on the role that KEK should play as a leading institute for SR research. We then modified the roadmap to reflect their proposals and finished it in March 2013. The KEK roadmap was reviewed by the international review committee in April and finally published in May 2013. The part concerning photon science states the following: “KEK will continue to advance photon science by upgrading the PF and Photon Factory Advanced Ring (PF-AR) to improve their performance and efficiency. At the same time, KEK will construct and then operate the compact energy recovery linac (cERL) and will demonstrate the key technologies required for the ERL. By proving the potential of the ERL as a new accelerator to open new scientific frontiers, KEK will work toward construction of a 3 GeV ERL facility. In addition, KEK will continue to play a leading role in the development of SR research in Japan.” The international review committee provided the following advice regarding the roadmap: “The construction of the cERL, building on the outstanding accelerator expertise existing at KEK, is making great progress. The completion of this project to demonstrate and gain experience of the key ERL technologies is very important. In the long term the ERL is an interesting prospect for a future light source and should be kept in the plans at KEK. The issue is for the mid-term gap: the community as represented by the Japanese Society for Synchrotron Research has identified the immediate need for a low-emittance, state-of-the-art storage ring. Both from geographic and technical points of view, KEK is ideally positioned to realize the needs of the community.” The ‘low-emittance, state-of-the-art storage ring’ mentioned in the review report is the future light source proposed for the master plan of the Science Council Japan by the JSSRR in March 2013. We are now discussing the realization of this storage ring through collaboration across Japan.

Upgrades of the PF and the PF-AR

The operation of the PF started in 1982. After two large upgrades in 1996 and 2005 the emittance was reduced from 130 to 36 nmrad. The top-up operation with constant electric current in the PF ring has been working well since 2009. As the PF ring is operating with the relatively low energy of 2.5 GeV and large current of 450 mA, we have an important advantage for science in the energy range of vacuum ultraviolet (VUV) and soft X-ray (SX). Actually, the PF has four VUV/SX beamlines (BL-2, -13, -16, -28) with undulators in the long straight sections. We have been focusing on upgrading these beamlines to

maintain our international competitiveness in the field of VUV/SX science. We are planning to complete the installation of the undulators and the reconstruction of these beamlines by the autumn of 2014. These beamlines, BL-2, -13, -16, and -28, are used to study solid state physics at surfaces/interfaces, surface chemistry, frontier science of SX spectroscopy with polarization switching, and strongly correlated electron materials. Meanwhile, we upgraded the X-ray beamlines (BL-1, -3, 17) by installing short gap undulators in the short straight sections to gain long-term competitiveness in the field of X-ray science. The last short straight section in which a short gap undulator is to be installed is in BL-15. This beamline will be dedicated to small-angle X-ray scattering and X-ray absorption fine structure/X-ray fluorescence analysis measurements to study soft matter materials, environmental science, and new energy source materials such as for batteries.

Operation of the PF-AR started in 1987 as a parasite SR of the booster synchrotron for high-energy physics and was dedicated to SR operation in 1998. The PF-AR is operating with the energy of 6.5 GeV to supply relatively high-energy X-rays for high-pressure science, crystal structure analysis with high-energy X-rays, and so on. The PF-AR is characterized by operation in full-time single-bunch mode; the single-bunch mode is advantageous for time-resolved experiments. We are planning to construct a direct beam transport line for the PF-AR to manage both the injection to the PF-AR and superKEKB for high-energy physics. This upgrade of the PF-AR will make it possible to inject with the full energy of 6.5 GeV and also to operate with a top-up mode. As a result of this upgrade, the brilliance will be increased.

PF Science Advisory Committee

The 7th PF science advisory committee (PF-SAC) held a meeting in February 2013. This committee is very important for us to gather various advice from an international perspective. The PF-SAC evaluates and advises on our light source, beamline developments, facility operation, science outputs by users and the PF staff, and the PF management and strategic plans. The PF-SAC is comprised of nine distinguished scientists, and has been chaired by Prof. Ingolf E. Lindau of Stanford University since 2011. We have seven subcommittees to give more specialist evaluations and advice; each subcommittee consists of experienced scientists including a member of the PF-SAC. In this 7th PF-SAC we reported on the present status of the PF and showed our future plans including upgrades of the PF and PF-AR. In the executive summary and closing remarks, the PF-SAC commended the PF management for its initiative to upgrade beamlines, supported our future plans, and appreciated the establishment of a new PF user's community, PF-UA. The SAC also found the individual meetings with young scientists extremely valuable.

Inter-university collaboration

KEK is promoting inter-university collaboration to activate joint research projects. Hokkaido University and KEK held a symposium at Sapporo in October 2012 to discuss collaboration in research using SR, neutrons, muons, and positrons. The symposium yielded new ideas for scientific co-development. Tohoku University and KEK have been promoting joint projects for the last several years. Actually, KEK is constructing a polarized neutron spectrometer in collaboration with Tohoku University at J-PARC (Japan Proton Accelerator Research Complex). In order to drive the project, Tohoku University is planning to set up a center for conducting science using quantum beams on the basis of the inter-university agreement. In order to establish the center, Tohoku University held a symposium to discuss quantum beam science. Meanwhile, Tsukuba University has established the KEK research promotion office in Tsukuba Research Center for Interdisciplinary Materials Science. The office provides advice on the use of beamlines of the PF and J-PARC/MLF (Materials and Life Science Experimental Facility). In this joint project, staff of Tsukuba University form a research team in collaboration with staff of KEK. The KEK also collaborates with the Graduate School of Frontier Science of the University of Tokyo, and held joint seminars in September 2012 and February 2013.

New projects

Two new research grants of the Ministry of Education, Culture, Sports, Science and Technology (MEXT) which are expected to use quantum beams were launched in 2012. One is the project concerning the platform for Drug Discovery, Informatics, and Structural Life Science, which was started in order to build a creative process for medical procedure and drug discovery through the development and common use of research infrastructure. KEK plays an important role as the core institute of structural analysis. The other project is the Element Strategy Initiative, which promotes the creation of innovative alternatives to such materials as rare elements which underpin Japan's industrial competitiveness, through close collaboration among materials design, development, and evaluation in the core research center. KEK/IMSS is promoting this MEXT project, with KEK/IMSS staff serving as the principal investigators for electronic materials and magnetic materials in collaboration with the Tokyo Institute of Technology and the National Institute of Materials Science, respectively.

Youichi Murakami

Memorials 2012

April 1, 2012
PF User Association (PF-UA) Established

The PF-Kondankai restarted as the PF User Association (PF-UA) in April 2012. The PF-UA is a user community to promote research activities in the PF. The first president is Professor Mamoru Sato of Yokohama City University.

July 2-3, 2012
ERL Advisory Committee

The 1st ERL Advisory Committee “International Advisory Committee of the 3GeV ERL Project” chaired by Ingolf Lindau (SLAC, SSRL) was held at KEK.

July 19, 2012
The 3rd TIA-nano Public Symposium

The global nanotechnology complex TIA-nano (Tsukuba Innovation Arena) created in Tsukuba City has been carrying out various activities since the joint policy statement was created in June 2009. The addition of KEK to TIA-nano as a new core institute in April 2012 has strengthened the TIA-nano infrastructure.

July 30-31, 2012
The 2nd compact ERL Science Workshop

The compact ERL (cERL) will start operation in March 2013. Science using the new light source of cERL was discussed at the workshop.

August 20-28, 2012
Summer Challenge

The 6th summer school on “particle and nuclear physics” and “material and biological science” was held at KEK. 90 undergraduate students from all over Japan attended this school, which included basic lectures, facility tours of the Tsukuba and Tokai campuses, and practical experiments.

September 2, 2012
Open House

There were a total of 4600 visitors to KEK on the day. All visitors enjoyed the pioneering world of modern materials, biology and accelerator science.

November 23-24, 2012
Summer Challenge in Autumn

The students who participated in the summer challenge in August performed actual experiments using synchrotron X-rays in the PF and PF-AR.

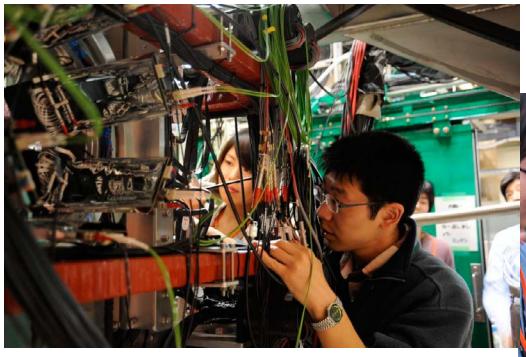

February 7-8, 2013
PF-SAC

The 7th Photon Factory SAC meeting chaired by Ingolf Lindau (Stanford University) was held at KEK.

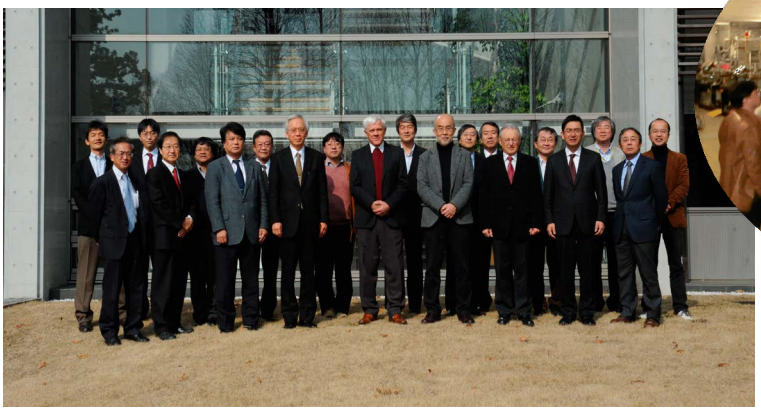

March 14, 2013
500-keV Electron Beam with High Current from a Photoemission Dc Gun was Successfully Generated

A high-brightness, high-current electron gun was developed for an energy recovery linac light source.

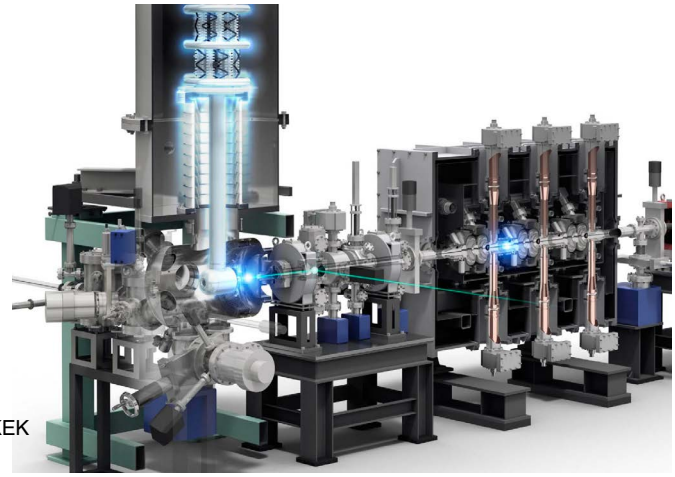

(c)Rey.Hori/KEK

March 14-15, 2013
The 1st IMSS Science Festa

The 1st IMSS science festa, which is a joint symposium hosted by PF, KENS and MLS, was held at EPOCAL TSUKUBA. Over 500 participants actively discussed comprehensive studies using quantum beams, X-rays, neutrons, muons, and slow positrons, owned by IMSS.

March 18, 2013
“PEARL” Chosen as Name of Next-generation Light Source

The name of the energy recovery linac, which was proposed by KEK as a next-generation light source, was chosen as PEARL (Photon Factory ERL Advanced Research Laboratory).

PEARL
Photon Factory

International Collaboration

August 8-10, 2012
AOFSRR in Thailand

AOFSRR (Asia-Oceania Forum for Synchrotron Radiation Research) was held in Bangkok, the capital of Thailand. The objectives of the AOFSRR are to establish a general framework of collaboration for the development of science and technology, which mutually benefits progress toward the research goals of the parties, and to promote comprehensive cooperation in the Asia Oceania region.

September 20-21, 2012
The 3rd India-Japan Symposium

The 3rd India-Japan Symposium on “Frontiers in Science & Technology: Successes & Emerging Challenges” was held at the Indian Embassy in Japan. The PF has an Indian beamline (BL-18B) for use by Indian researchers. Full-scale operation of the beamline started in 2011.

February 14-15, 2013
Workshop on Science Outlook and R&D Issues for an XFELO in POSTECH

The science outlook and R&D issues for an XFELO (X-Ray Free Electron Laser Oscillator) were widely discussed in the workshop.

February 20, 2013
Visit by Ambassadors of India

Ms. Deepa Gopalan Wadhwa, ambassador of India to Japan, and Dr. Chadaram Sivaji, counsellor (Science & Technology) in the Embassy of India, visited KEK and exchanged opinions concerning research cooperation.

February 25, 2013,
Thank you, Australian Beamline !

The Australian beamline BL-20B was constructed in 1992, and finally ceased operation at the end of March 2013. The beamline has been extremely productive, with more than 1,000 papers published from about 900 experimental projects.

Highlights

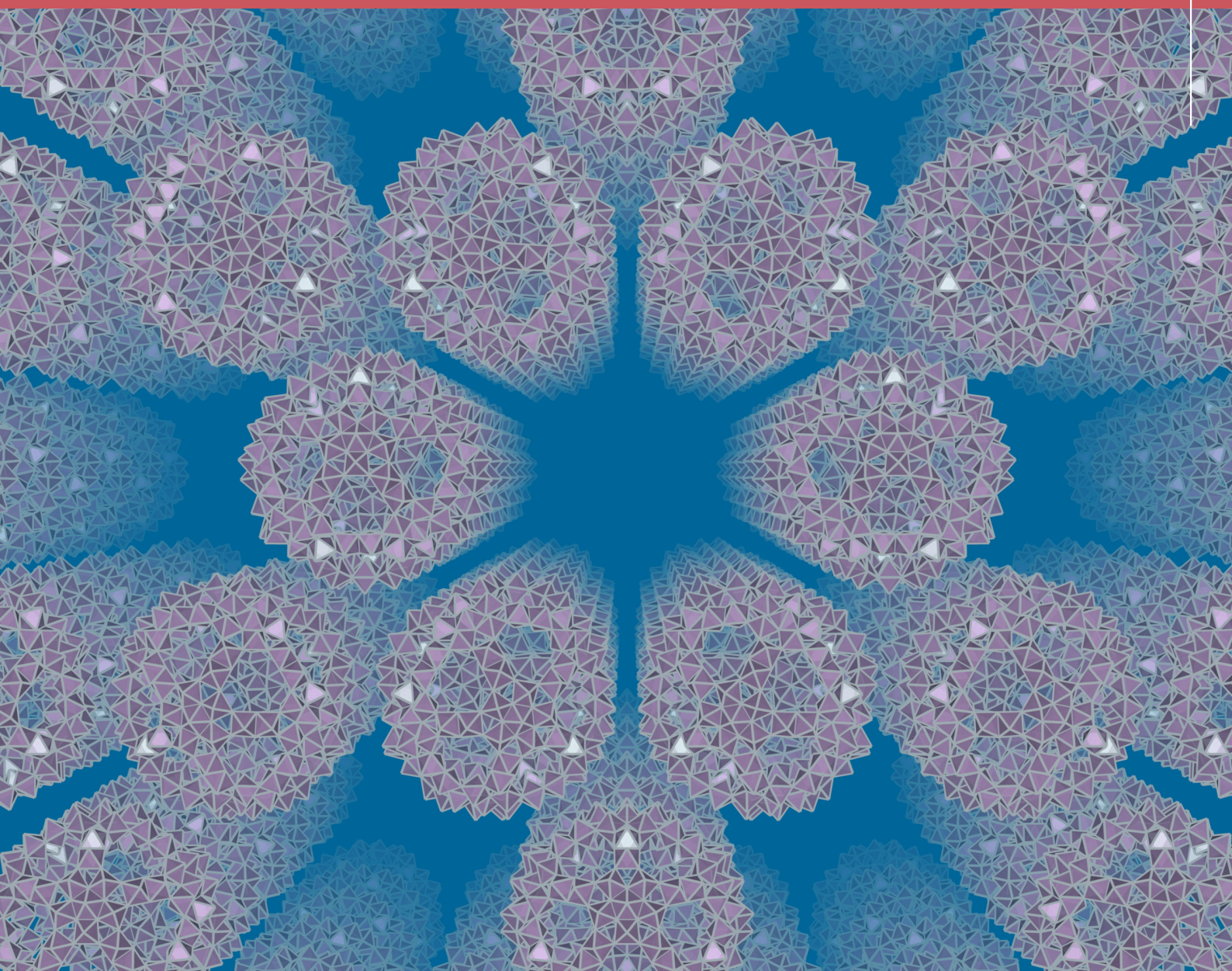

Highlights

Single-Photon $K^{-1}K^{-1}$ Double Core Ionization of C_2H_{2n} (n=1-3) Sequence Molecules as a Potential New Tool for Chemical Analysis

Production of two-site double core-hole ($K^{-1}K^{-1}$) states has been studied for C_2H_{2n} (n = 1-3) molecular series by multi-electron coincidence spectroscopy to verify the theoretical prediction of larger chemical shift than in conventional single core-hole states. A comparison among the cross sections of $K^{-1}K^{-1}$ states formed for these molecules indicates that the knock-out process is predominant in the production of the $K^{-1}K^{-1}$ states.

Electron spectroscopy for chemical analysis (ESCA) [1] is a very powerful analytical method relying on the chemical shift that reflects the environment of a given atom in a molecule. For hydrocarbon molecules this shift is generally very small, but Cederbaum et al. predicted in 1986 [2] that, in C_2H_{2n} (n = 1-3) molecules, the two-site double core-hole states ($K^{-1}K^{-1}$) show a much stronger effect than in single core-hole (K^{-1}) states. Therefore, we systematically studied the production of the $K^{-1}K^{-1}$ states for C_2H_2, C_2H_4 and C_2H_6 to verify the prediction [3]. In the past few years, much attention has been paid on the formation of the double core-hole (DCH) states in molecules with the advent of X-ray Free Electron Laser (X-FEL), which offers the possibility of creating DCHs in a two-photon process [4]. However, the present self-amplified spontaneous emission operation mode of XFELs results in low photon resolution, and is not always sufficient for the abovementioned present purpose.

The experiments were carried out at the undulator beamline BL-16A in single bunch top-up mode by multi-electron coincidence spectroscopy, where we developed a magnetic bottle analyzer with high collection efficiency to detect all the electrons in coincidence and to resolve them in terms of energy through multiple photoionization processes [5].

In Fig. 1, we plot the number of coincidence events as a function of the binding energy (BE) of the DCH states: $BE = h\nu - (E_{Ph1} + E_{Ph2})$ where $E_{Ph1} + E_{Ph2}$ is the sum of the energies of the two photoelectrons. We observe clearly the one-site DCH (K^{-2}) states and also satellite peaks ($K^{-2}V^{-1}V'$) where a valence electron from orbital V is excited simultaneously to a vacant orbital V′. The most important result, the production of the $K^{-1}K^{-1}$ states, can be perceived as small peaks at BE 590-600 eV. The experimental binding energies of the $K^{-1}K^{-1}$ states are 596.0±0.5 eV, 593.3±0.5 and 590.2±0.5 eV, respectively, for C_2H_2, C_2H_4 and C_2H_6. This observation can be compared to the BE of K^{-1} states for these three molecules, of which the chemical shift is at most 0.5 eV, and is considered to verify the abovementioned prediction. It should also be mentioned that the density-functional theory calculations shown by the vertical arrows reproduce the experimental observations quite well [3].

The branching ratios of $K^{-1}K^{-1}/K^{-1}$ can be obtained from the peak intensities in Fig. 1, and were found to be 2.0×10^{-5}, 1.34×10^{-5} and 1.26×10^{-5} for C_2H_2, C_2H_4 and C_2H_6, respectively. This systematic decrease of the ratios along the C_2H_{2n} sequence approximately scales as the inverse square of the C-C bond length (C≡C: 1.2 Å, C=C: 1.34 Å, C-C: 1.54 Å). This is a strong indication that the double site ionization process is predominantly caused by the knock-out mechanism, where the primary photoionized electron collides with a K-shell electron in the neighboring atomic site, which can escape the molecular field with the primary electron. It should be emphasized that this study was made possible thanks to the high performance and very stable single-bunch top-up mode operation at the 2.5-GeV PF ring.

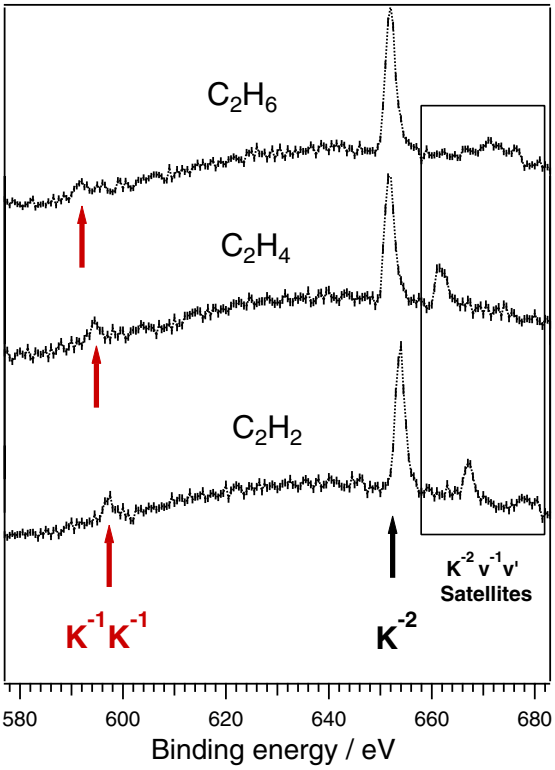

Figure 1: Spectroscopy of $K^{-1}K^{-1}$ double core-hole states of the C_2H_{2n} sequence molecules.

REFERENCES

[1] K. Siegbahn, C. Nordling, G. Johansson, J. Hedman, P.F. Heden, K. Hamrin, U. Gelius, T. Bergmark, L.O. Werme, R. Manne and Y. Baer, ESCA Applied to Free Molecules (North-Holland, Amsterdam, 1971).

[2] L.S. Cederbaum, F. Tarantelli, A. Sgamellotti and J. Schirmer, *J. Chem. Phys.* **85**, 6513 (1986).

[3] M. Nakano, F. Penent, M. Tashiro, T.P. Grozdanov, M. Žitnik, S. Carinato, P. Selles, L. Andric, P. Lablanquie, J. Palaudoux, E. Shigemasa, H. Iwayama, Y. Hikosaka, K. Soejima, I.H. Suzuki, N. Kouchi and K. Ito, *Phys. Rev. Lett.* **110**, 163001 (2013).

[4] N. Berrah, L. Fang, B. Murphy, T. Osipov, K. Ueda, E. Kukk, R. Feifel, P.V.D. Meulen, P. Salen, H.T. Schmidt, R.D. Thomas, M. Larsson, R. Richter, K.C. Prince, J.D. Bozek, C. Bostedt, S. Wada, M.N. Piancastelli, M. Tashiroi and M. Eharai, *Proc. Natl. Acad. Sci.* **108**, 16912 (2011).

[5] K. Ito, F. Penent, Y. Hikosaka, E. Shigemasa, I.H. Suzuki, J.H.D. Eland and P. Lablanquie, *Rev. Sci. Instrum.* **80**, 123101 (2009).

BEAMLINE

BL-16A

M. Nakano[1], F. Penent[2], M. Tashiro[3], T.P. Grozdanov[4], M. Žitnik[5], S. Carniato[2], P. Selles[2], L. Andric[2], P. Lablanquie[2], J. Palaudoux[2], E. Shigemasa[3], H. Iwayama[3], Y. Hikosaka[6], K. Soejima[6], I.H. Suzuki[7], N. Kouchi[8] and K. Ito[7] ([1]JAEA, [2]LCPMR, [3]IMS, [4]The Univ. of Belgrade, [5]IJS, [6]Niigata Univ., [7]KEK-PF, [8]Tokyo Inst. of Technology)

Electronic Ferroelectricity with Large Polarization Directed Antiparallel to Molecular Displacement in an Organic Crystal

Macroscopic electric polarization in displacive-type ferroelectrics is often considered within the traditional simplest framework described by an atomic displacement and static point charge. Here we show that intermolecular charge-transfer instead governs the ferroelectricity of a molecular crystal, in which electron donor and acceptor nonpolar molecules having incompletely ionic charges (±0.60*e*) dimerize along the molecular stacking chain. The observed large polarization was consistent with recent first-principles calculations and the poling effect on the absolute structural configuration can be interpreted in terms of electronic ferroelectricity, which not only exhibits polarity antiparallel to the ionic displacement but also enhances the polarization significantly more than that given by the point-charge model. Such a strongly interacting molecular system will lead to the future design of ferroelectrics for high-performance and high-frequency operations through the fast electronic processes.

The organic charge-transfer complex TTF-CA which comprises an electron donor, tetrathiafulvalene (TTF) and an acceptor, *p*-chloranil (CA) has been attracting much attention because of a novel neutral-to-ionic phase transition (NIT) [1]. The TTF-CA can be regarded as a displacive-type ferrolectrics because the crystal structure is symmetry-broken to the polar space group of *Pn* upon NIT. The donor and acceptor molecules displace pairwise in the alternately stacking chain along the crystallographic *a*-axis. Recently, in contrast to a conventional point-charge model (0.27 μCcm^{-2} along the *a*-axis), first-principles calculations suggested a much larger spontaneous polarization (3-10 μCcm^{-2} along the *a*-axis) with two contrasting candidates of electronic states in TTF-CA [2, 3]. The total polarization was predicted to be directed either parallel or antiparallel to the ionic polarization, depending on the antiferromagnetic or nonmagnetic state, respectively. Here we report the experimental determination of both the magnitude and the direction of the spontaneous polarization in TTF-CA [4].

The ferroelectric nature of TTF-CA was evident from a sharp peak anomaly on the temperature-dependent permittivity and large value of dielectric constant (ε_r) and Curie constant (*C*) are suggestive of a large spontaneous polarization as a proper ferroelectric. However, experimental evaluation of the spontaneous polarization (P_s) value has long been hindered by its narrow charge gap of ~0.7 eV and electric leakage caused by current-induced resistance switching under electric field higher than 10 kVcm^{-1}. We found that satisfactory observations of hysteresis were limited in a narrow range of both frequency and temperature. The coercive field (E_c) increases with increasing frequency or lowering temperature. The observed values from a well-defined parallelogram-like hysteresis were P_s of 6.3 μCcm^{-2} and E_c of 5.4 kVcm^{-1} at 59 K.

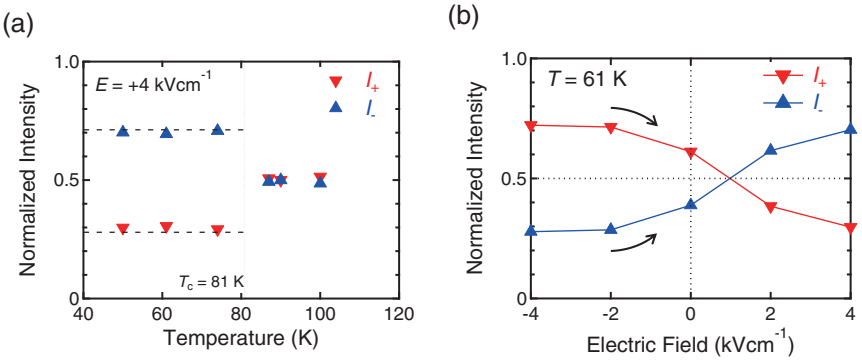

Figure 1: Normalized integrated intensity of Bijvoet pair reflection 101 and $\bar{1}0\bar{1}$. (a) Temperature dependence under constant electric field E = +4 kVcm^{-1} parallel to the *a*-axis. Horizontal broken lines correspond to the single domain values. (b) Electric field dependence increasing from E = –4 kVcm^{-1} to +4 kVcm^{-1} at 61 K.

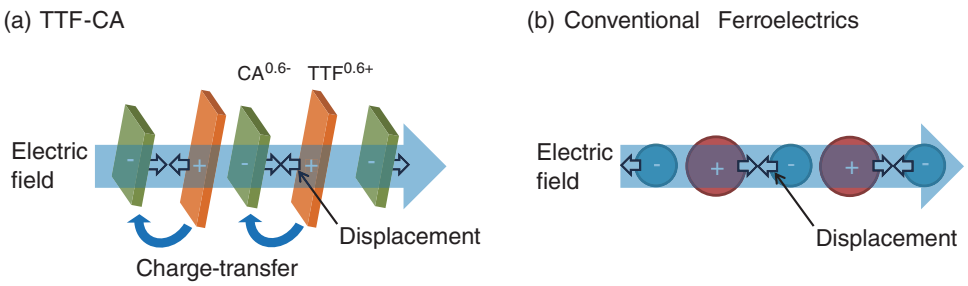

Figure 2: Schematic drawing of the ionic displacement under an electric field. (a) TTF-CA. Deep blue and open arrows indicate charge-transfer from TTF to CA and molecular displacement under the electric field, respectively. (b) Conventional displacive-type ferroelectrics.

To investigate the direction of spontaneous polarization, the degrees of symmetry-breaking in bulk and absolute configurations of the polar TTF-CA crystal structure under an electric field were examined by probing the difference in intensity between Bijvoet pair reflections. The synchrotron radiated X-ray of relatively long wavelength (λ = 1.55 Å) was used to exploit large anomalous scattering factors of the sulfur and chlorine atoms. The Bijvoet pair reflections 101 and $\bar{1}0\bar{1}$ exhibited the largest intensity difference according to a simulation based on the atomic coordinates obtained at T = 15 K [5] and 40 K [6]. Figure 1(a) depicts the temperature dependence of their normalized integrated intensity $I_+ \equiv I(101)/\{I(101) + I(\bar{1}0\bar{1})\}$ and $I_- \equiv I(\bar{1}0\bar{1})/\{I(101) + I(\bar{1}0\bar{1})\}$. Just below T_c, the observed I_+ and I_- readily approach 0.705 or 0.295 [horizontal broken lines in Fig. 1(a)], which correspond to the full polarization into either polarity according to the simulation. Therefore, the poling field of +4 kVcm^{-1} is regarded as sufficient for developing a single-domain state. The intensities of Bijvoet pair (I_+ and I_-) were interchanged by inverting the applied electric field direction due to polarization switching as shown in Fig. 1(b). By comparing the observed intensity of the Bijvoet pair with that obtained by the simulation, we found that the positively charged TTF molecules shift toward the positive electrode and the negatively charged CA toward the negative electrode as shown in Fig. 2(a).

These experimental observations confirm the recent first-principles calculations predicting an extreme contribution of the electronic polarization, which is directed antiparallel to the ionic displacement and governs the magnitude of polarization. The electronic ferroelectricity itself is currently one of the key issues for multiferroelectrics. The electronic response with lower energetic cost of lattice deformations promises both high-performance and high-frequency operations as well as new functionalities.

REFERENCES

[1] J.B. Torrance, J.E. Vazquez, J.J. Mayerle and V.Y. Lee, *Phys. Rev. Lett.* **46**, 253 (1981).
[2] G. Giovannetti, S. Kumar, A. Stroppa, J. van den Brink and S. Picozzi, *Phys. Rev. Lett.* **103**, 266401 (2009).
[3] S. Ishibashi and K. Terakura, *Physica B* **405**, S338 (2010).
[4] K. Kobayashi, S. Horiuchi, R. Kumai, F. Kagawa, Y. Murakami and Y. Tokura, *Phys. Rev. Lett.* **108**, 237601 (2012).
[5] P. García, S. Dahaoui, C. Katan, M. Souhassou and C. Lecomte, *Faraday Discuss.* **135**, 217 (2007).
[6] M. Le Cointe, M.H. Lemee-Cailleau, H. Cailleau, B. Toudic, L. Toupet, G. Heger, F. Moussa, P. Schweiss, K.H. Kraft and N. Karl, *Phys. Rev. B* **51**, 3374 (1995).

BEAMLINE

BL-8A

K. Kobayashi[1], S. Horiuchi[2,3], R. Kumai[1,3], F. Kagawa[3,4], Y. Murakami[1] and Y. Tokura[4,5] ([1]KEK-PF/CMRC, [2]AIST, [3]JST-CREST, [4]The Univ. of Tokyo, [5]ASI-RIKEN)

Experimental Realization of a Topological Crystalline Insulator in SnTe

Topological insulators are a novel quantum state of matter where an insulating bulk hosts unusual gapless metallic states protected by time-reversal symmetry (TRS). Their discovery stimulated the search for new topological states protected by other symmetries, and a recent theory predicted the existence of "topological crystalline insulators" (TCIs) in which the surface states are protected by mirror symmetry of the crystal. We have performed angle-resolved photoemission spectroscopy (ARPES) of narrow-gap IV-VI semiconductor tin telluride (SnTe) and show the first experimental evidence for the TCI phase in this material. Our ARPES result clearly demonstrates a signature of double Dirac-cone surface states, distinctly different from so-far discovered topological insulators, opening new avenues for exotic topological phenomena.

The surface state of three-dimensional topological insulators is characterized by a Dirac-cone energy dispersion protected by TRS. In topological insulators, the TRS plays a key role in characterizing the topological properties such as the quantum spin Hall effect and the magnetoelectric effect [1, 2]. In contrast, in TCIs, metallic surface states are protected by mirror symmetry of the crystal [3]. It was recently shown theoretically by Hsieh *et al.* [4] that the TCI phase is realized in an insulating crystal having the rocksalt structure when a band inversion occurs at the high-symmetry L points of the bulk Brillouin zone. They also predicted that IV-VI semiconductor SnTe is such a TCI, while the isostructural PbTe is not. It is thus of particular importance to experimentally examine the possibility of the TCI phase in these semiconductors, in order to establish the concept of this new topological state of matter and possibly to find novel topological phenomena beyond the framework of known topological materials.

To elucidate the electronic states of SnTe, we have performed high-resolution ARPES experiments at BL-28A and Tohoku University [5, 6].

Figure 1(a) shows the ARPES intensity of SnTe in the valence-band region plotted as a function of wave vector and binding energy, measured for the {001} surface along the $\bar{\Gamma}\bar{X}$ high-symmetry line in the surface Brillouin zone as shown in Fig. 1(b). The $\bar{X}$ point of the surface Brillouin zone corresponds to a projection of the L point of the bulk Brillouin zone where a direct bulk-band gap resides and the appearance of topological surface states is predicted [4]. Our ARPES data clearly demonstrate that the bulk-band maximum is indeed located around the $\bar{X}$ point. As shown in Fig. 1(c), the ARPES intensity at the Fermi level (E_F) measured with the photon energy $h\nu$ = 21.2 eV exhibits a bright intensity pattern centered around the $\bar{X}$ point and is elongated along the $\bar{\Gamma}\bar{X}$ direction. The near-E_F band dispersion along the $\bar{\Gamma}\bar{X}$ cut [Fig. 1(d)] exhibits two sets

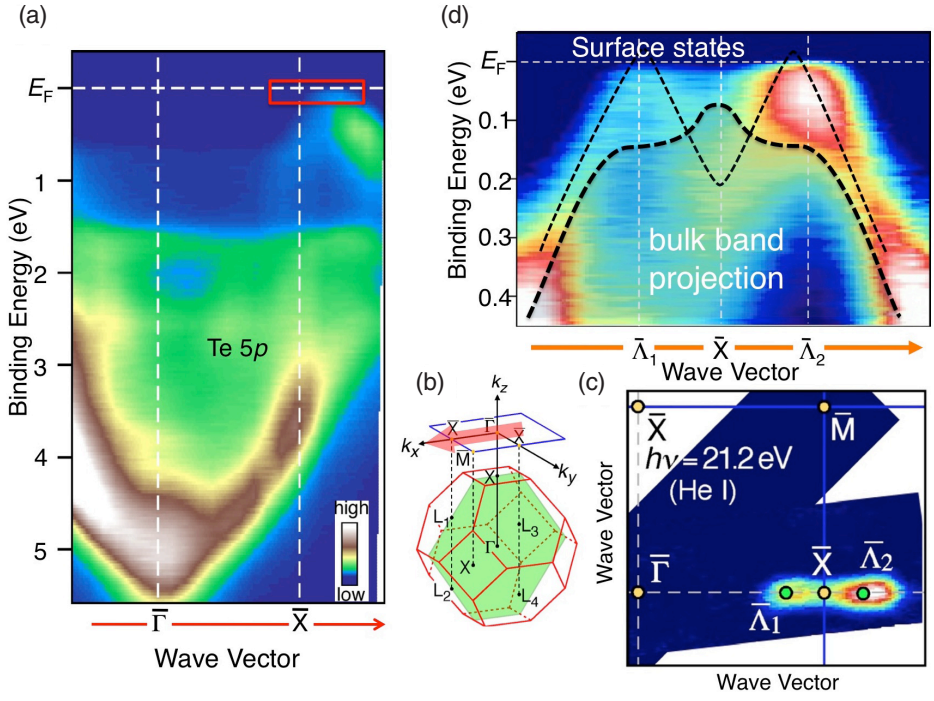

Figure 1: (a) Valence-band ARPES intensity of SnTe measured along the $\bar{\Gamma}\bar{X}$ cut. The red rectangle indicates the region where Dirac-cone dispersion exists. (b) Surface and bulk Brillouin zones of SnTe. (c) Fermi-surface mapping of SnTe. (d) Near-E_F band dispersion along the $\bar{\Gamma}\bar{X}$ cut.

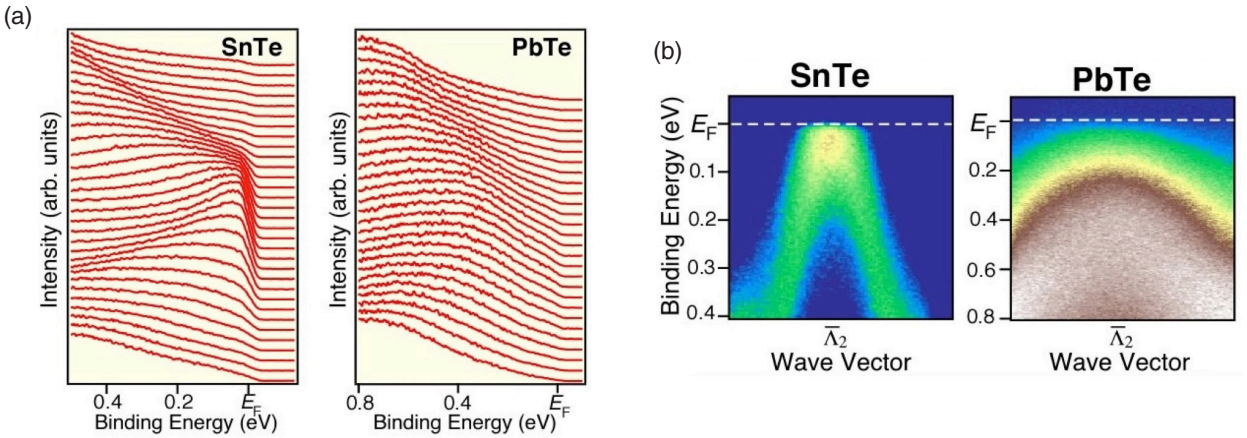

Figure 2: (a) Near-E_F ARPES spectra around the Dirac point (the $\bar{\Lambda}$ point) for SnTe and PbTe. (b) Corresponding ARPES-intensity plots.

of linearly dispersive bands crossing E_F, and the top of this Dirac-like band is located not at the $\bar{X}$ point but at a point slightly away from it (called here the $\bar{\Lambda}$ point). Such a characteristic "M"-shaped dispersion is not expected from the bulk-band calculations as can be seen from the plot of the bulk band projection [4] in Fig. 1(d), indicating that the observed Dirac-cone-like band originates from the surface states. The surface origin of the Dirac-cone band has also been confirmed by photon-energy dependent ARPES measurements where the Dirac-cone band shows negligible energy dispersion along the momentum perpendicular to the surface.

To clarify the uniqueness of SnTe among isostructural IV-VI semiconductors, we performed ARPES measurements of PbTe and directly compared the near-E_F electronic states around the Dirac point, as shown in Figs. 2(a) and (b). Intriguingly, the spectral feature of PbTe shows no evidence of the metallic Dirac-cone band, and displays only a broad feature originating from the top of the bulk valence band, suggesting that this material is an ordinary (trivial) insulator. This naturally suggests that a topological phase transition takes place in the solid-solution system $Pb_{1-x}Sn_xTe$ [6]. One can thus infer that the bulk-band gap closes at a critical x value, x_c, accompanied by a parity change of the valence-band wave function and an emergence/disappearance of the Dirac-cone surface state. Therefore, the present results have established for the first time the TCI phase in SnTe, which is in contrast to the trivial nature of isostructural PbTe. Our results unambiguously demonstrate the validity of the concept of TCI and suggest the existence of many more kinds of topological materials.

REFERENCES

[1] C.L. Kane and E.J. Mele, *Phys. Rev. Lett.* **95**, 146802 (2005).
[2] B.A. Bernevig, T.L. Hughes and S.-C. Zhang, *Science* **314**,1757 (2006).
[3] L. Fu, *Phys. Rev. Lett.* **106**, 106802 (2011).
[4] T.H. Hsieh, H. Lin, J. Liu, W. Duan, A. Bansil and L. Fu, *Nature Commun.* **3**, 982 (2012).
[5] Y. Tanaka, Z. Ren, T. Sato, K. Nakayama, S. Souma, T. Takahashi, K. Segawa and Y. Ando, *Nature Phys.* **8**, 800 (2012).
[6] Y. Tanaka, T. Sato, K. Nakayama, S. Souma, T. Takahashi, Z. Ren, M. Novak, K. Segawa and Y. Ando, *Phys. Rev. B* **87**,155105 (2013).

BEAMLINE

BL-28A

T. Sato[1], Y. Tanaka[1], Z. Ren[2], K. Nakayama[1], S. Souma[1], T. Takahashi[1], K. Segawa[2] and Y. Ando[2]
([1]Tohoku Univ., [2]Osaka Univ.)

Ordered and Foam Structures of Semifluorinated Block Copolymers in Supercritical Carbon Dioxide

We conducted *in situ* small-angle X-ray scattering (*in situ* SAXS) in supercritical carbon dioxide ($scCO_2$) using a high-pressure cell with diamond window to reveal the order-order transition (OOT) of semi-fluorinated block copolymers induced by $scCO_2$. $ScCO_2$ preferentially swells fluorinated polymers, which apparently increases the volume fraction of the fluorinated domain in block copolymers. By *in situ* SAXS, we observed swelling-induced OOT from cylinders to lamellae, and a unique transition from lamellae to a "foam" structure. This unique transition was revealed by *in situ* SAXS with a specifically designed high-pressure cell and the use of intense X-rays at the Photon Factory.

Block copolymers self-assemble into various ordered structures with 10 nm-scale periodicity, such as body-centered cubic (BCC) spheres, hexagonally-packed cylinders, lamellae, and bicontinuous structures such as gyroid [1]. The self-assembly is called microphase-separation, and is desired for applications such as bottom-up nanolithography. The structure is determined by the volume fraction of one component (f) and by the product of the interaction parameter between different domains (χ) and the degree of polymerization (N). Therefore, one method to control the structure is to change χ by tuning the temperature. Meanwhile, f is fixed for a given block copolymer, but can apparently be changed by adding components with selective affinity for one domain (*e.g.* homopolymers and selective solvents).

As a unique selective solvent, our group has been employing $scCO_2$, which is realized at 31.1ºC and 7.4 MPa or above and successfully induced OOT in semi-fluorinated block copolymers [2]. Most polymers do not dissolve in $scCO_2$ but are swollen with $scCO_2$ as a function of temperature and pressure. Among various polymers, fluoropolymers are the most CO_2-philic. Consequently, fluorinated domains in block copolymers are selectively swollen in $scCO_2$, which increases the apparent volume fraction (f_{eff}) of the fluorinated domain. In this method, f_{eff} depends on the temperature and pressure of CO_2, and so we can tune f_{eff} continuously and reversibly. In addition, CO_2 can be removed without destroying the swollen structure by freezing and gradual depressurization. During the depressurization process, the space occupied by CO_2 turns into nanopores, and hence a nanoporous structure can be obtained from the block copolymer template.

Recently we reported *in situ* analysis of CO_2-induced OOT [3]. While we have observed the frozen nanoporous structure, the swollen structure in CO_2 had not been investigated previously. Therefore, we conducted *in situ* SAXS, to reveal the swollen morphology and OOT. We used a semifluorinated block copolymer, poly(styrene-*b*-perfluorooctylethyl methacrylate) (PS-PFMA, M_n = 17,700 - 6,230 kg/mol). A custom-designed high-pressure vessel was connected with a pump and a backpressure regulator. Samples in the vessel were irradiated with X-rays through the diamond windows of the vessel. SAXS experiments were performed at BL-6A in the Photon Factory. SAXS profiles were calibrated with collagen from chicken tendon. We also prepared a frozen nanoporous sample by swelling a sample in CO_2 for 2 h at 60ºC, freezing the sample to –10ºC, and depressurizing CO_2 at a rate of 0.5 MPa/min.

Figure 1 shows SAXS profiles of PS-PFMA in CO_2 as a function of pressure. The as-cast sample showed several Bragg peaks with a peak ratio of 1 : $(3)^{1/2}$: 2, indicating a hexagonally-aligned structure. From this profile and composition ratio of PS-PFMA, we concluded that hexagonal cylinders with PFMA cores are formed in the as-cast specimen. The sample was then pressurized in CO_2 at 60ºC. At 10 MPa, the peak ratio changed to 1 : 2: 3, indicating that PFMA was preferentially swollen in CO_2 and OOT from cylinders to lamellae (a more PFMA-rich structure) was induced.

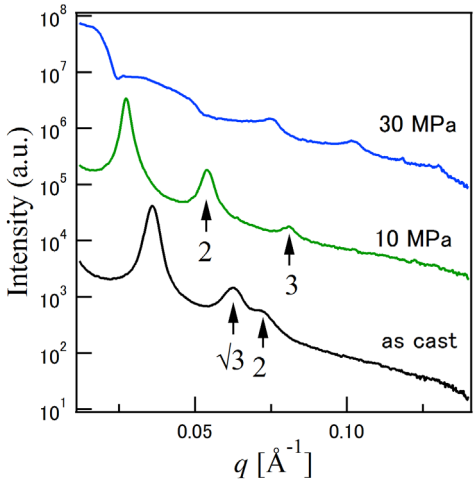

Figure 1: SAXS profiles of PS-PFMA as a function of CO_2 pressure at 60ºC. Data were taken from Ref. [3] (reproduced by permission of The Royal Society of Chemistry).

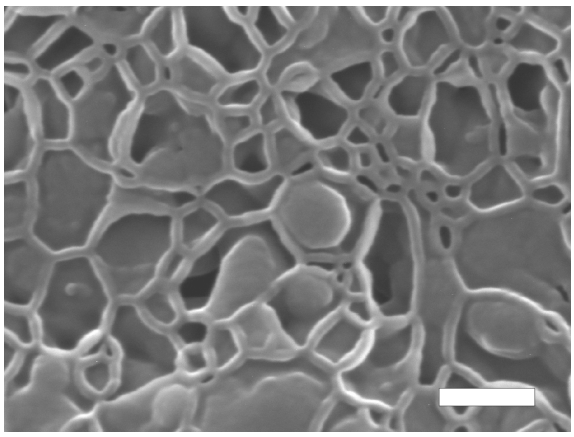

Figure 2: An SEM image of PS-PFMA treated with CO_2 at 30 MPa and at 60ºC. The horizontal scale bar indicates 200 nm.

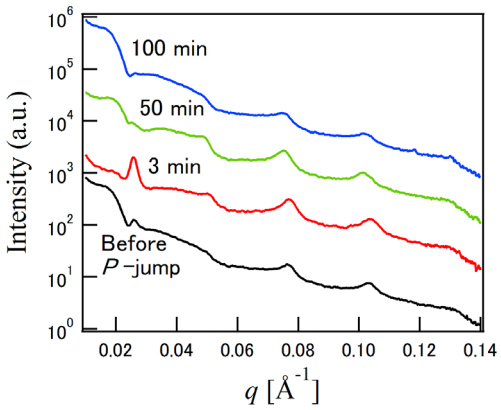

Figure 3: SAXS profiles as a function of time after pressurization from 25 to 30 MPa. 0 min denotes the time immediately before pressurization. This figure was taken from Ref. [3] (reproduced by permission of The Royal Society of Chemistry).

We raised the CO_2 pressure further, and observed that the Bragg peaks dissipated and other scattering in low-q emerged above 20 MPa. This indicates that lamellae were further transformed into another structure. From the fringe position of the new scattering pattern, we speculated that a sheet-shaped structure was formed. To confirm the structure, we prepared a nanoporous sample by freezing the swollen structure. By scanning electron microscope (SEM) measurements, we observed a "foam" structure, where PS-PFMA composes a bilayer membrane and 100 nm-scale cells are surrounded by a membrane (Fig. 2).

From SAXS experiments, we observed an intriguing pressure response of the foam. When we raised the pressure from 25 to 30 MPa stepwise, the form factor weakened temporarily and recovered gradually (see Fig. 3). This indicates that the foam structure was pressed by static pressure and returned to lamellae, and then gradually transformed into the foam again. By time-resolved SAXS with synchrotron radiation, we were able to observe not only the swollen structure, but also the unique relaxation process of the structure, such as the expansion of foam-like structures with increasing pressure.

REFERENCES

[1] V. Abetz and P.F.W. Simon, *Adv Polym. Sci.* **189**, 125 (2005).
[2] L. Li, H. Yokoyama, T. Nemoto and K. Sugiyama, *Adv. Mater.* **16**, 1226 (2004).
[3] T. Shinkai, M. Ito, K. Sugiyama, K. Ito and H. Yokoyama, *Soft Matter* **8**, 5811 (2012).

BEAMLINE

BL-6A

T. Shinkai[1], M. Ito[1], K. Sugiyama[2], K. Ito[1] and H. Yokoyama[1,3] ([1]The Univ. of Tokyo, [2]Hosei Univ., [3]PREST-JST)

Self-Energy and the Electronic Structure of Correlated Metal $SrVO_3$

The correlated electronic structure of $SrVO_3$ has been investigated by angle-resolved photoemission spectroscopy (ARPES) using *in situ* prepared thin films. Pronounced features of band renormalization have been observed as in the high-T_c cuprates, such as a sharp kink ~60 meV below the Fermi level (E_F). We have deduced the electron self-energy, which represents the interaction in a solid, in a wide energy range by applying the Kramers-Kronig relation to the photoemission spectra. The obtained self-energy indicates a large energy scale of ~0.7 eV, which is attributed to electron-electron interaction and gives rise to the incoherent peak ~1.5 eV below E_F. The present analysis enables us to obtain a consistent picture for both the high-energy incoherent state and the low-energy band renormalization.

The effect of many-body interaction on the electronic structure, such as electron correlation or electron-phonon interactions, is an important concept for understanding the physical properties of materials. In a correlated electron system, coupling of single-particle excitations with collective excitations such as phonons, leads to a pronounced energy-dependent band renormalization, a so-called kink, in the band dispersion. In the high-T_c cuprate superconductors, a kink has been observed around 60 meV below E_F [1] by angle-resolved photoemission spectroscopy (ARPES) and the origin of the kink has been under debate for a long time. Studies of kinks in transition-metal oxides other than the cuprates would give useful information.

$SrVO_3$ (SVO) is a perovskite-type transition-metal oxide (TMO) and is a prototypical Mott-Hubbard-type system with the d^1 electronic configuration. Therefore, SVO is an ideal system to study the fundamental physics of electron correlation and has been extensively studied by photoemission spectroscopy measurements. Recently, quasi-particle (QP) bands of SVO have been clearly observed by ARPES with the aid of the high-quality films having atomically flat surfaces grown by the pulsed laser deposition (PLD) technique [2, 3]. Here, we present an ARPES study of SVO epitaxial thin films and reveal a kink in the QP band dispersion as well as the self-energy in a wide energy range [4].

The chemical composition of SVO thin films was checked by core-level photoemission spectra measured at BL-2C and the ARPES measurements were performed at BL-28A. Correlation effects in the QP spectra were closely examined for the nearly two-dimensional d_{xy} band. An image plot of the d_{xy} band in energy-momentum space is shown in Fig. 1. There are two main features near E_F: the coherent part (the sharp QP peak within ~0.5 eV of E_F) and the broad incoherent part (often regarded as the remnant of the lower Hubbard band centered ~1.5 eV below E_F). As shown in Fig. 2(a), a kink is seen at around 60 meV below E_F very similar to those observed in the high-T_c cuprate superconductors. The kink in the high-T_c cuprates was associated with the oxygen half-breathing phonon mode of 60 meV by Lanzara *et al.* [1], while antiferromagnetic fluctuations and/or the magnetic resonance mode [5] have also been proposed as possible origins of the kink. Since SVO, unlike the cuprates, does not have low-energy spin fluctuations, the kink observed in the present study is likely due to a coupling of electrons with these phonon modes characteristic to the perovskite oxides.

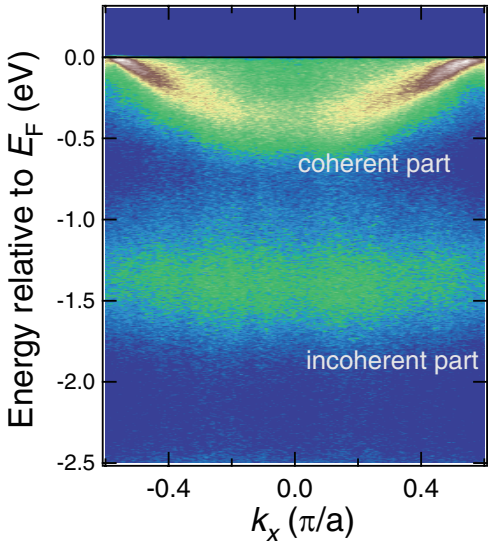

Figure 1: ARPES spectra of SrVO3 along the kx direction taken at the photon energy of 66 eV with linear polarization. The clear band dispersion near EF is the dxy band.

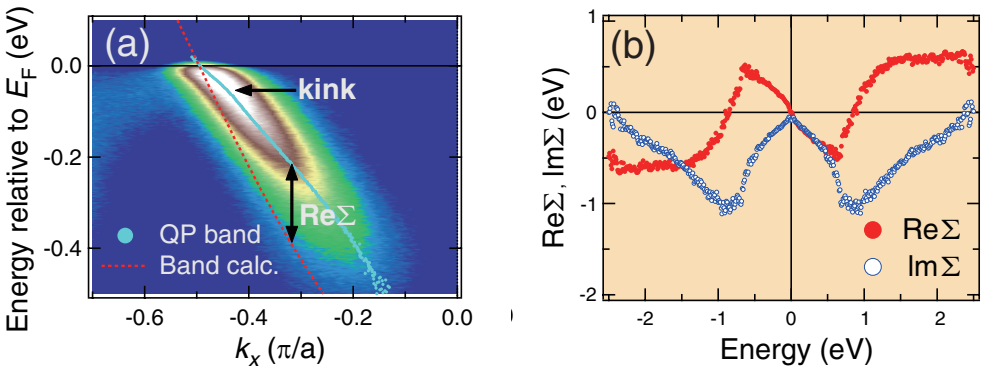

Figure 2: Band dispersions and self-energies in the vicinity of the Fermi level. (a) QP band dispersions are determined by the peak positions (blue dots). The position of the kink at 60 meV is shown by an arrow. The noninteracting band given by the band-structure calculation is shown by red curves. The real part of the self-energy ReΣ can be obtained as the difference between the QP band dispersion and the noninteracting band dispersion. (b) Self-energy deduced from the measured ARPES spectra using the KK transformation.

Not only the kink in the low energy scale, but also the high-energy incoherent structure has been examined by deducing the self-energy Σ(ω) in the high energy region. In the conventional method, the real part of the self-energy ReΣ can be obtained as the difference between the QP band dispersion and the noninteracting band dispersion as described in Fig. 2(a). However, the obtained self-energy Σ(ω) is limited to ~0.5 eV below E_F, which is the energy range of the coherent part, while the behavior of the self-energy over a wider energy range including the incoherent part needs to be clarified to understand the role of electron correlation. Therefore, we have developed a new method to deduce the self-energy in a wider energy range using the Kramers-Kronig (KK) relation [4].

Figure 2(b) shows the experimentally deduced self-energy ReΣ(ω) and ImΣ(ω) using the KK relation. The deduced self-energy shows remarkably similar behavior to the self-energy calculated for SVO by the dynamical-mean-field-theory method [6]. The self-energy ReΣ(ω) shows a large energy scale of 0.7 eV reflecting electron-electron interaction and giving rise to the incoherent peak 1.5 eV below E_F. The present result provides a self-consistent procedure to experimentally deduce the self-energy in correlated electron systems; this procedure will be useful for future studies of strongly electron correlated systems such as the high-T_c superconductors.

REFERENCES

[1] A. Lanzara, P.V. Bogdanov, X.J. Zhou, S.A. Kellar, D.L. Feng, E.D. Lu, T. Yoshida, H. Eisaki, A. Fujimori, K. Kishio, J.-I. Shimoyama, T. Noda, S. Uchida, Z. Hussain and Z.-X. Shen, *Nature* **412**, 510 (2001).
[2] M. Takizawa, M. Minohara, H. Kumigashira, D. Toyota, M. Oshima, H. Wadati, T. Yoshida, A. Fujimori, M. Lippmaa, M. Kawasaki, H. Koinuma, G. Sordi and M. Rozenberg, *Phys. Rev. B* **80**, 235104 (2009).
[3] K. Yoshimatsu, K. Horiba, H. Kumigashira, T. Yoshida, A. Fujimori and M. Oshima, *Science* **333**, 319 (2011).
[4] S. Aizaki, T. Yoshida, K. Yoshimatsu, M. Takizawa, M. Minohara, S. Ideta, A. Fujimori, K. Gupta, P. Mahadevan, K. Horiba, H. Kumigashira and M. Oshima, *Phys. Rev. Lett.* **109**, 056401 (2012).
[5] P.D. Johnson, T. Valla, A.V. Fedorov, Z. Yusof, B.O. Wells, Q. Li, A.R. Moodenbaugh, G.D. Gu, N. Koshizuka, C. Kendziora, Sha Jian and D.G. Hinks, *Phys. Rev. Lett.* **87**, 177007 (2001).
[6] I.A. Nekrasov, K. Held, G. Keller, D.E. Kondakov, Th. Pruschke, M. Kollar, O.K. Andersen, V.I. Anisimov and D. Vollhardt, *Phys. Rev. B* **73**, 155112 (2006).

BEAMLINES

BL-28A and BL-2C

T. Yoshida[1], S. Aizaki[2], K. Yoshimatsu[2], M. Takizawa[2], M. Minohara[2], S. Ideta[2], A. Fujimori[2], K. Gupta[3], P. Mahadevan[3], K. Horiba[4], H. Kumigashira[4], and M. Oshima[2], ([1]Kyoto Univ. [2]The Univ. of Tokyo, [3]SNBNCB, [4]KEK-PF)

Anisotropic Thermal Expansion and Cooperative Invar/ Anti-Invar Effects in MnNi Alloy

Thermal expansion of a tetragonal $Mn_{88}Ni_{12}$ alloy, which exhibits significant anisotropy, was investigated by EXAFS and path-integral quantum mechanical simulations. The EXAFS reveals that the Mn local environment is actually tetragonally distorted, while the Ni one retains its inherent cubic-like symmetry. The large thermal expansion along the *a* axis originates from the anti-Invar effect, while the negligibly small thermal expansion along the *c* axis originates from the cooperative Invar effect. Namely, the tetragonally distorted more stable antiferromagnetic Mn state gives a significantly smaller (slightly longer) atomic radius along *a* (*c*) than that of the spherical paramagnetic state.

An Invar alloy $Fe_{66}Ni_{34}$ that shows anomalously small thermal expansion over a wide temperature range was discovered by Guillaume in 1897 [1]. The Invar effect has been utilized in various kinds of precision devices and instruments such as semiconductor and flat-panel-display manufacturing systems, molded imprints, astronomical telescopes and so forth. In a phenomenological model of the Invar effect, there exist at least two types of electronic states in Fe, typically called high-spin (HS) and low-spin (LS) states [2]. In this two-state model, the HS state with a larger atomic radius is slightly more stable at a temperature of 0 K than the LS state. This results in the compensation of thermal expansion due to increasing density of the LS state at higher temperature. However, the detailed origin of the Invar effect is the subject of much discussion even today. In recent electronic structure calculations based on the density-functional theory [3], a much more complicated electronic structure was proposed, where non-collinear magnetic moments with different magnitudes are distributed, depending on the local environment. On the other hand, the thermal expansion was very recently investigated from a different viewpoint of thermal vibration, by combining temperature-dependent EXAFS measurements with the path integral effective classical potential (PIECP) Monte-Carlo (MC) simulations [4]. In this work, cooperative anisotropic thermal expansion in face-centered tetragonal (fct) $Mn_{88}Ni_{12}$ alloy was studied, where one axis shows the Invar effect and the other shows the anti-Invar effect [5].

In this work, we performed temperature-dependent Mn and Ni K-edge EXAFS measurements at BL-9C using the transmission mode. The temperature range of the EXAFS measurements was 11-300 K. Powder XRD measurements were also performed by using laboratory equipment. The 113 and 311 diffractions were mainly used to determine the fct lattice constants *a* and *c*.

Figure 1 gives the bond distances around Mn and Ni determined by EXAFS. The analysis clearly shows that the environment around Mn is really tetragonally distorted with meaningfully different bond distances between Mn(*l*) and Mn(*s*). On the other hand, the environment around Ni is regarded as cubic because of a negligible difference between Ni(*l*) and Ni(*s*). It should be noted here that in spite of the fact that the average X-ray structure is fct, the local structures of Mn and Ni

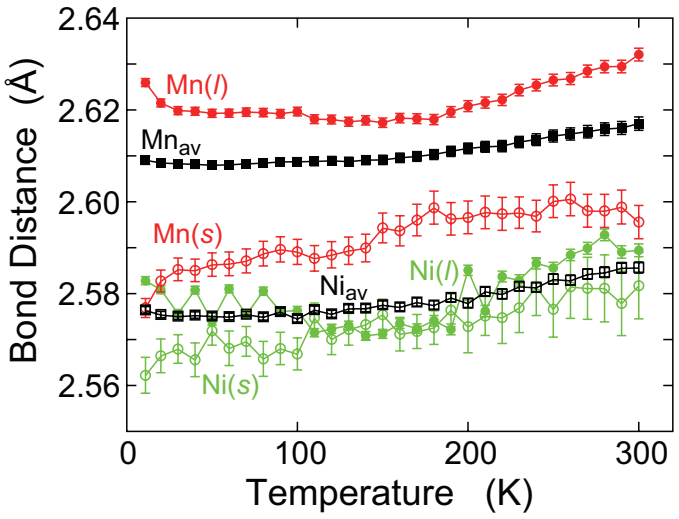

Figure 1: Experimental bond distances in $Mn_{88}Ni_{12}$ determined by Mn and Ni *K*-edge EXAFS. *l*, *s*, and av denote the longer and shorter bonds and the average, respectively.

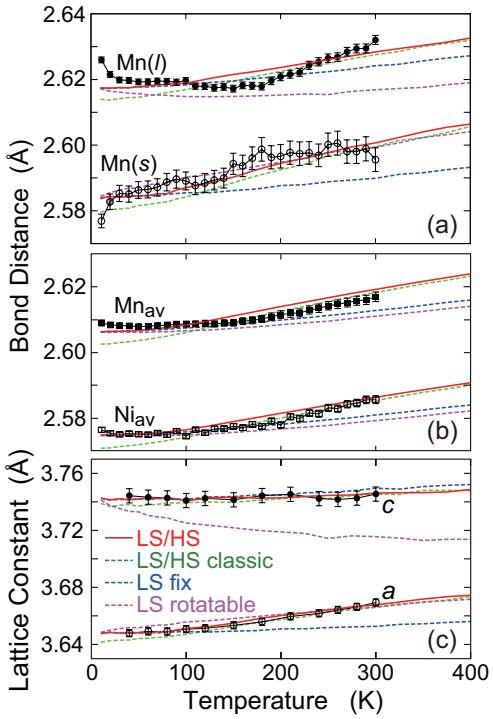

Figure 2: Simulated bond distances for (a) Mn(*l*) and Mn(*s*) and (b) Mn_{av} and Ni_{av}, and (c) fct lattice constants *a* and *c*, together with the experimental EXAFS and XRD data with error bars. Four kinds of simulated results are depicted: the quantum LS-HS model (red solid line), the classic LS-HS model (green dashed), the tetragonal-axis fixed LS model (blue dashed), and the tetragonal-axis rotatable model (purple dashed).

determined by EXAFS are essentially different. Figure 2 gives the experimental and PIECP-simulated results for the bond distances and the lattice constants. In the lattice constants in Fig. 2(c), *a* (*a*<*c*) shows somewhat larger thermal expansion than usually expected, while the lattice constant *c* exhibits almost no thermal expansion, indicating cooperative Invar/anti-Invar effects. It is clearly found that in the PIECP simulations, the LS/HS two-state model successfully reproduces all the experimental lattice constants and bond distances. In the tetragonal-axis rotatable LS model, the calculated lattice constant *c* gradually decreases with temperature, while the experiment shows nearly no thermal expansion. In the tetragonal-axis fixed LS model, where only the Mn LS state is allowed and the Mn axis is fixed at [001], thermal expansion of the lattice constant a is estimated to be too small compared to the experiments. The classic LS/HS model is rather good, but the lattice constants are erroneously temperature dependent even at low temperature, implying the importance of the vibrational quantum effect. In the quantum mechanical LS/HS model, the bond distances as well as the lattice constants agree quite well with the experimental results. This confirms that the two inequivalent bonds in EXAFS are regarded as the bonds within the *bc*/*ca* and *ab* planes. Consequently, the present anisotropic thermal expansion is explained by the cooperative Invar/anti-Invar effects in the Mn atom, where the tetragonally distorted more stable LS Mn state gives a smaller atomic radius within the *ab* plane and a larger radius along the *c* axis than the spherical one of the HS state.

In summary, the fct lattice constant *a* (*a*<*c*) shows somewhat larger thermal expansion than usual, while the lattice constant *c* exhibits almost no thermal expansion. This behavior is explained by the cooperative Invar/anti-Invar effects in the Mn atom, where the tetragonally distorted Mn state coupled antiferromagnetically to the neighboring atoms is more stable than the spherical paramagnetic HS state and as a result, gives a significantly smaller atomic radius within the *ab* plane and a slightly larger radius along the *c* axis than the spherical one of the HS state. The present observation is not a rare case; similar thermal expansion behaviors can be seen in $Mn_{87}Pd_{13}$ and $Mn_{85}Zn_{15}$, although they have not been discussed so far. Mn atoms are tetragonally distorted associated with the lattice distortion, while Ni atoms retain cubic symmetry. From the local point of view, it is not unusual that different structural behaviors in randomly distributed different elements are observed. It should be noted that XRD gives only the average structure and the local structure is not always the same in random alloy/solid solution systems. Recently, there have been reports on several kinds of metal alloys that exhibit anomalous thermal expansion properties like negative or zero thermal expansion. Since these works have focused on the lattice thermal expansion, it will be interesting to investigate the thermal expansion from the present viewpoint of local thermal expansion.

REFERENCES

[1] C.E. Guillaume, *C. R. Acad. Sci.* **125**, 235 (1897); E.F. Wasserman, *Ferromagnetic Materials*, edited by K.H.J. Bushow and E.P. Wohlfarth (Elsevier Science Publishers B.V., 1990). Vol. **5**, 237.
[2] R.J. Weiss, *Proc. R. Soc. Lond. A* **82**, 281 (1963).
[3] M. van Schilfgaarde, I.A. Abrikosov and B. Johansson, *Nature* **400**, 46 (1999).
[4] T. Yokoyama and K. Eguchi, *Phys. Rev. Lett.* **107**, 065901 (2011).
[5] T. Yokoyama and K. Eguchi, *Phys. Rev. Lett.* **110**, 075901 (2013). This work was introduced as an IMSS topic in http://imss.kek.jp/news/2013/topics/0207invar/index.html and also in Japanese newspapers of Nikkan Kogyo Shimbun (Feb. 8, 2013) and in Kagaku Shimbun (Feb. 22).

BEAMLINE

BL-9C

T. Yokoyama[1,2] and K. Eguchi[2] ([1]IMS, [2]The Grad. Univ. for Adv. Stud.)

Structural Study of a Purely Organic Single-Component Metal with Symmetric Hydrogen Bond

Purely organic materials are generally insulating. Here, we report a new type of purely organic single-component molecular conductor that utilizes strong hydrogen-bonding interactions between tetrathiafulvalene-based electron-donor molecules. We found that these conductors are composed of highly symmetric molecular units constructed by strong intra-unit hydrogen bonding, and that charge carriers are produced by the partial oxidation of the donor molecules and delocalized through the formation of symmetric intra-unit hydrogen bonds. To the best of our knowledge, our conductors show the highest room-temperature electrical conductivity and the metallic state under the lowest physical pressure among purely organic single-component systems.

The realization of purely organic single-component molecular metals has been a long-standing open problem in chemistry, physics, and materials science. As is well known, purely organic materials are normally insulating. Recently, we unveiled a new type of purely organic single-component molecular conductor based on a catechol-fused ethylenedithiotetrathiafulvalene, H_2Cat-EDT-TTF, and its diselena analogue, H_2Cat-EDT-ST, which were designed and synthesized by us [1]. These conductors are unprecedented single-component systems composed of molecular units, H_3(Cat-EDT-TTF)$_2$ and H_3(Cat-EDT-ST)$_2$, with a highly symmetric intra-unit hydrogen bond. The higher electrical conductivity observed in our systems is attributed to the hydrogen bond-promoted delocalization of charge carriers, which are generated through the partial oxidation of the H_2Cat-EDT-TTF and H_2Cat-EDT-ST molecules [2].

A new type of purely organic single-component molecular conductors, κ-H_3(Cat-EDT-TTF)$_2$ and κ-H_3(Cat-EDTST)$_2$, hereinafter described as κ-S and κ-Se, respectively, were obtained as black plate-like crystals by electrochemical oxidation of the corresponding donor molecules, H_2Cat-EDT-TTF and H_2Cat-EDT-ST, in the presence of the base, 2,2'-bipyridine. Crystal structure analysis was carried out at PF BL-8A. The minimal molecular unit, the H_3(Cat-EDT-TTF)$_2$ composition (Fig. 1), is established by the formation of an intra-unit hydrogen bond, O..H..O, between the catechol moieties of the donor molecules, where the one hydroxyl proton is deprotonated. The oxygen–oxygen distance in the hydrogen bond, d(O..O), is 2.486(5) Å and 2.509(8) Å at room temperature, and 2.453(5) Å and 2.443(8) Å at 50 K and 30 K for κ-S and κ-Se, respectively, which are much shorter than the length of the normal O-H..O type hydrogen bond, d(O..O) 2.7-3.0 Å. Because of this strong hydrogen bonding nature, the bonded hydrogen atom is located at nearly the center between two oxygen atoms, in contrast to the asymmetric hydrogen distribution in normal hydrogen bonds. The minimal molecular units are assembled into the purely organic single-component crystal.

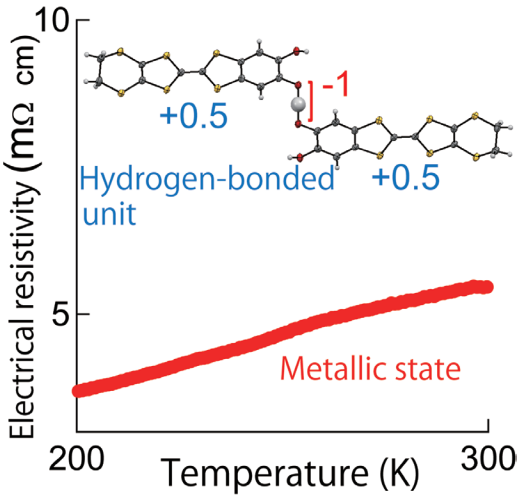

Figure 1: Structure of the molecular unit and the metallic state under ~1 GPa in the purely organic single-component conductor, k-H_3(Cat-EDT-ST)$_2$. The hydrogen bonding unit is open-shell and neutral since the oxidized TTF parts are +0.5 and the [O-..H+..O-] hydrogen bonding part is –1.

The electrical conductivity at room temperature is significantly high, 3.5 and 19 S cm^{-1} for κ-S and κ-Se, respectively. To the best of our knowledge, these values are one or two orders of magnitude higher than the highest reported value, $\sigma_{rt} = 10^{-1}$ S cm^{-1}, among purely organic single-component systems. We observed dramatic changes in the temperature variation in the electrical resistivity under pressure for κ-Se. At pressures above 1.3 GPa, the electrical resistivity monotonically decreases with reducing temperature down to around 150 K, in striking contrast with the semiconducting behavior at ambient pressure, although the resistive curve starts to increase at low temperature. Thus, the metallic states emerge with suppression of the semiconducting energy gap by applying a pressure of only ~1 GPa. We believe this is the lowest metallization pressure among purely organic single-component systems.

Our system demonstrates that the symmetric hydrogen bond constructs a new type of purely organic single-component molecular conductor composed of highly symmetric molecular units. Moreover, we found that the formation of the symmetric hydrogen bond promoted the intermolecular delocalization of the generated carriers, associated with the enhancement of the electrical conductivity. We believe that our new type of molecular conductors with symmetric intra-unit hydrogen bond will lead to the first purely organic single-component molecular metal at ambient pressure. A tetraselenafulvalene (TSF)-type analogue, in which all the sulfur atoms in the TTF part of the present system are replaced with selenium atoms, is a promising candidate for the ambient-pressure metal, because the intermolecular interactions are expected to be further enhanced.

REFERENCES

[1] H. Kamo, A. Ueda, T. Isono, K. Takahashi and H. Mori, *Tetrahedron Lett.*, **53**, 4385 (2012).
[2] T. Isono, H. Kamo, A. Ueda, K. Takahashi, A. Nakao, R. Kumai, H. Nakao, K. Kobayashi, Y. Murakami and H. Mori, *Nature Commun.*, **4**, 1344 (2013).

BEAMLINE

BL-8A

H. Mori[1], T. Isono[1], A. Ueda[1], K. Takahashi[2], A. Nakao[3], R. Kumai[4], H. Nakao[4], K. Kobayashi[4] and Y. Murakami[4]
([1]The Univ. of Tokyo, [2]Kobe Univ., [3]CROSS, [4]KEK-PF/CMRC)

X-Ray Photo-Induced Phase Transition Enabled by Impurity Doping in Layered Manganite

In the charge-orbital order (COO) phase of perovskite manganite $Pr_{0.7}Ca_{0.3}MnO_3$, photo-conversion phenomena have been observed, such as a melting of the COO phase by X-ray irradiation, which corresponds to the transition from the COO phase to a charge-orbital disordered phase. In contrast, the X-ray photo-induced effect has not been observed in impurity undoped layered perovskite manganite $La_{0.5}Sr_{1.5}MnO_4$. In this study, we investigated the effect of impurity doping on the X-ray photo-induced phenomena in Fe-doped layered perovskite manganite $La_{0.5}Sr_{1.5}Mn_{0.97}Fe_{0.03}O_4$.

Phase transition triggered by light irradiation, or so-called photo-induced phase transition (PIPT), has attracted much research for photonic and materials science. Many PIPT materials have been found to exhibit novel transient phases not observed in thermal equilibrium. In general, the photo-induced phases are rather unstable and their lifetimes are very short, typically being between picoseconds and microseconds. To achieve a persistent photo-induced phase conversion, the initial and final states should be separated by a high potential barrier. If the free energy allows bistability between the initial and final phases, photo-excitation may induce phase conversion beyond the potential barrier between the two phases by the assistance of cooperative interactions in photo-excited states.

Impurity undoped $La_{0.5}Sr_{1.5}MnO_4$ is a typical crystal showing the charge-orbital order (COO) and CE-type antiferromagnetic (AFM) phase with inherent phase competition with the ferromagnetic (FM) phase (Fig. 1). In the AFM/COO phase, photo-conversion phenomena have been observed, such as a partial melting of the COO phase by X-ray irradiation, which corresponds to the transition from the COO phase to a charge-orbital disordered (DO) phase. In this study, we investigated X-ray PIPT phenomena in Fe-doped layered perovskite manganite $La_{0.5}Sr_{1.5}Mn_{0.97}Fe_{0.03}O_4$. The substitution of Mn ions with Fe ions would destroy the CE-type AFM order locally and form a small FM cluster, and finally the phase-separated state between the AFM/COO and FM/DO phases would be realized. The doping impurity, as a quenched disorder, may have the effect of enhancing the photo-conversion effect and lowering the threshold for the emergence of PIPT.

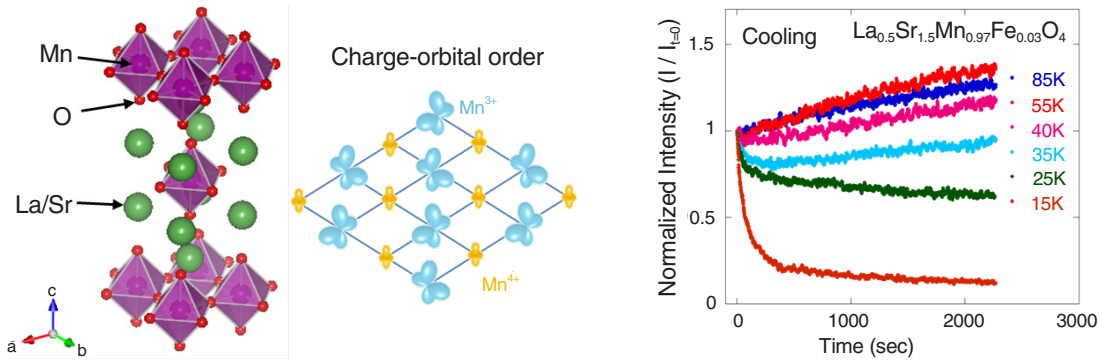

Figure 1: (left panel) Schematic of crystal structure and charge-orbital order in $La_{0.5}Sr_{1.5}MnO_4$. (right panel) The X-ray exposure time dependence of OO intensities for (1/4 7/4 0) in $La_{0.5}Sr_{1.5}Mn_{0.97}Fe_{0.03}O_4$. The incident X-ray energy was tuned to 6.5 keV and the X-ray photon flux was 2.5×10^{16} photons/m^2s.

It was revealed that 3% doping of Fe for Mn reduces the orbital order (OO) intensity by ~1/30, indicating that only a few percent of the Fe ions, functioning as quenched disorders, effectively suppress the long-range OO phase. Accordingly, this doping induces a weak ferromagnetism (FM) below 40 K. The produced ferromagnetism is subject to the magnetic field annealing effect, where the value of the saturation moment smoothly increases with an increase in the annealing magnetic field, which is generic of phase-separated states.

We found that impurity doping leads to dramatic enhancement of the X-ray induced effect. As shown in Fig. 1, the OO intensity for (1/4 7/4 0) reflection decreases during X-ray exposure with negligible incubation time below 35 K. The ac susceptibility is enhanced during X-ray exposure at 15 K, indicating that X-ray PIPT corresponds to phase conversion from the OO phase to the FM phase. In contrast, a reverse phase conversion from the FM phase to the OO phase was observed above 40 K (Fig. 1). As a consequence, this material exhibits persistent and bidirectional X-ray induced phase transition, whose direction is switched with varying temperature.

The initial state can be considered to be a metastable state protected by a potential barrier from which the incident X-ray can induce transition to the thermodynamically stable state. Switching of the direction of X-ray PIPT can be elucidated by postulating an alteration of the most stable state with varying temperature. In the present case, impurity doping plays a crucial role in forming the phase separated state and also in determining the rate of X-ray PIPT. Tuning of the impurity concentration and selection of the dopant element may provide fertile ground for clarifying X-ray PIPT phenomena and discovering new PIPT materials.

REFERENCE

[1] Y. Yamaki, Y. Yamasaki, H. Nakao, Y. Murakami, Y. Kaneko and Y. Tokura, *Phys. Rev. B* **87**, 081107 (R) (2013).

BEAMLINES

BL-3A and BL-4C

Y. Yamaki[1], Y. Yamasaki[1], H. Nakao[1], Y. Murakami[1], Y. Kaneko[2] and Y. Tokura[2,3] ([1]PF-CMRC, [2]RIKEN-CEMS and [3]The Univ. of Tokyo)

Three-Way Switching in a Multifaceted [CoFe] Chain

The drive to develop new materials that show *bistability*, that is, the ability to exist in more than one stable physical state under identical environmental conditions, is stimulated by the potential applications that such materials may have in future switching or data storage technologies. A heterometallic cobalt-iron ([CoFe]) chain complex was synthesized and found to be thermally-convertible between paramagnetic semiconducting and diamagnetic insulating phases and to display photo-switchable single chain magnetism at low temperatures. The *multibistability* of electronic and magnetic properties shown by the [CoFe] complex opens up exciting possibilities for the future of nano-scale switchable components.

Cyanide ions can act as linear bridges between metal ions, mediating significant electronic and magnetic coupling between nearest neighbors. Some multinuclear cyanide-bridged transition metal clusters can have more than one stable state (electronic, magnetic, chromic, etc.) under identical physical conditions. Such materials can be described as displaying *bistability*, and have the potential to operate as nano-scale switches: their states are interconverted upon application of appropriate external stimuli (heat, light, pressure, etc.). In particular, heterometallic iron/cobalt cyanide-bridged compounds can display a phenomenon termed electron-transfer-coupled spin transition (ETCST), in which a paramagnetic Co^{II}(HS)-Fe^{III}(LS) (HS = high spin state, LS = low spin state) high-temperature (HT) phase can be reversibly converted to a diamagnetic Co^{III}(LS)-Fe^{II}(LS) state at low temperature (LT) as a result of $Co^{II} \rightarrow Fe^{III}$ electron transfer and subsequent Co^{III} spin state transition (HS→LS). The transition can be reversed at very low temperatures if the sample is irradiated by light of sufficient energy, allowing a meta-stable (HT*) magnetic phase to be trapped [1]. This research aimed to investigate the interplay between electronic conductivity (and/or permittivity) and ETCST, an area as yet unexplored for molecular ETCST-active systems but with great potential importance in future switching technologies.

A chiral heterometallic chain coordination polymer was synthesized, in which cobalt and iron building blocks were combined in a square-wave type structure (Fig. 1) [2]. The [CoFe] chain showed thermal ETCST with wide hysteresis between a paramagnetic HT phase and a diamagnetic LT phase at close to room temperature. Single-crystal X-ray diffraction data collected at BL-8B at the Photon Factory meant that the structural changes associated with the HT→LT transition could be followed in a single crystal, thus elucidating the effects of the ETCST phenomenon. The [CoFe] chain also showed light-induced ETCST to a meta-stable HT* phase at low temperature, in which it displayed single chain magnet (SCM) properties. Thus the complex could be converted to two distinct states, HT and HT*, from the LT state.

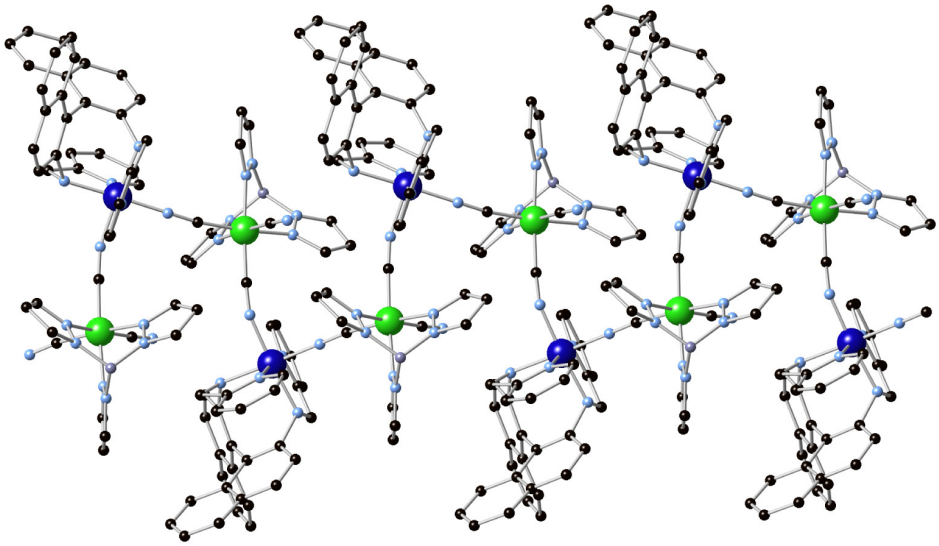

Figure 1: X-ray determined crystal structure of the [CoFe] chain (collected on BL-8B). Iron ions in green and cobalt in blue.

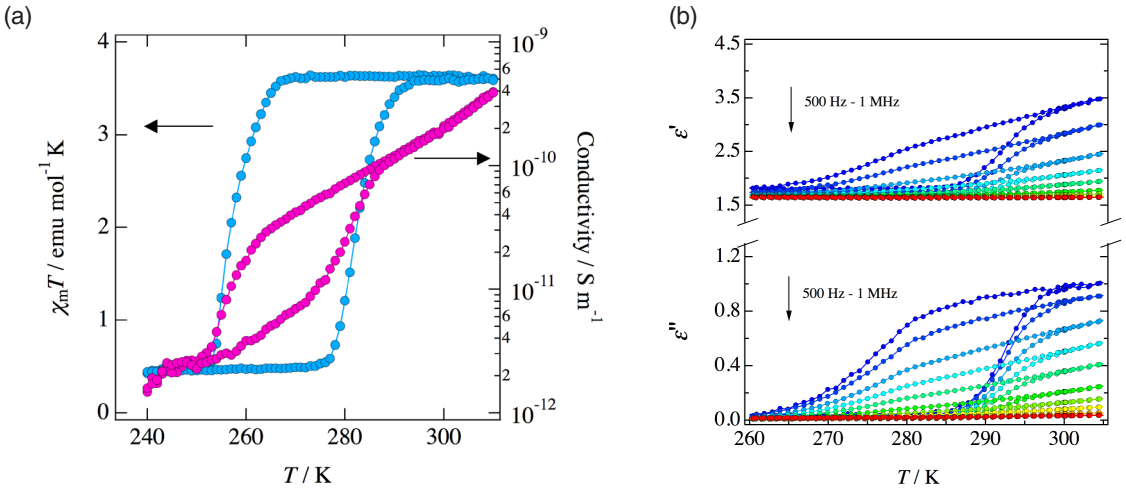

Figure 2: (a) Temperature dependences of the dc conductivity (pink) and magnetic susceptibility (blue) of the [CoFe] chain; (b) frequency dependence of the dielectric constant (ε') and dielectric loss (ε") versus temperature.

The one-dimensional nature of the chain, coupled with the observation of thermal ETCST, made it an interesting candidate to investigate the effects of the intermetallic electron transfer and associated dipolar switching on its conductivity and permittivity. The temperature dependence of the dc conductivity (σ_{dc}) and magnetic susceptibility were measured simultaneously (Fig. 2), and the data indicated a strong correlation between magnetic HT→LT transition and semiconductor to insulator phase transition. The conductivity measurements exhibited a wide hysteresis loop with an activation energy of 0.38 eV.

The dielectric response was also measured in the thermal ETCST temperature range, and exhibited a similar hysteretic response, likely brought about by the flipping of the dipolar orientations from Co^{II}→Fe^{III} to Fe^{II}→Co^{III} as the electron-transfer processes occurred. By fitting the frequency dependence of the permittivity to a modulus model, the group determined the activation energy (of the relaxation of the dipolar orientations) to be 0.42 eV. The similarity of the two activation energies obtained from the measured data suggests that the charge carrier overcomes the same energy barrier in both conduction and relaxation modes, and that the conduction and permittivity responses rely upon the thermal ETCST.

This is the first example of a link between ETCST and electric conductivity and permittivity in a molecular species, and illustrates the complementary manner in which different physical properties can be combined in switchable coordination compounds, and how different stimuli can be used to access contrasting electronic states. This result may pave the way for the rational design of low-dimensional materials with novel functionalities and applications as multiresponsive components in future technologies.

REFERENCES

[1] G.N. Newton, M. Nihei and H. Oshio, *Eur. J. Inorg. Chem.* **2011**, 3031 (2011).
[2] N. Hoshino, F. Iijima, G.N. Newton, N. Yoshida, T. Shiga, H. Nojiri, A. Nakao, R. Kumai, Y. Murakami and H. Oshio, *Nat. Chem.* **4**, 921 (2012).

BEAMLINE

BL-8B

N. Hoshino[1], F. Iijima[1], G.N. Newton[1], N. Yoshida[1], T. Shiga[1], H. Nojiri[2], A. Nakao[3], R. Kumai[3], Y. Murakami[3] and H. Oshio[1] ([1]Univ. of Tsukuba, [2]Tohoku Univ.,[3]KEK-PF)

Real-Time Observation of Molecular Orientation during the Adsorption Process by Means of Wavelength-Dispersive X-Ray Absorption Spectroscopy with Polarization Switching

A novel technique has been developed by combining wavelength-dispersive X-ray absorption spectroscopy with switching between the vertical and horizontal linear polarizations, and the molecular orientation of NO and N_2O during adsorption on Ir(111) is observed. It is revealed that NO adsorbs keeping its molecular axis at ~20° from the surface normal during the whole adsorption process. In contrast, the adsorption process of N_2O consists of three periods according to its coverage. Up to 2/3 of the saturation coverage, the orientation angle of N_2O is almost constant at ~35°. Then the average orientation angle gradually increases to ~40° until the N_2O coverage reaches ~4/5 of its saturation, and very slowly increases to ~45° at the saturation coverage. Such a complicated behavior is interpreted by assuming different adsorption sites.

X-ray absorption spectroscopy (XAS) is one of the most powerful techniques to distinguish chemical species on the surface and to determine the orientation as well as the amount of adsorbed molecules. It is necessary to measure at least two XAS data with two different linear polarizations, or to rotate the sample at a fixed polarization, in order to determine the molecular orientation. Therefore, real-time observation of the molecular orientation during an unrepeatable process, e.g., a surface chemical reaction, is quite difficult by using the conventional step-by-step energy scan. We have achieved real-time observation of the molecular orientation by combining two experimental techniques: polarization switching and wavelength-dispersive XAS [1]. The technique for switching between vertical and horizontal linear polarizations, as well as between right and left circular polarizations, had been developed at BL-16A, by installing two APPLE-II type undulators in the tandem configuration and by modulating the electron orbit through the undulators [2]. On the other hand, the time resolution of the wavelength-dispersive XAS technique in the soft X-ray region, by which the XAS data is recorded without the energy scan, had been improved to 33 ms/spectrum [3]. We have applied this novel technique to the adsorption process of NO and N_2O on an Ir(111) surface.

Figure 1 shows series of N K-edge XAS data for the vertical and horizontal linear polarizations taken during the adsorption process, which were obtained by using 1-Hz switching. Here, the vertical polarization corresponds to the *s* polarization, in which the electric vector of the X-rays lies in the surface plane, while the angle between the electric vector and the surface normal is 55° for the horizontal polarization, which is called the "magic angle".

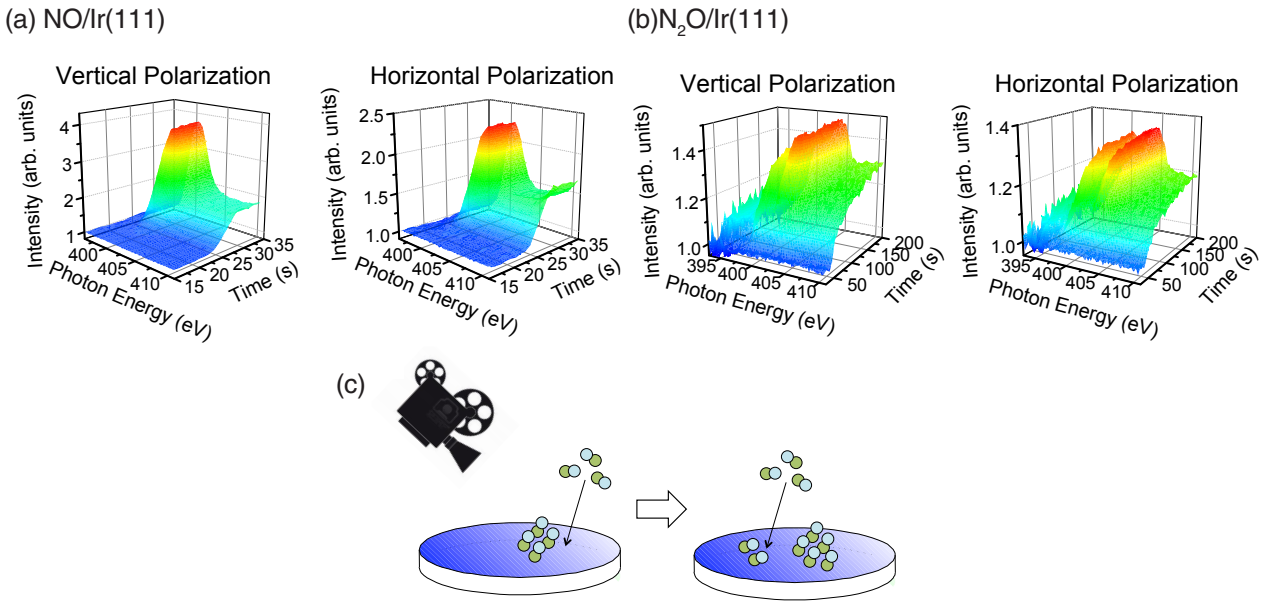

Figure 1: Series of N K-edge XAS data for vertical and horizontal polarizations simultaneously taken by using 1-Hz polarization switching during exposure of the Ir(111) surface to (a) 5×10^{-8} Torr NO and (b) 1×10^{-7} Torr N_2O, and (c) schematic illustration of the real-time observation of the molecular orientation.

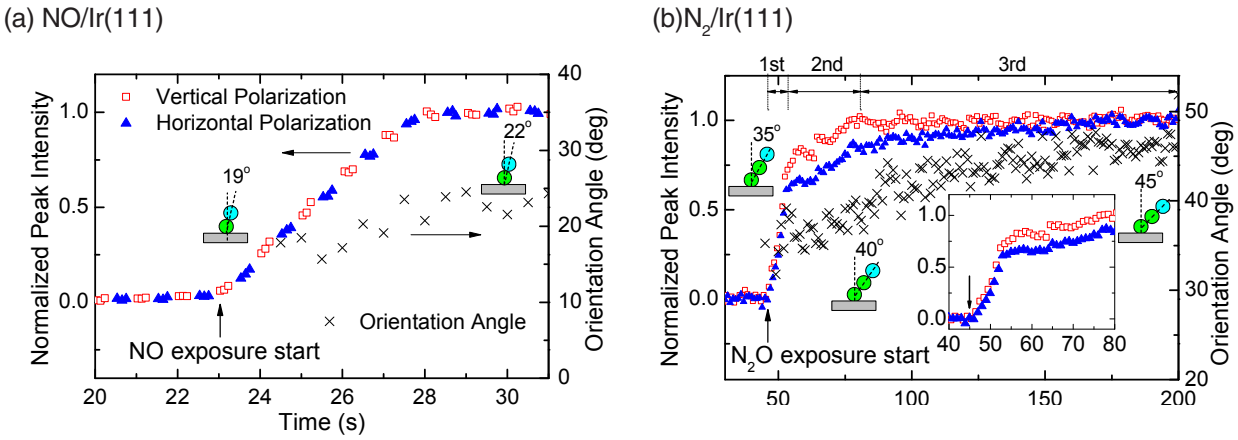

Figure 2: Normalized peak intensity for vertical and horizontal polarizations in the (a) NO and (b) N_2O adsorption process. Estimated molecular orientation angle is also plotted.

To quantitatively estimate the molecular orientation, the time (t) evolution of the normalized peak intensity for the vertical and horizontal polarizations is plotted in Fig. 2. The averaged orientation angle is estimated from the ratio between the peak intensities for the two polarizations. The peak-intensity ratio remains almost constant in the case of NO adsorption, as shown in Fig. 2(a), which directly shows that the orientation angle of NO is unchanged during the whole adsorption process. The estimated molecular orientation angle at each t is also plotted in Fig. 2.

For N_2O adsorption, in contrast, a different behavior between two polarizations is observed, suggesting some changes in the molecular orientation during the adsorption process. The adsorption process consists of three periods as indicated in Fig. 2(b). Since the coverage of the adsorbate is proportional to the peak intensity at the magic angle condition, it is revealed that N_2O rapidly adsorbs up to ~2/3 of the saturation coverage in the first period, t = ~45–52 s, then the adsorption rate drastically decreases in the second period and the coverage reaches ~4/5 of the saturation at t = ~80 s, and the coverage further increases very slowly in the third period, t = ~80-200 s.

As for the molecular orientation, the orientation angle in the first period is almost constant at ~35° from the surface normal, then it gradually increases in the second period and reaches ~40° at t = ~80 s. Since the observed angle is an average over all adsorbed molecules, it seems reasonable to suppose that N_2O starts to occupy a different adsorption site with larger orientation angle than that in the first period. In the third period, the orientation angle very slowly approaches ~45°. This technique can be applied to the real-time observation of the molecular orientation of reaction intermediates, which is essential to understand the mechanism of surface chemical reactions.

REFERENCES

[1] K. Amemiya, M. Sakamaki, S. Nakamoto, M. Yoshida, K. Suzuki, H. Kondoh, T. Koide, K. Ito, K. Tsuchiya, K. Harada, H. Sasaki, T. Aoto, T. Shioya, T. Obina, S. Yamamoto and Y. Kobayashi, *Appl. Phys. Lett.* **101**, 161601 (2012).
[2] K. Amemiya, M. Sakamaki, T. Koide, K. Ito, K. Tsuchiya, K. Harada, T. Aoto, T. Shioya, T. Obina, S. Yamamoto and Y. Kobayashi, *J. Phys.: Conf. Ser.* **425**, 152015 (2013).
[3] K. Amemiya, Y. Kousa, S. Nakamoto, T. Harada, S. Kozai, M. Yoshida, H. Abe, R. Sumii, M. Sakamaki and H. Kondoh, *Appl. Phys. Lett.* **99**, 074104 (2011).

BEAMLINE

BL-16A

K. Amemiya[1], M. Sakamaki[1], S. Nakamoto[2], M. Yoshida[2], K. Suzuki[2], H. Kondoh[2], T. Koide[1], K. Ito[1], K. Tsuchiya[3], K. Harada[3], H. Sasaki[3], T. Aoto[3], T. Shioya[3], T. Obina[3], S. Yamamoto[1] and Y. Kobayashi[3] ([1]KEK-IMSS, [2]Keio Univ., [3]KEK-ACCL)

Valence Control of Rh Dopants in $SrTiO_3$ Water-Splitting Photocathodes

Doped transition metal oxides have been widely studied as potentially useful water-splitting photocathode materials for producing hydrogen from water under solar illumination. Rh:$SrTiO_3$ has received particular attention as it appears to be a reasonably efficient hydrogen evolution photocatalyst. In this project, we used high-resolution XPS to show that the $Rh^{4+/3+}$ valence in the surface layer of epitaxial Rh:$SrTiO_3$ thin films can be controlled by changing the ambient oxygen pressure during synthesis. The photoresponse of the thin film photocathodes exceeded the efficiency of equivalent powder samples by an order of magnitude.

The phenomenon of photoelectrochemical water splitting has recently drawn renewed interest because the reaction can potentially be used to harvest solar energy and produce renewable hydrogen fuel from water. An ideal photocatalyst has to satisfy several conflicting constraints regarding the band gap, photocarrier dynamics, work function, and surface stability in water. Several transition metal oxides, particularly among the titanates, satisfy most of these conditions, except for the band gap, which tends to be above 3 eV (ultraviolet), while the optimal value is close to 2 eV (visible). One possible solution to the problem is to dope a wide-gap titanate, such as $SrTiO_3$, with additional cations that form in-gap impurity levels, effectively reducing the band gap of the parent material. Indeed, Rh:$SrTiO_3$ has been identified as a reasonably efficient hydrogen-evolution photocatalyst with a visible light water-splitting response.

For a hydrogen-evolution photocatalyst, it is important to choose a dopant that reduces the band gap primarily by raising the valence band edge, rather than reducing the energy of the conduction band bottom. Rhodium is a suitable dopant for $SrTiO_3$ in this regard, as the occupied Rh 4d levels form in-gap states just above the oxide valence band. As illustrated in Fig. 1, however, the precise location of Rh-related in-gap levels is dependent on the Rh valence [1]. The effect of the Rh dopant valence on the electronic structure of $SrTiO_3$ can be seen visually as a color change between purple for Rh^{4+}:$SrTiO_3$ and yellow for Rh^{3+}:$SrTiO_3$.

In this work, the valence of the Rh dopant was studied in thin film samples, where the oxygen stoichiometry was controlled by changing the ambient oxygen pressure during thin film growth. High-resolution XPS was used to determine the valence state of Rh in the surface layer of the Rh:$SrTiO_3$ films. As shown in Fig. 2, the Rh valence dependent color change could be successfully reproduced in the thin film samples [2].

In a semiconducting photocatalyst, electron-hole pairs formed by light irradiation are separated and electrons or holes are transferred to the surface due to the presence of an internal electric field formed in the band bending region at the semiconductor-water interface. The electronically active region in the photocatalyst is therefore only a few tens of nanometers thick and it is important to determine the valence of Rh in this surface layer. Although the average valence of a dopant in a thick film or powder can be determined by optical absorption measurements, a surface-sensitive technique is needed to measure the dopant valence in the electronically active surface layer. For this purpose, high-resolution XPS was used at BL-13A to measure the 3d core-level spectra of Rh and determine the Rh valence in the thin film surface layer.

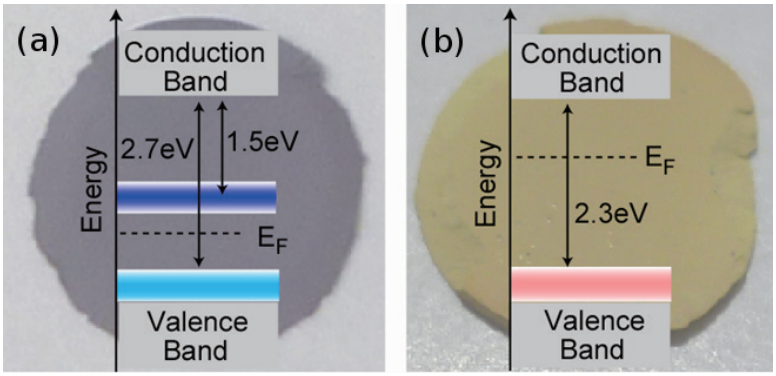

Figure 1: (a) Purple Rh^{4+}:$SrTiO_3$ and (b) yellow Rh^{3+}:$SrTiO_3$ pellets. Schematic energy level diagrams are shown for both cases.

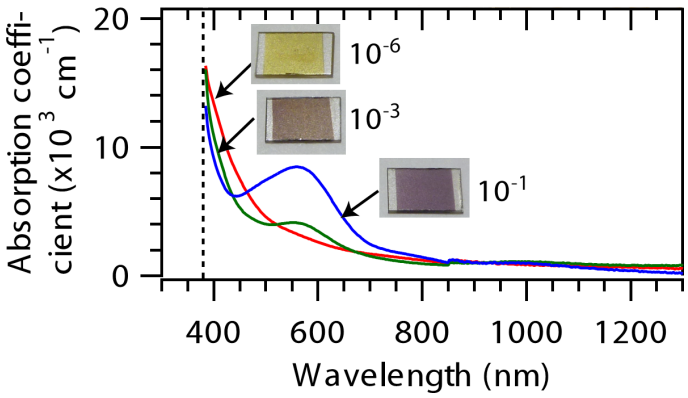

Figure 2: Optical absorption spectra and photographs of Rh:$SrTiO_3$ thin film samples grown at an oxygen pressure of 10^{-1} Torr (purple, Rh^{4+}), 10^{-3} Torr (brown, $Rh^{4+/3+}$), and 10^{-6} Torr (yellow, Rh^{3+}).

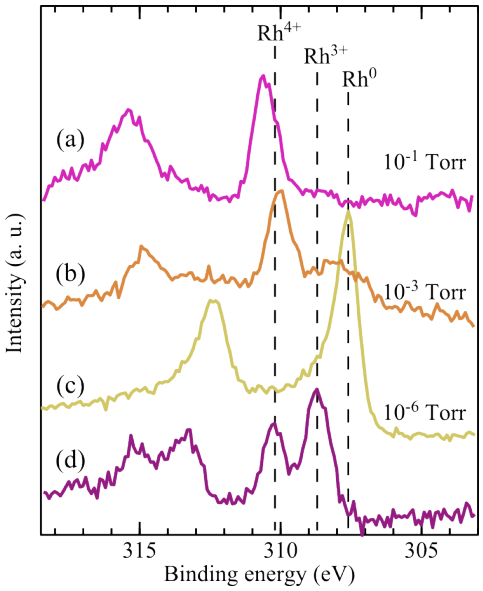

Figure 3: X-ray photoelectron spectra of Rh(5%):$SrTiO_3$ films grown at 700°C and various oxygen pressures: (a) 10^{-1} Torr, (b) 10^{-3} Torr, and (c) 10^{-6} Torr. The film in (d) was grown at 10^{-1} Torr and annealed at 10^{-6} Torr for 2 h.

The XPS results are shown in Fig. 3, comparing the Rh 3d core-level positions for films grown at various pressures. A pure Rh^{4+} valence state was obtained at the highest oxygen pressure and a systematic shift towards reduced species was seen for the lower growth pressures. As shown by plot (c), a reduction to metallic Rh occurs at the lowest growth pressure, which means that the photocatalytic activity may be affected by the presence of a metallic co-catalyst on the surface. A better way of preparing a film with a stable Rh^{3+} valence is to reduce a film grown at high pressure, as shown by spectrum (d). In this case, no metallic Rh forms at the surface. It should be noted that the presence of metallic Rh may also occur in bulk powder samples, but this cannot be observed by optical absorption spectroscopy. These experiments show that surface-sensitive composition and valence state analysis is essential for accurately correlating the photocatalytic activity of a doped material with the assumed composition of a photocatalyst.

REFERENCES

[1] S. Kawasaki, K. Akagi, K. Nakatsuji, S. Yamamoto, I. Matsuda, Y. Harada, J. Yoshinobu, F. Komori, R. Takahashi, M. Lippmaa, C. Sakai, H. Niwa, M. Oshima, K. Iwashina and A. Kudo, *J. Phys. Chem. C* **116**, 24445 (2012).

[2] S. Kawasaki, K. Nakatsuji, J. Yoshinobu, F. Komori, R. Takahashi, M. Lippmaa, K. Mase and A. Kudo, *Appl. Phys. Lett.* **101**, 033910 (2012).

BEAMLINE

BL-13A

S. Kawasaki[1], K. Nakatsuji[1], J. Yoshinobu[1], F. Komori[1], R. Takahashi[1], M. Lippmaa[1], K. Mase[2] and A. Kudo[3] ([1]The Univ. of Tokyo, [2]KEK-PF, [3]Tokyo Univ. of Science)

Structural and Electronic Properties of the Triplet State of Ruthenium (II)-*tris*-2,2'-bipyridine Observed by Picosecond Time-Resolved Ru *K*-Edge X-Ray Absorption Fine Structure

Time-resolved X-ray absorption fine structure (TR-XAFS) measurements of ruthenium (II)-*tris*-2,2'-bipyridine ($[Ru^{II}(bpy)_3]^{2+}$) in the triplet metal-to-ligand charge transfer (^{3}MLCT) excited state were conducted and analyzed to investigate transient structural changes directly related to the photophysical properties of the complex. The results from visible (400 nm) and UV (267 nm) excitation indicate that electrostatic interaction between the oxidized Ru atom and the reduced bipyridine ligand is the dominant factor affecting the Ru-N bond contraction. An increase of the Debye-Waller factor from the EXAFS analysis suggests that fast localized structural distortion due to electron hopping exists in the ^{3}MLCT excited state.

Ruthenium (II)-*tris*-2,2'-bipyridine ($[Ru^{II}(bpy)_3]^{2+}$) is a key transition metal complex that acts as a photosensitizer. Because $[Ru^{II}(bpy)_3]^{2+}$ shows high photosensitivity in the visible region originating from a characteristic metal to ligand charge transfer (MLCT) transition, its long-lived triplet MLCT (^{3}MLCT) state, which is the lowest excited state, serves as an extremely efficient photocatalyst [1, 2]. The intramolecular energy transfer reaction combined with the molecular structural transformation of the ^{3}MLCT state directly determines the energy level of $[Ru^{II}(bpy)_3]^{2+}$ and has important consequences for the character of the photocatalytic reaction [1, 2]. Thus, it is essential to investigate the molecular structure of the ^{3}MLCT state. However, such studies have mainly been performed using optical spectroscopic methods [3, 4], with which it is difficult to estimate the molecular structure with atomic resolution. Therefore, a detailed structural study of the ^{3}MLCT state of $[Ru^{II}(bpy)_3]^{2+}$ at atomic resolution in the hard X-ray region is crucially important.

X-ray absorption fine structure (XAFS) measurements reveal the atomic distance between the absorbing atom and coordinated atoms via extended X-ray absorption fine structure (EXAFS) measurements. This is suitable for the structural analysis of disordered systems such as the solution phase. XAFS yields not only structural information but also the energy level of molecular orbitals by X-ray absorption near edge structure (XANES) analysis. Recently, time-resolved XAFS (TR-XAFS) measurements of the excited structure andthe electronic state of metal complexes, using pulsed X-rays from synchrotron radiation for the probe and a laser pulse for excitation, have been developed and are becoming a powerful method to investigate the photochemical reactions of metal complexes [5-7].

TR-XAFS measurements were conducted at the undulator beamline NW14A of the Photon Factory Advanced Ring (PF-AR) [8]. The black circle in Fig. 1 shows the XANES spectrum of the ground state. The difference spectra between the ground and transient states at 50 ps after photoexcitation at 400 and 267 nm are presented in the bottom of Fig. 1 by solid red circles and empty blue circles, respectively. Both difference spectra show the edge-shift to higher energy relative to the ground state. These edge-shifts are due to the change of the oxidation state from Ru(II) to Ru(III). This result indicates that the initial excited state formed at 267 nm is mainly converted to the ^{3}MLCT state in the subnanosecond time scale. This photochemical property is particularly important for an efficient photosensitizer with a wide absorption band.

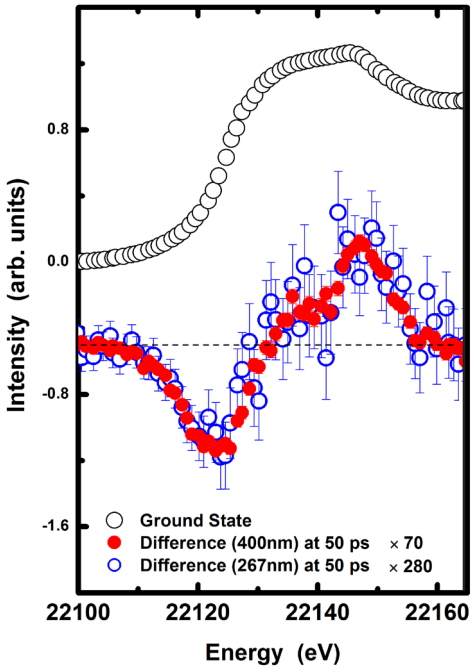

Figure 1: Ground-state Ru *K*-edge XANES spectrum of $[Ru^{II}(bpy)_3]^{2+}$ (black) and the transient difference spectra with 400 nm excitation (red) and 267 nm excitation (blue) at 50 ps. The dotted line indicates zero difference.

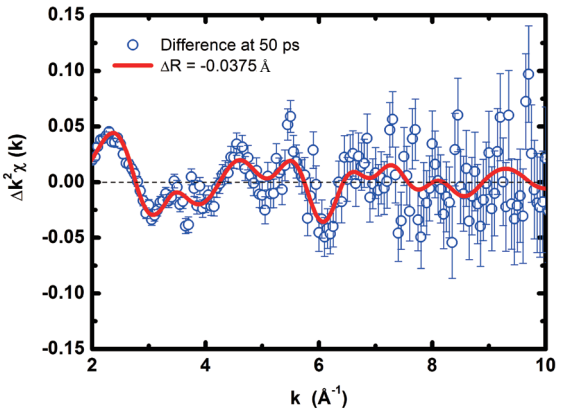

Figure 2: The experimental data at 50 ps (blue circle) and the EXAFS fitting result (red line).

Table 1: Structural parameters obtained from the EXAFS analysis

	shell	R (Å)	σ^2 (Å)
Graound State	Ru-N	2.06 (1)	0.004 (1)
^{3}MLCT State	Ru-N	2.02 (1)	0.014 (1)

Figure 2 shows the transient difference spectrum at +50 ps and the EXAFS fitting result. In order to obtain the photo-excited EXAFS spectrum, a quantum yield of 3% was assumed by a reduced chi square value in the EXAFS analysis [7]. The Ru-N bond lengths and Debye-Waller factors of the ground and excited states are presented in Table 1. TR-EXAFS analysis at the Ru *K*-edge revealed a 0.04 Å contraction in the Ru-N bond lengths in the ^{3}MLCT state compared with the ground state. EXAFS analysis showed that the Debye-Waller factor slightly increased in the ^{3}MLCT state compared with that in the ground state. The increase of the Debye-Waller factor suggests that a structurally distorted state exists in the ^{3}MLCT state with a shorter lifetime than the X-ray pulse duration of 60 ps.

A schematic summary of this study is shown in Fig. 3. Transient structure analysis suggested that the decreasing Ru-N bond lengths provided stability in the ^{3}MLCT excited state. Therefore, the bpy ligand, where hopping electrons localize, will be a long-lived, optically-active center in the photocatalyzed reaction of $[Ru^{II}(bpy)_3]^{2+}$. Our results provide a better understanding of photocatalytic reactions by providing structural information for the theoretical calculation of the reorganization energy of electron transfer reactions beginning with the ^{3}MLCT state, and will be useful for designing artificial photochemical systems.

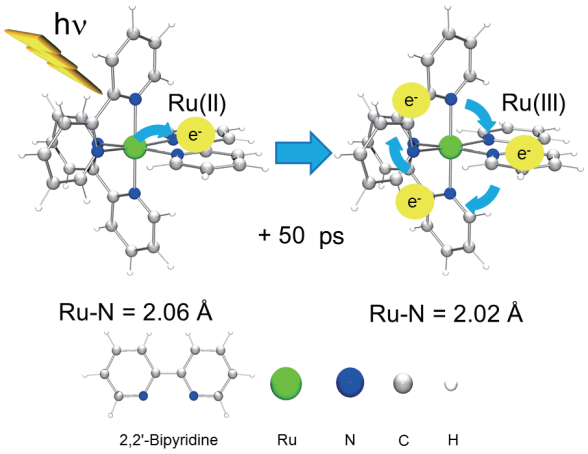

Figure 3 : A schematic summary of this study.

REFERENCES

[1] J. Ferguson, F. Herren, E.R. Krausz, M. Maeder and J. Vrbancich, *J. Coord. Chem. Rev.* **64**, 21 (1985).

[2] A. Juris, V. Balzani, F. Barigelletti, S. Campagna, P. Belser and A. Von-Zelewsky, *Coord. Chem. Rev.* **84**, 85 (1988).

[3] N.H. Damrauer, G. Cerullo, A. Yeh, T.R. Boussie, C.V. Shank and J.K. McCusker, *Science* **275**, 54 (1997).

[4] T.A. Yeh, V.V. Shank and J.K. McCusker, *Science* **289**, 935 (2000).

[5] T. Sato, S. Nozawa, K. Ichiyanagi, A. Tomita, M. Chollet, H. Ichikawa, H. Fujii, S. Adachi and S. Koshihara, *J. Synchrotron. Rad.* **16**, 110 (2009).

[6] S. Nozawa, T. Sato, M. Chollet, K. Ichiyanagi, A. Tomita, H. Fujii, S. Adachi and S. Koshihara, *J. Am. Chem. Soc.* **132** (1), 61 (2010).

[7] T. Sato, S. Nozawa, A. Tomita, M. Hoshino, S. Koshihara, H. Fujii and S. Adachi, *J. Phys. Chem. C* **116**, 14232 (2012).

[8] S. Nozawa, S. Adachi, J. Takahashi, R. Tazaki, L. Guérin, M. Daimon, A.Tomita, T. Sato, M. Chollet, E. Collet, H. Cailleau, S. Yamamoto, K. Tsuchiya, T. Shioya, H. Sasaki, T. Mori, K. Ichiyanagi, H. Sawa, H. Kawata and S. Koshihara, *J. Synchrotron Rad.* **14**, 313 (2007).

BEAMLINE

AR-NW14A

T. Sato[1], S. Nozawa[1], A. Tomita[1], M. Hoshino[2], S. Koshihara[2], H. Fujii[3] and S. Adachi[1] ([1]KEK-PF, [2]Tokyo Inst. of Tech., CREST-JST, [3]IMS)

Formation of a Kagome Lattice with Huge Channels by Very Large Spherical Anions

A very large spherical polyoxometalate anion known as the Keplerate, $[Mo^{VI}_{72}Mo^{V}_{60}O_{372}(CH_3COO)_{30}(H_2O)_{72}]^{42-}$, has been crystallized into an unprecedented hexagonal phase with the unit cell dimensions of a = 61.530(1) and c = 63.896(1) Å when precipitated with Sr^{2+} cations. Single-crystal X-ray diffraction at the AR-NW2A beamline revealed that the compound shows a unique structure where the large spherical anions with the I_h symmetry are packed into a superposed kagome lattice possessing huge channels with the approximate diameter of 3.0 nm.

Nature abhors a vacuum and, as a consequence, crystals prefer close packed structures. Ionic crystals are no exception; a frequently adopted mechanism to achieve a dense packing for an ionic crystal is to arrange larger ions into a close-packed structure and smaller ones into the interstices between the larger ones. For example, the sodium chloride structure is regarded as a cubic close-packed array of the chloride anions with the sodium cations in its octahedral interstices. In principle, the larger the discrepancy between the radii of the cation and the anion is, the more effectively this mechanism should work. Therefore, it seems reasonable that the extremely large Keplerate-type spherical polyoxometalates, the $[Mo^{VI}_{72}Mo^{V}_{60}O_{372}(CH_3COO)_{30}(H_2O)_{72}]^{42-}$ anion (abbreviated as $\{Mo_{132}\}$ hereafter) [1] and its derivatives that measure approximately 3.0 nm in diameter, crystallize into cubic or trigonal space group types where the huge spherical anions adopt strict or slightly distorted cubic close packing arrays.

However, the $\{Mo_{132}\}$ anion that consists of 12 pentagonal $[Mo^{VI}_{6}O_{21}(H_2O)_6]^{6-}$ and 30 $[Mo^{V}_{2}O_4(CH_3COO)]^{+}$ units (Fig. 1) does not adopt the completely spherical symmetry but better approximates the I_h symmetry. The I_h symmetry is not compatible with the site symmetry of the spheres in any type of close packings (O_h for the cubic close packing and D_{3h} for the hexagonal one, for example). Therefore, introduction of intermolecular interactions specific to the structures of $\{Mo_{132}\}$ could lead to a different and less dense arrangement of the anions. A looser arrangement of the anions thus constructed would yield interstices with larger volume than those in the close packed structures. It is worth noting that the use of the large spherical anions as building blocks will intrinsically preclude the formation of interpenetrating structures, which often form when thin stick-like building blocks are employed. By using Sr^{2+}, a multivalent cation that can potentially interact with $\{Mo_{132}\}$ in a site-specific manner, we obtained a new hexagonal crystal of $Sr_{18.5}(NH_4)_5[Mo^{VI}_{72}Mo^{V}_{60}O_{372}(CH_3COO)_{30}(H_2O)_{72}]\cdot149.25H_2O$ (compound **1**).

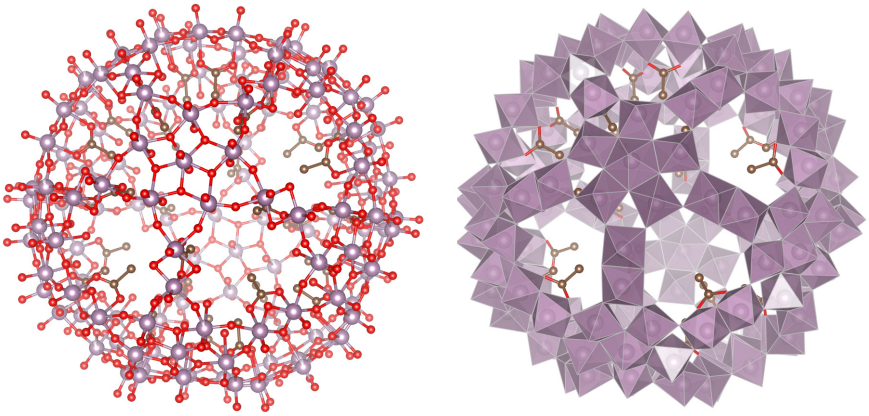

Figure 1: Structure of the $[Mo^{VI}_{72}Mo^{V}_{60}O_{372}(CH_3COO)_{30}(H_2O)_{72}]^{42-}$ anion in ball-and-spoke (left) and polyhedral (right) representations (prepared by using VESTA 3.1.6 [3]).

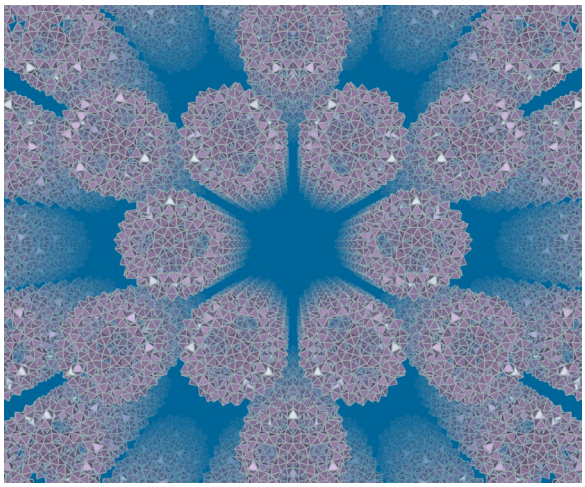

Figure 2: Crystal packing of the Sr^{2+} salt of $[Mo^{VI}_{72}Mo^{V}_{60}O_{372}(CH_3COO)_{30}(H_2O)_{72}]^{42-}$ anion viewed along the *c* axis (prepared by using VESTA 3.1.6 [3]).

Compound **1** crystallizes in the space group $P6_3/mmc$ with the unit cell dimensions of a = 61.530(1) and c = 63.896(1) Å. Single-crystal X-ray diffraction at the AR-NW2A revealed that $\{Mo_{132}\}$ anions are located at the 2/*m* sites to make a superposed kagome lattice. The $\{Mo_{132}\}$ anions are connected so as to sandwich hydrated Sr^{2+} cations with their Mo_9O_9 pores, each of which is surrounded by three $[Mo^{VI}_6O_{21}(H_2O)_6]^{6-}$ and three $[Mo^{V}_2O_4(CH_3COO)]^{+}$ units. Each connection is supported by two additional Sr^{2+} cations that are directly bound to the terminal O atoms of the two $\{Mo_{132}\}$ anions. Due to the I_h symmetry, $\{Mo_{132}\}$ can accommodate up to only four Mo_9O_9 pores on a great circle. Therefore, this type of interaction leads to a kagome-lattice sheet of $\{Mo_{132}\}$ spanning parallel to the crystallographic *ab* plane. Six $\{Mo_{132}\}$ surrounding the large void point their $[Mo^{V}_2O_4(CH_3COO)]^{+}$ moieties to the space and they cannot establish similar interactions with another $\{Mo_{132}\}$ in this cavity. As a result, the cavity is left unoccupied and presumably filled with disordered water molecules. The kagome-lattice sheets are superposed to form a three-dimensional framework as shown in Fig. 2. The sheets are connected by a similar interaction between two $\{Mo_{132}\}$ through their Mo_9O_9 pores. As a result, the kagome-lattice sheets are arranged so that the cavities of one sheet fall exactly above those of the sheet below, leading to a channel running through the crystal along the *c* axis, whose diameter measures approximately 3.0 nm.

In summary, we have successfully prepared an unprecedentedly arranged array of the Keplerate type $[Mo^{VI}_{72}Mo^{V}_{60}O_{372}(CH_3COO)_{30}(H_2O)_{72}]^{42-}$ anion, whose structure was successfully determined by exploiting synchrotron radiation. The current strategy for the design of crystals with huge channels could be applied to the development of catalyses, ionic conductors and small molecule storing materials.

REFERENCES

[1] A. Müller, E. Krickemeyer, H. Bögge, M. Schmidtmann and F. Peters, *Angew. Chem. Int. Ed.* **37**, 3360 (1998).
[2] M. Saito and T. Ozeki, *Dalton Trans.* **41**, 9846 (2012).
[3] K. Momma and F. Izumi, *J. Appl. Crystallogr.* **44**, 1272 (2011).

BEAMLINE

AR-NW2A

M. Saito and T. Ozeki (Tokyo Inst. of Tech.)

High Entropy State Pt-Ru Anode Catalyst with Completely Random Distribution

Residential fuel cell systems are expected to be widely used in the near future. Catalysts having the maximum number of Pt-Ru bondings are ideal catalysts for CO oxidation. Pt-Ru / C(RM) shows the combination of $N_{Pt\text{-}Ru}$ / ($N_{Pt\text{-}Ru}$ + $N_{Pt\text{-}Pt}$) of 0.59 ≒ 0.60 and $N_{Ru\text{-}Pt}$ / ($N_{Ru\text{-}Pt}$ + $N_{Ru\text{-}Ru}$) of 0.37 ≒ 0.40. Pt and Ru atoms were distributed with almost random distribution. Entropy tends to be the driving force at high temperature ($\Delta G = \Delta H - T\Delta S$). A high entropy state of dispersion of Pt and Ru is maintained by rapid quenching from a high temperature, resulting in the maximum number of Pt-Ru bondings. The CO tolerance of Pt-Ru / C(RM) is much higher than that of Pt-Ru / C(CM).

Residential fuel cell (PEFC: polymer electrolyte fuel cell) systems are expected to be widely used because of their efficiency of power generation as shown in Fig. 1. Generally, H_2 gas is produced from city gas composed of CH_4 by the reforming reaction. Since CO is contained in reformed H_2, the anode catalyst is deactivated by the adsorption of CO. Catalysts having the maximum number of Pt-Ru bondings are ideal catalysts for CO oxidation, but it is difficult to make such catalysts because Pt-Ru systems prefer homo-bonding owing to different stable structures. Recently we found that the quick quenching of Pt-Ru reduced at high temperature provides a CO-tolerant anode catalyst [1]. In order to count the number of Pt-Ru bondings and confirm its relation to the catalytic performance, EXAFS measurements were carried out in the Photon Factory. The energy and current of the storage ring were 2.5 GeV and 300 mA, respectively. Pt L3-edge EXAFS spectra were recorded at a BL-12C beamline. Ru K-edge EXAFS measurements were carried out at beamline NW10A of PF-AR (6.5 GeV). The sample was reduced under H_2 in the cell and the EXAFS spectra were measured without exposure to air.

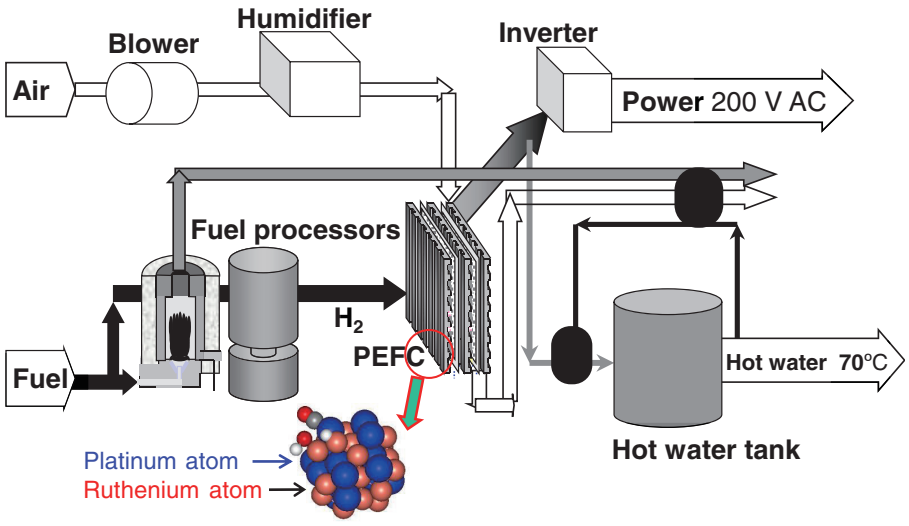

Figure 1: Residential fuel cell systems.

Table 1 : Ratio of coordination numbers

	$N_{Pt\text{-}Ru} / (N_{Pt\text{-}Ru} + N_{Pt\text{-}Pt})$	$N_{Ru\text{-}Pt} / (N_{Ru\text{-}Pt} + N_{Ru\text{-}Ru})$
Pt-Ru / C (RM)	0.59	0.37
Pt-Ru / C (CM)	0.44	0.32
Complete random model (Calculation)	0.60	0.40

Ratios of coordination numbers are summarized in Table 1. The molar ratio of Pt (M_{Pt}) to Ru (M_{Ru}) is 2:3. (M_{Ru} / (M_{Pt} + M_{Ru}) = 0.60 and M_{Pt} / (M_{Ru} + M_{Pt}) = 0.40). Pt has an fcc structure, while Ru has an hcp structure; therefore, bondings between like atoms were more preferably formed than were bondings between Pt-Ru bonding. The ratios of $N_{Pt\text{-}Ru}$ / ($N_{Pt\text{-}Ru}$ + $N_{Pt\text{-}Pt}$) (0.44) and $N_{Ru\text{-}Pt}$ / ($N_{Ru\text{-}Pt}$ + $N_{Ru\text{-}Ru}$) (0.32) for a commercial catalyst, Pt-Ru / C(CM), were less than those expected from a randomly mixed case. On the other hand, quick-quenched Pt-Ru/C(RM) shows the combination of $N_{Pt\text{-}Ru}$ / ($N_{Pt\text{-}Ru}$ + $N_{Pt\text{-}Pt}$) of 0.59 ≒ 0.60 and $N_{Ru\text{-}Pt}$ / ($N_{Ru\text{-}Pt}$ + $N_{Ru\text{-}Ru}$) of 0.37 ≒ 0.40. Pt and Ru atoms were distributed with almost random distribution.

Now we consider the change of entropy by alloy formation. Subscript f means the state after alloy formation, while subscript i means the state before alloy formation.

$G_i = H_i - TS_i \quad G_f = H_f - TS_f \quad G_f - G_i = H_f - H_i - T(S_f - S_i)$

Δ means the change by alloy formation (i.e. $\Delta S = S_f - S_i$). Pt and Ru atoms were mixed with molar ratio (Pt and Ru = 2 : 3).

$\Delta H = H_f(\text{Pt-Ru}) - (0.4\ H_i(\text{Pt}) + 0.6\ H_i(\text{Ru}))$

$\Delta S = k \ln (W_f) - k \ln (W_i)$

W: number of microstates in the particle, k: Boltzmann constant, *l*: number of atoms in Pt-Ru alloy, L: Avogadro constant

If Pt-Ru alloy consists of pure Pt nanoparticles and pure Ru nanoparticles without mixing,

$W_i = 1 \qquad S_i = k \ln (W_i) = k \ln 1 = 0$

When it is mixed atomically, entropy will be as follows.

$S_f(\text{Pt-Ru}) = k \ln (W_f) = k \ln (l!/((0.6\ l)!\ \text{x}\ (0.4\ l)!))$

$= k (\ln (l!) - \ln ((0.6\ l)!) - \ln ((0.4\ l)!))$

$= k (l \ln l - l - 0.6\ l \ln (0.6\ l) + 0.6\ l - 0.4\ l \ln (0.4\ l) + 0.4\ l)$

$= k (l \ln l - 0.6\ l \ln (0.6\ l) - 0.4\ l \ln (0.4\ l))$

$= -k\ l\ (0.6 \ln 0.6 + 0.4 \ln 0.4)$

$\Delta S = -R\ (0.6 \ln 0.6 + 0.4 \ln 0.4) \qquad (l = L)$

Entropy tends to be the driving force at high temperature ($\Delta G = \Delta H - T\Delta S$), while enthalpy is the driving force at low temperature. A high entropy state of Pt and Ru nanoparticles (random distribution) is realized at high temperature and is maintained by the rapid quenching, resulting in the maximum number of Pt-Ru bondings. This is the first report of a completely randomly distributed Pt-Ru alloy catalyst with highest entropy state. The CO tolerance of Pt-Ru / C(RM) is much higher than that of Pt-Ru / C(CM) since Pt-Ru / C(RM) has more Pt-Ru bondings.

REFERENCE

[1] T. Takeguchi, T. Yamanaka, K. Asakura, E.N. Muhamad, K. Uosaki and W. Ueda, *J. Am. Chem. Soc.* **134**, 14508 (2012).

BEAMLINES

BL-12C and AR-NW10A

T. Takeguchi[1] and K. Asakura[2] ([1]Iwate Univ., [2]Hokkaido Univ.)

Alkali-Promoted Pt/TiO_2 Opens a New Pathway to Formaldehyde Oxidation at Ambient Temperatures

Catalytic oxidation of formaldehyde (HCHO) to CO_2 under ambient conditions is of great interest for indoor HCHO purification. Pt/TiO_2 catalysts have low activity and stability for the total oxidation of HCHO at room temperature. Here, we report that the addition of alkali ions significantly promotes the activity of Pt/TiO_2 catalysts for the HCHO oxidation reaction by inducing an atomically dispersed Pt-O(OH)x-alkali species and opening a new low-temperature reaction pathway. Accordingly, the atomically dispersed Pt-O(OH)x-alkali species could effectively activate H_2O and then catalyze a simple reaction between surface OH and formate species to total oxidation products.

Figure 1 shows the conversion of HCHO to CO_2 as a function of temperature over 1% Pt/TiO_2 and 2% Na-1% Pt/TiO_2 samples at a GHSV of 120,000 h^{-1} and HCHO inlet of 600 ppm. All gas streams were humidified to around RH = 50%. Before each activity test, the samples were reduced in H_2 at 300ºC for 30 min. The Na-free catalyst had low activity for the HCHO oxidation reaction, with HCHO conversion being only ca. 19% at 15ºC. The addition of alkali ions significantly promoted the activity of Pt/TiO_2, and 100% HCHO conversion to CO_2 and H_2O was measured over 2% Na-1% Pt/TiO_2 at 15ºC. The 2% Na-promoted sample also had excellent stability as confirmed by long isothermal tests. At a GHSV of 300,000 h^{-1} and with other reaction conditions being the same, approximately 80% HCHO conversion was maintained over a 72 h-long test, as shown in Fig. 1 (inset). Li and K were equally effective promoters as Na and imparted the same high activity and stability to the Pt species.

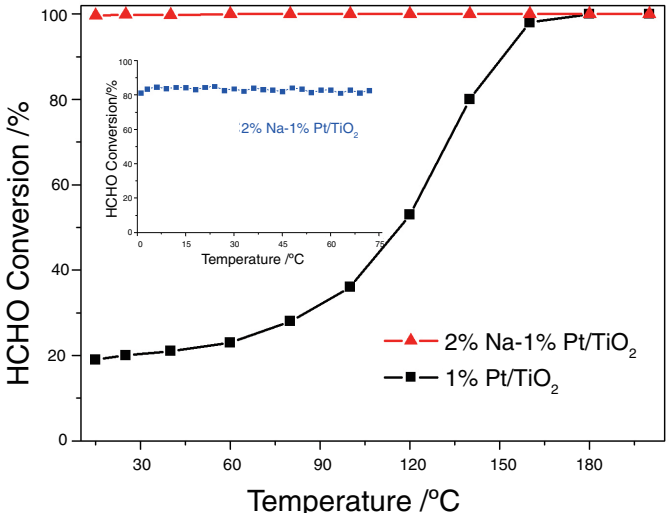

Figure 1: HCHO conversion over 1% Pt/TiO_2 and 2% Na-1% Pt/TiO_2 catalysts as a function of temperature. Reaction conditions: HCHO 600 ppm, O_2 20 vol.%, RH: ~50%, He balance, total flow rate of 50 cm^3 min^{-1}, and GHSV 120,000 h^{-1} (inset: stability test of 2% Na-1% Pt/TiO_2 at 25ºC, GHSV 300,000 h^{-1} with other reaction conditions being the same).

Table 1: Fitting parameters of the curve-fitted k^3-weighted EXAFS analysis of 1% Pt/TiO_2 and 2% Na-1% Pt/TiO_2 catalysts

Samples	Shell	CN	R(Å) (±0.01)	DW(Å)	R factor
Pt-foil	Pt-Pt	12.0±2.3	2.77	0.77±0.010	0.8
PtO_2	Pt-O	6.0±1.2	2.02	0.061±0.020	3.0
	Pt-O-Pt	4.0±1.0	3.14	0.061±0.012	
1 Pt/TiO_2[a]	Pt-O	3.7±1.2	2.02	0.061±0.020	0.6
	Pt-Cl	2.3±1.0	2.30	0.051±0.057	
2 Na-1Pt[a]	Pt-O	5.4±1.2	2.02	0.061±0.020	8.7
1 $Pt-TiO_2$[b]	Pt-Pt	5.6±1.2	2.77	0.097±0.010	1.3
2 Na-1Pt[b]	Pt-Pt	2.4±0.5	2.77	0.097±0.010	7.2
1 Pt/TiO_2[c]	Pt-Pt	4.7±1.0	2.77	0.097±0.010	0.4
	Pt-Cl	0.6±0.2	2.30	0.051±0.057	
2 Na-1Pt[c]	Pt-O	2.8±0.6	2.02	0.092±0.010	9.8

a: Samples calcined in static air, 400°C, 2 h; b: Samples after *in situ* H_2 reduction in 10% H_2/Ar at 300°C for 30 min; c: Samples exposed to ambient air after H_2 reduction.

XAFS measurements were conducted to study the structure of samples before/after Na addition and after H_2 reduction under atmospheric pressure. Fitting parameters of the curve-fitted k^3-weighted EXAFS analysis of 1% Pt/TiO_2 and 2% Na-1% Pt/TiO_2 catalysts are given in Table 1. Prior to H_2 reduction, all Pt was coordinated with O or Cl, and the Pt-Pt coordination was zero on all catalysts. After *in situ* H_2 reduction at 300°C, all Pt species were reduced to the metallic phase, yet the Pt-Pt coordination number was clearly lowered with 2% Na addition. Once the pre-reduced catalysts were exposed to air, as in realistic operation for HCHO oxidation, surface structures were changed due to oxygen adsorption [1]. The Na-free Pt/TiO_2 sample showed a Pt-Pt coordination shell as in Pt metal and a small residual Pt-Cl coordination shell. With 2% Na added, only a Pt-O shell was detected, indicating that 2% Na addition can completely suppress the formation of Pt-Pt bonds in the presence of O_2 and induce atomically dispersed Pt-O species on the TiO_2 surface.

The atomically dispersed Pt-O(OH)x-Na species induced by Na addition could easily activate H_2O and then open a new pathway for HCHO oxidation under ambient conditions. The HCHO oxidation reaction on Na-free samples follows the formate ($HCOO^-$) decomposition route ($HCHO \rightarrow HCOO^- \rightarrow CO \rightarrow CO_2$), with formate decomposing into CO being the rate determining step [2]. In contrast, the HCHO oxidation over the Na-promoted Pt/TiO_2 catalyst follows a simple pathway with reaction between surface OH and formate species to total oxidation products ($HCHO \rightarrow HCOO + OH \rightarrow H_2O + CO_2$), thus greatly enhancing the HCHO oxidation activity.

REFERENCES

[1] C. Zhang, F. Liu, Y. Zhai, H. Ariga, N. Yi, Y. Liu, K. Asakura, M. F.-Stephanopoulos and H. He, *Angew. Chem. Int. Ed.* **51**, 9628 (2012).
[2] C. Zhang, H. He and K. Tanaka, *Appl. Catal. B* **65**, 37 (2006).

BEAMLINES

BL-12C and BL-7C

C. Zhang[1], F. Liu[1], Y. Zhai[2], H. Ariga[3], N. Yi[2], Y. Liu[1], K. Asakura[3], M. F.-Stephanopoulos[2] and H. He[1]
([1]CAS-RCEES, [2]Tufts Univ., [3]Hokkaido Univ.)

Chlorination of Carbon during Thermochemical Behavior of Lead by Using X-Ray Absorption Spectroscopy

We examined the thermochemical role of Pb in the formation of chlorinated aromatics (aromatic-Cls) in MSW fly ash at a key temperature window for maximum yield by using X-ray absorption spectroscopy. In the presence of lead oxide alone, aromatic-Cls formation was suppressed. Promotion can occur by the thermochemical partial oxidation of $PbCl_2$. Real complex solid phase increases the thermochemical oxidation reactivity of $PbCl_2$. The presence of $PbCl_2$ influences the balance of the bonding state of chlorine with Cu and Fe atoms at various temperatures. So, Pb in real MSW fly ash functions as an "adjuster" in the generation of aromatic-Cls.

Regarding the toxicity and resource recovery of lead, various speciation studies have reported the redox chemical state of lead in postcombustion fly ash from thermal processes such as municipal solid waste (MSW) incineration and coal combustion. A large amount of lead exists as chloride, oxide, or sulfide in the thermal solid phase. Lead chloride ($PbCl_2$) promotes the formation of toxic chlorinated aromatic compounds (aromatic-Cls) such as polychlorinated dibenzo-*p*-dioxins (PCDDs), furans (PCDFs), biphenyls (PCBs), and benzenes (CBzs), after heating of model fly ash. Lead oxide (PbO) inhibits the formation of PCDDs, PCDFs, PCBs, and CBzs. Lead metallurgical processes can also be used to generate PCDDs, PCDFs, and PCBs. The thermochemical behaviors of metals in the solid phase likely play a role in the formation and inhibition of aromatic-Cls, which is supported by our recent mechanism-based thermochemical studies of strong metal catalysts (Cu [1, 2] and Fe [3]) and a metal inhibitor (Zn [4]). In the present study [5], we evaluated the thermochemical behavior of lead using quantitative and X-ray spectroscopic techniques.

We prepared single-addition and coexistence-addition model fly ashes (MFAs) and real fly ashes (RFAs). Three RFAs from MSW incineration plants were analyzed by Pb L_3-edge X-ray absorption near-edge structure (XANES) spectroscopy to identify the chemical forms of lead. Concentrations of PCBs and CBzs in MFAs under single and coexistence conditions were quantified using gas chromatography/mass spectrometry (GC/MS). Thermochemical chlorine behaviors of MFAs were analyzed using Cl K-edge near-edge X-ray absorption fine structure (NEXAFS) spectroscopy at BL-11B and BL-9A.

Aromatic-Cls formation was suppressed in the presence of lead oxide alone. One of the mechanisms of suppression was partial chlorination of PbO by an inorganic chlorine source in the solid phase, based on in situ Pb L_3-edge XANES data. In contrast, we found that aromatic-Cls formation was promoted by the coexistence of $PbCl_2$ with other metal catalysts more effectively at 400°C than at 300°C (Fig. 1). One possible mechanism of this promotion is related to the thermochemical partial oxidation of $PbCl_2$. More specifically, real complex solid phase increases the thermochemical oxidation reactivity of $PbCl_2$.

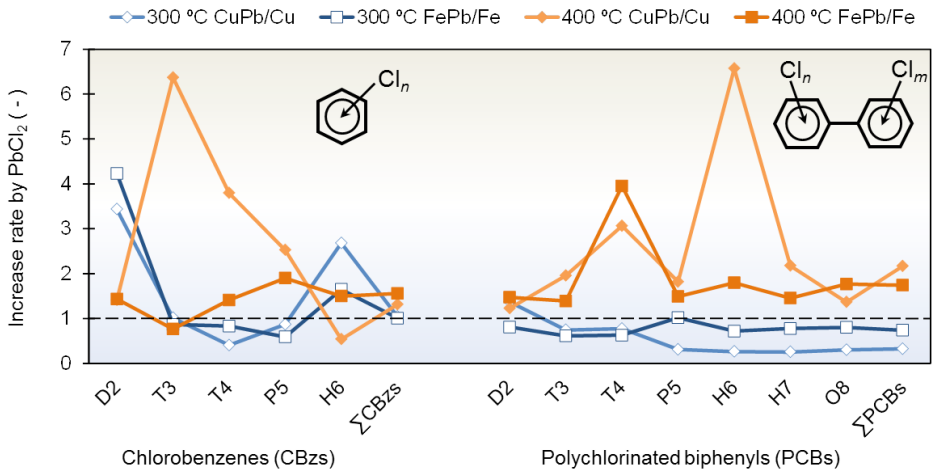

Figure 1: Mixed effect of $PbCl_2$ in the solid phase according to the concentrations of CBzs and PCBs after heating.

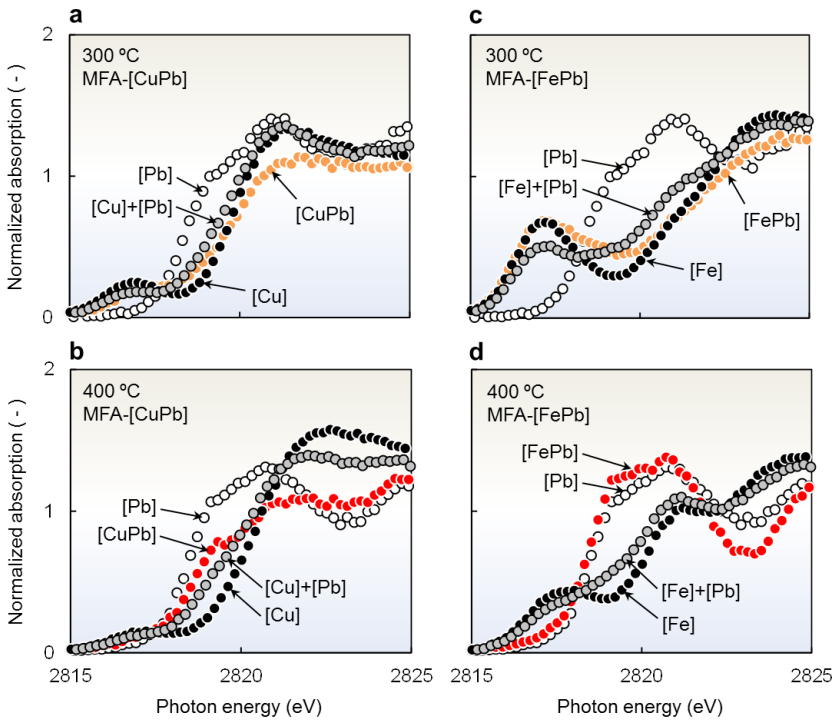

Figure 2: Cl K-edge NEXAFS spectra of various MFAs. MFA-[CuPb] after heating at (a) 300°C and (b) 400°C. MFA-[FePb] after heating at (c) 300°C and (d) 400°C. Reference spectra of MFA-[Cu], -[Fe], and -[Pb] after heating at each temperature are also shown. [Cu] + [Pb] and [Fe] + [Pb] indicate theoretical spectra generated by linear combinations of MFA-[Cu] and -[Fe], respectively, with MFA-[Pb].

We performed Cl K-edge NEXAFS measurements to explore the thermochemical mechanism of $PbCl_2$ in the presence of other metal catalysts. According to a comparison of the measured spectrum with the theoretical spectrum, Cl K-edge NEXAFS analyses revealed the coexistence effect of $PbCl_2$ with other metal catalysts, such as $CuCl_2$ and $FeCl_3$ (Fig. 2). The shapes of the MFA-[CuPb] and MFA-[FePb] spectra were closer to those of MFA-[Cu] (Fig. 2a) and MFA-[Fe] (Fig. 2c), respectively, at 300°C. This suggests that the observed amounts of chlorine bonded with copper and iron were greater than the theoretical amounts. So, the relatively mild inhibition of aromatic-Cls at 300°C is caused in part by decreased dechlorination by metal catalysts. At 400°C, both the spectra of MFA-[CuPb] (Fig. 2b) and MFA-[FePb] (Fig. 2d) were similar to that of MFA-[Pb]. The chlorine amounts bonded with Pb and Cu/Fe were higher and lower, respectively, than in the theoretical spectrum. The promotion at 400°C is caused by increased dechlorination by metal catalysts. Thus, the coexistence of $PbCl_2$ influences the imbalance of the bonding state of chlorine caused by heating temperature.

In real MSW fly ash, Pb exists in both oxide and chloride forms. Aromatic-Cls formation depends on the balance between inhibition by lead oxide and promotion by lead chloride. Because Pb coexists with other metal catalysts in real MSW fly ash, the coexistence effect of $PbCl_2$ had to be considered. Overall, our mechanism-oriented study suggests that Pb in MSW fly ash functions as an “adjuster” in the generation of aromatic-Cls, depending on the lead oxide/chloride ratio and coexistence conditions with metal catalysts.

REFERENCES

[1] M. Takaoka, A. Shiono, K. Nishimura, T. Yamamoto, T. Uruga, N. Takeda, T. Tanaka, K. Oshita, T. Matsumoto and H. Harada, *Environ. Sci. Technol.* **39**, 5878 (2005).
[2] T. Fujimori and M. Takaoka, *Environ. Sci. Technol.* **43**, 2241 (2009).
[3] T. Fujimori, M. Takaoka and S. Morisawa, *Environ. Sci. Technol.* **44**, 1974 (2010).
[4] T. Fujimori, Y. Tanino and M. Takaoka. *Environ. Sci. Technol.* **45**, 7678 (2011).
[5] T. Fujimori, Y. Tanino and M. Takaoka, *Environ. Sci. Technol.* **47**, 2169 (2013).

BEAMLINES

BL-11B and BL-9A

T. Fujimori and M. Takaoka (Kyoto Univ.)

Formation of Stable Monomeric Zn^0 and Zn^+ Species in MFI-Type Zeolite: Insight from *in-situ* XAFS Spectroscopy and DFT Calculation

In this work, we examined the H_2-activation in ZnMFI and found a new and fascinating phenomenon that a stable Zn^0 species is formed through the reaction with H_2 at 423 K, followed by evacuation at 573 K, on the M7 site with S2 configuration of aluminum atoms in ZnMFI. The DFT calculation, combined with XAFS, IR, and UV-Vis-DR spectra, provided evidence that the formed species is composed of an atomic Zn^0 which is stabilized in the confined space. In addition, we also obtained a surprising finding that this stable Zn^0 species responds to UV-light, resulting in the formation of a novel Zn^+ species which exhibits an unusual reactivity with O_2 at 300 K.

In the ZnMFI-H_2 system, IR spectra show the behavior characteristic of heterolytic dissociation of H_2 below the temperature of 423 K; the dissociation of H_2 takes place heterolytically and with simultaneous formation of zinc hydride (ν = 1933 cm^{-1}) and Brønsted acidic site (ν = 3615 cm^{-1}). The changing processes of these species are also examined by the UV-Vis DR spectral method, as shown in Fig. 1. First, the sample evacuated at 873 K shows a weak band at around 39,000 cm^{-1} which may be assignable to the band resulting from the 3d-4s transition of Zn^{2+} (spectrum 1). On this surface, the H_2 molecules are introduced; a small change in the spectrum took place after the treatment temperature was raised to 423 K (spectrum 2). Subsequent evacuation at 473 K brought about the appearance of distinct bands at 42,000 and 47,000 cm^{-1} (spectrum 3). These bands increase in their intensities with increasing evacuation temperature, and reached a maximum intensity by treatment at 523 or 573 K (spectra 4 and 5). The changes of IR spectra in these processes are also given in this figure as the difference spectra with the spectrum of the H_2-treated sample (at 423 K). It is clearly found that the amount of formed -ZnH species decreases through evacuation at temperatures higher than 473 K, whereas the amount of -OH increases. Taking account of the IR data, these behaviors can be reasonably interpreted by assuming the formation of the zinc metal species (reaction 2), where Z_A and Z_B mean the MFI-type zeolite lattice sites including Al atoms:

$$Z_A\text{–O–}Zn^{2+}\text{–O–}Z_B + H_2 \rightarrow Z_A\text{–O–}(ZnH)^+ + Z_B\text{–}OH^+ \quad \text{(first reaction)} \quad (1)$$

$$Z_A\text{–O–}(ZnH)^+ \rightarrow Zn^0 + Z_A\text{–}OH^+ \quad \text{(second reaction)} \quad (2)$$

$$Z_A\text{–O–}Zn^{2+}\text{–O–}Z_B + H_2 \rightarrow Zn^0 + Z_A\text{–}OH^+ + Z_B\text{–}OH^+ \quad \text{(total reaction)}$$

To verify the formation of metal species after H_2 treatment of ZnMFI at 423 K and subsequent evacuation at 573 K, we measured the XANES spectra for the sample treated with H_2 at 423 K, followed by evacuation at 573 K, as shown in Fig. 2. In connection with ZnMFI treated with H_2 at various temperatures, the change in the XANES spectra was very small. If the spectra are examined in detail, a shoulder band can be seen at the lower energy side in the first main band for the sample treated with H_2 at 423 K, followed by evacuation at 573 K. The XANES spectrum of atomic zinc vapor was reported by Mihelič *et al.* [1]; their datum is also depicted in this figure, clearly indicating the appearance of the highest band at around 9.66 keV. This fact strongly supports the presence of metal species in our sample: atomic zinc species. This band decreased in intensity after evacuation at 873 K and finally reverted to its original intensity. These facts give clear evidence that the reversible redox cycle is completely repeated: $Zn^{2+} \rightarrow ZnH \rightarrow Zn^0 \rightarrow Zn^{2+}$.

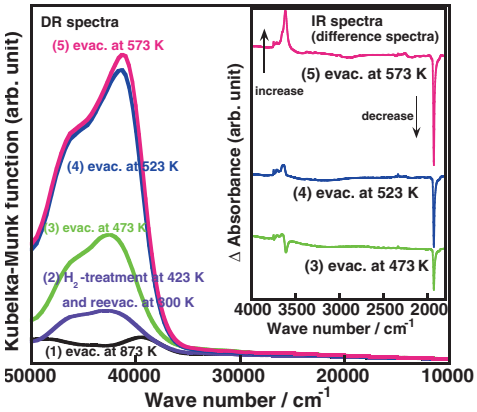

Figure 1: UV-Vis diffuse reflectance and IR spectra.

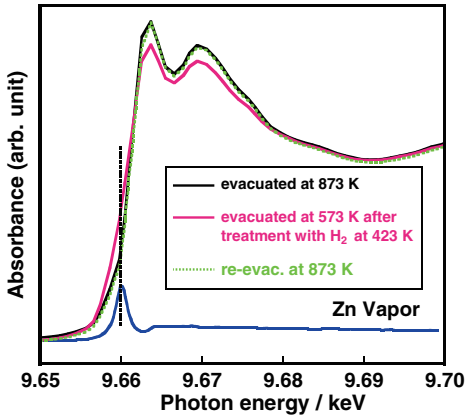

Figure 2: XANES spectra.

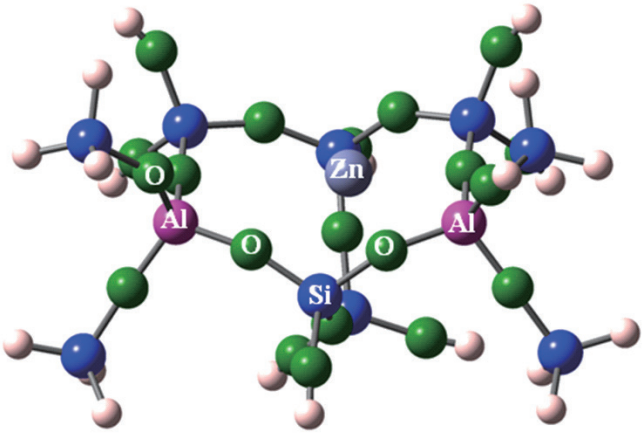

Figure 3: The M7-S2 model: $ZnAl_2Si_9O_{20}H_{20}$.

The heterolytic dissociation process of H_2 was followed with the aid of the DFT calculation method adopting the M7-S2 model (Fig. 3) that includes two aluminum atoms inserted into the skeleton of the MFI lattice in the six-membered ring, 6-MR, of the M7 site instead of two silicon atoms. First, we examined the possibility of simultaneous compensation of charges emanating from two alternative aluminum atoms to silicon atoms with a single Zn^{2+} ion. Furthermore, the formation of -ZnH species, together with -OH, as well as the formation process of an atomic Zn^0 species, is completely explained by utilizing this model with the aid of the DFT calculation method [2].

In the next stage, the paramagnetic Zn^+ species was, for the first time, successfully prepared by excitation with UV light in the region being ascribable to the absorption band due to the 4s-4p transition of an atomic Zn^0 species encapsulated in the MFI-type zeolite. The formed species gives a specific ESR band at $g = 1.998$ and also peculiar absorption bands at around 38,000 and 32,500 cm^{-1}, which are clearly indicating the formation of the Zn^+ species in MFI. The transformation process ($Zn^0 \rightarrow Zn^+$) was explained by considering the mechanism via the excited triplet state (^3P) caused by the intersystem crossing from the excited singlet state (^1P) of an atomic Zn^0 species grafted in MFI; the transformation process was well reproduced with the aid of the DFT calculation method. The thus-formed Zn^+ species exhibits a characteristic reactivity at room temperature with an O_2 molecule, forming a η^1-type of Zn^{2+}-O_2^- species [3].

REFERENCES

[1] A. Mihelič, A. Kodre, I. Arčon, J.P. Gomilšek and M. Borowski, *Nucl. Instrum. Methods Phys. Res. Sect. B* **196**, 194 (2002).
[2] A. Oda, H. Torigoe, A. Itadani, T. Ohkubo, T. Yumura, H. Kobayashi and Y. Kuroda, *Angew. Chem. Int. Ed.* **51**, 7719 (2012).
[3] A. Oda, H. Torigoe, A. Itadani, T. Ohkubo, T. Yumura, H. Kobayashi and Y. Kuroda, *J. Am. Chem. Soc.* **135**, 18481 (2013).

BEAMLINES

AR-NW10A and BL-9C

A. Oda[1], H. Torigoe[1], A. Itadani[1], T. Ohkubo[1], T. Yumura[2], H. Kobayashi[2] and Y. Kuroda[1] ([1]Okayama Univ., [2]Kyoto Inst. of Tech.)

Superplasticity in Hydrous Melt-Bearing Dunite and its Implications for Shear Localization in the Earth's Upper Mantle

In order to explore the effect of intergranular fluids on the plastic flow of olivine in the Earth's upper mantle, deformation experiments on hydrous melt-bearing dunite were conducted under the conditions of the upper mantle (pressure: 1.3-5.7 GPa; temperature: 1270-1490 K). Superplasticity dominated the deformation of olivine, and the creep strength of hydrous melt-bearing dunite was 2-5 times lower than that of melt-free dunite. Superplasticity is the dominant creep mechanism of olivine in fluid-bearing fine-grained peridotites at low temperatures. Therefore, geological fluids are likely to play an important role in the shear localization and thus the initiation of subduction in the upper mantle.

Olivine is the major constituent mineral in the Earth's upper mantle and controls its dynamics. Many experimental studies have been performed on the plastic flow behavior of olivine at high temperature (i.e., the temperatures in the upper mantle). Previous studies showed that the plastic flow of olivine at high temperature is controlled by two creep mechanisms: power-law dislocation creep and diffusion creep [1]. Some authors argued that other creep mechanisms such as dislocation-accommodated grain boundary sliding and diffusion-accommodated grain boundary sliding also play an important role in the upper mantle. Both of these mechanisms are often called "superplasticity" [2].

It has been recognized that the dynamics of the asthenospheric upper mantle need to be discussed based on the rheology of hydrous olivine rather than on anhydrous olivine. Not only dissolved water but also intergranular melt/fluid phases decrease the creep strength of olivine. In the olivine-basalt and olivine-aqueous fluid systems, power-law dislocation creep and diffusion creep are enhanced by the presence of a melt/fluid phase [3, 4]. However, the effects of intergranular fluids on the creep strength of olivine aggregates have not been evaluated at the pressures found in the Earth's upper mantle (pressure range in previous studies: 0.3-0.6 GPa).

Based on deformation experiments on hydrous melt-bearing dunite (92 vol.% of olivine and 8 vol.% of pyroxenes with less than 2.5 vol.% of the melt phase) under the conditions of the Earth's upper mantle, we showed that superplasticity is an important creep mechanism for the deformation of fluid-bearing peridotites in the upper mantle [5]. We conducted deformation experiments on hydrous melt-bearing dunite at pressures of 1.3-5.7 GPa, temperatures of 1270-1490 K, and a constant strain rate (in the range of $0.7\text{-}8.2\times10^{-5}$ s^{-1}) using a deformation-DIA apparatus (D-CAP) installed in MAX-III at the AR-NE7A beamline. Strain of the samples was measured by the distance between two platinum strain-markers which were monitored by using *in-situ* monochromatic X-ray radiography (Fig. 1). Axial differential stress and generated pressure were measured by using the radial diffraction of monochromatic X-rays (energy 50 keV, wavelength 0.245 Å). See [5] for the details of the experiments.

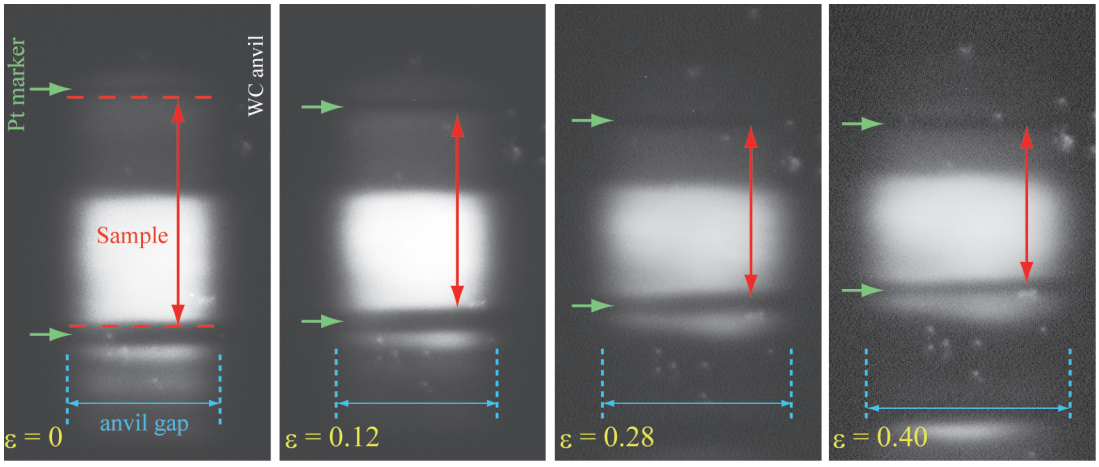

Figure 1: X-ray radiographs acquired before (ε = 0) and during the deformation (ε = up to 0.40) at 1.7 GPa and 1370 K. Positions of platinum strain markers (black lines) are shown by green arrows. Blue and red double arrows represent the anvil gap and the range of sample, respectively. ε represents the sample strain.

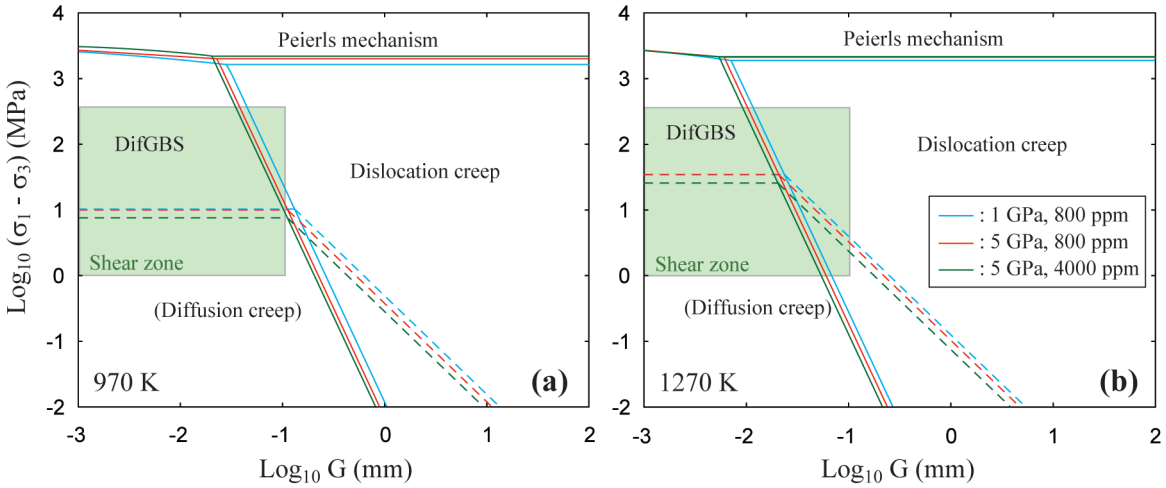

Figure 2: Deformation mechanism maps for olivine in the hydrous melt-bearing dunite at pressures of 1 and 5 GPa and temperatures of (a) 970 K and (b) 1270 K. Water content in olivine was fixed at 800 or 4000 ppm H/Si for calculating the maps. The solid lines represent the boundaries between deformation fields (DifGBS: diffusion-accommodated GBS). Because diffusion creep of olivine has not been reported in fluid-bearing dunite, the diffusion creep dominant region is hypothetically shown by dashed lines. The green-shaded area in (a) and (b) represents the conditions observed in natural peridotite shear zones [7]. $\sigma_1 - \sigma_3$: differential stress; G: grain size.

The strain rate was proportional to steady-state creep strength to the 2.1 power, and the steady-state creep strength was proportional to grain size to the ~3 power. The activation energy of the deformation was found to be 329 kJ/mol. This value is close to the activation energy for diffusion creep of "wet" olivine (295 kJ/mol: [6]), suggesting that the creep mechanism is mainly controlled by the diffusion process. These results show that the dominant deformation mechanism of olivine is diffusion-accommodated grain boundary sliding (i.e., superplasticity). The creep strength of the melt-bearing samples was factors of 2-4 lower than that of olivine controlled by the power-law dislocation creep of hydrous olivine in the case of the same water content. Deformation mechanism maps of hydrous-melt bearing dunite as a function of stress and grain size under mantle wedge conditions are shown in Fig. 2. The region of diffusion-accommodated grain boundary sliding (GBS) is distributed in the area of fine-grain (< 0.1 mm) and high-stress (> 10 MPa) conditions. The diffusion-accommodated GBS field expands with decrease in temperature. Therefore, diffusion-accommodated GBS would be the dominant creep mechanism of olivine in fluid-bearing fine-grained peridotites under the conditions of low temperature and high stress (i.e., mylonites in shear zones). In fact, many petrological observations have shown that grain-size-sensitive creep processes promote strain localization in fine-grained mylonites in shear zones [7]. Shear localization caused by the diffusion-accommodated GBS is expected to play an important role in the initiation of subduction of the oceanic lithosphere.

REFERENCES

[1] S. Karato, M.S. Paterson and J.D. Fitzgerald, *J. Geophys. Res.* **91**, 8151 (1986).
[2] D.L. Goldsby and D.L. Kohlstedt, *J. Geophys. Res.* **106**, 11017 (2001).
[3] G. Hirth and D.L. Kohlstedt, *J. Geophys. Res.* **100**, 15441 (1995).
[4] R.D. McDonnel, C.J. Peach, H.L.M. van Roermund and C.J. Spiers, *J. Geophys. Res.* **105**, 13535 (2000).
[5] T. Ohuchi, Y. Nishihara, T. Kawazoe, D. Spengler, R. Shiraishi, A. Suzuki, T. Kikegawa and E. Ohtani, *Earth Planet. Sci. Lett.* **335**, 59 (2012).
[6] S. Mei and D.L. Kohlstedt, *J. Geophys. Res.* **105**, 21457 (2000).
[7] J.M. Warren and G. Hirth, *Earth. Planet. Sci. Lett.* **248**, 438 (2006).

BEAMLINE

AR-NE7A

T. Ohuchi[1], Y. Nishihara[1], T. Kawazoe[2], D. Spengler[3], R. Shiraishi[4], A. Suzuki[4], T. Kikegawa[5] and E. Ohtani[4]
([1]Ehime Univ., [2]Univ. Bayreuth, [3]Univ. Potsdam, [4]Tohoku Univ., [5] KEK-PF)

Crystal Structure of Human Tyrosylprotein Sulfotransferase: Insights into Substrate-Binding and Catalysis of Post-Translational Protein Tyrosine Sulfation

Post-translational protein modification by tyrosine sulfation plays an important role in extracellular protein-protein interactions, with implications for immune response, inflammation, hemostasis, and viral infection including that of the human immunodeficiency virus (HIV). The sulfation reaction is catalyzed by the Golgi enzyme called tyrosylprotein sulfotransferase (TPST). We reported the first crystal structure of the human TPST complexed with a substrate peptide (designated C4P5Y3) derived from a tyrosine-sulfated protein, complement C4, and 3'-phosphoadenosine-5'-phosphate (PAP), a degradation product of the sulfate donor, 3'-phosphoadenosine-5'-phosphosulfate (PAPS). The structural information, in conjunction with the mutational analysis data, provides a molecular basis for substrate-binding and catalysis, and explains how TPST can accommodate a variety of substrate proteins.

Protein tyrosine sulfation is a ubiquitous posttranslational modification that occurs in multicellular eukaryotic organisms. This unique modification has been demonstrated in a variety of secretory and membrane-bound proteins, such as complement factor C4, immunoglobulins, hirudin, P-selectin glycoprotein ligand-1, secreted signal peptides, and chemokine receptors, which are involved in a variety of physiological processes including immune response, hemostasis, development, and inflammation. In many cases, the sulfated tyrosine residues contribute to extracellular protein-protein interactions such as the antigen recognition of antibodies, inflammatory leukocyte adhesion to blood vessel walls, and the binding between chemokine receptors and their ligands. In the case of the chemokine receptor CCR5, its N-terminal extracellular region carrying the sulfated tyrosine residues has been shown to be crucial in mediating HIV binding/infection.

The protein tyrosine sulfation is catalyzed by the tyrosylprotein sulfotransferase (TPST) located in the Golgi apparatus. However, since no TPST structure is currently available, the mechanisms underlying the catalysis of the tyrosine sulfation reaction and the recognition of substrate proteins remain unclear.

We reported the first crystal structure of the human TPST (hTPST), complexed with a substrate peptide derived from complement C4 protein and PAP, a degradation product of the sulfate donor, PAPS, at 1.9 angstrom resolution [1] (Fig. 1). The structure revealed, for the first time, a detailed atomic view of the catalytic mechanism and substrate binding. The TPST is similar in catalytic mechanism to other types of sulfotransferases, but differ substantially in substrate recognition mode.

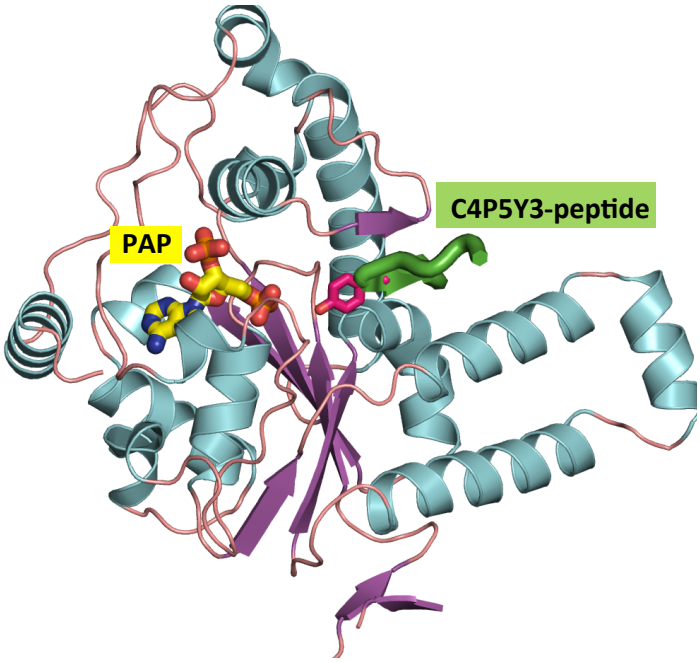

Figure 1: Overall structure of hTPST.

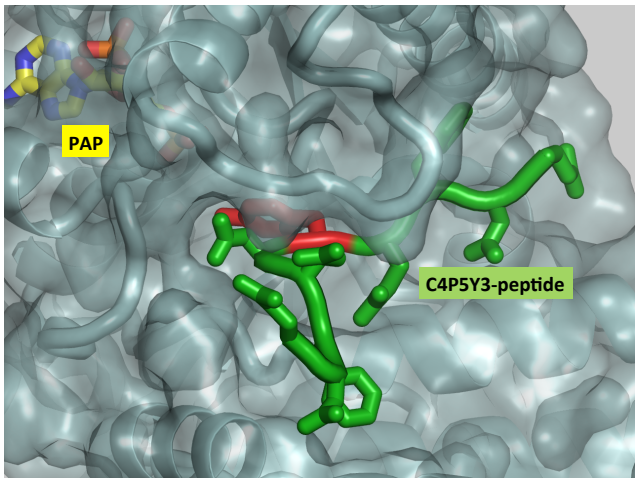

Figure 2: Substrate binding site of hTPST

The ternary structure of hTPST-PAP-C4P5Y3 provides atomic details concerning the reaction mechanism of TPST. When PAPS is superimposed onto PAP, the hydroxyl group of $Y^{acceptor}$ is located 2.6 Å from the sulfur atom of PAPS. The location of the sulfonate group is consistent with a S_N2-like in-line displacement mechanism as previously proposed for other sulfotransferases. The residues Arg78, Glu99, Lys158 and Ser285 of hTPST are in proper positions to play a catalytic role in the sulfonate transfer reaction. Superposition of hTPST with the active site of SULT1D1 with PAPS and *p*-nitrophenol and that of HS3OST3 with PAP and tetrasaccharide also indicate the catalytic functions of the above-mentioned residues of hTPST. Data from the mutational studies provide further support for the roles of Arg78, Glu99, Lys158, and Ser285 as, respectively, catalytic acid, catalytic base, stabilization of transition state, and stabilization of transition state.

The substrate peptide binds in the deep cleft of the hTPST2 and forms an L-shaped structure by using a short parallel β-sheet type interaction (Fig. 2). The structural, mutational, and other information reveal that an essential requirement for the substrate is to have only one acceptor tyrosine residue located in an intrinsically flexible region in order to fit into the deep cleft of hTPST. Other observed specific interactions may just serve to strengthen the affinity of the substrate and therefore are not essential for substrate binding. Probably because the aspartic acid residue located at the -1 position most highly strengthens the affinity by hydrogen bonding with the main chain of hTPST, this residue is most commonly found among the target sequences. Many other hydrophobic and electrostatic interactions are also utilized in diverse substrate amino acid sequences around tyrosine sulfation sites of proteins.

Surprisingly and interestingly, the mode of recognition for substrate peptide seems to resemble that observed for the receptor type tyrosine kinases. Because both these two types of enzymes are involved in post-translational modification on Tyr residue, the similarity might be the result of convergent evolution regardless of their distinct intracellular locations and substrate proteins.

To summarize, the molecular description of the hTPST crystal structure provides a framework for understanding the reaction mechanisms of protein tyrosine sulfation, which is one of the major posttranslational protein modifications. The information should be useful for the structure-based design of specific inhibitors of TPST.

REFERENCE

[1] T. Teramoto, Y. Fujikawa, Y. Kawaguchi, K. Kurogi, M. Soejima, R. Adachi, Y. Nakanishi, E.Mishiro-Sato, M-C. Liu, Y. Sakakibara, M. Suiko, M. Kimura and Y. Kakuta, *Nat. Commun.* **4**,1572 (2013).

BEAMLINE

AR-NW12A

T. Teramoto[1], Y. Fujikawa[1?], Y. Kawaguchi[1], K. Kurogi[2?], M. Soejima[1], R. Adachi[1], Y. Nakanishi[1?], E. Mishiro-Sato[2], M.-C. Liu[3], Y. Sakakibara[2], M. Suiko[2], M. Kimura[1] and Y. Kakuta[1] ([1]Kyushu Univ., [2]Univ. of Miyazaki, [3]The Univ. of Toledo)

Long-Awaited Structural Information of the *Helicobacter pylori* CagA Oncoprotein

The CagA protein of *Helicobacter pylori* plays an important role in gastric carcinogenesis. Upon delivery into gastric epithelial cells, CagA localizes to the plasma membrane, where it acts as an oncogenic scaffold/hub. CagA comprises a solid N-terminal region and an intrinsically disordered C-terminal tail that directs versatile protein interactions. X-ray crystallographic analysis revealed that the N-terminal CagA has a completely new structure comprising three discrete domains. Domain I constitutes a mobile CagA N-terminus, while Domain II tethers CagA to the membrane by interacting with phosphatidylserine. Domain III interacts intramolecularly with the disordered C-terminal CagA, which potentiates the oncogenic CagA action.

Chronic infection with *Helicobacter pylori cagA*-positive strains plays a critical role in the development of gastric carcinoma, the second-most common cause of cancer-related deaths worldwide. The *cagA* gene-encoded CagA protein is delivered into host gastric epithelial cells via the *H. pylori* type IV secretion system and is tethered to the inner leaflet of the plasma membrane, where it undergoes tyrosine phosphorylation at the Glu-Pro-Ile-Tyr-Ala (EPIYA) motif that is present in variable numbers in the C-terminal region by Src family kinases. Upon tyrosine phosphorylation, CagA acts as a pathogenic scaffold/hub protein that promiscuously interacts with a number of host proteins, most notably SHP2, an SH2 domain-containing tyrosine phosphatase activating mutation which is associated with a variety of human malignancies, and the polarity-regulation serine/threonine kinase PAR1/MARK. As a consequence, CagA delivery exerts unconstrained mitogenic stimulation while inducing junctional and polarity defects in polarized gastric epithelial cells. Sustained exposure to CagA also activates cell-reprogramming machinery by ectopically inducing stemness-related transcription factors in gastric cells. Such multifaceted actions of *H. pylori* CagA may cooperatively act to predispose host cells towards malignant transformation. Indeed, systemic expression of CagA in transgenic mice gives rise to spontaneous development of gastrointestinal and hematopoietic neoplasms, confirming its oncogenic potential in mammals. But why does a bacterial protein exert this kind of pathogenic action? It is well understood that protein function and structure are intimately interrelated. A research article by Hayashi *et al* [1] reported success for the first time in determining the tertiary structure of the entire CagA protein (1186 amino-acid residues) by combining X-ray crystallography and NMR spectroscopy. The crystal structure of CagA was determined by the SAD method using synchrotron radiation at PF AR-NE3A. CagA has a unique form, consisting of a solid N-terminal region (residues 1-876) and an intrinsically disordered C-terminal tail (residues 877-1186) (Fig. 1). The crystal structure of the N-terminal core predicts a square plate-like shape with approximate dimensions of 110 × 80 × 55 $Å^3$. The N-terminal CagA contains 23 α-helices and comprises three discrete domains, termed Domains I to III. Domain I, the most N-terminal domain, is composed of 10 α-helices, having a small interacting surface area (374 $Å^2$) with Domain II but has no interaction with Domain III. Because of this weak interaction, Domain I appears to be quite mobile and flexible. Domain II and Domain III comprise a protease-resistant structural core of CagA that displays an N-shaped dimodular architecture. Domains II and III are connected by a long helix α19. Domain II also contains a large anti-parallel β-sheet, which has an inserted subdomain (residues 370-446). This subdomain, located at the center of the CagA N-terminal region, tightly interacts with the β-sheet, suggesting that it comprises a rigid core of CagA. A cluster of basic residues termed the “basic patch”, which comprises a part of the Domain II surface, attaches to the acidic membrane phospholipid, especially phosphatidylserine, which is concentrated to the inner membrane surface through electrostatic interaction. This makes the CagA C-terminal tail hang freely and thereby enables Src kinases to attach a phosphate group to the EPIYA motifs in the tail. Furthermore, the flexible C-terminal tail loops back onto the solid N-terminal core to form a lariat that strengthens association of the CagA C-terminal tail with host target proteins such as PAR1 and SHP2 (Fig. 1). Elucidation of the tertiary structure significantly improves our understanding of CagA as a bacterial pathogenic scaffold/hub that is critically involved in gastric carcinogenesis. This research, which has for the first time elucidated the structural basis through which CagA promotes gastric carcinogenesis, will be of great value in developing new strategies in targeting CagA for the prevention and/or treatment of gastric cancer.

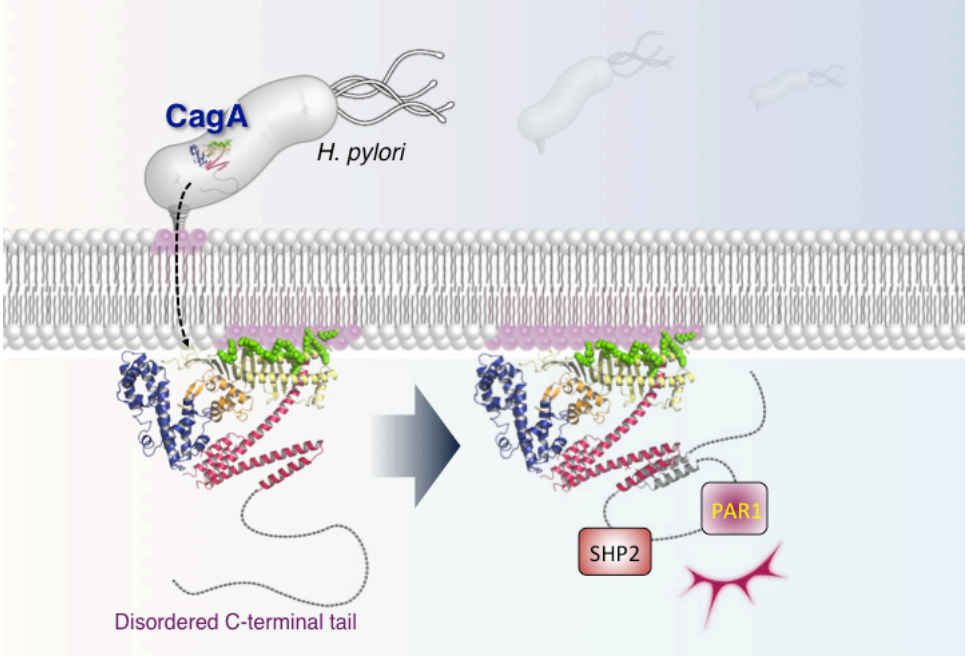

Figure 1: Tertiary structure-dependent regulation of the oncogenic potential of *H. pylori* CagA.
H. pylori CagA is delivered into host gastric epithelial cells via a bacterial micro-syringe termed the type IV secretion system, where it acts as an oncogenic scaffold/hub by perturbing intracellular signaling. The work by Hayashi *et al.* revealed that the CagA protein consists of structured N-terminal and disordered C-terminal regions [1]. Folded N-terminal CagA has a new protein structure with three distinct domains shown in blue, yellow, and red. Domain I forms the N-terminus, while Domain II tethers CagA to the inner plasma membrane via the basic patch (green)-phosphatidylserine (pink) interaction. Interaction with Domain III potentiates interaction of the disordered CagA C-terminal tail with PAR1 and SHP2, thereby enhancing the oncogenic scaffold/hub function CagA.

REFERENCE

[1] T. Hayashi, M. Senda, H. Morohashi, H. Higashi, M. Horio, L. Nagase, D. Sasaya, T. Shimizu, N. Venugopalan, H. Kumeta, N.N. Noda, F. Inagaki, T. Senda and M. Hatakeyama, *Cell Host Microbe* **12**, 20 (2012).

BEAMLINE

AR-NE3A

M. Hatakeyama[1, 2], T. Hayashi[1, 2], M. Senda[2, 3, 5] and T. Senda[4, 5] ([1]The Univ. of Tokyo, [2]JST-CREST, [3]JBIC [4]AIST, [5]KEK-PF&SBRC)

Trapping a Whole Protein in a Well-Defined Molecular Capsule

Encapsulation of a molecule in a capsular structure is a widely-used phenomenon in natural and artificial systems to achieve unique functions such as storage, emission, and control of the accommodated molecules. Proteins are attractive target molecules but the encapsulation of a protein in a well-defined molecular capsule has not been realized due to the limited size of artificial capsules. In the present study, Professor Makoto Fujita's group in the Department of Applied Chemistry and Professor Koichi Kato at the Okazaki Institute for Integrative Bioscience confined a single ubiquitin molecule within a 7-nm synthetic capsule, whose structure was clearly revealed by NMR, mass spectrometry, and finally synchrotron X-ray crystallography.

In nature, encapsulation of biomolecules, such as proteins or DNA, in huge capsular materials like virus capsids serves to control their structures and bioactivities and to store them. In artificial chemical systems, the encapsulation of small organic molecules within hollow larger capsular molecules, called "host molecules", also functions to control the structures or activities of the encapsulated guest molecules. The encapsulation of biomolecules in artificial host molecules is expected to pave the way for controlling their structures and functions at will, however, huge biomolecules like proteins have never been encapsulated because the sizes of artificial capsular molecules with precise structures are usually limited to up to 2 nm in diameter.

In 2006, we reported that a huge capsular molecule with a diameter of 4.6 nm accommodated several small organic molecules inside the host [1]. The internal chemical environment was modified to be fluorophilic by decorating the internal wall of the host with fluoroalkyl chains, and fluorous guests were extracted from the external solvent into the host. The structure of the host was precisely designed and well defined through a self-assembly process from organic molecules and transition metal ions.

In 2012, the self-assembled huge host was further extended to a diameter of 7.3 nm, and the encapsulation of a whole protein was first achieved within the synthesized capsular molecule (Fig. 1) [2]. An organic molecule tethering a protein, ubiquitin with a molecular weight of 8,600 Da, was synthesized under moderate reaction conditions to maintain the folded protein structure [3]. Then the molecule bearing a protein was mixed in a flask with another organic molecule bearing a sugar chain and palladium (II) ions in the water/acetonitrile solvent. The coordination bonds between the starting materials automatically formed to construct the product including one organic molecule bearing a protein, 23 organic molecules bearing a sugar moiety, and 12 palladium (II) ions with 100% yield. The protein was wrapped in the clustered sugar moieties, and the product showed high stability at room temperature in air.

Solution nuclear magnetic resonance (NMR) spectra showed broad signals, which indicate the formation of a huge structure, and diffusion analysis by 2D DOSY spectra revealed the diffusion coefficient, which showed that the host framework and encapsulated ubiquitin behave as a single molecule through the "host-guest" interaction.

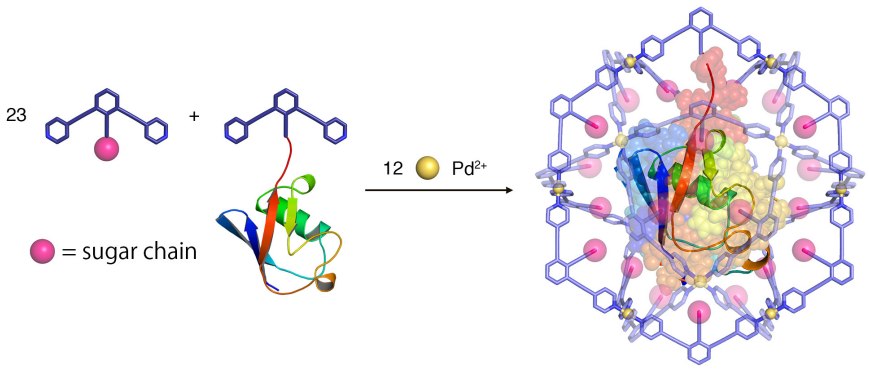

Figure 1: The self-assembly of a huge capsular molecule encapsulating a whole protein is schematically illustrated. The protein was surrounded by clustered hydrophilic sugar moieties.

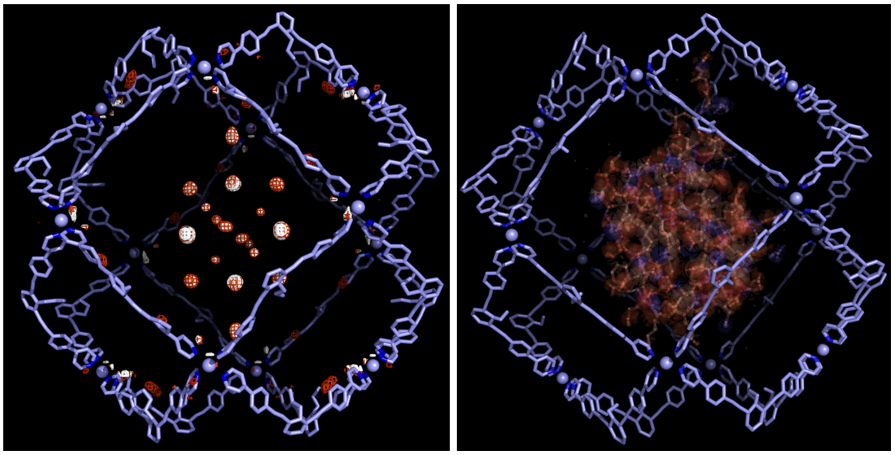

Figure 2: The protein encapsulation was confirmed by crystallographic studies in a crystalline state. (left) The mapping of electron density (red) derived from the trapped ubiquitin in the artificial host (blue). (right) The computationally simulated model structure of the product, where ubiquitin is shown in red and the host in blue.

Determination of the molecular weight was first attempted using cold-spray ionization time-of-flight mass spectrometry (CSI-TOF-MS), but the results were not satisfactory. Next, analytical ultracentrifugation (AUC) in sedimentation velocity measurement mode clearly showed the high monodispersity of the product in solution, and AUC in sedimentation equilibrium measurement mode was used to estimate the molecular weight, which was consistent with the sum of the host framework and one ubiquitin.

The three-dimensional structure of the product could not be accessed by the above-mentioned NMR and ultracentrifugation analyses, and the final structural elucidation relied on single crystal diffraction studies as a solid, crystalline state. Careful selection of the crystallization conditions led to the formation of beautiful single crystals, but a structural analysis of these single crystals could not be carried out successfully by using laboratory diffractometers. This failure could be attributed to the large unit cell of around 60 Å and volume of around 195,900 $Å^3$ and the severely disordered solvents inside and outside the host. Only strong, sharp synchrotron X-rays generated by the advanced equipment at KEK PF AR-NE3A and BL-17A and SPring-8 BL38B1, BL41XU, BL26B1, and BL26B2 finally elucidated the crystal structure of the host framework with up to 1.8Å resolution. Further analysis by the maximum entropy method (MEM) enabled visualization of the electron density for the encapsulated protein at the center of the host (Fig. 2).

REFERENCES

[1] S. Sato, J. Iida, K. Suzuki, M. Kawano, T. Ozeki and M. Fujita, *Science* **313**, 1273 (2006).
[2] D. Fujita, K. Suzuki, S. Sato, M. Y.-Utsumi, Y. Yamaguchi, N. Mizuno, T. Kumasaka, M. Takata, M. Noda, S. Uchiyama, K. Kato and M. Fujita, *Nature Commun.* **3**, 1093 (2012).
[3] D. Fujita, K. Suzuki, S. Sato, M. Y.-Utsumi, E. Kurimoto, K. Kato and M. Fujita, *Chem. Lett.* **41**, 313 (2012).

BEAMLINES

AR-NE3A and BL-17A

S. Sato and M. Fujita (The Univ. of Tokyo)

Rotation Mechanism of V_1-ATPase

Vacuolar ATPases (V-ATPases) function as ATP-driven ion pumps, which are located on membranes of various living organisms. Human V-ATPase is a promising drug target for osteoporosis and cancer metastasis. V_1-ATPase (the hydrophilic part of V-ATPase) is a rotary motor, in which a central stalk DF complex rotates inside a catalytic A_3B_3 complex with the ATP hydrolysis. We have solved the A_3B_3 complex and the V_1-ATPase from the bacterium *Enterococcus hirae*, and have proposed a model of the rotation mechanism based on their asymmetric structures.

The ion-translocating rotary ATPases (V-ATPases and F-ATPases) have evolved from a common ancestral enzyme. F-ATPases in mitochondria, chloroplasts and oxidative bacteria function as ATP synthase (ATP is the major energy currency of life) and V-ATPases in acidic organelles and plasma membranes of eukaryotic cells function as H^+ pumps. These ATPases have similar overall structures that consist of a hydrophilic portion (F_1 and V_1) and a membrane-embedded ion-transporting portion (F_o and V_o), and they have a similar reaction mechanism that occurs through rotation. *E. hirae* V-ATPase transports Na^+ or Li^+, instead of H^+. This is composed of nine subunits that are homologous to the corresponding subunits of eukaryotic enzymes. The catalytic part of the V_1 consists of a hexameric arrangement of alternating A- and B-subunits (A_3B_3), and V_1-ATPase is composed of A_3B_3 and central stalk DF complex.

We determined the crystal structures of the nucleotide-free A_3B_3 (eA_3B_3) and AMPPNP-bound A_3B_3 (bA_3B_3) at first by using BL41XU, SPring-8 [1]. Both of the A_3B_3 hexamers assembled asymmetrically, but different combinations of conformation were contained. In eA_3B_3, one of the three A adopts a closed conformation (A_C), which shifts the structure into the center of the A_3B_3, whereas the other two A adopt similar open conformations (A_O and $A_{O'}$), Similarly, one of the three B shows a closed conformation (B_C) compared to the others (B_O and $B_{O'}$) (Fig. 1**a**-**d**). The conserved nucleotide-binding sites were located between the three different combinations: A_OB_C, $A_{O'}B_O$ and $A_CB_{O'}$ pairs. In bA_3B_3, AMPPNP molecules were bound at two $A_CB_{O'}$ each, and not at the other A_OB_C (Fig. 1 **e**-**h**).

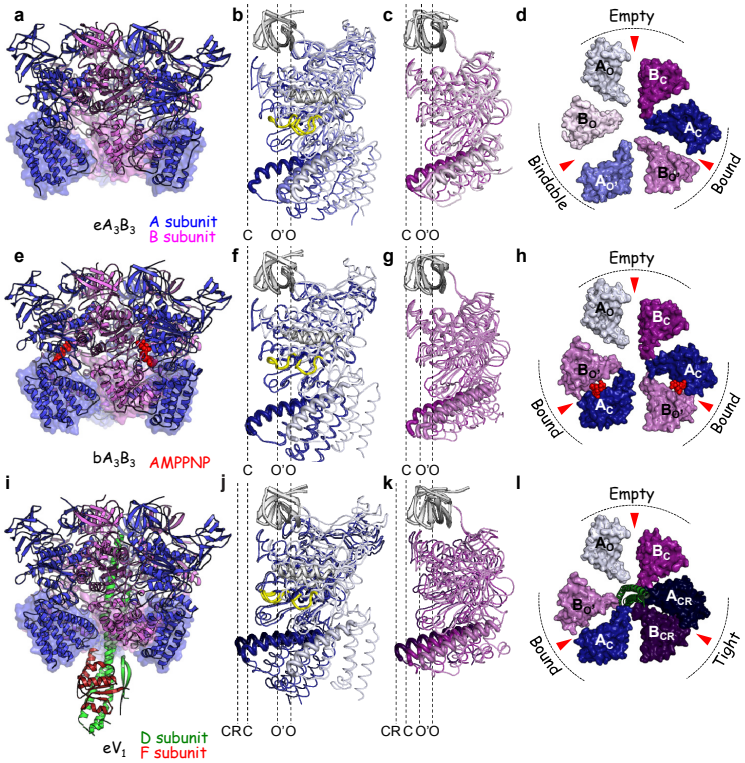

Figure 1: Structure of the A_3B_3 and A_3B_3DF complexes **a**, Side view of the nucleotide-free A_3B_3 structure (eA_3B_3). **b**, **c**, Superimposed structures at the N-terminal β-barrel (white) of the three structures of A (b) and B (c) in eA_3B_3. Open (O and O') and closed (C) conformations of A and B are shown in light and darker colors, respectively. **d**, Top view of the C-terminal domain (shown in **a** as transparent surface) of eA_3B_3 from the N-terminal β-barrel side. Red triangles indicate the nucleotide-binding sites. **e**-**h**, Structures of the AMPPNP-bound A_3B_3 complex (bA_3B_3), and **i**-**l**, Structures of the nucleotide-free A_3B_3DF complex (eV_1) viewed and colored as in **a**-**d**.

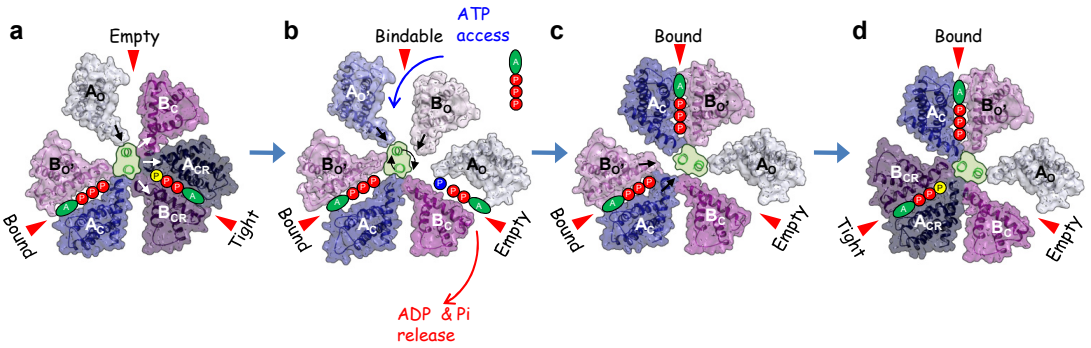

Figure 2 : Rotation model of V_1-ATPase. Top view of the C-terminal domain viewed as in Fig. 1 **d**, **h** and **l**. ATP with yellow "P" in **a** and **d** represents an ATP molecule that is committed to hydrolysis. The blue "P" in **b** represents a phosphate molecule after ATP hydrolysis. **a**, The AMPPNP-bound V_1: Two ATPs are bound in the "Bound" and "Tight" forms at first. The reaction is triggered by the ATP hydrolysis in the "Tight" form. **b**, The nucleotide-free A_3B_3: By the conversion to ADP and phosphate, the conformation of the A_3B_3 part in V_1-ATPase may return to eA_3B_3 (ground structure of A_3B_3 complex) in a cooperative manner. The "Tight" form changes to the "Empty" form with the release of ADP and phosphate and the "Empty" form changes to the "Bindable" form. **c**, The AMPPNP-bound A_3B_3: By new ATP binding to the "Bindable" form, the conformation changes to bA_3B_3, which has two "Bound" forms with two ATP, and then the DF rotates. **d**, The "Bound" form from the beginning changes to the next "Tight" form, induced by DF binding and the V_1-ATPase returns to the initial state with 120° rotation.

Compared with conformations of these pairs, we designated A_OB_C and $A_CB_{O'}$ as the "Empty" and "Bound" form, respectively. The $A_{O'}B_O$ in eA_3B_3 seemed to change to $A_CB_{O'}$ by binding with the AMPPNP molecule. We designated this unique $A_{O'}B_O$ of eA_3B_3 as the "Bindable" form. These asymmetries suggest that the formation of A_3B_3 imposes a restriction on the AB to induce conformational changes that cooperatively generate one "Empty" (ATP-unbound form), one "Bindable" (ATP-accessible form) and one "Bound" (ATP-bound form) conformation, which in turn determines the order of nucleotide binding.

Next, we determined the crystal structures of the V_1-ATPase (A_3B_3DF) by using BL-1A, AR-NE3A and AR-NW12A. The asymmetry of A_3B_3DF was increased. By the interaction with the DF complex, the "Bindable" form ($A_{O'}B_O$) of eA_3B_3 changes to the "Bound" form ($A_CB_{O'}$) of V_1 and the "Bound" form ($A_CB_{O'}$) of eA_3B_3 changes to the new "Tight" form ($A_{CR}B_{CR}$) of V_1. The new "Tight" form is composed of closer conformations of A and B (A_{CR} and B_{CR}, respectively). In the "Tight" form, the position of conserved Arg350 on B_{CR}, which helps ATP hydrolysis, seemed to approach the nucleotide binding site. The ATP hydrolysis is stimulated by this approach triggered by the movement of Arg350, which is induced by binding between the DF complex and A_3B_3.

Based on these asymmetric structures, a rotation model of V_1-ATPase was proposed. In AMPPNP-bound V_1 (Fig. 2 **a**), two ATP molecules are bound in the "Bound" and "Tight" form at first. The "Tight" form with the ATP molecule is presumed to be the hydrolysis awaiting state, therefore the ATP hydrolysis in the "Tight" form initiates the rotary reaction. By the conversion to ADP and phosphate, the conformation of the A_3B_3 part in V_1-ATPase may return to eA_3B_3 (ground structure of A_3B_3) in a cooperative manner. The "Tight" form changes to the "Empty" form with the release of ADP and phosphate and the "Empty" form changes to the "Bindable" form. However, the interaction between the DF and "Tight" form might prevent these structural changes, and an intermediate state may exist instead of the state of Fig. 2 **b**. After that, the new ATP molecule approaches and binds to the "Bindable" form, and the conformation changes to the "Bound" form; as a result, the A_3B_3 portion has two "Bound" forms with two ATP molecules and one "Empty" form, the structure of which corresponds to bA_3B_3, and then the DF rotates (Fig. 2 **c**). At last, the "Bound" form from the beginning changes to the next "Tight" form, induced by DF binding (Fig. 2 **d**) and the V_1-ATPase returns to the initial state (Fig. 2 **a**).

REFERENCE

[1] S. Arai, S. Saijo, K. Suzuki, K. Mizutani, Y. Kakinuma, Y. I.-Katsura, N. Ohsawa, T. Terada, M. Shirouzu, S. Yokoyama, S. Iwata, I. Yamato and T. Murata, *Nature* **493**, 703 (2013).

BEAMLINES

BL-1A, AR-NE3A and AR-NW12A

S. Saijo[1], I. Yamato[2] and T. Murata[3, 4] ([1]KEK-PF, [2]Tokyo Univ. of Science, [3]Chiba Univ., [4]JST-PRESTO)

Mechanistic Insights into the Activation of Rad51-Mediated Strand Exchange from the Structure of a Recombination Activator: the Swi5-Sfr1 Complex

Rad51 forms a helical filament on single-stranded DNA and promotes strand exchange between two homologous DNA molecules during homologous recombination. The Swi5-Sfr1 complex interacts directly with Rad51 and stimulates strand exchange. We describe structural and functional aspects of the complex. Swi5 and the C-terminal domain of Sfr1 form an essential activator complex with a parallel coiled-coil heterodimer. The resultant coiled-coil is sharply kinked, generating an elongated crescent-shaped structure suitable for binding within the helical groove of the Rad51 filament. Our data suggest that the snug fit resulting from the complementary geometry of the heterodimer activates and stabilizes the Rad51 filament.

Homologous recombination (HR) plays a central role not only in genetic diversity but also in preserving genomic integrity, and thus defects in HR may result in susceptibility to cancer. RecA-family DNA recombinases are key players in HR. In eukaryotes, there are two known classes of the recombinases, Rad51 and Dmc1; the former functions generally in both mitotic and meiotic HR and HR-mediated DNA repair, and the latter acts specifically in meiosis. Recombinases bind to single-stranded DNA (ssDNA), and the resultant functional complex, termed a presynaptic filament, carries out DNA strand exchange; binding and strand exchange are the central reactions of HR. Auxiliary factors (referred to as mediators) are required to form/activate the presynaptic filament of eukaryotic recombinases.

The Swi5-Sfr1 complex from the fission yeast is one of the auxiliary proteins. Swi5 (85 residues) and Sfr1 (299 residues) are both widely conserved from yeast to humans. The Swi5-Sfr1 complex binds to the Rad51 presynaptic filament, directly stimulates Rad51-mediated displacement of RPA from ssDNA, and stabilizes the Rad51 filament that has already formed on the ssDNA. It is of great interest how Swi5-Sfr1 stimulates Rad51-driven strand exchange. To address this issue, we undertook structural analyses of the fission yeast Swi5-Sfr1 complex.

We produced a truncated Sfr1 lacking the N-terminal 180 residues, hereafter referred to as Sfr1C. Sfr1C forms a complex with Swi5. To gain structural insight into the mechanism of Swi5-Sfr1-mediated activation of the Rad51 filament, we determined the crystal structure of the Swi5-Sfr1C complex (2.3 Å resolution) [1]. Swi5 and Sfr1C form a parallel coiled-coil heterodimer and the Swi5-Sfr1C complex has an elongated shape (Fig. 1).

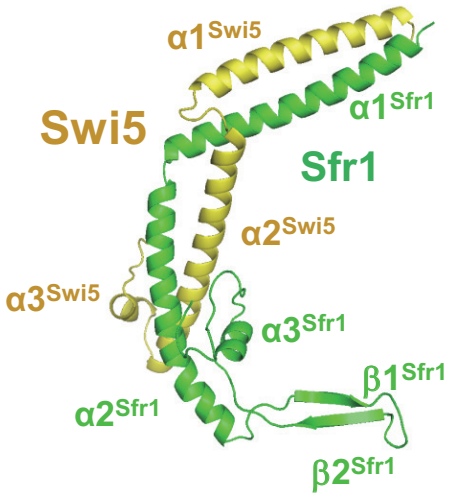

Figure 1: Ribbon representation of the Swi5-Sfr1C complex. Swi5 and Sfr1C are presented in yellow and green, respectively.

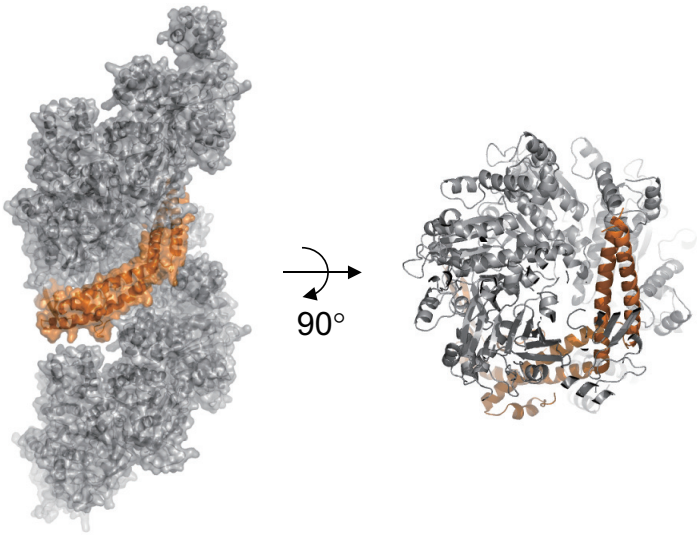

Figure 2: Docking model of the Swi5-Sfr1 complex (orange) into the Rad51 filament (gray) viewed from the side (left) and top (right). Molecules are shown as a ribbon drawing and transparent molecular surface (left). The Rad51 filament is modeled by a RadA structure (PDB id:2FPM).

The Swi5 and Sfr1C subunits of the heterodimers are firmly joined by two leucine zippers and a bundle structure at the bottom. The C-terminal regions in both Swi5 and Sfr1 fold back to the second leucine zipper and form a globular domain resembling a four-helix bundle that is stabilized primarily by van der Waals interactions. Hydrophobic residues from $\alpha 2^{sfr1}$, $\alpha 3^{sfr1}$, and the loop are buried in the interior of the bundle, where they pack together and stabilize the heterodimer.

Remarkably, the structure of the Swi5-Sfr1C complex is sharply kinked (130°). Beyond this kink, the structure is held together by the second leucine zipper. The kinked region is stabilized by several interactions. These interactions maintain the relative orientation between the two leucine zippers.

Residues participating in the interaction between the leucine zippers and the bundle are highly conserved across species. This conservation suggests that, in various species, Swi5 in complex with Sfr1C adopts a structural architecture similar to that observed in the S. pombe Swi5-Sfr1 complex.

The kinked structure of Swi5-Sfr1C fits snugly into the helical groove of the Rad51 filament, as revealed by molecular docking (Fig. 2). A single Swi5-Sfr1C complex seems to interact with up to four to five Rad51 molecules to bind into the filament. SAXS data revealed that the Swi5-SfrFL complex is approximately twice as long as the Swi5-Sfr1C [2]. This molecular “vine”, composed of the Swi5-Sfr1 complex, seems to wind itself around the Rad51 filament, which is composed of up to 10 Rad51 molecules. This structural feature agrees well with the fact that the stimulation was most effective when the Swi5-Sfr1:Rad51 ratio was 1:10 to 1:20. We propose that Swi5-Sfr1 may transiently and repeatedly interact with the filament via the groove, inducing a local conformational change that activates the strand-exchange activity. Our present results provide the first exploration of the mechanistic aspects of the functional interactions between recombinases and their activators at atomic resolution.

REFERENCES

[1] T. Kuwabara Y. Murayama, H. Hashimoto, Y. Kokabu, M. Ikeguchi, M. Sato, K. Mayanagi, Y. Tsutsui, H. Iwasaki and T. Shimizu, *Structure* **20**, 440 (2012).

[2] Y. Kokabu, Y. Murayama, N. Kuwabara, T. Oroguchi, H. Hashimoto,Y. Tsutsui, N. Nozaki, S. Akashi, S. Unzai, T. Shimizu, H. Iwasaki, M. Sato and M. Ikeguchi, *J. Biol. Chem.* **286**, 43569 (2011).

BEAMLINES

AR-NW12A and BL-17A

T. Shimizu (The Univ. of Tokyo)

Fungal Antifreeze Protein Consists of a Unique β-Solenoid Structure

We solved the first crystal structure of a 223-residue monomeric antifreeze protein (AFP) from snow mold fungus, *Typhura ishikariensis* (*Tis*AFP6). It forms a semipear-shaped globular structure, whose principal constituent is a 6-loop right-handed β-solenoid with a triangular cross-section, in which the N- and C-terminal loops are uniquely adjacent to each other within the solenoid. The sequence of the loops exhibited no repetitive property, whose lengths are ranging from 18 to 27 residues. This β-solenoid locates a putative ice-binding site in one of the three faces of *Tis*AFP6, whose irregularity is remarkable compared with that identified in the known AFPs.

AFP is a macromolecule that specifically binds to an ice crystal to inhibit its growth, facilitating the freeze tolerance of AFP-containing organisms such as fishes, insects, bacteria, and fungi living in cold environments. We have examined the biochemical property and the ice-binding activity of two isoforms of 223-residue fungal AFP from *Typhura ishikariensis* (*Tis*AFP6 and 8) [1]. The primary sequences of the two *Tis*AFP isoforms exhibited no similarity to that of "hyperactive AFPs" from insects and bacteria consisting of tandem repeat sequences. Nevertheless, the two fungal AFP isoforms were capable of binding to both prism and basal planes of an ice crystal similarly to the hyperactive AFPs. Here we determined the 0.95-Å high-resolution crystal structure of *Tis*AFP6, and characterized its ice-binding site (IBS) [2]. The *Tis*AFP6 isoform constructs a 52-Å-long semipear-shaped structure, whose principal constituent is a six-loop right-handed β-helix (β-solenoid) having a triangular cross-section as well as a 20-residue α-helix that lies alongside and parallel to the β-solenoid. A prominent feature of this β-solenoid is that the β1 loop or coil originating from near the N-terminus lies adjacent to the β6 loop from the C-terminus. In this way, the terminal loops are side by side within the parallel β-helix as illustrated by the spectrum colors showing blue next to red (Fig. 1). The six loops consist of no repetitive sequence, and their lengths range from 18 to 27 residues. The three 18-residue loops (β1, β6, and β5) are consecutively arrayed at the top of the molecule, while the bottom loops (β4, β3, and β2) have 3- to 9-residue insertions that extend outward on the same side to form the pear-like shape.

The β-helical fold of *Tis*AFP6 is stabilized by the following elements: (i) The hydrogen-bonding network between peptide CO and NH groups parallel to the β-helical axis. (ii) The cap structures stabilizing the edges of the β-strands in the terminal loops β1 and β2 to cover a hydrophobic core constructed in the β-solenoid. Note that the capping structures normally reside at the N- and C termini of a β-solenoid protein, but in *Tis*AFP6 they are formed internally between β1 and the α-helix and between the α-helix and β2. (iii) Approximately 48 aliphatic and aromatic residues construct the hydrophobic core without the support of disulfide bonds. (iv) The long α-helix that runs the length of the β-solenoid. There are 12 hydrophobic residues at the interface between the α-helix and β-solenoid.

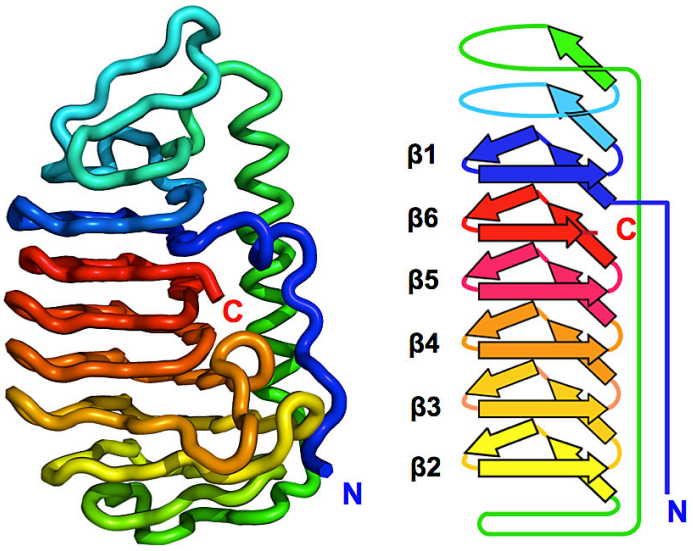

Figure 1: Backbone structure and its schematic diagram of *Tis*AFP6 to represent the construction of an irregularly ordered β-solenoid, in which the N- and C-terminal loops are side by side.

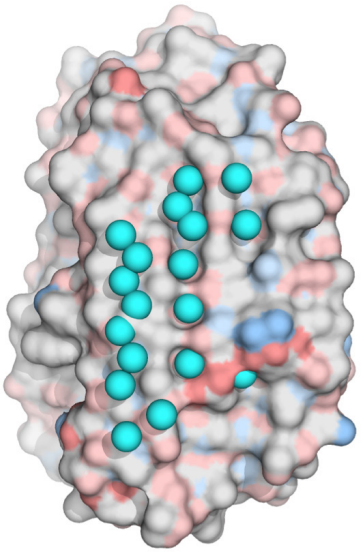

Figure 2: A selected surface of *Tis*AFP6 that locates an ice-binding site (IBS), in which the water molecules are immobilized in a few grooves. They are thought to anchor the AFP-ice interaction.

The IBS of *Tis*AFP6 was examined by steric mutations in which a tyrosyl residue replaced a short-chain amino acid. The antifreeze activity of mutants T82Y, N178Y, and V221Y, where the substitutions appeared in the middle of the three faces of the triangle, was compared with that of wild-type *Tis*AFP6. The data clearly showed that the N178Y mutation caused a significant (60%) loss in the activity. In contrast, T82Y and V221Y lost only 15% of the wild-type activity. With the help of fluorescence-based ice plane affinity (so-called FIPA) analysis of these mutants, we determined that one of the molecular surfaces including N178 locates a relatively flat IBS. Interestingly, this IBS had irregularly arrayed surface-bound water molecules (Fig. 2), which is probably due to the irregularly-ordered β-solenoid of *Tis*AFP6, which is completely distinct from the known hyperactive AFPs that locate regularly arrayed water molecules on their tandem repeat sequence. The water molecules were thought to share the positions of the ice lattice at the moment AFP attaches onto ice. A comparison of the primary sequence between the AFPs reported for various microorganisms suggests that the above-described structural features might be adopted in many other fungal AFPs.

REFERENCES

[1] T. Hoshino, M. Kiriaki, S. Ohgiya, M. Fujiwara, H. Kondo, Y. Nishimiya, I. Yumoto and S. Tsuda, *Can. J. Botany*, **81**, 1175 (2003).

[2] H. Kondo, Y. Hanada, H. Sugimoto, T. Hoshino, C.P. Garnham, P.L. Davies and S. Tsuda, *Proc. Natl. Acad. Sci.,* **109**, 9360 (2012).

BEAMLINES

BL-5A, BL-17A and AR-NW12A

H. Kondo[1, 2], Y. Hanada[1] and S. Tsuda[1, 2] ([1]Hokkaido Univ. [2]AIST)

A Structural Study of IFIT2/ISG54 Suggests its Functional Mechanism on its Anti-Viral Activity and Cellular Functions

IFIT1/ISG56 family members are well-known as interferon stimulated genes with antiviral activities. However, the mechanisms of the antiviral activities of these proteins were not clear. We determined the structure of IFIT2/ISG54, the first structure reported in the protein family. Our results showed that ISG54 is a domain swapped dimer in solution. It is an RNA binding protein which can specifically bind AU-rich RNAs. The specific RNA binding ability of ISG54 is required for its anti-viral activity. Furthermore, our results showed that ISG54 can bind some cellular RNA elements, suggesting its functional mechanism in cells.

Upon infection by virus, interferon is produced by cells, which then stimulates the expression of many genes to fight the infection. These genes are called Interferon Stimulated Genes (ISGs) [1]. The functions of some ISGs have been studied, such as ISG15 [2]. ISG56 family proteins are well-known anti-viral proteins [3], but the mechanisms of these proteins involved in their anti-viral effect were not clear. It was reported that ISG56 and ISG54 proteins can bind protein translational elongation factors, such as eIF3c and eIF3e, thus blocking the viral protein translation process [4]. However, two other investigations showed that ISG56 or ISG54 inhibit viruses with specific modification at the viral mRNA 5' end [5, 6]. To understand the exact mechanism of ISG56 family proteins, we determined the structure of human ISG54 which is the first structure reported in the ISG56 family using the facilities in BL-5A of the PF [7].

ISG54 is a super-helical structure built up by TPR repeat-like helices (Fig. 1). However, ISG54 is not a monomer but unexpectedly a domain swapped dimer through some helices in the middle of the protein, making the whole structure resemble the letter X. Interestingly, when the structure is shown as a surface electrostatic presentation, the inner surface of the C-terminal part of the super-helical protein is exclusively positively charged. This structural feature strongly suggests that ISG54 is a nucleic acid binding protein. Therefore, we performed an EMSA experiment to test the binding of ISG54 with some model RNAs. Our results showed that ISG54 can bind AU-rich double-strand model RNAs but not GC-rich RNAs. Phosphate modification at the 5' end or methylation state on the Cap structure of viral mRNA is not required for the binding. To test whether the RNA binding ability of ISG54 is required for its antiviral activity, we used VSV and Sendai virus as model systems to perform the anti-viral activity experiment. The results showed that over-expression of wild-type ISG54 can block the replication of these viruses in HEK293 cells; however, disruption of RNA binding ability of ISG54 impaired or decreased the anti-viral activity of this protein, suggesting that the RNA binding ability of ISG54 is required for anti-VSV and Sendai virus activity. Besides the anti-viral activity, we also considered the potential mechanisms of ISG54 in its cellular functions. The crystal structure was determined by the SAD method by selenium derivative by using the KEK radiation facilities and Shanghai synchrotron radiation facilities.

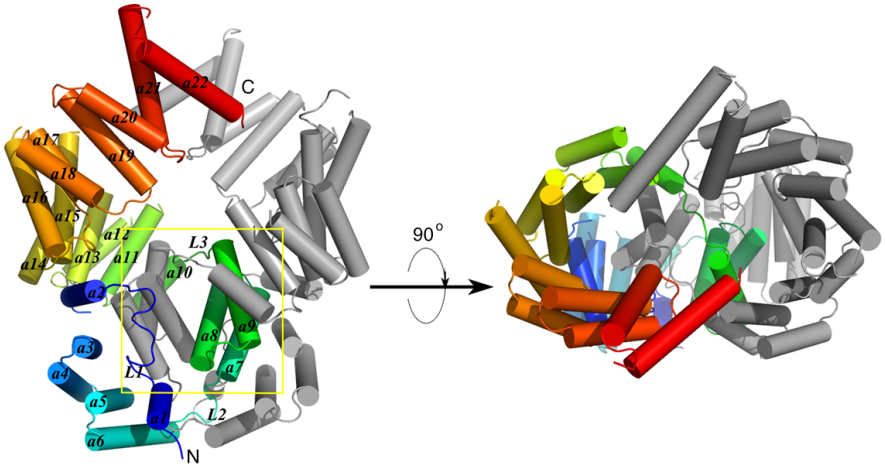

Figure 1: IFIT2/ISG54 is a domain swapped dimer with a super-helical structure at its C-terminal. One monomer is shown in gray and the other one is shown in spectral colors, from blue at the N-terminal to red at the C-terminal. The secondary structure elements are labeled. In the ISG54 dimer, helixes 7-9 from one monomer insert into the other monomer, forming the domain swapped interface, as shown in the yellow box. Left panel: side view of the structure; Right panel: top view.

REFERENCES

[1] N. Yan and Z.J. Chen, *Nat. Immunol.* **13**, 214 (2012).
[2] J. Narasimhan, M. Wang, Z. Fu, J.M. Klein, A.L. Haas, J.-Ja and P. Kim, *J. Biol. Chem* **280**, 27356 (2005).
[3] V. Fensterl and G.C. Sen, *J. Interferon Cytokine Res.* **31**, 71 (2011).
[4] J. Guo, D.J. Hui, W.C. Merrick and G.C. Sen, *The EMBO J.* **19**, 6891 (2000).
[5] A. Pichlmair, C. Lassnig, C-A. Eberle, M.W. Górna, C.L. Baumann, T.R. Burkard, T. Bürckstümmer, A. Stefanovic, S. Krieger, K.L. Bennett, T. Rülicke, F. Weber, J. Colinge, M. Müller and G. Superti-Furga, *Nat. Immunol.* **12**, 624 (2011).
[6] S. Daffis, K.J. Szretter, J. Schriewer, J. Li, S. Youn, J. Errett, T.-Yu Lin, S. Schneller, R. Zust, H. Dong, V. Thiel, G.C. Sen, V. Fensterl, W.B. Klimstra, T.C. Pierson, R.M. Buller, M. Gale Jr, P.-Yong Shi and M.S. Diamond, *Nature* **468**, 452 (2010).
[7] Z. Yang, H. Liang, Q. Zhou, Y. Li, H. Chen, W. Ye, D. Chen, J. Fleming, H. Shu and Y. Liu, *Cell Res.* **22**, 1328 (2012).

BEAMLINE

BL-5A

Z. Yang[1], H. Liang[1], Q. Zhou[2], Y. Li[2], H. Chen[3], W. Ye[2], D. Chen[3], J. Fleming[1], H. Shu[2] and Y. Liu[1]([1]CAS, [2]Wuhan Univ., [3]Peking Univ.)

Cooperative Protein Structural Dynamics of Homodimeric Hemoglobin

Proteins serve as molecular machines in performing their functions, but the detailed structural propagations are difficult to observe in their native aqueous environments in real time. For example, despite extensive studies, the solution-phase structures of the intermediates along the allosteric pathways for the propagations between the relaxed (R) and tense (T) forms have remained elusive. In this work, we employed picosecond X-ray solution scattering [1] and novel structural analysis [2] to track the detailed structural dynamics of wild-type homodimeric hemoglobin (HbI) from the clam *Scapharca inaequivalvis* and its F97Y mutant over a wide time range.

The allosteric structural transition of hemoglobin induced by ligand binding is an important process that is directly related to the biological function and reactivity of the protein. Because of the heteromeric nature of human tetrameric hemoglobin (HbA), the structural transition between allosteric sites involving cooperative ligand binding and subsequent tertiary and quaternary structural changes is complex. As a result, it has been difficult to characterize the structure and kinetics of singly, doubly, or multiply liganded species that are transiently formed along the allosteric pathways. In this regard, HbI has a simpler homodimeric structure and thus is a convenient model system for studying allosteric structural changes. However, even for this simpler system, the allosteric process involving cooperative ligand binding and subsequent tertiary and quaternary structural change is complex, and its detailed structural dynamics have yet to be understood completely.

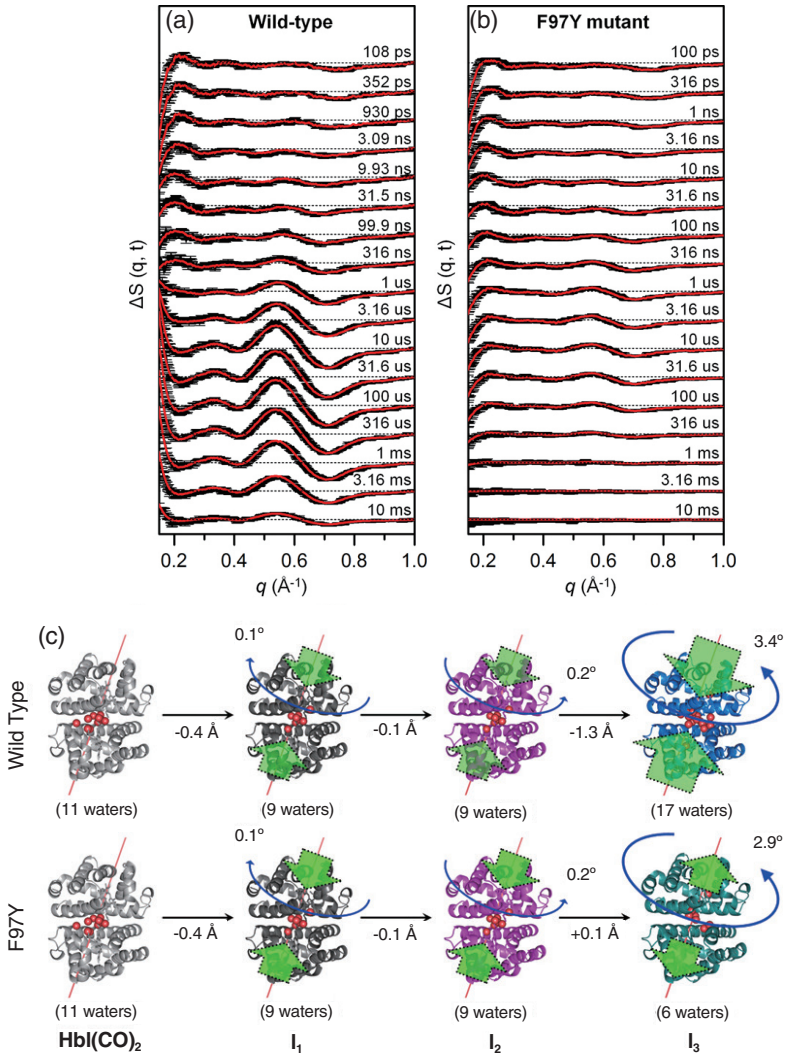

Figure 1: The picosecond pump-probe X-ray solution scattering data for (a) wild-type $HbI(CO)_2$ and (b) its F97Y mutant are shown. The time delay after photoexcitation is indicated above each curve. Experimental curves (black) are compared with theoretical curves (red) that were generated from data analysis. The extracted structural dynamics are summarized in (c). The green and blue arrows in (c) are used to indicate the relative magnitudes and directions of the changes in the heme-heme distance and subunit rotation angle relative to $HbI(CO)_2$.

In this work, to investigate directly the structural dynamics of HbI in the solution phase, we applied pump-probe X-ray solution scattering (which is globally sensitive to secondary, tertiary, and quaternary structural changes of proteins in solution) to visualize the detailed allosteric structural transition of HbI in solution in real time. By applying a novel structural analysis using Monte Carlo simulations to the measured X-ray solution scattering data, we describe in detail the structural dynamics involved in the allosteric transitions of wild-type HbI and its F97Y mutant.

Time-resolved X-ray solution scattering data were acquired using the pump-probe method at the NW14A beamline at PF-AR. Aqueous solution samples of HbI ligated with CO ligands [$HbI(CO)_2$] and its F97Y mutant were prepared using a previously established protocol [3]. The samples contained in a capillary of 1 mm thickness were excited with ~35 ps laser pulses at 532 nm. Time-resolved scattering curves were collected at 40–70 pump-probe time delays between the laser pump pulse and the X-ray probe pulse in the range from 100 ps to 56.2 ms as well as at a reference time delay of -5 μs. To attain a signal-to-noise ratio good enough for data analysis, about 20 images were acquired and averaged at each time delay. The measured time delays were spread evenly on a logarithmic time scale. Taking the difference between the scattering curve measured at each time delay point and the reference scattering curve measured at -5 μs yielded the difference scattering curve $\Delta S(q, t)$ as shown in Fig. 1(a) and 1(b).

From kinetic analysis, we identified three structurally distinct intermediates and their kinetic pathways common for both the wild type and the mutant. The data revealed that the singly ligated and unligated forms of each intermediate share the same structure, providing direct evidence that the ligand photolysis of only a single subunit induces the same structural change as that induced by the complete photolysis of both subunits. In addition, by applying novel structural analysis to the scattering data, we elucidated the detailed structural changes in the protein, including changes in the heme-heme distance, the quaternary rotation angle of subunits, and interfacial water gain/loss. The structural transitions from $HbI(CO)_2$ to I_2 via I_1 are identical for the wild type and the mutant. In contrast, for the transition from I_2 to I_3, interfacial water molecules enter in the wild type and exit in the mutant, and the extent of the structural change is smaller for the mutant. Especially, the heme-heme distance of I_3 (F97Y) is not reduced relative to that of I_2, whereas I_3 (wild type) exhibits a smaller heme-heme distance than that of I_2. A summary of the extracted structural dynamics is provided in Fig. 1(c).

The ability to keep track of the detailed movements of the protein in aqueous solution in real time will provide new insights into the structural dynamics of proteins.

REFERENCES

[1] H. Ihee, M. Lorenc, T.K. Kim, Q.Y. Kong, M. Cammarata, J.H. Lee, S. Bratos and M. Wulff, *Science* **309**, 1223 (2005).
[2] K.H. Kim, S. Muniyappan, K.Y. Oang, J.G. Kim, S. Nozawa, T. Sato, S. Koshihara, R. Henning, I. Kosheleva, H. Ki, Y. Kim, T.W. Kim, J. Kim, S. Adachi and H. Ihee, *J. Am. Chem. Soc.* **134**, 7001 (2012).
[3] C.M. Summerford, A. Pardanani, A.H. Betts, A.R. Poteete, G. Colotti and W.E. Royer, *Protein. Eng.* **8**, 593 (1995).

BEAMLINE

AR-NW14A

Kyung Hwan Kim[1, 2], Srinivasan Muniyappan[1, 2], Key Young Oang[1, 2], Jong Goo Kim[1, 2], Hosung Ki[1, 2], Youngmin Kim[1, 2], Tae Wu Kim[1, 2] and Hyotcherl Ihee[1, 2] ([1]Inst. for Basic Science, [2]KAIST)

X-Ray Waveguiding in Resonance with a Periodic Structure

Novel X-ray waveguides are designed based on the concept of photonic crystals. The waveguides consist of a pair of claddings sandwiching a core with a periodic structure. X-rays that undergo multiple interference are confined in the core by total reflection at the core-cladding interfaces to form a characteristic waveguide mode whose field distribution matches the periodicity of the core. Because the propagation loss in this mode, which is in resonance with a periodic structure, becomes distinctively low, substantial single-mode propagation of X-rays can be achieved. This concept will open up new fields in X-ray optics.

Collimated X-ray beams with high spatial coherency have attracted much attention because of their remarkable advantages in analytical and diagnostic applications. X-ray waveguides (WGs) using one- or two-dimensional nano-scale gaps, which enable the propagation of X-rays on individual discrete modes, have been proposed. However, the width of the gaps in the direction of X-ray confinement needs to be extremely small to achieve the formation of a coherent X-ray beam by satisfying the single-mode propagation conditions. Here, we propose a novel X-ray WG based on the physics of photonic crystals in the X-ray regime [1].

The structure of the WG and the underlying concept are schematically shown in Fig. 1. The WG consists of a core with a periodic structure and a pair of claddings sandwiching the core. The X-rays undergoing multiple interference in the periodic core can be confined by total reflection at the core-cladding interfaces, when the Bragg angle for the periodic structure is sufficiently smaller than the total reflection angle. The periodicity-resonant WG mode is resonant with both the total thickness and the periodicity of the core. The electric field profile of this resonant mode has fine fringes with the same periodicity as that of the core, and the antinodes of the field are located in the layers with a lower absorption coefficient, as shown in Fig. 1. On the other hand, the shape of the envelope shows that the field is concentrated in the center of the core. Because of these two features of the formed fields, the resonant mode achieves an exceptional low propagation loss.

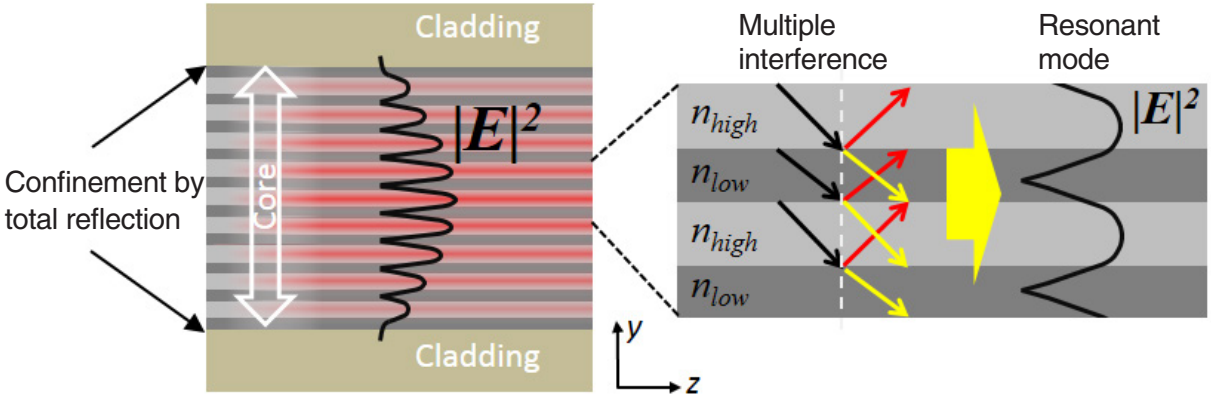

Figure 1: The concept of the periodicity-resonant X-ray waveguide.

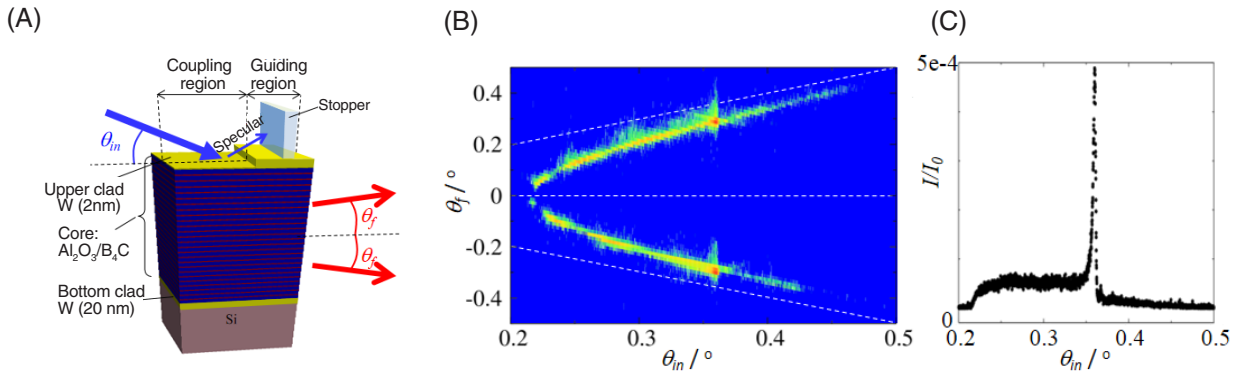

Figure 2: (A) The structure of the waveguide and the measurement geometry, (B) dependence of the far-field pattern on the incident angle θ_{in}, (C) dependence of the normalized X-ray intensity on θ_{in}.

The structure of the waveguide used for the experiment is schematically shown in Fig. 2(A). The core is an Al_2O_3/B_4C multilayer, which is sandwiched by a pair of tungsten claddings. The thickness of the Al_2O_3 and B_4C is 3 nm and 12 nm, respectively, and the number of pairs is 100. The thickness of the claddings is 20 nm except for the coupling region with a ~2 nm thickness. The experiments for the waveguide were performed at the BL-4A using X-rays with 10 keV, which was monochromated using a Si (111) double-crystal monochromator. The beam was shaped into 150 μm height x 1000 μm width. The divergence angle and the energy band width $\Delta E/E$ of the beam were ~0.002° and ~2x10^{-4}, respectively. The X-ray beam was impinged on the coupling region of the waveguide at a grazing angle θ_{in}, and the spatial distribution of the emitted X-rays, the far-field pattern, was recorded using a 2D detector.

The dependence of the far-field pattern on the incident angle is graphically shown in Fig. 2(B). A pair of symmetric bright lines with respect to θ_f (emission angle) = 0° is observed, which are caused by the 0th order Fraunhofer diffraction originating from the near-field distribution of the waveguide modes. As shown in Fig. 2(B), a pair of spots with large intensity is observed at an incident angle slightly smaller than the Bragg angle for the multilayer. These are formed by the X-rays propagated on the periodicity-resonant waveguide mode. The origin of this resonant mode is multiple interference in the periodic core, which makes the consequent X-ray beam spatially coherent. The X-ray beam created by this novel waveguide will find various innovative applications in X-ray optics using its unique spatial coherency as well as small divergence angle.

REFERENCE

[1] K. Okamoto, T. Noma, A. Komoto, W. Kubo, M. Takahashi, A. Iida and H. Miyata, *Phys. Rev. Lett.* **109**, 233907 (2012).

BEAMLINE

BL-4A

H. Miyata[1], K. Okamoto[1], T. Noma[1], A. Komoto[1], W. Kubo[1], M. Takahashi[1] and A. Iida[2] ([1]Canon Inc., [2]KEK-PF)

Effect of an Ultraflat Substrate on the Epitaxial Growth of Chemical-Vapor-Deposited Diamond

The performance of diamond power devices depends on the crystalline quality of the drift layer, which is a semiconducting diamond layer. Because the layers of diamond power devices are usually grown by chemical vapor deposition, it is important to analyze the critical factors determining crystalline quality during this process. An important related issue is the reduction of the density of dislocations in the epitaxial layer: the density of dislocations increases during chemical vapor deposition. We show that, when using an ultraflat substrate, existing dislocations remain in the epitaxial layer but no new dislocations are formed.

Semiconducting diamond has attracted considerable attention as a material for power devices owing to its high breakdown characteristics and high carrier mobility in high-temperature, high-voltage environments [1]. Recently, the development of a diamond Schottky barrier diode (SBD) that exhibited stable performance at temperatures greater than 200°C has been reported [2-4]. However, the reported performances of diamond power devices are poorer than expected. For the development of high-performance devices, the density of defects is thought to be critical, especially in the drift layer [5, 6].

The permissible defect concentration can be determined using Murphy's yield model [7]. For example, using the model, one can obtain the permissible defect density for a high-current device. By setting the electrode size to 1×10^{-4} cm^2 and using Murphy's yield model, while assuming the performance of the electrode deposited on a threading dislocation to be poor, one can find the dislocation density. If the dislocation density is approximately 10^4 cm^{-2}, most of the electrodes (more than 60%) will be inferior. The results of calculations based on Murphy's yield model suggest that a high-quality diamond, which has a defect density of less than 10^3 cm^{-2}, is essential for developing actual devices.

In the case of diamond SBD, a lightly boron-doped diamond layer (p^- layer) is deposited as the drift layer, and the SBD breakdown characteristics will depend on the quality of this layer.

Some researchers have suggested that pretreatment of the substrate is effective for improving the quality of epitaxial diamond [8, 9], so we investigated the effect of an ultraflat polished substrate on the quality of the p^- layer using X-ray topography (XRT) images. For comparison, a scaife-polished substrate was used as a conventional technique.

Since we assumed that the quality of the epitaxial layer might depend on the dislocation density and variations in the distribution of defects in the substrate, we used the same substrate throughout the experiment. This was done to evaluate the effect of the substrate surface flatness on the epitaxial growth of the CVD diamond layer.

The polished substrate was a type-Ib diamond (001) plate. Each p^- layer was deposited using microwave-plasma-assisted chemical vapor deposition. Hydrogen, methane, carbon dioxide, and trimethyl borate were used as the source gases. The thickness of the p^- layer was 10 μm.

UV-assisted polishing is basically mechanical polishing combined with a UV-induced photochemical reaction. This is an effective method of polishing diamond to an ultraflat finish. The carbon atoms at the surface of the diamond layer are oxidized by active species such as oxygen radicals and removed in the form of CO and CO_2. Details of this system were reported previously by Touge *et al.* and Kubota *et al.* [10, 11]. The average roughness, Ra, of the scaife-polished surface and the ultraflat surface was 70.0 Å and 21.5 Å, respectively.

XRT produces two-dimensional images of X-ray diffraction intensities, and these images can provide a projective distribution map of the defects in a single crystal [12]. The bright areas represent areas virtually free of all defects. XRT-based measurements were carried out at BL-15C [13]. Figure 1 is a schematic representation of the experimental set-up for XRT. Exposure time is adjusted by the shutter. The geometry of the sample and detector is asymmetric Bragg-case diffraction. The diffraction plane is (-404) because the diffraction intensity is sufficient to detect XRT images with clear contrast and the incident angle of the X-ray is too shallow

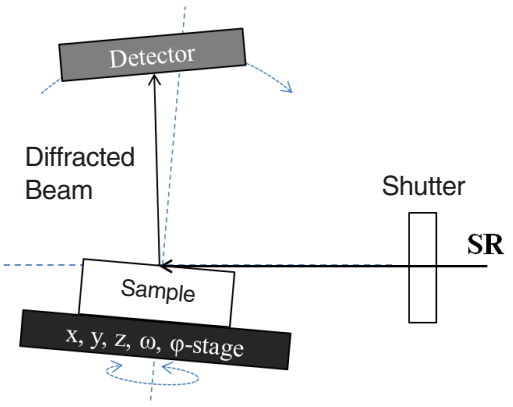

Figure 1: Schematic representation of the experimental setting.

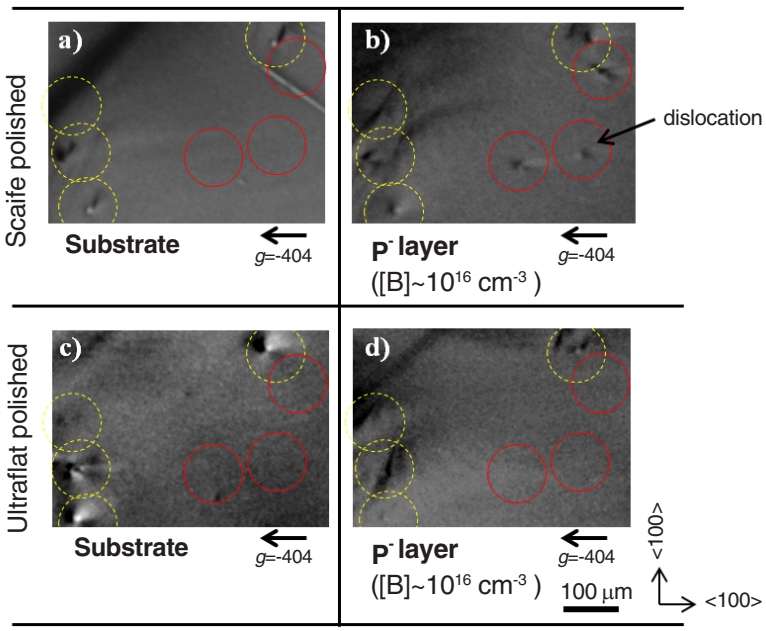

Figure 2: XRT images of the substrates and their p⁻ layers (g = –404). Each circle represents the area that contained the discussed dislocations. (a) scaife-polished substrate, (b) p⁻ layer on the scaife-polished substrate, (c) ultraflat polished substrate and (d) p⁻ layer on the ultraflat polished substrate.

to measure the surface-sensitive XRT for observation of the epitaxial layer. XRT images of a scaife-polished surface and p⁻ layer deposited on this substrate are shown in Figs. 2(a) and (b), respectively. The circles denote areas containing the discussed dislocations. In the yellow dashed circles, a threading dislocation from the substrate to the p⁻ layer was observed. In the red open circles, no defects were observed, as can be seen from Fig. 2(a); however, new dislocations that grew from the interface were observed in Fig. 2(b). Figures 2(c) and (d) show the XRT images of the ultraflat polished substrate and the p⁻ layer on this substrate taken under the same conditions as those for the images shown in Figs. 2(a) and (b). The observed area is the same as in Figs. 2(a) and (b). In this case, no dislocations were observed in the red circle.

To summarize, although the density of all types of dislocation could not be controlled using the ultraflat substrate, the polished substrate was led to a reduction in the growth of new dislocations from the interface. It was found that the ideal surface roughness, Ra, is less than 21.5 Å. In this study, we used UV-assisted polishing to obtain a substrate with an ultraflat surface. Other techniques for smoothening surfaces have been reported, including for (110) or (111) surfaces grown by CVD [14, 15], however, these techniques have not been applied to (001) surfaces grown by CVD, with this particular orientation being the one commonly used for diamond devices.

In a future study, we intend to perform a quantitative analysis of the effect of decreasing the dislocation density by using a substrate exhibiting a low defect density.

REFERENCES

[1] S. Shikata, K. Ikeda, R. Kumaresan, H. Umezawa and N. Tatsumi, *Mater. Sci. Forum* **615**, 999 (2009).
[2] H. Umezawa, K. Ikeda, R. Kumaresan and S. Shikata, *Mater. Sci. Forum* **645**, 1231 (2010).
[3] K. Kodama, T. Funaki, H. Umezawa and S. Shikata, *IEICE Electron. Express* **7**, 1248 (2010).
[4] K. Ikeda, H. Umezawa, K. Ramanujam and S. Shikata, *Appl. Phys. Express* **2**, 011202 (2009).
[5] T. Katsuno, Y. Watanabe, H. Fujiwara, M. Konishi, T. Yamamoto and T. Endo, *Jpn. J. Appl. Phys.* **50**, 04DP04 (2011).
[6] H. Fujiwara, H. Naruoka, M. Konishi, K. Hamada, T. Katsuno, T. Ishikawa, Y. Watanabe and T. Endo, *Appl. Phys. Lett.* **101**, 042104 (2012).
[7] B.T. Murphy, *Proc. IEEE* **52**, 1537 (1964).
[8] Y. Mokuno, A. Chayahara and H. Yamada, *Diam. Relat. Mater.* **17**, 415 (2008).
[9] A. Tallaire, J. Achard, F. Silva, R.S. Sussmann, A. Gicquel and E. Rzepka, *Phys. Status Solidi* **201**, 2419 (2004).
[10] J. Watanabe, M. Touge and T. Sakamoto, *Diam. Relat. Mater.* **39**, 14 (2013)
[11] A. Kubota, S. Fukuyama, Y. Ichimori and M. Touge, *Diam. Relat. Mater.* **24**, 59 (2012).
[12] M.P. Gaukroger, P.M. Martineau, M.J. Crowder, I. Friel, S.D. Williams and D.J. Twitchen, *Diam. Relat. Mater.* **17**, 262 (2008).
[13] Y. Kato, H. Umezawa, H. Yamaguchi and S. Shikata, *Jpn. J. Appl. Phys.* **51**, 090103 (2012).
[14] H. Watanabe, D. Takeuchi, S. Yamanaka, H. Okushi, K. Kajimura and T. Sekiguchi, *Diam. Relat. Mater.* **8**, 1272 (1999).
[15] N. Tokuda, H. Umezawa, S.-G. Ri, M. Ogura, K. Yamabe, H. Okushi and S. Yamasaki, *Diam. Relat. Mater.* **17**, 1051 (2008).

BEAMLINE

BL-15C

Y. Kato[1], H. Umezawa[1], S. Shikata[1] and M. Touge[2]
([1]AIST, [2]Kumamoto Univ.)

In situ Removal of Carbon Contamination from the Whole Optics in a Vacuum Ultraviolet and Soft X-Ray Undulator Beamline Using Oxygen Activated by Non-Monochromatized Synchrotron Radiation

We developed an *in situ* method to remove carbon contamination from the whole optics in a vacuum ultraviolet and soft X-ray (VSX) beamline. The carbon contamination of the optics was removed by exposing them to oxygen at a pressure of 10^{-1}-10^{-4} Pa for 17–20 h and simultaneously irradiating them with non-monochromatized synchrotron radiation. After a series of operations to remove carbon contamination, the decrease in the photon intensity in the carbon *K*-edge region was reduced from 64-65% to 2-4%. The base pressure of the beamline recovered to 10^{-7}-10^{-8} Pa in one day without baking. The beamline can be used without adjusting the optics.

When optics are irradiated with synchrotron radiation (SR) in the presence of residual hydrocarbon gases, they are contaminated with carbon [1]. The carbon contamination causes a significant decrease in the reflectivity of the optics. The photon flux loss in the carbon *K*-edge region is especially critical because it reduces the quality of experimental data, such as near-edge X-ray absorption fine structure (NEXAFS), resonant photoemission, and resonant soft X-ray emission spectra. Therefore, it is crucial to remove carbon contamination from optics in synchrotron radiation facilities. To solve this issue, we focused on an *in situ* SR-activated oxygen cleaning method proposed by Warburton and Pianetta [2]. Applying this method we succeeded in removing carbon contamination from the whole optics in a VSX undulator beamline, BL-13A [3]. BL-13A is equipped with a Monk-Gillieson-type monochromator to cover a wide energy range of 30-1600 eV [4, 5]. BL-13A consists of a focusing pre-mirror (M1), a plane mirror (M2), two varied-line-spacing plane gratings (VLSGs, 300 and 1000 line/mm), an exit slit, and two focusing post-mirrors (M3 and M3′) as shown in Fig. 1. M1, M2, VLSGs, M3, and M3′ are coated with gold. The base pressure of BL-13A is less than 1×10^{-8} Pa. However, the photon intensity in the carbon *K*-edge region had decreased by as much as 64-65% after 300 days of operation. The thickness of the carbon contamination on M1, M2, VLSGs, M3, and M3′ was estimated to be 3-4 nm based on calculations of the reflectivity performed by using the Web page of the Center for X-Ray Optics (http://henke.lbl.gov/optical_constants/layer2.html).

In situ removal of carbon contamination from the optics was carried out four times. Figure 2 shows photon intensity spectra measured with the 300-line/mm VLSG and M3 before and after the third *in situ* removal of carbon contamination. For the spectrum before the carbon removal we ascribed the sharp dip at 285.1 eV to the C $1s \rightarrow \pi^*$ transition of graphite-like carbon with a flat-on configuration on M1 and M3, and the sharp dip at 291.5 eV mainly to the C $1s \rightarrow \sigma^*$ transition of graphite-like carbon with a flat-on configuration on M2 and the VLSG on the basis of the polarization-dependent NEXAFS spectra of graphite [6]. The oxygen pressures in the M1, M2/VLSG, and M3/M3′ chambers were maintained in the ranges of 2×10^{-4} to 6×10^{-4} Pa, 5×10^{-3} to 1.5×10^{-2} Pa, and 1×10^{-5} to 4×10^{-5} Pa, respectively. M1, M2, the 300-line/mm VLSG, and M3 were irradiated with non-monochromatized SR for 20 h. The averaged ring current was 450 mA. The sharp dips due to the carbon contamination were reduced to 2-4% after the carbon removal as shown in Fig. 2. The base pressure of BL-13A recovered to 10^{-7}-10^{-8} Pa in one day without baking. The carbon contamination on the 1000-line/mm VLSG and M3′ was removed in a similar manner. BL-13A can be used without adjusting the optics.

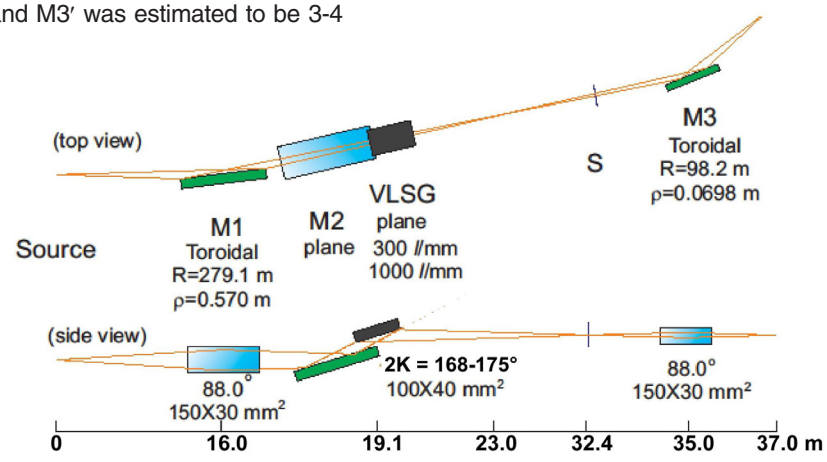

Figure 1: Optics of BL-13A.

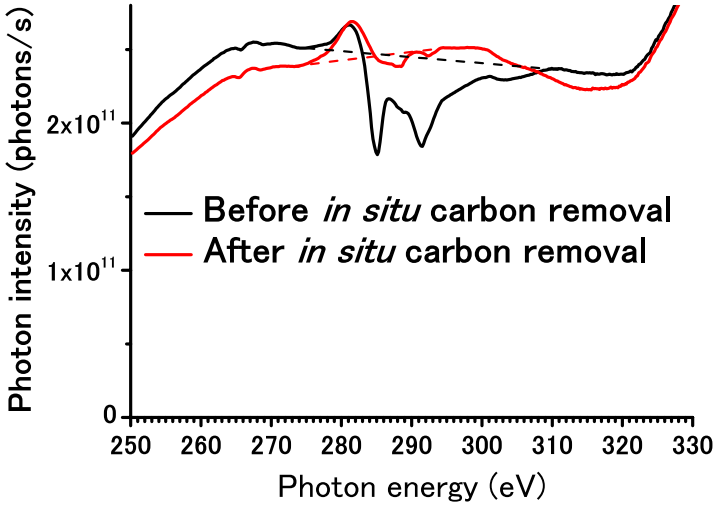

Figure 2: Photon intensity spectra measured before and after the third *in situ* carbon removal; the measurements were made with the 300-line/mm VLSG and M3 [3]. The dashed lines represent the baselines.

The key requirements for the present *in situ* carbon removal method are as follows. 1) The surface of the optics must be made of a material that is inert to activated oxygen. 2) The vacuum in the optics chambers must be hydrocarbon-free. The base pressure of the chambers should be less than 5×10^{-8} Pa. 3) A differential pumping system and an interlock system must be installed to prevent the degradation of the vacuum of the storage ring. 4) Oil-free turbomolecular pumps should be attached to the optics chambers to remove oxygen and reacted gases. 5) The recommended oxygen pressure is 10^{-3}-10^{-4} Pa for the first mirror and 10^{-2}-10^{-3} Pa for the other optics when the thickness of the carbon contamination is 3-4 nm. The typical SR irradiation time is less than 20 h. 6) Non-evaporable getter pumps should be used to facilitate the rapid recovery of the base pressure.

We propose the following model for the mechanism of the carbon removal. The first step is the interaction of oxygen molecules with electrons emitted from the optics under SR irradiation, generating active oxygen species such as oxygen atoms, excited oxygen molecules, and ions. Then the active oxygen species react with the carbon contamination and produce carbon oxides. The advantages of the present carbon removal method are as follows. 1) The carbon contamination of the whole optics in a VSX beamline can be removed within 20 h. 2) The base pressure of the beamline can be recovered to 10^{-7}-10^{-8} Pa in one day without baking. 3) The beamline can be used without adjusting the optics. 4) This method is especially suited for undulator beamlines because the carbon removal rate is expected to be proportional to the photon flux.

REFERENCES

[1] K. Boller, R.-P. Haelbich, H. Hogrefe, W. Jark and C. Kunz, *Nucl. Instrum. Methods Phys. Res. A* **208**, 273 (1983).
[2] W.K. Warburton and P. Pianetta, *Nucl. Instrum. Methods Phys. Res. A* **319**, 240 (1992).
[3] A. Toyoshima, T. Kikuchi, H. Tanaka, J. Adachi, K. Mase and K. Amemiya, *J. Synchrotron Rad.* **19**, 722 (2012).
[4] A. Toyoshima, H. Tanaka, T. Kikuchi, K. Amemiya and K. Mase, *J. Vac. Soc. Jpn.* **54**, 580 (2011).
[5] A. Toyoshima, T. Kikuchi, H. Tanaka, K. Mase, K. Amemiya and K. Ozawa, *J. Phys.: Conf. Ser.* **425**, 152019 (2013).
[6] R.A. Rosenberg, P.J. Love and V. Rehn, *Phys. Rev. B* **33**, 4034 (1986).

BEAMLINE

BL-13A

A. Toyoshima[1], T. Kikuchi[1], H. Tanaka[1], J. Adachi[1], K. Mase[1] and K. Amemiya[1] ([1]KEK-PF)

Experimental Facilities

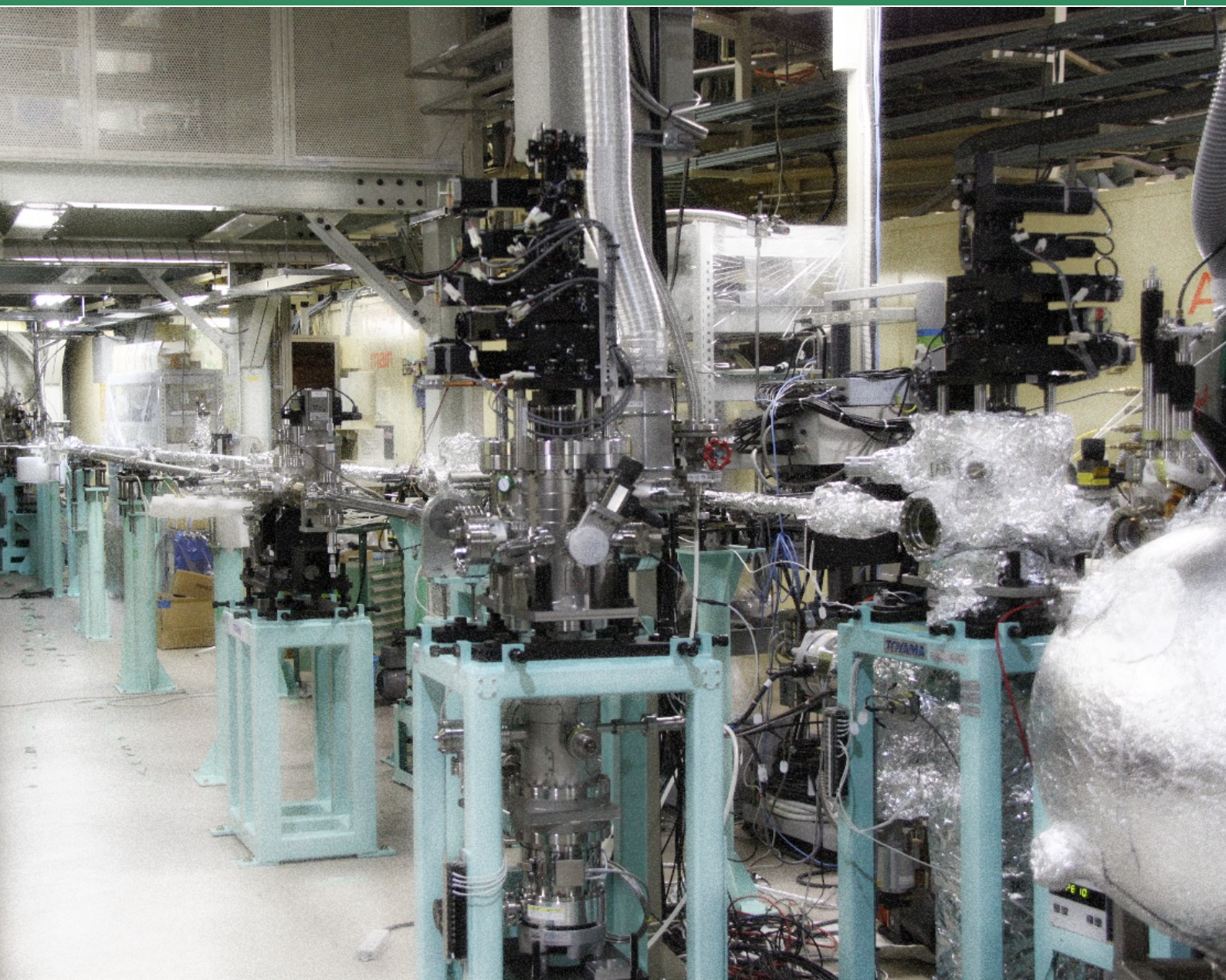

Experimental Facilities

1 Newly Developed Experimental Facilities

1-1 Overview

The Photon Factory (PF) started user operations in 1982, and has been providing valuable resources for X-ray research for more than 3,000 users annually from universities, industries, and government institutions. The PF has been carrying out a beamline refurbishment program since 2006, in which the main strategy is to concentrate investments on competent beamlines which use insertion devices as light sources. With the upgrade of the 2.5-GeV PF ring for lengthening the straight sections, the lengths of the long and medium straight sections have been increased so that state-of-the-art insertion devices can be installed to cover the vacuum ultraviolet and soft X-ray region. Four new straight sections have also been created to allow the installation of short period and small gap undulators (SGU) to supply well-focused hard X-rays. We have already constructed three HX beamlines at the short straight sections: BL-3 for materials science, and BL-1 and -17 for macromolecular crystallography. At the fourth straight section, we are constructing a new beamline for both small-angle X-ray scattering (SAXS) and X-ray absorption spectroscopy (XAFS/XRF) at BL-15. The details are described below.

Beamlines BL-13, -16, and -28 were originally constructed for sharing the photon beam between VSX and HX users by operating the insertion device in the undulator and multipole wiggler mode. Among the three beamlines, BL-28 was renewed first as a high-performance spectroscopic beamline dedicated to photoelectron spectroscopy in the VSX region in 2006. The second branch of BL-28 has been open as a free port. BL-16 was completely upgraded as a soft X-ray spectroscopic beamline with fast polarization switching capabilities. Two tandem APPLE-II type undulators are installed to generate different polarizations such as right- and left-hand circular polarizations, and the polarization is switched by modulating the electron orbit through the undulators, as reported in the previous activity report [1,2]. BL-13 was recently reconstructed as a VSX spectroscopic beamline for studying organic thin films absorbed on well-defined surfaces using angle-resolved photoelectron spectroscopy and X-ray absorption spectroscopy; the detailed performance is also described below.

The VSX beamline refurbishment program has required the replacement of the insertion devices at BL-13 and BL-28, which were constructed in the 1980s for supplying photon beams in the VSX and HX regions. These old insertion devices do not always meet the needs of VSX users and are not adequate for utilizing the full performance of the newly constructed beamlines. Furthermore, during the test operation of the PF ring and the beamlines in June 2011, after the Great East Japan Earthquake on March 11, 2011, we found some troubles caused by earthquake damage to these old insertion devices. Therefore, these two old undulators should be replaced by appropriate new ones for the renewed beamlines. BL-2 was the first undulator based VSX beamline constructed in the early 1980s, and has been operated for over 25 years. The BL-2 undulator is 3.6-m long, while the length of the straight section is 9 m following the upgrade in 2005. We have decided to add a 16-cm period undulator, and to construct a new beamline in collaboration with Hitachi, Ltd. The new beamline optics consist of a grazing-incidence grating monochromator and a double-crystal monochromator, and will supply VUV and soft X-rays of 30–4000 eV. Construction of the new beamline started in February 2013, and the new undulator will be installed in the spring of 2014.

The Slow Positron Facility (SPF) is affiliated with the PF, and three stations are currently available: (i) one for the photodetachment of the positronium negative ion (Ps-) and its application to the production of an energy-tunable positronium beam, (ii) one for positronium time-of-flight (Ps-TOF) spectroscopy, and (iii) one for reflection high-energy positron diffraction (RHEPD).

REFERENCES

[1] *Photon Factory Activity Report 2010* **#28**, (2012).
[2] *Photon Factory Activity Report 2011* **#29**, (2013).

1-2 Construction of New High-Brilliance XAFS/XRF/SAXS Beamline, BL-15A

The last SGU section, BL-15A, is being built for SAXS and XAFS/XRF activities. The SAXS scientific programs at BL-15A are structural studies of functional membranes, time-resolved X-ray scattering and large hierarchical structure analysis, using highly collimated intense X-ray photons derived from the SGU#15. In particular, grazing incidence SAXS (GI-SAXS) using vertically small-size softer beams in the range 2.1–3.0 keV will help to control the depth of the membrane structure analysis and reduce the roughness defects of an imperfect membrane. For the XAFS/XRF studies, the semi-micro focus beam available in a wide range of photon energies is used for analyzing the local structures of the elements and valence of inhomogeneous samples in the fields of environmental science and new energy source science. The 2.1-keV X-rays provide access to the absorption edges of phosphor and sulfur, which are very important targets for those fields. The combination

of SAXS and XAFS yields diverse structural information from fine atomic structures to low and medium resolution. It can be beneficial to build these instruments as two stations on the same beamline. BL-15A is oriented toward joint advanced studies by using the two techniques.

We have completed the beamline design of BL-15A (Fig. 1). The SGU#15 covers the wide continuous energy range required by XAFS/XRF studies; the undulator has a periodic length of 17.6 mm and the number of periods is 27. The minimum gap is 4.0 mm, giving a Kmax of 1.61. We will use the 1st to 9th harmonics including the 2nd harmonic to cover the large energy gap between the 1st and 3rd harmonics. Synchronization between the ID gap and energy setting of a monochromator will be developed in the control system for quick energy scanning, by a configuration similar to the one proposed at NSLS-II [1]. Encoder reading of the updated ID gap is directly fed to the monochromator controller. The closed loop adjustments of the monochromator axes follow the gap in real time. The main optics are a horizontal collimating mirror, a liquid nitrogen cooling double-crystal monochromator, a vertical focusing mirror and a pair of asymmetrically horizontal focusing mirrors which employ a secondary source. These deliver a stable, semi-micro focus or collimated beam. The monochromator crystals are Si(111), and their lowest energy is limited to 2.1 keV. The two horizontal focusing mirrors are bimorph ones [2]. The secondary source aperture is controlled with a set of slits. Tuning the mirror surfaces and setting the size of the slits adjusts the size of the beam at the sample position. A vertical double-mirror system is also installed in the last section in order to eliminate higher-order reflections. The experimental hutch is separated into two tandem stations because of the very different beam requirements of SAXS and XAFS/XRF experiments. The upstream and downstream stations are BL-15A1 for the XAFS/XRF activity and BL-15A2 for the SAXS activity, respectively. The second horizontal focusing mirror has double-mirror surfaces that provide a highly focused and collimated X-ray beam for A1 and A2 stations, respectively. The demagnification ratios for XAFS/XRF/XRD and SAXS are approximately 16.7:1 and 1:2 (or 1:1), respectively. The front-end is retrofitted with several differential pumps for windowless operation. Windowless operation allows the beamline to utilize softer X-ray beams of up to 2.1 keV.

In order to check the beam performance, ray-tracing simulations were performed using the programs XOP and SHADOW [3,4]. Table 1 shows some results of these calculations at different focal points at different energies. Thanks to the high-brilliance light source, the windowless beamline design and the double surface bimorph mirror, sufficient beam performance for both techniques can be obtained in the entire energy range of interest. The photon flux of the 2nd harmonic range, which is used only for XAFS studies, is almost the same as those in the adjacent range.

We started the construction just after the end of the PF-ring operation of FY2012 (Fig. 2). The first beam will be delivered in October 2013. After the commissioning of the beamline components and the experimental apparatus, we will start the user beamline operation at the end of FY2013.

REFERENCES

[1] T. Tanabe, D. Chabot, O. V. Chubar, L. R. Dalesio, D. A. Harder and J. Rank, *Proc. of ICALEPCS* 776 (2009).

[2] R. Signorato, O. Hignette and J. Goulon, *J. Synchrotron Rad.* **5**, 797 (1998).

[3] M. Sanchez del Rio, N. Canestrari, F. Jiang and F. Cerrina, *J. Synchrotron Rad.* **18**, 708 (2011).

[4] M. Sanchez del Rio and R. J. Dejus, *AIP Conf. Proc.* **705**, 784 (2004).

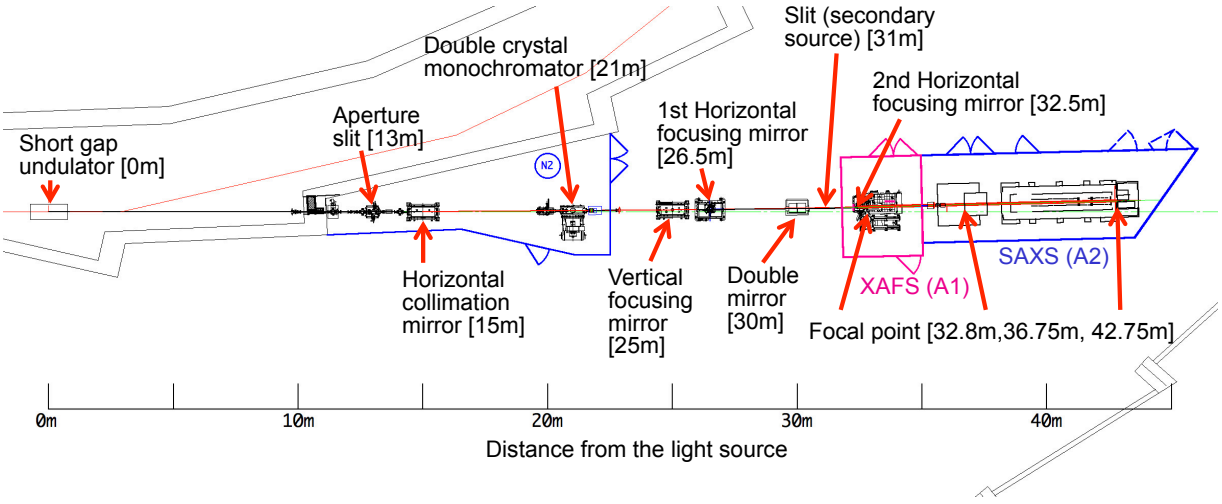

Figure 1: Layout of new BL-15A.

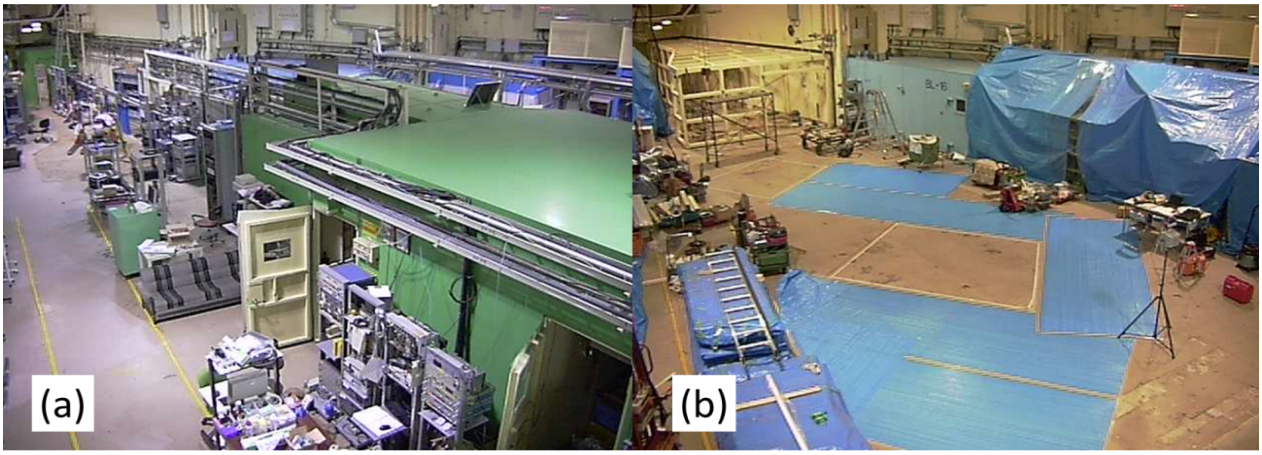

Figure 2: Photos of BL-15 site (a) before the end of the PF-ring operation of FY2012 and (b) at the end of FY2012.

Table 1: Ray-tracing simulation using the programs SHADOW and XOP.

Energy (ev)	2101	2800	4406	7344	10281	13218
Harmonics	1st	2nd	3rd	5th	7th	9th
K value	1.10	1.61	1.61	1.61	1.61	1.61
XAFS at 32.8 m [secondary source size: 0.1 mm (H) x 0.5 mm (V)]						
Beam Size (mm)	0.017 (H) x 0.009 (V)					
Photon Flux (phs/s)	1.3×10^{11}	1.2×10^{11}	6.3×10^{11}	4.7×10^{11}	2.4×10^{11}	1.7×10^{11}
SAXS at 42.75 m [secondary source size: 0.05 mm (H) x 3.0 mm (V)]						
Beam Size (mm)	0.339 (H) x 0.018 (V)					
Divergence (mrad)	0.058 (H) x 0.109 (V)					
Photon Flux (phs/s)	9.1×10^{10}		3.0×10^{11}	2.3×10^{11}	1.5×10^{11}	9.4×10^{10}
GI-SAXS at 36.75 m [secondary source size: 0.1 mm (H) x 3.0 mm (V)]						
Beam Size (mm)	0.275 (H) x 0.012 (V)					
Divergence (mrad)	0.157 (H) x 0.160 (V)					
Photon Flux (phs/s) w/o terminal window	1.9×10^{11} 6.1×10^{11}		6.1×10^{11} 6.8×10^{11}	4.5×10^{11}	2.7×10^{11}	2.0×10^{11}

1-3 Construction of BL-13B, Optics for Photoelectron Spectroscopy

Optics for photoelectron spectroscopy for the study of surface chemistry (BL-13B, Fig. 3 and Fig. 4) were constructed in March 2012. BL-13B involves a plane mirror for suppressing higher harmonics with a grazing angle of 2° (Mp, Fig. 5), an exit slit, two post-focusing mirrors, and an apparatus to monitor photon intensity and resolution [1]. The upper, middle, and lower areas of Mp are coated with nickel, gold, and chrome, respectively. The calculated reflectivity of Mp is also shown in Fig. 5 for the grazing angle of 2° and p-polarization. Nickel- and chrome-coated mirrors will be used mainly for X-ray absorption measurements in the nitrogen and carbon K-edge regions, respectively. The photon energy region and photon energy resolution of BL-13B are almost the same as those of BL-13A (Fig. 6). BL-13B will be opened for users in October 2013.

REFERENCES

[1] A. Toyoshima, H. Tanaka, T. Kikuchi, K. Amemiya and K. Mase, *J. Vac. Soc. Jpn.* **54**, 580 (2011).
[2] A. Toyoshima, T. Kikuchi, H. Tanaka, K. Mase, K. Amemiya and K. Ozawa, *J. Phys.: Conf. Ser.* **425**, 152019 (2013).

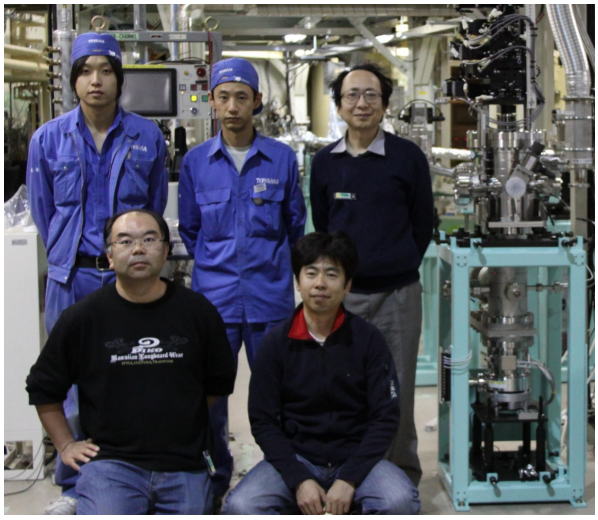

Figure 3: Photograph of BL-13B.

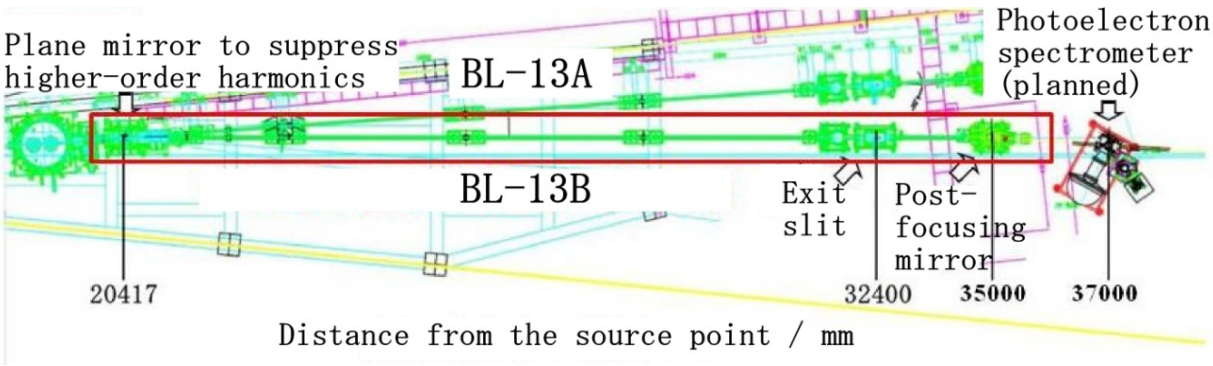

Figure 4: Floor layout of optics for photoelectron spectroscopy (BL-13B).

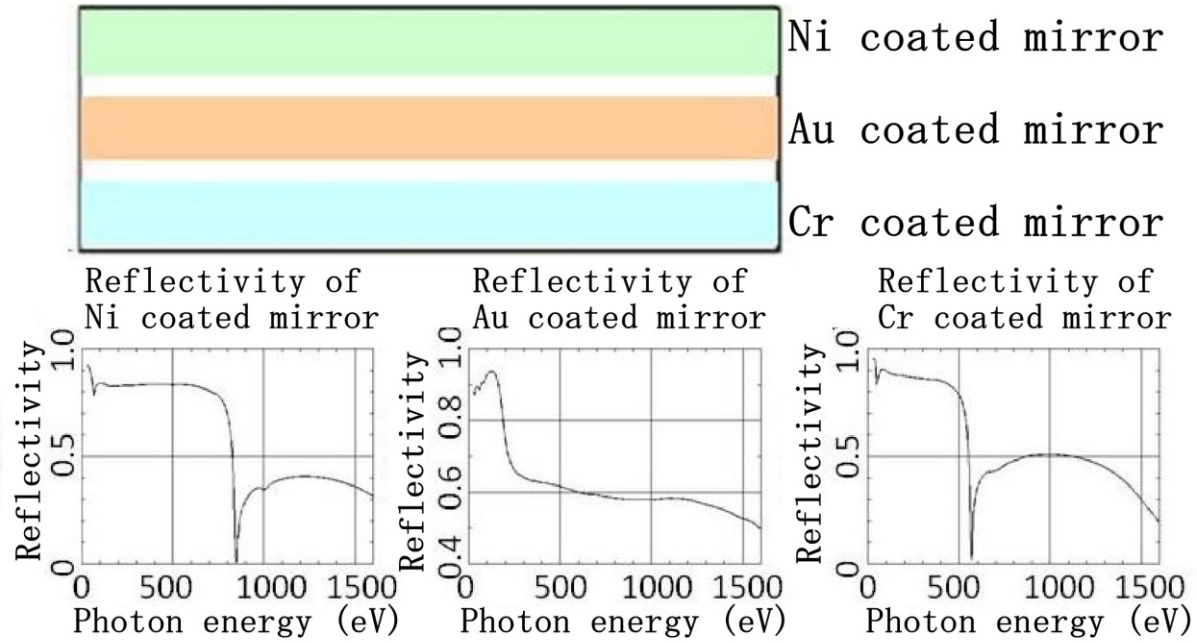

Figure 5: Plane mirror for suppressing higher harmonics (Mp), and its reflectivity for the grazing angle of 2° and *p*-polarization calculated using the web page of the Center for X-Ray Optics (*http://henke.lbl.gov/optical_constants/layer2.html*).

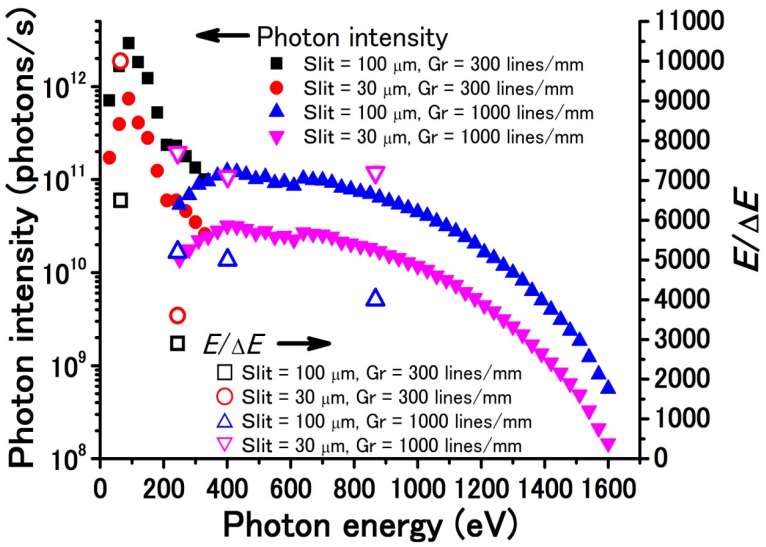

Figure 6: Typical photon intensity and photon energy resolution (E/ΔE) of BL-13A in the photon energy region of 30–1600 eV [2].

1-4 New Simultaneous SAXS/WAXD Measurement System Combining Two Pixel Detectors at BL-6A, and Improvement of Data Quality at BL-10C

BL-6A is used for the structural analysis of hard and soft materials studied by small-angle X-ray scattering. X-ray intensified CCD detectors and a flatpanel sensor have been installed and used in BL-6A for SAXS and WAXD simultaneous experiments in order to obtain structural information in both the nanoscale and the mesoscale. However, the dynamic ranges of these CCDs and the flatpanel sensor are quite narrow, perhaps around 10 bits, because of high noise level. Therefore, a new simultaneous SAXS/WAXD measurement system was constructed at BL-6A (Fig. 7), with the new installation of hybrid pixel detectors, PILATUS 300K and 100K, and an in-vacuum X-ray shutter which synchronizes with the detectors. Although the detectable area of these PILATUSs is somewhat small, they have high dynamic range, high-speed readout (7 and 2.3 msec) and quite a low noise level. Moreover, we redeveloped the measurement software and the image viewer of PILATUS with a GUI as standard software of the Photon Factory (Fig. 8). It has been used not only at SAXS beamlines but also at several XAFS beamlines.

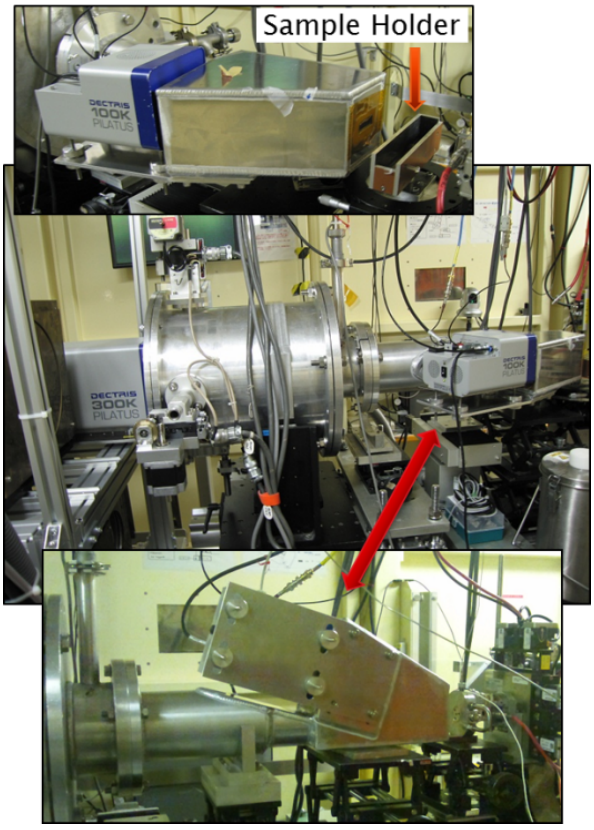

Figure 7: New SAXS/WAXD measurement system with two PILATUS detectors. The WAXD detector, PILATUS 100K, is fixed to the vacuum chamber, and the angle of this detector can be changed from the horizontal direction to the vertical direction.

BL-10C is also dedicated to small-angle X-ray scattering mainly for measuring solution samples such as biomolecule solutions. We aimed to improve the data quality of BL-10C in this fiscal year (Fig. 9). Although there was a long air section around the sample in the previous settings, we replaced the out-vacuum X-ray shutter and scattering guard slit to in-vacuum ones in the summer of 2012 in order to minimize the effects of air scattering and absorbance on the data. Moreover, we newly installed a pinhole as a scattering guard just before the sample. In addition to these installations, we also optimized the settings of the monochromator and the focusing mirror. As a result, the beam size at the focal point became smaller, and the beam stopper size also became smaller since the background level of image data decreased remarkably. Finally, the small angle resolution improved from 800 Å to 1100 Å at the camera length of 2 m.

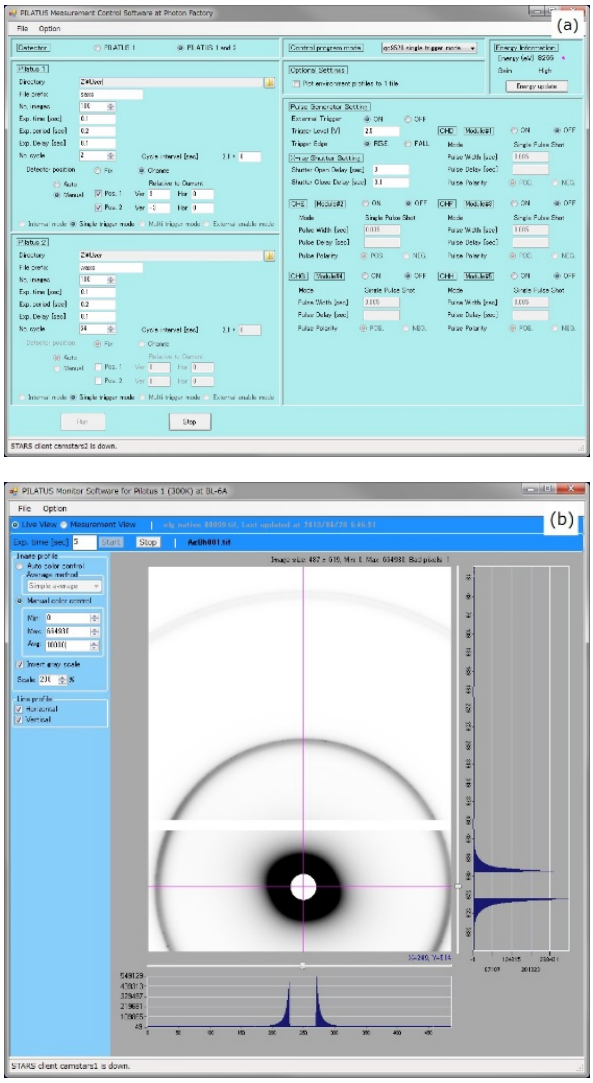

Figure 8: (a) The GUI measurement software of PILATUS. Users can collect data by using two PILATUSs, controlling an X-ray shutter and a pulse generator. (b) Image viewer of PILATUS. It has two modes: live view and measurement view. Live view is a video-like viewer mode, and measurement is executed repeatedly with the inputted exposure time. Measurement view is the automatic loader mode; the latest image is displayed automatically every second.

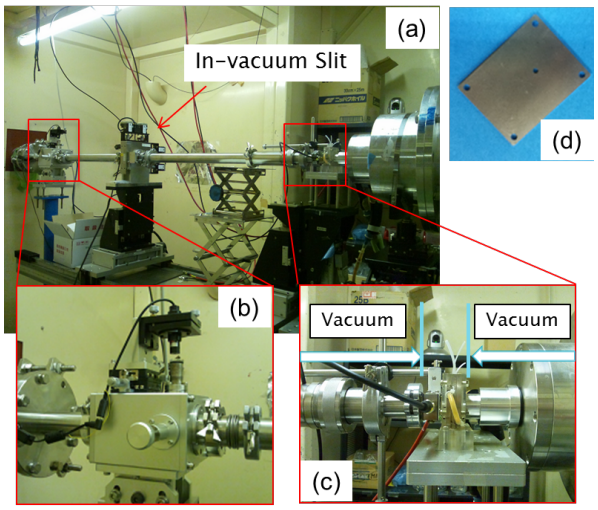

Figure 9: (a) New beam collimation system at BL-10C. (b) In-vacuum X-ray shutter and laser system (Rigaku Aihara Seiki). (c) Current status around the sample position. (d) A pinhole (1.6–1.8 mm) installed as a scattering guard in the micro ion chamber.

1-5 The Multipurpose X-ray Scattering Facility at the Indian Beamline, BL-18B, PF

The Indian beamline has been developed as a multipurpose beamline using beamport 18B of the Photon Factory ring. This beamline uses the existing beamline optics, mirrors, monochromators, slits, and so on, and we developed the experimental facilities in an existing experimental hutch at BL-18B. Presently, the available facilities are: (a) powder diffraction under ambient conditions, at low temperatures down to 10 K and at high temperatures up to 1200 K, (b) single-crystal diffraction from epitaxial multilayers and other nano-structures, (c) X-ray reflectivity and diffuse scattering from solid surfaces and interfaces, and (d) X-ray reflectivity, diffuse scattering and grazing incidence diffraction from liquid surface and liquid-liquid interfaces. For carrying out all these different types of X-ray scattering experiments, uniquely designed coupled goniometers have been installed in the experimental hutch of 18B (Fig. 10). The first goniometer is a four-circle goniometer and is used

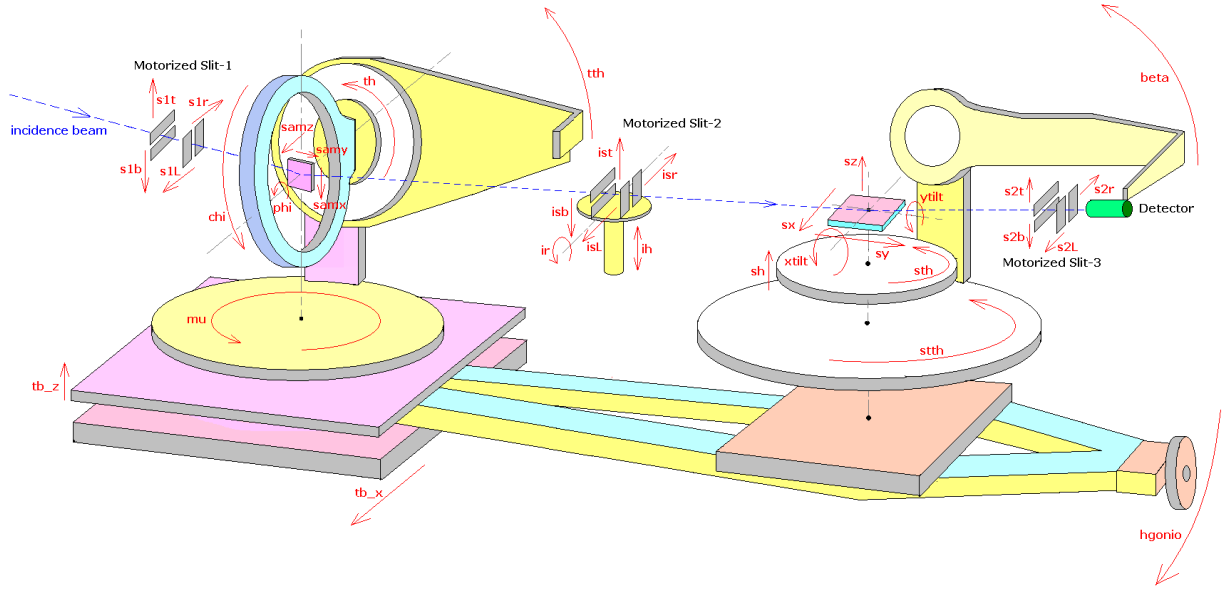

Figure 10: Schematic diagram of the experimental setup at the Indian beamline, BL-18B indicating all the motor controlled elements.

for powder diffraction in various sample environments: reflectivity, diffuse scattering, and diffraction experiments from solid samples (Fig. 11). The second goniometer is an eight-circle goniometer and is mounted on a rotation stage by air-wheel motion whose axis of rotation passes through the center of the first goniometer. This design enables us to perform experiments from a liquid surface where the Ge(111) crystal mounted on the first goniometer bends the beam down to the liquid surface and the air-wheel rotation coupled with vertical downward motion of the whole goniometer assembly tracks the beam onto the liquid sample. The beamline has one point detector (Cyberstar) and a 100K Pilatus detector. Installation of the high-pressure powder diffraction facility will be completed soon and for this purpose we are procuring a focusing optics (compact refractive lens) and a bigger 2D detector (1M Pilatus). We also plan to install a facility to study the in-situ growth and structural characterization of thin films and nanostructures. The second eight-circle goniometer, focusing optics and the 1M Pilatus detector will be used for this set-up. The 1M Pilatus detector and the long distance between the detector arm of the second goniometer and the sample stage of the first goniometer will also allow us to collect small-angle scattering data in reflection and transmission geometry. The Indian beamline at the Photon Factory (PF) is sponsored by the Department of Science and Technology (DST), Government of India, with the Saha Institute of Nuclear Physics (SINP) as the main institute implementing the project.

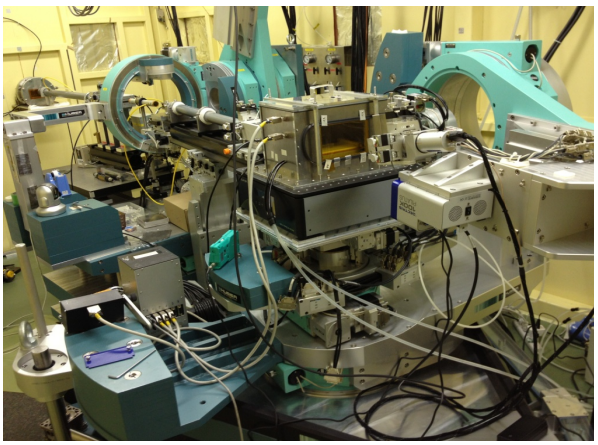

Figure 11: A picture of the experimental setup consisting of two goniometers at the Indian beamline, BL-18B. The first goniometer (in the back) can have the sample mounted for reflectivity and diffuse scattering experiments in the vertical plane, the second goniometer (at the front) has an active vibration table and Langmuir-Blodgett trough mounted on the sample stage for liquid surface experiments. The detectors (Cyberstar and 100K Pilatus) mounted on the second goniometer can be scanned in both the vertical and horizontal scattering planes.

1-6 Development of Beamlines for Structural Biology

A new diffractometer for in situ crystallography has been developed (Fig. 12). With this diffractometer, droplets in a crystallization plate can be directly exposed to an X-ray beam at room temperature. Combining the new diffractometer with the high-throughput crystallization screening described above enables a much more efficient evaluation of crystallization conditions.

A new VPN gateway dedicated for remote access to the structural biology beamlines in the PF has been installed at the KEK computing research center. This enables users to access beamline control from outside KEK. In addition, a remote access service has begun to be provided to limited users (industrial or project-involved users). In this service, a user sends cryo-cooled samples stored in a container for our sample exchange system and a beamline operator sets the samples in a beamline; the user then carries out experiments remotely. To operate this service correctly, PReMo (PF Remote Monitoring system) was updated to organize communication among operators and users. PReMo was also extended to manage all information derived from beamline operations, including experimental data, beam-time applications, beam-time schedule, and beamline-operation reports [1]. This enables the users and beamline staff to handle discursive data more efficiently.

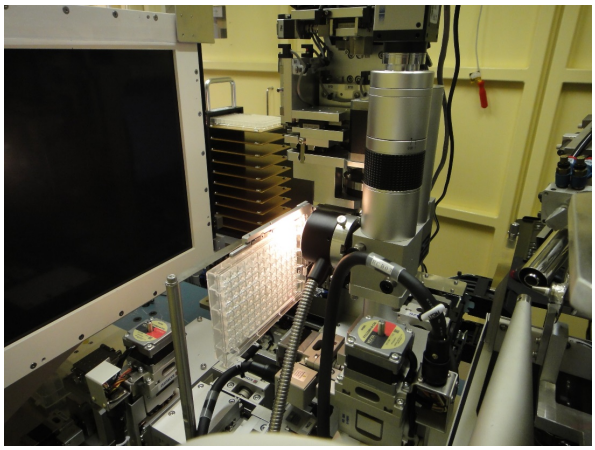

Figure 12: A new diffractometer for in situ crystallography, which consists of a plate holder, on-axis viewing system, and plate stacker. It is placed on an existing detector table.

REFERENCE

[1] Y. Yamada, N. Matsugaki, L. M. G. Chavas, M. Hiraki, N. Igarashi and S. Wakatsuki, J. Phys.: Conf. Ser. 425, 012017 (2013).

2 Structural Biology Research Center

2-1 Overview

The Structural Biology Research Center (SBRC) was established in May 2000 at the Photon Factory (PF) located in the Institute of Material Structure Science (IMSS). The main tasks of the Center are to provide user support for X-ray synchrotron radiation studies of bio-macromolecules, encourage advanced technical development, and boost in-house structural biology research. In the last 12 years, the SBRC has published significant research studies under the leadership of Prof. Soichi Wakatsuki. After Prof. Wakatsuki moved to Stanford University in January 2013, Prof. Toshiya Senda joined the SBRC as director. The Center has approximately 40 members (Fig. 1), including one professor (Dr. T. Senda), five associate professors (Drs. R. Kato, N. Igarashi, M. Kawasaki, N. Shimizu, and F. Yumoto), one vice-associate professor (Dr. M. Hiraki), and three assistant professors (Drs. N. Matsugaki, Y. Yamada, and L. Chavas) as the core members. About half of the SBRC members are engaged in beamline operation and development, and the others are involved in structural biology research. In beamline operation and development, Drs. Shimizu and Igarashi are responsible for small-angle X-ray scattering (SAXS), and Dr. Hiraki is responsible for robotics and automation. X-ray crystallography activities are carried out under the leadership of Drs. Matsugaki, Yamada, Chavas, Hiraki, and Igarashi.

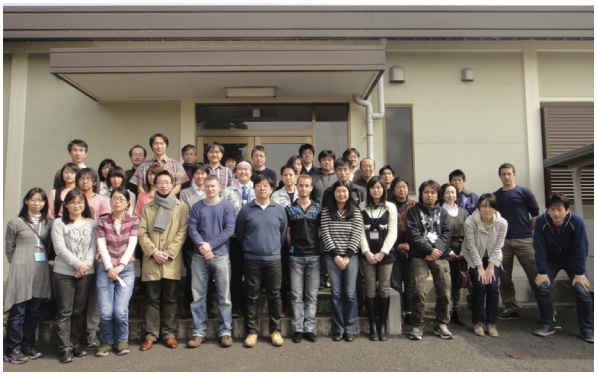

Figure 1: Members of the Structural Biology Research Center.

Figure 2: Structural Biology Research Center.

The structural biology building was built in April 2001 (430 m^2), and its area was later almost doubled to 765 m^2 (Fig. 2). All necessary structural biology experiments can be carried out in this laboratory. It has cell culture systems (bacteria, insect, and mammalian cells), liquid chromatography systems, a fully automated crystallization system, and equipment for physicochemical analysis (Biacore, DLS, MALS, MS, etc.). In-house biological research is carried out under the leadership of Drs. Senda, Kato, and Kawasaki.

The SBRC has constructed five beamlines for protein crystallography: BL-1A, BL-5A, BL-17A, PF-AR NW12, and PF-AR NE3A. BL-5A was constructed using "Special Coordination Funds for Promoting Science and Technology" (FY2001–FY2003) from the Japan Science and Technology (JST) Agency. During the "Development of System and Technology for Advanced Measurement and Analysis" project, we developed a micro-beam beamline, BL-17A, which is the first beamline developed at the PF with a short-gap undulator as a light source. BL-1A was constructed in the "Targeted Proteins Research Program" by MEXT/JST (FY2007–FY2011).

Under the PF Program Advisory Committee (PAC) system, the SBRC accepts many researchers from outside KEK who wish to collect diffraction data for their own macromolecular crystals. The number of academic proposals and users has reached 100–120 in recent years. As a result of advances in structure-based drug design, pharmaceutical companies require a large amount of beam time. Many Japanese companies have been using the bio-macromolecular crystallography beamlines of KEK-PF. The Tsukuba Consortium, which is composed of seven companies (four from another Pharmaceutical Consortium for Structure Analysis and three other companies), is using our beamlines. Among them, Astellas Pharma, Inc. financed the construction of the beamline AR-NE3A for their research.

2-2 Leads the National Project for Structural Life Science –PDIS Starting from FY2012

The SBRC plays a key role in a national project for structural life science, the Platform for Drug Discovery, Informatics, and Structural Life Science (PDIS). The PDIS, which was launched with the support of MEXT in FY2012, is an open platform providing comprehensive support for life-science researchers. The support includes protein production, bioinformatics, 3D-structure

analysis, compound-library screening, etc. The PDIS is composed of three platforms: platforms of structural life science, drug discovery, and informatics. The SBRC is the head of the platform of structural life science. We plan to develop beamlines for protein crystallography and bio-SAXS and will provide services for researchers in biology fields to accelerate studies in structural life science. The SBRC also provides a high-throughput crystallization service using an automated crystallization and observation robot (PXS), which will undergo further development in this project. In FY2012, we installed a SONICC (Second Order Nonlinear Imaging of Chiral Crystals) system as a new crystal observation system (Fig. 3). SONICC is based on the principle of second harmonic generation (SHG), where two low-energy photons combine to form a higher-energy photon under intense electric fields. The SHG signal is generated only in chiral crystals such as protein crystals. However, salt crystals, which are mostly achiral, generate no SHG signals. Therefore, protein crystals can be selectively observed with SONICC. The SONICC system will be installed into PXS in FY2013. The SBRC has also studied the sulfur-SAD method using low energy X-rays. Diffraction data for sulfur-SAD have been collected at BL-1A with a newly installed Pilatus 2M detector using the longest available wavelength of 3.3 Å (Fig. 4). We succeeded in determining the crystal structure of a test protein (glucose isomerase) by the sulfur-SAD method. Further development of the sulfur-SAD method at BL-1A will be performed in the PDIS.

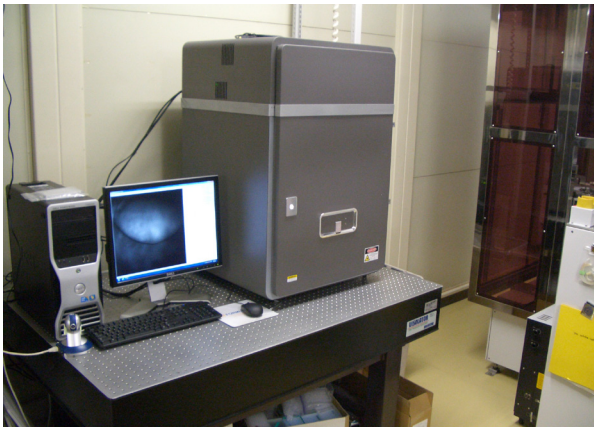

Figure 3: SONICC system installed in the Structural Biology Building.Since a second harmonic signal is generated in most protein crystals but not salt crystals, SONICC can selectively detect protein crystals.

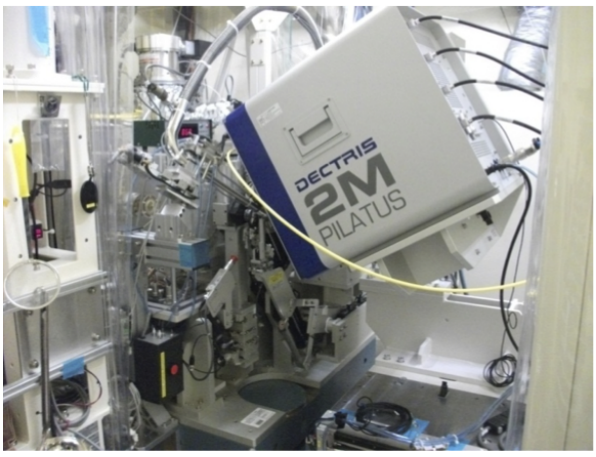

Figure 4: A newly installed Pilatus 2M detector at BL-1A.

2-3 Research Progresses under Several External Grants

In addition to the PDIS, the SBRC has obtained several external grants, such as CREST from JST, “Key strategic research for the use of X-ray free-electron lasers” from MEXT, and KAKEN-HI from MEXT/JSPS. The SBRC initiated new in-house structure biology projects in FY2012. The first one is the structural biology of epigenetic information of histone proteins to understand their mechanisms and functions. The main targets of this project are histone chaperones, which are involved in nucleosome assembly and disassembly; this project is supported by KAKEN-HI. The second project is the structural biology of the CagA oncoprotein derived from *Helicobacter pylori*, which causes some stomach diseases including stomach cancer. The crystal structure of CagA has already been determined using the beamline NE-3A in PF-AR (Highlight 5-2). [1] The SBRC is currently working to reveal the crystal structure of the CagA-PAR1-SHP2 complex with the support of CREST/JST. The CagA-PAR1-SHP2 complex perturbs normal signaling in the cell, causing the formation of stomach cancer. Tertiary structural information of the CagA-PAR1-SHP2 complex will give an insight into the molecular mechanism of stomach cancer formation by *Helicobacter pylori*. In addition to these new projects, the SBRC is continuing with existing structural biology researches [2, 3].

REFERENCES

[1] T. Hayashi, M. Senda, H. Morohashi, H. Higashi, M. Horio, Y. Kashiba, L. Nagase, D. Sasaya, T. Shimizu, N. Venugopalan, H. Kumeta, N. N. Noda, F. Inagaki, T. Senda and M. Hatakeyama, *Cell Host & Microbe* **12**, 20 (2012).

[2] K. Nakamura, Z. Man, Y. Xie, A. Hanai, H. Makyio, M. Kawasaki, R. Kato, H. W. Shin, K. Nakayama and S. Wakatsuki, *J. Biol. Chem.* **287**, 25478 (2012).

[3] H. Makyio, M. Ohgi, T. Takei, S. Takahashi, H. Takatsu, Y. Katoh, A. Hanai, T. Ueda, Y. Kanaho, Y. Xie, H. W. Shin, H. Kamikubo, M. Kataoka, M. Kawasaki, R. Kato, S. Wakatsuki and K. Nakayama, *EMBO J.* **31**, 2590 (2012).

3 Condensed Matter Research Center

3-1 Overview

The aim of the Condensed Matter Research Center (CMRC) is to pursue cutting-edge research through the comprehensive use of multi-probes supplied by the Institute of Materials Structure Science (IMSS), such as synchrotron radiation, neutrons, muons, and slow positrons in collaboration with researchers at universities and other institutes. The CMRC has four research groups: the correlated electron matter group, the surface/interface group, the matter under extreme conditions group, and the soft matter group. Through collaboration among these four groups, the CMRC has been promoting seven bottom-up projects: the hybridized orbital ordering project, the geometrical correlation project, the molecular crystal project, the oxide hetero-structure project, the surface/interface project, the extreme condition project, and the soft matter project. One more project, the hydrogen project, will soon join the CMRC. This year, the IMSS joined in the cooperative effort of the Element Strategy Initiative of the Ministry of Education, Culture, Sports, Science and Technology (MEXT) to form a Core Research Center. In addition to the abovementioned bottom-up projects, the CMRC is working on this MEXT project involving electronic materials and magnetic materials in collaboration with the Tokyo Institute of Technology and the National Institute of Materials Science, respectively.
(http://cmrc.kek.jp/english/index_eng.html)

3-2 CMRC Projects

The Hybridized Orbital Ordering Project [1, 2]

The ordered states of the electronic degrees of freedom (charge, spin, and orbital) play very important roles in strongly correlated electron systems. In particular, the hybridization effect of the electronic orbitals has been a central issue in this field for a long time. In this project, both the hybridized orbital ordering between localized and itinerant electrons and the charge/spin/orbital orderings will be studied under high pressure or a strong magnetic field. Resonant hard/soft X-ray scattering and inelastic neutron scattering techniques are used complementarily.

The Geometrical Correlation Project [3]

Geometrical frustration often produces novel phenomena in strongly correlated electron systems, such as the heavy fermion state in which anomalous mass enhancement occurs. The objective of this project is to determine a characteristic correlation time for fluctuation in itinerant systems with strong electron correlation under the influence of geometrical frustration using muons, neutrons, and synchrotron X-ray, which have different probing time scales.

The Molecular Crystal Project [4-8]

The electronic correlation in molecular crystal systems is being investigated to elucidate novel phenomena such as superconductivity and charge ordering. We are analyzing the crystal structures of molecular crystals under high pressure and/or at low temperature to elucidate the origins of phase transitions.

The Oxide Hetero-Structure Project [9]

The goal of this project is to design novel physical properties appearing at the hetero-interface of strongly correlated oxides. The physical properties arise from strong mutual coupling among the spin, charge, and orbital degrees of freedom in the interface region between two different oxides. In order to control such properties, it is necessary to clarify the interfacial electronic, magnetic, and orbital structures. We are therefore using synchrotron radiation spectroscopic techniques having elemental selectivity to probe these structures in the nm-scale at the oxide hetero-interface.

The Surface/Interface Project [10]

The surface and interface of magnetic thin films play essential roles in the appearance of extraordinary magnetic properties such as perpendicular magnetic anisotropy and the giant magneto-resistance effect. We are investigating the crystalline, magnetic and electronic structures at the surface and interface of magnetic thin films and multilayers, in order to reveal the origin of fascinating magnetic properties that cannot be realized in bulk materials.

The Extreme Condition Project

Materials under pressure and temperature show many interesting behaviors unlike those under ambient conditions. In this project, we will develop a new in-situ technique to investigate physical and chemical properties of Earth and planetary materials including iron and hydrogen under extreme conditions.

The Soft Matter Project [11]

Soft matter is a subfield of condensed matter comprising a variety of physical states that are easily deformed by thermal stresses or thermal fluctuations. They include liquids, colloids, polymers, liquid crystals, amphiphilic molecules, and a number of biological materials. These materials often self-organize into mesoscopic physical structures that are much larger than the microscopic scale (the arrangement of atoms and mol-

ecules), and yet are much smaller than the macroscopic scale of the material. The properties and interactions of these mesoscopic structures may determine the macroscopic behavior of the material. In spite of the various forms of these materials, many of their properties have common physicochemical origins, such as a large number of internal degrees of freedom, weak interactions between structural elements, and a delicate balance between entropic and enthalpic contributions to the free energy. These properties lead to large thermal fluctuations, a wide variety of forms, sensitivity of equilibrium structures to external conditions, macroscopic softness, and metastable states.

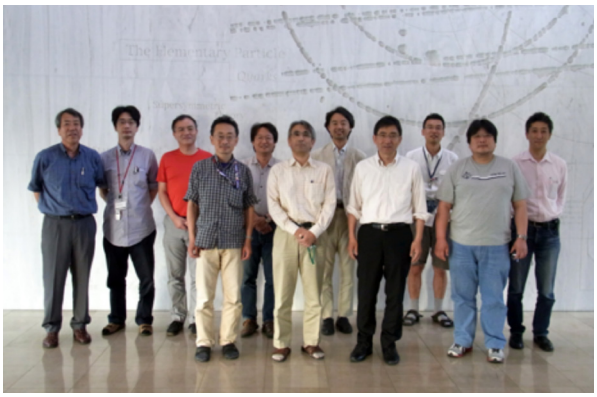

Figure 1: Project leaders of the Condensed Matter Research Center (CMRC).

REFERENCES

[1] H. Wadati, J. Okamoto, M. Garganourakis, V. Scagnoli, U. Staub, Y. Yamasaki, H. Nakao, Y. Murakami, M. Mochizuki, M. Nakamura, M. Kawasaki and Y. Tokura, *Phys. Rev. Lett.* **108**, 047203 (2012).

[2] D. Bizen, H. Nakao, K. Iwasa, Y. Murakami, T. Osakabe, J. Fujioka, T. Yasue, S. Miyasaka and Y. Tokura, *J. Phys. Soc. Jpn.* **81**, 024715 (2012).

[3] R. Kadono, A. Koda, W. Higemoto, K. Ohishi, H. Ueda, C. Urano, S. Kondo, M. Nohara and H. Takagi, *J. Phys. Soc. Jpn.* **81**, 014709 (2012).

[4] K. Kobayashi, S. Horiuchi, R. Kumai, F. Kagawa, Y. Murakami and Y. Tokura, *Phys. Rev. Lett.* **108**, 237601 (2012).

[5] N. Hoshino, F. Iijima, G. N. Newton, N. Yoshida, T. Shiga, H. Nojiri, A. Nakao, R. Kumai, Y. Murakami and Hiroki Oshio, *Nature Chemistry* **4**, 921 (2012).

[6] S. Horiuchi, F. Kagawa, K. Hatahara, K. Kobayashi, R. Kumai, Y. Murakami and Y. Tokura, *Nature Commun.* **3**, 1308 (2012).

[7] T. Isono, H. Kamo, A. Ueda, K. Takahashi, A. Nakao, R. Kumai, H. Nakao, K. Kobayashi, Y. Murakami and H. Mori, *Nature Commun.* **4**, 1344 (2013).

[8] M. Ikawa, T. Yamada, H. Matsui, H. Minemawari, J. Tsutsumi, Y. Horii, M. Chikamatsu, R. Azumi, R. Kumai and T. Hasegawa, *Nature Commun.* **3**, 1176 (2012).

[9] S. Aizaki, T. Yoshida, K. Yoshimatsu, M. Takizawa, M. Minohara, S. Ideta, A. Fujimori, K. Gupta, P. Mahadevan, K. Horiba, H. Kumigashira and M. Oshima, *Phys. Rev. Lett.* **109**, 056401 (2012).

[10] M. Sakamaki, K. Amemiya, M. O. Liedke, J. Fassbender, P. Mazalski, I. Sveklo and A. Maziewski, *Phys. Rev. B* **86**, 024418 (2012).

[11] Y. Sumino, H. Kitahata, Y. Shinohara, N. L. Yamada and H. Seto, *Langmuir* **28**, 3378 (2012).

4 Slow Positron Facility

4-1 Overview

The Slow Positron Facility of the Photon Factory, equipped with a dedicated 55 MeV, 600 W linac, provides a high intensity, pulsed slow positron beam [1, 2]. The electrons accelerated by the linac are bombarded on a Ta converter, where Bremsstrahlung produces electron-positron pairs. The positrons so produced are moderated using a W foil moderator. The pulse width is determined by the pulse structure of the linac: it is 1 μs (long pulse mode) or 1–10 ns (variable, short pulse mode) at frequencies of up to 50 Hz.

A variable high electrostatic tension (up to 35 kV) is applied to the slow positron production unit (Ta converter and W foil moderator); the obtained energy-tunable slow positron beam is magnetically guided to the experiment hall and then branched to experimental stations. The transportation of the beam with energy of up to 35 keV through a grounded beamline duct gives flexibility for experiments with grounded apparatus. This high energy transport capability is unique among high-intensity positron beam facilities in the world.

The beam intensities are 5×10^{7} slow-e^{+}/s in the long-pulse mode, and 5×10^{6} slow-e^{+}/s in the short-pulse mode.

In FY2012, the racks for the coil current supply, which were standing near the stations, were relocated to make more space for the near-future expansions of the beamlines. Consequently all the wirings from the current supply to the coils of the beamline were renewed. All the experimental stations were also relocated; the reflection high-energy positron diffraction (RHEPD) station connected to the beamline SPF-B1 was moved to SPF-A3, the station for the photodetachment of the positronium negative ion (Ps^{-}) connected to SPF-A3 was moved to SPF-B1, and the positronium time-of-flight (Ps-TOF) station connected to SPF-A1 was moved to SPF-B2. The purpose of this rearrangement was twofold: (1) to use the lab space more effectively and (2) to aggregate the stations that use short pulses in the Klystron Gallery Lab on the ground floor and those that use long pulses in the Test Hall on the basement floor. Specifically, in addition to the RHEPD apparatus transferred from the Japan Atomic Energy Research Agency (JAEA), Takasaki, a new apparatus was constructed.

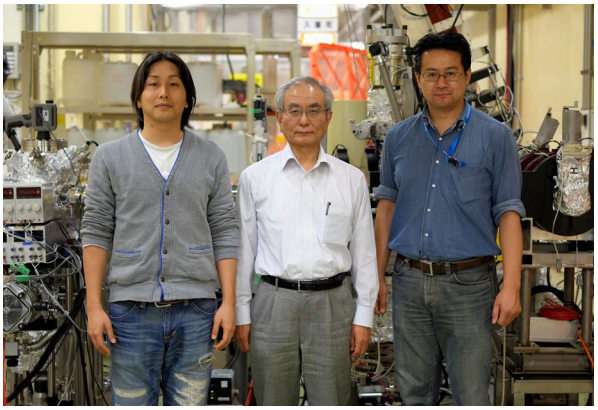

Figure 1: Members of Slow Positron Facility (SPF).

The currently available stations and the connected beamline branches are summarized below:

SPF-A3: reflection high-energy positron diffraction (RHEPD)
SPF-B1: photodetachment of the positronium negative ion (Ps-)
SPF-B2: positronium time-of-flight (Ps-TOF)

4-2 Two Projects Running in Connection with the Activities

Grant-in-Aid for Scientific Research (S) "Development of High-Brightness and High-Intensity Positron Diffraction and its Application to Surface Studies" (Project Leader: Toshio Hyodo (KEK))

Reflection high-energy positron diffraction (RHEPD), the positron version of reflection high-energy electron diffraction (RHEED), is in operation for surface structure analysis. A station for low- energy positron diffraction (LEPD), the positron version of low-energy electron diffraction (LEED) is under development for the same purpose. Positron diffractions are easier to interpret than electron diffractions because: (1) the exchange interaction with material electrons is absent; (2) the surface sensitivity of the positron is higher owing to larger inelastic scattering cross section, (3) the scattering factor for the positron falls off as smoothly as that of X-rays because it is repelled by the nuclei, and (4) total reflection takes place owing to the positive crystal potential energy for the positron.

Since the positron is an antiparticle and so not found in everyday life, it is not easy to make a high-brightness and high-intensity beam for diffraction experiments in the laboratory. This project solves this problem by making use of the high-intensity slow-positron beam of the Slow Positron Facility and enhances its brightness.

The extremely high sensitivity of positron diffraction to the surface makes it possible to determine the details of surface atomic configurations which cannot easily be done by X-ray or electron diffractions or scanning tunneling microscope (STM). The direct determination of surface atomic geometry will be attempted in two ways: by analyzing the RHEPD patterns taken under total reflection conditions with the Patterson function, and

by using the holographic reconstruction of the atomic arrangement using the LEPD spectra taken at various energies.

Progress in FY2012: The results of measurements on a Pt-deposited Ge surface conducted in FY2011 were published [3]. Construction of a second RHEPD station was started on beamline SPF-B1 in the Test Hall on the basement floor to make effective use of experiment space. A brightness enhancement unit using a transmission-type W film (100 nm) remoderator was installed, which enhances the brightness of the magnetically guided beam by about 50,000 times. Using this refined beam, the development of total reflection high-energy positron diffraction, investigation of the structure of the TiO2 surface, and that of silicene have started.

Grant-in-Aid for Scientific Research (S) "The Evolution of Positronium Beam Science using the Technique of Photodetachment of the Positronium Negative Ion" (Project Leader: Yasuyuki Nagashima (Tokyo University of Science)

This project is being conducted in a laboratory of the Tokyo University of Science and the Slow Positron Facility at KEK. Only a general introduction and the performance at KEK are described here.

The bound state of an electron and a positron, is called positronium (Ps). Ps is the lightest "atom" which is metastable against self-annihilation into γ-rays with a lifetime of 125 ps or 142 ns. An energy-tunable beam of Ps will be a powerful tool for investigating material surfaces. However, the production of a beam with sufficient intensity and appropriate energy range was difficult to realize; the only beam of Ps produced before this project started used charge exchange between positrons and gas molecules in the energy range below 400 eV [4].

This project aims to produce an energy-tunable Ps beam using photodetachment of positronium negative ion (Ps^-), a bound state of two electrons and a positron, in an ultra-high-vacuum environment. Recently Nagashima (project leader) et al. found that the Ps^- is emitted efficiently from alkali metal coated tungsten surfaces when bombarded with slow positrons [5]. Since the ion has a negative charge, it can be easily accelerated with an electric field. The photodetachment of Ps^- to neutral Ps after the acceleration produces an energy-tunable Ps beam [6, 7]. In order to photodetach Ps^-, which has a short lifetime (479 ps), it must be irradiated with a high-power pulsed YAG laser light synchronized with the production of Ps^-. The linac based beam at the Slow Positron Facility is suitable for this purpose.

Since Ps has negative affinity for most materials, the beam will be useful for analyzing the topmost layers of solids. Furthermore, the beam is not influenced by the charge-up of surfaces even if it is incident on insulators.

Progress in FY2012: The positrons generated in the short pulse mode were transported in UHV and injected into a Na coated polycrystalline tungsten target. The pulsed Ps^- ions emitted from the target were successfully photodetached in FY2010. Following this, production of an energy tunable Ps beam was confirmed by direct time-of-flight measurement of the beam in FY2011 [8, 9]. In FY2012, the spatial profile of the Ps beam was measured with a position-sensitive MCP. The detailed mechanism of the efficient formation of Ps^- on an alkali metal coated W surface is not yet understood. In order to shed light on this issue, time-of-flight measurement of the Ps emitted from a Na coated W surface was conducted. In contradiction to the expected negligible effect of the Na deposition since Ps is neutral consisting of one electron and one positron, the yield of the Ps increased drastically [10]. This is another interesting surface phenomenon awaiting clarification.

REFERENCES

[1] K. Wada, T. Hyodo, A. Yagishita, M. Ikeda, S. Ohsawa, T. Shidara, K. Michishio, T. Tachibana, Y. Nagashima, Y. Fukaya, M. Maekawa and A. Kawasuso, *Eur. Phys. J. D* **66**, 37 (2012).

[2] K. Wada, T. Hyodo, T. Kosuge, Y. Saito, M. Ikeda, S. Ohsawa, T. Shidara, K. Michishio, T. Tachibana, H. Terabe, R. H. Suzuki, Y. Nagashima, Y. Fukaya, M. Maekawa, I. Mochizuki and A. Kawasuso, *J. Phys. Conf. Ser.* **443**, 012082 (2013).

[3] I. Mochizuki, Y. Fukaya, A. Kawasuso, K. Wada, T. Hyodo, K. Yaji, A. Harasawa and I. Matsuda, *Phys. Rev. B* **85**, 245438 (2012).

[4] N. Zafar, G. Laricchia, M. Charlton and A. Garner, *Phys. Rev. Lett.* **76**, 1595 (1996).

[5] Y. Nagashima, T. Hakodate, A. Miyamoto and K. Michishio, *New J. Phys.* **10**, 123029 (2008).

[6] K. Michishio, T. Tachibana, H. Terabe, A. Igarashi, K. Wada, T. Kuga, A. Yagishita, T. Hyodo and Y.Nagashima, *Phys. Rev. Lett.* **106**, 153401 (2011).

[7] *Photon Factory Activity Report 2010* **#28**, A 68 (2012).

[8] K. Michishio, T. Tachibana, R. H. Suzuki, K. Wada, A. Yagishita, T. Hyodo and Y. Nagashima, *Appl. Phys. Lett.* **100**, 254102 (2012).

[9] *Photon Factory Activity Report 2011* #**29**, A 60 (2013).

[10] H. Terabe, S. Iida, K. Wada, T. Hyodo, A. Yagishita and Y. Nagashima, *J. Phys. Conf. Ser.* **443**, 012075 (2013).

5 IMSS Instrument R&D Team

The IMSS Instrument R&D team has been developing new detector systems for material science and biology since May 2010. Here we introduce two R&D projects ongoing in the Photon Factory and their results obtained in FY2012.

5-1 Ultra-Fast Signal Processing System for a Si-APD Array X-ray Detector

The project team developed a prototype detector consisting of a 64-ch Si-APD linear array and its ultra-fast application-specific IC (ASIC) circuits, in FY2011. The linear array had 64 pixels of 100 μm × 200 μm with a pitch of 150 μm. The array device had a thickness of 10 μm to obtain a good time resolution of 100 ps. The front-end ASIC was newly designed to process fast pulses of nanosecond width and a high count-rate obtained from the Si-APD operating in the linear mode. In test measurements carried out at BL-14A, the prototype system revealed a 10-ns time resolution and a high count-rate of > 10^7 s^{-1} per pixel. Then, in FY2012, the team successfully measured the count distribution by 1-ns sampling with a new system using improved front-end ASICs and field programmable gate arrays (FPGAs). Figure 1 shows a result of the count distribution obtained from the No. 15 channel of the system in the hybrid-mode operation of the Photon Factory ring. The hybrid mode consists of single-bunch and multi-bunch electrons revolving in the accelerator ring. A fine X-ray beam of 8 keV hit the No. 15 pixel of the APD linear array. A time resolution of 1.4 ns (FWHM) was measured from the peak width of the No. 15 channel, fitted in the single-bunch part. To investigate laser-induced structural changes in some organic molecules, it is useful to record their X-ray diffraction patterns using a detector with a time resolution of less than 2 ns. Moreover, the 1-ns sampling will greatly decrease the measuring time in time-resolved experiments by using X-rays of 2-ns interval in the multi-bunch part.

5-2 Auger-Electron Detector System for Depth-Resolved X-ray Magnetic Circular Dichroism (XMCD)

The group working for beamline BL-16 has been preparing a multi-anode MCP detector system, which has an angle-resolution and a fast digital data read-out of 30 channels, instead of the system consisting of a CCD and a fluorescence screen. In the 10-Hz polarization switching of the insertion devices installed in BL-16, the new MCP system improved the S/N ratio and the dynamic range of output counts in XMCD measurements. In FY2012, a fast counting system using fast pulse-amplifier ASICs was tested for data acquisition at higher count rates of more than 10^7 s^{-1} per channel. The system is now undergoing improvements to the threshold-level setting in signal inputs and to the cross-talk of counting between ASIC channels.

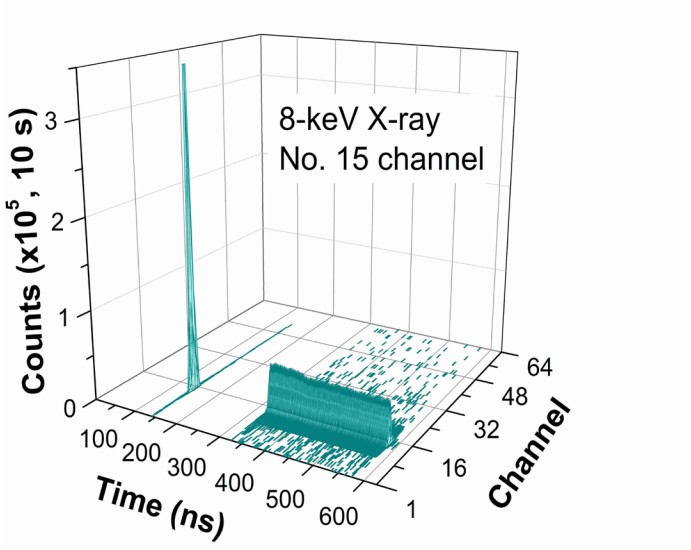

Figure 1: Continuous time distribution of 8-keV X-ray counts measured in the hybrid-mode operation of the Photon Factory ring.

6 Summary of Experimental Stations

About 57 experimental stations are operated at the PF storage ring, the PF-AR and the slow positron facility (SPF), as shown in Figs. 1, 2 and 3. 36 stations are dedicated to research using hard X-rays, 16 stations for studies in the VUV and soft X-ray energy regions, and 5 stations for studies using slow positrons. Tables 1, 2 and 3 summarize the areas of research carried out at the experimental stations at the PF storage ring, PF-AR and SPF. The specifications in terms of the optics and performance of each experimental station differ according to experimental requirements and methodology. Tables 4, 5 and 6 list the details of the optics of the hard X-ray stations, the soft X-ray / VUV stations and the slow positron stations. The principal performance parameters, including energy range, energy resolution, beam-spot size, and photon flux at the sample position for PF and PF-AR, and energy range, pulse width, frequency, and positron flux for SPF are shown.

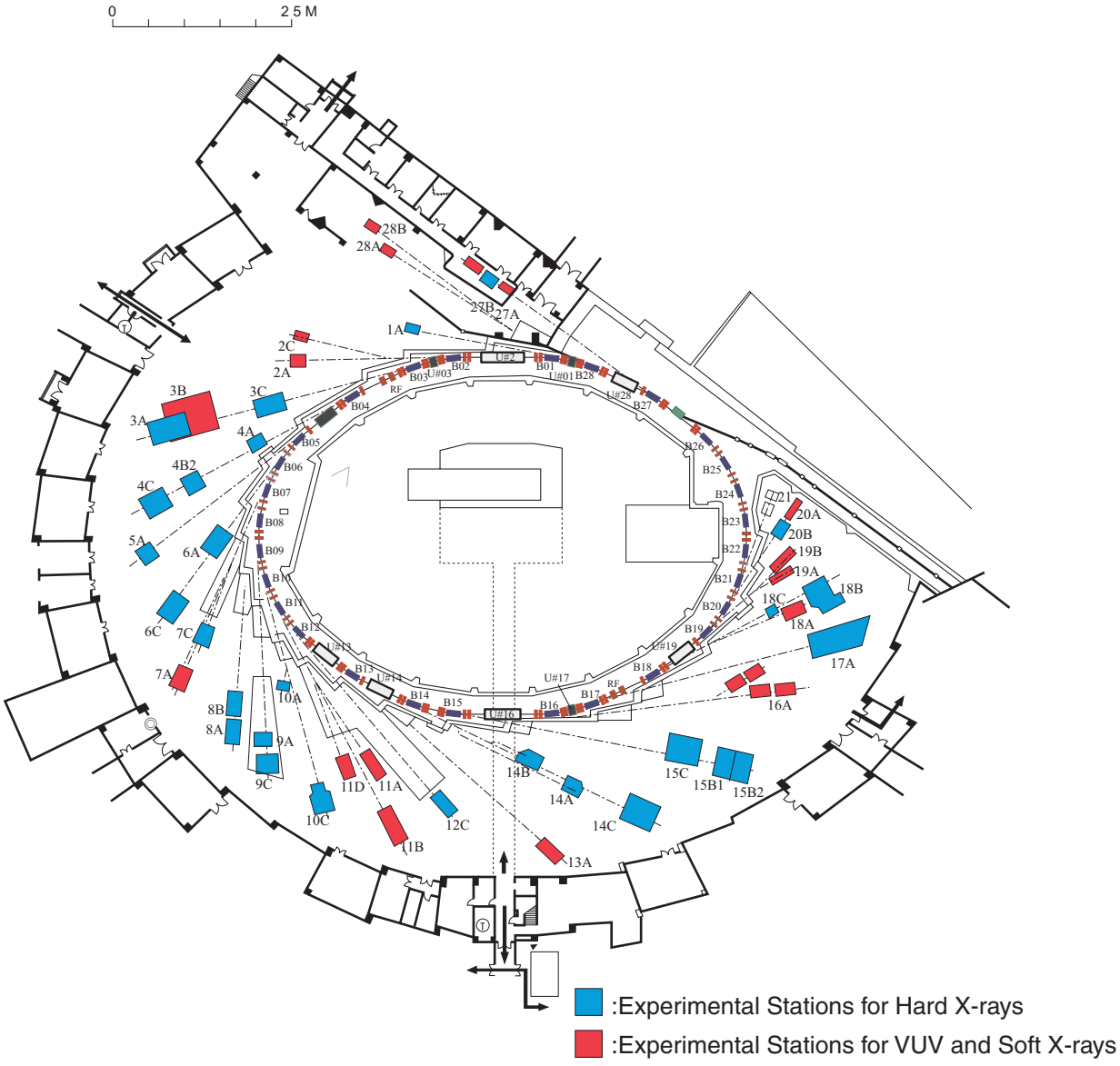

Figure 1: Plan view of the PF experimental hall, showing hard X-ray experimental stations (blue), and VUV and soft X-ray experimental stations (red).

Table 1: List of experimental stations at the PF storage ring.

Experimental Station		Person in Charge
BL-1	(Short Gap Undulator)	
A	Macromolecular crystallography	N. Matsugaki
BL-2	(Undulator)	
A*	Soft X-ray spectroscopy	Y. Kitajima
C*	Soft X-ray spectroscopy	J. Adachi
BL-3	(A: Short Gap Undulator)	
A	X-ray diffraction and scattering station for materials science	H. Nakao
B	VUV and soft X-ray spectroscopy(◊)	H. Kato [Hirosaki Univ.], A. Yagishita
C	Characterization of X-ray optical elements/White X-ray magnetic diffraction	K. Hirano
BL-4		
A	Trace element analysis, X-ray microprobe	A. Iida
B2	High resolution powder diffraction(♠)	T. Ida [Nagoya Inst. Tech.], H. Nakao
C	X-ray diffraction and scattering	Y. Yamasaki
BL-5	(Multipole Wiggler)	
A	Macromolecular crystallography	Y. Yamada
BL-6		
A	Small-angle X-ray scattering	N. Igarashi
C	X-ray diffraction and scattering(♠)	S. Sasaki [Tokyo Inst. Tech.] H. Kawata
BL-7		
A	Soft X-ray spectroscopy(♦)	J. Okabayashi [RCS], K. Amemiya
C	X-ray spectroscopy and diffraction	H. Sugiyama
BL-8		
A	Weissenberg camera for powder/Single-crystal measurements under extreme conditions	R. Kumai
B	Weissenberg camera for powder/Single-crystal measurements under extreme conditions	R. Kumai
BL-9		
A	XAFS	H. Abe
C	XAFS	H. Abe
BL-10		
A	X-ray diffraction and scattering	Y. Yamasaki
C	Small-angle X-ray scattering	N. Shimizu
BL-11		
A	Soft X-ray spectroscopy	Y. Kitajima
B	Surface EXAFS, soft X-ray spectroscopy	Y. Kitajima
D	Characterization of optical elements used in the VSX region	K. Ito
BL-12		
C	XAFS	H. Nitani

Experimental Station		Person in Charge
BL-13	(Undulator)	
A	Soft X-ray photoemission spectroscopy and XAFS	K. Mase
BL-14	(Vertical Wiggler)	
A	Crystal structure analysis and detector development	S. Kishimoto
B	High-precision X-ray optics	K. Hirano
C	Medical applications and general purpose (X-ray)	K. Hyodo
BL-15		
B1**	White X-ray topography and X-ray experiments for general purpose	H. Sugiyama
B2**	Surface and interface X-ray diffraction	H. Sugiyama
C**	High-resolution X-ray diffraction	K. Hirano
BL-16	(Variable Polarization Undulator)	
A	Soft X-ray spectroscopies with circular and linear polarization	K. Amemiya
BL-17	(Short Gap Undulator)	
A	Macromolecular crystallography	Y. Yamada
BL-18		
A	Angle-resolved photoelectron spectroscopy of surfaces and interfaces(♦)	K. Yaji [ISSP], A. Yagishita
B	Multipurpose monochromatic hard X-ray station(♦)	S. Velaga [India, Saha Institute], N. Igarashi
C	High pressure X-ray powder diffraction (DAC)(♠)	S. Nakano [NIMS], T. Kikegawa
BL-19	(Revolver Undulator)	
A	Spin-resolved photoelectron spectroscopy (Mott detector)(♦)	K. Yaji [ISSP], A. Yagishita
B**	Soft X-ray emission spectroscopy(♦)	K. Yaji [ISSP], A. Yagishita
BL-20		
A	VUV spectroscopy(◊)	N. Kouchi [Tokyo Inst. Tech], K.Ito
B**	White and monochromatic beam general-purpose X-ray station(♦)	J. B. Aitken [ASCo.], H. Kawata
BL-27	(Beamline for experiments using radioisotopes)	
A	Radiation biology, soft X-ray photoelectron spectroscopy	N. Usami
B	Radiation biology, XAFS, X-ray diffuse scattering	N. Usami
BL-28	(Elliptical / Helical Undulator)	
A/B	High-resolution VUV-SX beamline for angle-resolved photoemission High-resolution VUV-SX spectroscopy	K. Ono

♠ User group operated beamline
♦ External beamline
◊ Operated by University
* Shutdown at the end of FY2012 for reconstruction
** Shutdown at the end of FY2012

RCS: Research Center for Spectrochemistry, the University of Tokyo
ISSP: Institute for Solid State Physics, the University of Tokyo
ASCo.: Australian Synchorotron Co-operation

Table 2: List of experimental stations at the PF-AR.

Experimental Station		Person in Charge
AR-NE1	(Multipole Wiggler)	
A	Laser-heating high pressure X-ray diffraction and nuclear resonant scattering (DAC)	T. Kikegawa
AR-NE3	(Undulator)	
A	Macromolecular crystallography	Y. Yamada
AR-NE5		
C	High pressure and high temperature X-ray diffraction (MAX-80)	T. Kikegawa
AR-NE7		
A	High pressure and high temperature X-ray diffraction (MAX-III), X-ray imaging	K. Hyodo
AR-NW2	(Undulator)	
A	XAFS/Dispersive XAFS/Time-resolved-X-ray diffraction	H. Abe
AR-NW10		
A	XAFS	H. Nitani
AR-NW12	(Undulator)	
A	Macromolecular crystallography	L.M.G. Chavas
AR-NW14	(Undulator)	
A	Time-resolved X-ray diffraction, scattering and absorption	S. Adachi

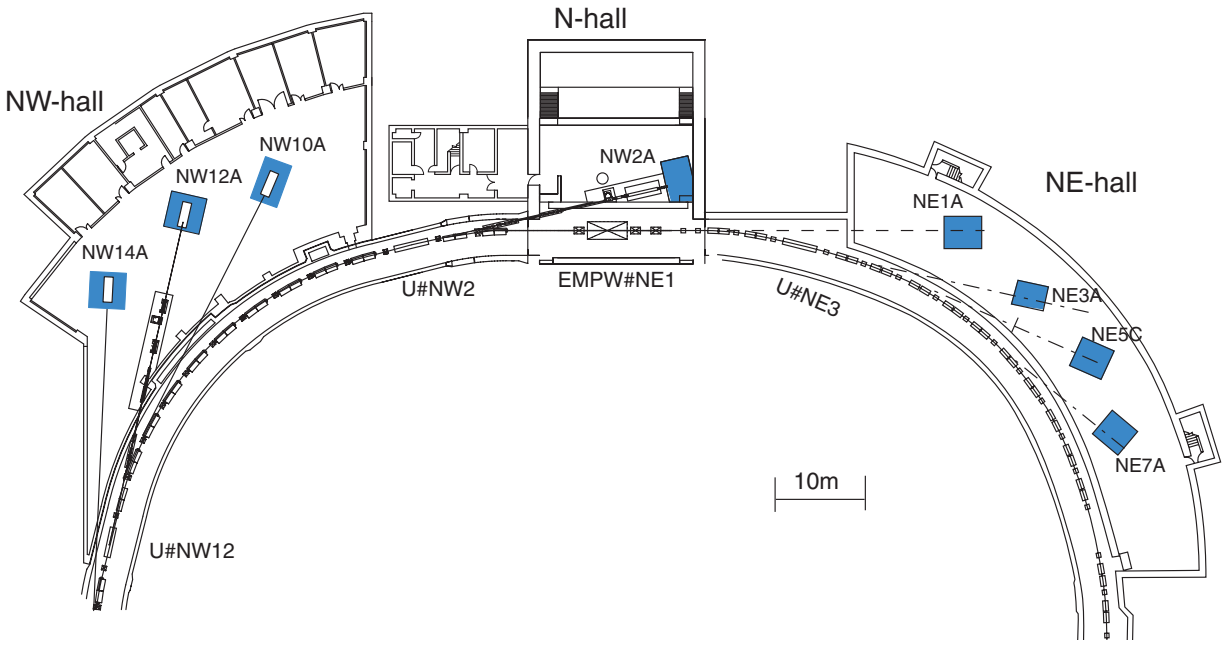

Figure 2: Plan view of beamlines in the PF-AR north-east, north, and north-west experimental halls.

Table 3: List of experimental stations at the Slow Positron Facility.

Experimental Station		Person in Charge
SPF-A1 A	General purpose	T. Hyodo
SPF-A2 A	Reflection high-energy positron diffraction	T. Hyodo
SPF-A3 A	General purpose	T. Hyodo
SPF-B1 A	General purpose (Positronium negative ion)	T. Hyodo
SPF-B2 A	Positronium time-of-flight	T. Hyodo

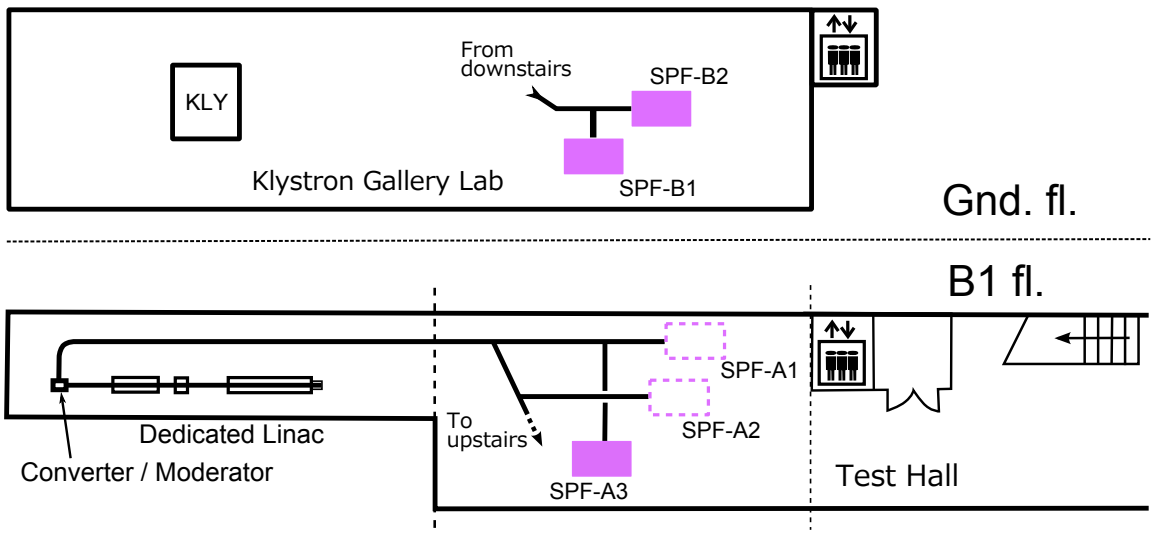

Figure 3: View of beamlines in the Slow Positron Facility.

Table 4: Specifications of X-ray beamline optics.

Branch Beamline	Horizontal Acceptance (mrad)	Type of Monochromator	Mirror	Photon Energy (keV)	Beam Size (H×V) (mm)	Photon Flux at Sample Position (/s)	Energy Resolution ($\Delta E/E$)×10^{-4}	Reference
BL-1A	0.15	Channel-Cut Si(111) Liquid N_2 Cooling	Bimorph Si Rh-Coated Si Rh-Coated	3.7 ~ 4.5 11.2 ~ 12.9	0.05×0.01	4×10^{11}@11.2 keV (0.025×0.01mm^2)	~2	
BL-3A	1	Flat Double Crystal Si(111)	Bent Cylinder	4 ~ 14	0.7×0.2	6×10^{12}	~5	1, 2
BL-3C	1.75	Double Crystal Si(111)	None	4 ~ 20 or white	20×6(mono) 0.1×0.1(white)		~2	
BL-4A	6	Double Crystal Si(111)	Vertical Focusing Mirror	4 ~ 20	50×4		~2	3
BL-4B2	4.5	Flat Double Crystal Si(111)	Bent Cylinder	6 ~ 20	13×2		~2	4, 5
BL-4C	2	Flat Double Crystal Si(111)	Bent Cylinder	5 ~ 19	0.7×0.5		~5	6, 7
BL-5A	0.5	Micro-Channel Double Crystal Si(111)	Bent Plane Si Rh-Coated Bent Cylinder Si Rh-Coated	6.5 ~ 17	1.2×0.4	3×10^{11} (0.2×0.2 mm^2)	~2	
BL-6A	2	Bent Crystal Ge(111) (α = 8.0°)	Bent Plane ULE	8.3 (fixed)	0.5×0.2	1.0×10^{12}/mm^2 (Slit full-open)	~10	8
BL-6C	2	Flat Double Crystal Si(111)	Bent Cylinder	5 ~ 12 (~25 non-Focus)	1.2×1.2			
BL-7C	4	Double Crystal Si(111) Sagittal Focusing	Double Mirror Fused Quartz Focusing	4 ~ 20 (4 ~ 13)	5×1	1×10^{10}/6mm^2 (8 keV, 300 mA) (1×10^{11} when focused)	~2	9 - 11
BL-8A	2.22	Flat Double Crystal Si(111)	Bent Cylinder	5 ~ 19	0.82×0.52	3.2×10^{11} (12.4keV, 400mA)	~5	12
BL-8B	2.21	Flat Double Crystal Si(111)	Bent Cylinder	5 ~ 19	0.75×0.45	2.2×10^{11} (12.4keV, 400mA)	~5	12

Branch Beamline	Horizontal Acceptance (mrad)	Type of Monochromator	Mirror	Photon Energy (keV)	Beam Size (H×V) (mm)	Photon Flux at Sample Position (/s)	Energy Resolution ($\Delta E/E$)×10^{-4}	Reference
BL-9A	3	Double Crystal Si (111)	Collimating and Focusing Bent Conical Mirrors (Rh-Coated) Double Flat Mirror (Ni-Coated)	2.1 ~ 15	0.5×0.3	6×10^{11}(7keV, 450 mA)	2	13, 14
BL-9C	3.5	Double Crystal Si(111)	Bent Cylinder Rh-Coated Si	4 ~ 23	0.8×0.6	1×10^{11}(8keV, 450 mA)	~2	
BL-10A	1	Si(111), Si(311) Quartz(100) PG(002) Curved Si(111) (α~ 4°, 8°)	Plane Pt Coated Fused Quartz	5 ~ 25	10×3		10 ~5	15
BL-10C	4	Double Crystal Si(111)	Bent Cylinder	8.3 (fixed)	1.0×0.5	5.0 x 10^{11} (Slit full-open)	2	16
BL-12C	2	Double Crystal Si(111)	Bent Cylinder Double Flat Mirror (Ni-Coated)	4 ~ 23	0.6×0.6	9×10^{10}(8 keV, 450mA)	~2	17
BL-14A	1.28 (Vertical)	Double Crystal Si (111) Si (311) Si (553)	Bent Cylinder Rh-Coated Fused Quartz	5.1 ~ 19.1 9.9 ~ 35.6 22.7 ~ 84.5	2×1 at focus 5×38		2	18
BL-14B	2.2 (Vertical)	Flat Double Crystal Si(111)	None	10 ~ 57	5×14		2	19
BL-14C	1.96 (Vertical)	Double Crystal Si(111), Si(220)	None	5 ~ 100 or white	6×70		2	20, 21
BL-15B1** B2**	2	Double Crystal Si (111)	Bent Cylinder	5 ~ 20 or white	0.6×0.4	1.0×10^{12}/mm^2 (8 keV, 430 mA)	~2	
BL-15C**	2	Double Crystal Si (111)	None	4 ~ 30	60×6			
BL-17A	0.1 ~ 0.2	Double Crystal Si(111) Liquid N_2 Cooling	Bent Plane Si Rh-Coated Bent Plane Si Rh-Coated	6 ~ 9 11 ~ 13	0.25×0.04	10^{10} (12.4 keV, 450mA, 0.02×0.02mm^2)	~2	22, 23

Branch Beamline	Horizontal Acceptance (mrad)	Type of Monochromator	Mirror	Photon Energy (keV)	Beam Size (H×V) (mm)	Photon Flux at Sample Position (/s)	Energy Resolution ($\Delta E/E$)×10^{-4}	Reference
BL-18B [India, DST]	2	Double Crystal Si(111)	Plane and Bent Cylinder	6 ~ 20			~2	
BL-18C	1	Double Crystal Si(111)	Cylinder Fused Quartz Pt-Coated	6 ~ 25	0.07×0.04		~2	
BL-20B** [ASCo.]	2	Channel Cut Si(111) Channel Cut Si(311) Sagittal Focusing Si(111) Double Crystal	None	4.5 ~ 21 10 ~ 36 4.5 ~ 25	25×2 25×1.5 0.6×1		~2 ~1 ~2	24
BL-27B	4	Double Crystal Si(111)	None	4 ~ 20	100×6		~2	25
AR-NE1A	0.28	Micro-Channel Double Crystal Si(111), High-Resolution Channel Cut Si(4,2,2)&(12,2,2)	Bent Plane W/C Multilayer Coated Si	6 ~ 50	0.8×0.2	8×10^{11} ($0.2\times0.2mm^2$)	~2	
AR-NE3A	H:0.2 V:0.1	Double Crystal Si(111) Liquid N_2 Cooling	Pre-Mirror Bent Flat Si Rh-Coated Post-Mirror Bent Cylinder Fused Quartz Rh-Coated	6.5 ~ 17	0.8×0.2	8×10^{11} ($0.2\times0.2mm^2$)	~2	26, 27
AR-NE5C	3	Double Crystal Si(111)	None	30 ~ 100 or white	60×5		5	28
AR-NE7A	4	Double Crystal Si(111)		25 ~ 50 or white	80×3		5	
AR-NW2A	H:1.0 V:0.2	Double Crystal Si(111) Liquid N_2 Cooling	Bent Cylinder Si Rh-Coated Bent Flat Si Rh-Coated	5 ~ 25	0.6×0.2 ~10×0.06	6×10^{12}(12keV, 60mA)	~2	29 - 31

Branch Beamline	Horizontal Acceptance (mrad)	Type of Monochromator	Mirror	Photon Energy (keV)	Beam Size (H×V) (mm)	Photon Flux at Sample Position (/s)	Energy Resolution ($\Delta E/E$)×10^{-4}	Reference
AR-NW10A	1.2	Si(311)	Pt-Coated Bent Cylinder Double Flat Mirror (Rh-Coated)	8 ~ 42	2.2×0.5	1×10^{10}(22 keV, 60mA)	~1	32
AR-NW12A	H:0.3 V:0.1	Double Crystal Si(111) Liquid N_2 Cooling	Pre-Mirror Bent Flat Si Rh-Coated Post-Mirror Bent Cylinder Si Rh-Coated	6.5 ~ 17	1.3×0.3	2×10^{11} (0.2×0.2 mm^2)	~2	33, 34
AR-NW14A	H:0.3 V:0.1	Double Crystal Si(111) Liquid N_2 Cooling	Bent Cylinder Rh-Coated Bent Flat Rh-Coated	4.9 ~ 25	0.45×0.25	5×10^{12}	~2	35

** Shutdown at the end of FY2013

ASCo.: Australian Synchrotron Co-operation
India DST: Department of Science & Technology

REFERENCES

[1] *Photon Factory Activity Report 2006*, **#24**, A 64 (2008).
[2] *Photon Factory Activity Report 2006*, **#24**, A 104 (2008).
[3] A. Iida *et al.*, *Rev. Sci. Instrum.* **66**, 1373 (1995).
[4] Powder Diffraction User Group, *KEK Report* **94-11** (1995).
[5] H. Toraya, H. Hibino and K. Ohsumi, *J. Synchrotron Rad.* **3**, 75 (1996).
[6] H. Iwasaki *et al.*, *Rev. Sci. Instrum.* **60**, 2406 (1989).
[7] *Photon Factory Activity Report 1995* **#13**, E-1 (1996).
[8] N. Shimizu *et al.*, *J. Phys.: Conf. Ser.* **425**, 202008 (2013).
[9] M. Nomura and A.Koyama, *KEK Internal,* **93-1** (1993).
[10] M. Nomura *et al.*, *KEK Report,* **91-1** (1991).
[11] M. Nomura and A. Koyama, in *"X-ray Absorption Fine Structure"*, ed. by S. S. Hasnain, Ellis Horwood, Chichester, 667 (1991).
[12] A. Nakao *et al.*, *AIP Conf. Proc.* **1234**, *367* (2010).
[13] M. Nomura and A. Koyama, *J. Synchrotron Rad.* **6**, 182 (1999).
[14] M. Nomura and A. Koyama, *Nucl. Instrum. Meth.* **A467-468**, 733 (2001).
[15] S. Sasaki, *Rev. Sci. Instrum.* **60**, 2417 (1989).
[16] N. Igarashi *et al.*, *J. Phys.: Conf. Ser.* **272**, 012026 (2011).
[17] M. Nomura and A. Koyama, *KEK Report,* **95-15** (1996).
[18] Y. Satow and Y. Iitaka, *Rev. Sci. Instrum.* **60**, 2390 (1989).
[19] M. Ando *et al.*, *Nucl. Instrum. Meth.* **A246**, 144 (1986).
[20] *Photon Factory Activity Report 1999,* **#17**, A 92 (2000).
[21] *Photon Factory Activity Report 1999*, **#17**, A 103 (2000).
[22] N. Igarashi *et al.*, *AIP Conf. Proc.* **879**, 812 (2007).
[23] N. Igarashi *et al.*, *J. Synchrotron Rad.* **15**, 292 (2008).
[24] R.F. Garret *et al.*, *Rev. Sci. Instrum.* **66**, 1351 (1995).
[25] H. Konishi *et al.*, *Nucl. Instrum. Meth.* **A372**, 322 (1996).
[26] Y. Yamada *et al.*, *AIP Conf. Proc.* **1234**, 415 (2010).
[27] M. Hiraki *et al.*, *AIP Conf. Proc.* **1234**, 673 (2010).
[28] T. Kikegawa *et al.*, *Rev. Sci. Instrum.* **66**, 1335 (1995).
[29] T. Mori *et al.*, *AIP Conf. Proc.* **705**, 255 (2004).
[30] H. Kawata *et al.*, *AIP Conf. Proc.* **705**, 663 (2004).
[31] Y. Inada *et al. AIP Conf. Proc.* **879**, 1230 (2007).
[32] M. Nomura *et al.*, *AIP Conf. Proc.* **882**, 896 (2007).
[33] L.M.G. Chavas *et al.*, *J. Synchrotron Rad.* **19**, 450 (2012).
[34] L.M.G. Chavas *et al.*, *J. Phys.: Conf. Ser.* **425**, 012008 (2013).
[35] S. Nozawa *et al.*, *J. Synchrotron Rad.* **14**, 313 (2007).

Table 5: Specifications of VUV and soft X-ray beamline optics.

Beamline	Acceptance H × V (mrad) or Undulator Parameters	Type of Monochromator	Groove Density (ℓ/mm)	Energy Range (eV)	Beam Size H × V (mm)	Resolving Power (E/ΔE) Photon Flux (photons/s)	Reference
BL-2A* Undulator	K = 0.5 ~ 2.2 λ_u = 6 cm	Double Crystal InSb (111), Si (111)	——	1740 ~ 5000	< 1ϕ	2000, 8000 10^{11}	1 - 4
BL-2C* Undulator	K = 0.55 ~ 2.2 λ_u = 6 cm	Varied-Line-Space Plane Grating	1000 2200	250 ~ 1400	0.9 × 0.1	5000 ~ 10000 10^{11} ~ 10^{10}	5 - 7
BL-3B	10 × 2	Grazing Incidence R = 24 m α+β = 165° 1800	200 600	10 ~ 280	< 2ϕ	200 ~ 3000 10^{12} ~ 10^{9}	8, 9
BL-7A [RCS]	6 × 1	Varied-Line-Space Plane Grating	300 650	50 ~ 1300	2.5 × 0.5	1000 ~ 9000 10^{12} ~ 10^{9}	10
BL-11A	5 × 1	Varied-Line-Space Plane Grating	300 800 1200	70 ~ 1900	2 × 1	500 ~ 5000 10^{12} ~ 10^{9}	11 - 14
BL-11B	4 × 0.6	Double Crystal InSb (111), Si (111)		1724 ~ 5000	5 × 2	2000 10^{10}	3 15 - 17
BL-11D	4 × 2	Grazing Incidence Varied Deviation-Angle On-Blaze Mount R_1 = 52.5 m R_3 = 22.5 m	2400	60 ~ 245 200 ~ 900	1 × 0.1	2000 10^{11}	18, 19
BL-13A Undulator	K_{max} = 8 λ_u = 18 cm	Variable-Included-Angle Varied-Line-Spacing Plane Grating	300 1000	30 ~ 330 100 ~ 1600	~0.2 × 0.04	4000 ~ 10000 10^{12} ~ 10^{9}	20 - 22
BL-16A Undulator	K_{max} = 2.37 (Circular Polarization) K_{max} = 3.12 (Horizontal Linear Polarization) K_{max} = 1.98 (Vertical Linear Polarization) K_{max} = 1.73 (45-deg Linear Polarization) λ_u = 5.6 cm	Variable-Included-Angle Varied-Line-Spacing Plane Grating	500 1000	250 ~ 1500	~0.2 × 0.1	4000 ~ 8000 10^{12} ~ 10^{11}	23, 24
BL-18A [ISSP]	2 × 2	Grazing Incidence R = 3 m α+β = 160° R = 6.65 m α+β = 167.5°	300 600 1000	15 ~ 150	< 1ϕ	1000~2000 10^{11} ~10^{9}	25
BL-19A Revolver Undulator [ISSP]	[K = 1.0 ~ 9.0 λ_u = 16.4 cm K = 0.5 ~ 1.25 λ_u = 5 cm K = 0.5 ~ 2.5	Grazing Incidence R = 2 m α+β = 160° R = 4 m α+β = 170°	600 1200 600 1200	12 ~ 250	< 0.7ϕ	1000 10^{12}	26, 27
BL-19B** Revolver Undulator [ISSP]	λ_u = 7.2 cm K = 1.0 ~ 5.0 λ_u = 10 cm	Varied-Line-Space Plane Grating	800 2400	10 ~ 1200	< 0.5ϕ	400-4000 10^{12} ~10^{11}	28, 29

Beamline	Acceptance H × V (mrad) or Undulator Parameters	Type of Monochromator	Groove Density (ℓ/mm)	Energy Range (eV)	Beam Size H × V (mm)	Resolving Power (E/ΔE) Photon Flux (photons/s)	Reference
BL-20A	28 × 5	3m Normal Incidence	1200 2400	5 ~ 40	2 × 1	300 ~ 30000 10^{12} ~ 10^{8}	30
BL-27A	5 × 0.5	Double Crystal InSb (111)		1800 ~ 4000		2000	31
BL-28A/B Helical Undulator	K_x = 0.23 ~ 3 K_y = 0.23 ~ 6 K_y = 0.23 ~ 6	Varied-Line-Space Plane Grating	400	30 ~ 300	0.15 × 0.05	30000 10^{12}	32

* Shutdown at the end of FY2012 for reconstruction
** Shutdown at the end of FY2012

RCS: Research Center for Spectrochemistry, the University of Tokyo
ISSP: Institute for Solid State Physics, the University of Tokyo

REFERENCES

[1] H. Maezawa *et al.*, *Nucl. Instrum. Meth.* **A246**, 310 (1986).
[2] Y. Kitajima *et al.*, *Rev. Sci. Instrum.* **63**, 886 (1992).
[3] Y. Kitajima, *J. Elec. Spec. Relat. Phenom.* **80**, 405 (1996).
[4] Y. Kitajima, *J. Synchrotron Rad.* **6**, 167 (1999).
[5] Y. Yan and A. Yagishita, *KEK Report* **95-9**, (1995).
[6] M. Watanabe *et al.*, *Proc. SPIE* **3150**, 58 (1997).
[7] M. Watanabe *et al.*, *Nucl. Instrum. Meth.* **A467-468**, 512 (2001).
[8] A. Yagishita *et al.*, *Nucl. Instrum. Meth.* **A306**, 578 (1991).
[9] S. Masui *et al.*, *Rev. Sci. Instrum.* **63**, 1330 (1992).
[10] K. Amemiya *et al.*, *J. Elec. Spectrosc. Relat. Phenom.* **124**, 151 (2002).
[11] K. Amemiya *et al.*, *J. Synchrotron Rad.* **3**, 282 (1996).
[12] K. Amemiya *et al.*, *Proc. SPIE Proceedings* **3150**, 171 (1997).
[13] Y. Kitajima *et al.*, *J. Syncrotron Rad.* **5**, 729 (1998).
[14] Y. Kitajima *et al.*, *J. Elec. Spectrosc. Relat. Phenom.* **101-103**, 927 (1999).
[15] T. Ohta *et al.*, *Nucl. Instrum. Meth.* **A246**, 373 (1986).
[16] M. Funabashi *et al.*, *Rev. Sci. Instrum.* **60**, 1983 (1989).
[17] T. Iwazumi *et al.*, *Rev. Sci. Instrum.* **66**, 1691 (1995).
[18] *Photon Factory Activity Report 1997* **#15**, A 101 (1998).
[19] T. Hatano and S. Aihara, *J. Phys.: Conf. Ser.* **425**, 152018 (2013).
[20] K. Mase *et al.*, *AIP Conf. Proc.* **1234**, 709 (2010).
[21] A. Toyoshima *et al.*, *J. Vac. Soc. Jpn.* **54**, 580 (2011).
[22] A. Toyoshima *et al.*, *J. Phys.: Conf. Ser.* **425**, 152019 (2013).
[23] K. Amemiya *et al.*, *AIP Conf. Proc.* **1234**, 295 (2010).
[24] K. Amemiya et al., *J. Phys.: Conf. Ser.* **425**, 152015 (2013).
[25] S. Suzuki *et al.*, *Activity Report of SRL-ISSP* **60**, (1989).
[26] A. Kakizaki *et al.*, *Rev. Sci. Instrum.* **60**, 1893 (1989).
[27] A. Kakizaki *et al.*, *Rev. Sci. Instrum.* **63**, 367 (1992).
[28] M. Fujisawa *et al.*, *Nucl. Instrum. Meth.* **A467-468**, 309 (2001).
[29] M. Fujisawa *et al.*, *Nucl. Instrum. Meth.* **A467-468**, 313 (2001).
[30] K. Ito *et al.*, *Rev. Sci. Instrum.* **66**, 2119 (1995).
[31] H. Konishi *et al.*, *Nucl. Instrum. Meth.* **A372**, 322 (1996).
[32] K. Amemiya and T. Ohta, *J. Synchrotron Rad.* **11**, 171 (2004).

Table 6: Specifications of the beamlines at Slow Positron Facility.

Beamline	Beam Energy	Pulse Width	Frequency	Intensity	Reference
SPF-A1	100eV - 35keV	1-10ns	≤ 50Hz	5x10^{6} e+/s	
SPF-A2	100eV - 35keV	1μs	≤ 50Hz	5x10^{7} e+/s	
SPF-A3	100eV - 35keV	1μs	≤ 50Hz	5x10^{7} e+/s (5x10^{6} e+/s after brightness enhancement)	3,4
SPF-B1	100eV - 35keV	1-10ns	≤ 50Hz	5x10^{6} e+/s	1,2,3,4
SPF-B2	100eV - 35keV	1-10ns	≤ 50Hz	5x10^{6} e+/s	5,6

REFERENCES

[1] T. Tachibana, *et. al., Nucl. Instrum. Methods Phys. Res., Sect. A* **621**, 670 (2010).
[2] K. Michishio, *et al., Phys. Rev. Lett.* **106**, 153401 (2011).
[3] K. Wada, *et al., Eur. Phys. J. D* **66**, 37 (2012).
[4] K. Michishio, *et al., Appl. Phys. Lett.* **100**, 254102 (2012).
[5] K. Wada, *et al., J. Phys.: Conf. Ser.* **443**, 012082 (2013).
[6] H. Terabe, S. Iida, K. Wada, T. Hyodo, A. Yagishita and Y. Nagashima, *J. Phys.: Conf. Ser.* **443**, 012075 (2013).

Accelerators

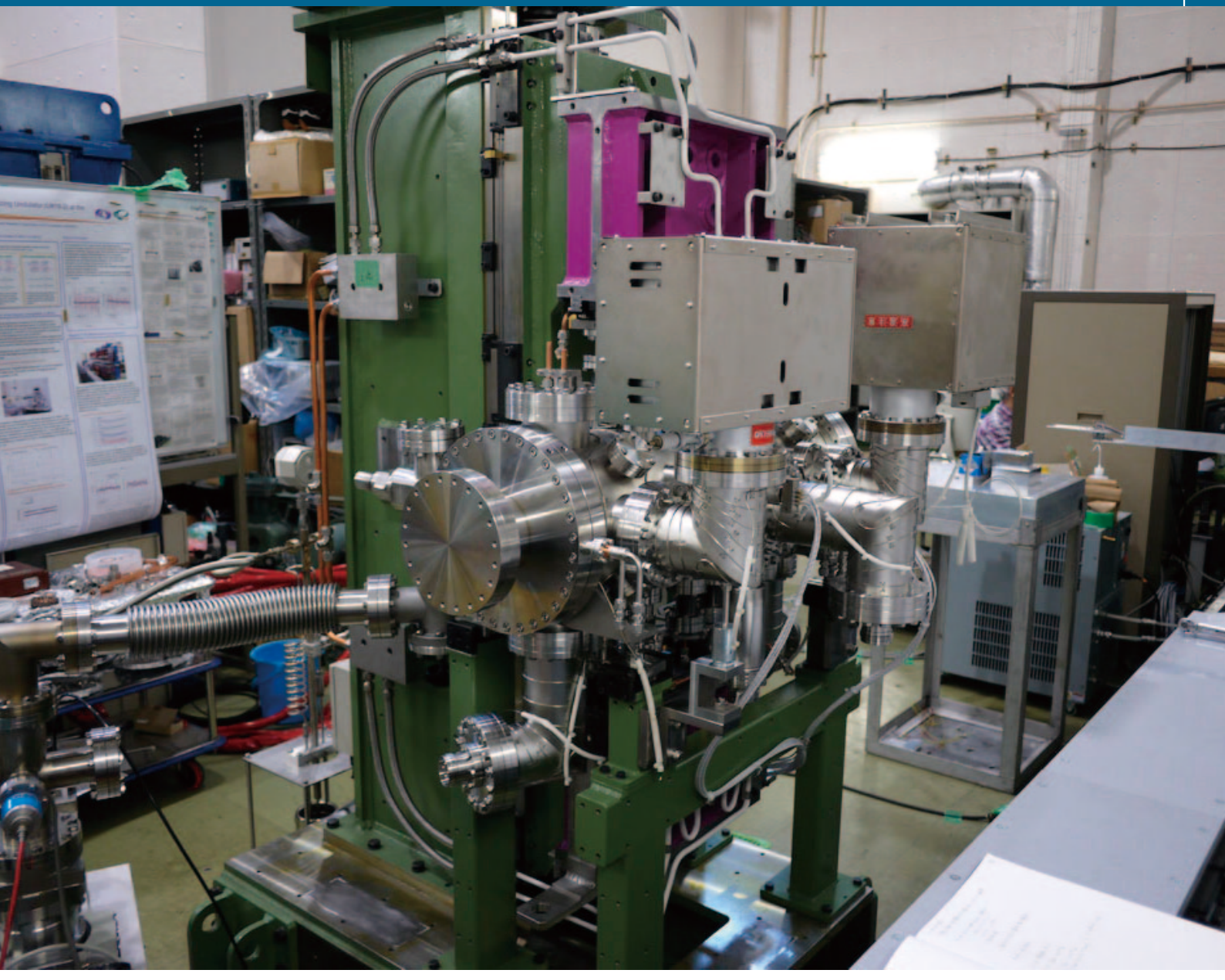

Accelerators

1 Outline of the Accelerators

Two electron storage rings, the PF ring and the PF-AR, as dedicated light sources were stably operated at the Photon Factory. The KEK linear accelerator with a maximum electron energy of 8 GeV is employed to inject an electron beam into the rings. The full energy injection of 2.5 GeV is carried out at the PF ring, while the injection energy of 3 GeV needs to be increased to the operation energy of 6.5 GeV at the PF-AR.

The machine parameters of the rings and the calculated spectral performances are listed in Table 1 and Table 2, respectively. The spectral distributions of synchrotron radiation (SR) from the bending magnets and the insertion devices are shown in Fig. 1.

Table 1: Principal beam parameters of the PF ring and PF-AR.

	PF	PF-AR
Energy	2.5 GeV	6.5 GeV
Natural emittance	34.6 nm rad	293 nm rad
Circumference	187 m	377 m
RF frequency	500.1 MHz	508.6 MHz
Bending radius	8.66 m	23.2 m
Energy loss per turn	0.4 MeV	6.66 MeV
Damping time		
Vertical	7.8 ms	2.5 ms
Longitudinal	3.9 ms	1.2 ms
Natural bunch length	10 mm	18.6 mm
Momentum compaction factor	0.00644	0.0129
Natural chromaticity		
Horizontal	−12.9	−14.3
Vertical	−17.3	−13.1
Stored current	450 mA	60 mA
Number of bunches	252	1
Beam lifetime	20-25 hrs (at 450 mA)	20-25 hrs (at 60 mA)

Table 2: Calculated spectral performances of the bend source and all the insertion devices at the PF ring (2.5 GeV, 450 mA) and the PF-AR (6.5 GeV, 60 mA). λ_u: period length, *N*: number of the periods, *L*: length of undulator or wiggler, $G_y(G_x)$: minimum vertical (horizontal) gap height, $B_y(B_x)$: maximum vertical (horizontal) magnetic field, Type of magnet, H: hybrid configuration, S.C.: super conducting magnet, σ_x,σ_y: horizontal or vertical beam size, σ_x',σ_y': horizontal or vertical beam divergence, $K_y(K_x)$: vertical (horizontal) deflection parameter, *D*: photon flux density (photons/sec/mrad^2/0.1%b.w.), *B*: brilliance (photons/sec/mm^2/mrad^2/0.1%b.w.), P_T: total radiated power. Different operating modes of undulator and wiggler are denoted by -U and -W, respectively.

Name	*E*/*I*	λ_u	*N*	*L*	$G_y(G_x)$	$B_y(B_x)$	Type of magnet	σ_x	σ_y	$\sigma_{x'}$	$\sigma_{y'}$	$K_y(K_x)$	$\varepsilon_1/\varepsilon_c$	*D*	*B*	P_T
	GeV/mA	cm		m	cm	T		mm	mm	mrad	mrad		keV			kW
PF	**2.5/450**															
Bend								0.41	0.059	0.178	0.012		4	5.38E+13	3.48E+14	
SGU#01		1.2	39	0.5	0.4	0.7	P(NdFeB)	0.6	0.012	0.088	0.029	0.78		4.56E+16	9.90E+17	0.4
U#02		6	60	3.6	2.8	0.4	H(NdFeB)	0.65	0.042	0.054	0.008	2.3		2.73E+17	1.55E+18	1.07
SGU#03		1.8	26	0.5	0.4	1	P(NdFeB)	0.6	0.012	0.088	0.029	1.68		2.50E+16	5.44E+17	0.82
MPW#05-W		12	21	2.5	2.64	1.4	H(NdFeB)	0.71	0.045	0.078	0.009	16	5.9	2.22E+15	1.10E+16	8.83
MPW#13-W		18	13	2.5	2.71	1.5	H(NdFeB)	0.74	0.02	0.094	0.019	25	6.2	1.45E+15	1.47E+16	9.73
MPW#13-U												2		1.70E+16	1.57E+17	0.06
VW#14					5	5	S.C.	0.53	0.045	0.128	0.008		20.8	5.42E+13	3.59E+14	
U#16-1 & 16-2		5.6	44	2.5	2.1	0.6(0.38)	P(NdFeB)	0.654	0.042	0.055	0.008	3(2)		1.03E+18	1.82E+17	0.88
SGU#17		1.6	29	0.5	0.4	0.92	P(NdFeB)	0.6	0.012	0.088	0.029	1.37		7.88E+15	1.71E+17	0.69
Revolver#19		5	46	3.6	2.8	0.28	H(NdFeB)	0.7	0.045	0.078	0.009	1.3		1.31E+17	6.48E+17	0.31
		7.2	32			0.4	H(NdFeB)					2.7		7.17E+16	3.52E+17	0.63
		10	23			0.54	H(NdFeB)					5		4.53E+16	2.22E+17	1.15
		16.4	14			0.62	P(NdFeB)					9.5		2.02E+16	9.81E+16	1.52
EMPW#28-U		16	12	1.92	3(11)		P(NdFeB)	0.53	0.045	0.127	0.008	3(3)		1.55E+16	1.00E+16	0.26
PF-AR	**6.5/60**															
Bend								1	0.2	0.593	0.036		26	3.90E+13	3.11E+13	
EMPW#NE1W		16	21	3.36	3(11)	1(0.2)	P(NdFeB)	1.07	1.07	0.268	0.032	15(3)	28(90%)	1.84E+15	2.54E+15	5.52
EMPW#NE1U												3(3)		4.09E+15	5.64E+15	0.42
U#NE3		4	90	3.6	1	0.8	P(NdFeB)	1.57	0.17	0.312	0.029	3		1.29E+16	7.66E+15	3.708
U#NW2		4	90	3.6	1	0.8	P(NdFeB)	1.57	0.17	0.312	0.029	3		1.29E+16	7.66E+15	3.708
U#NW12		4	95	3.8	1	0.8	P(NdFeB)	1.57	0.17	0.312	0.029	3		1.29E+16	7.66E+15	3.912
U#NW14-36		3.6	79	2.8	1	0.8	P(NdFeB)	1.35	0.14	0.338	0.036	2.8		7.69E+15	6.49E+15	3.12
U#NW14-20		2	75	1.5	0.8	0.63	P(NdFeB)	0.75	0.07	0.383	0.038	1.17		7.69E+15	6.49E+15	0.936

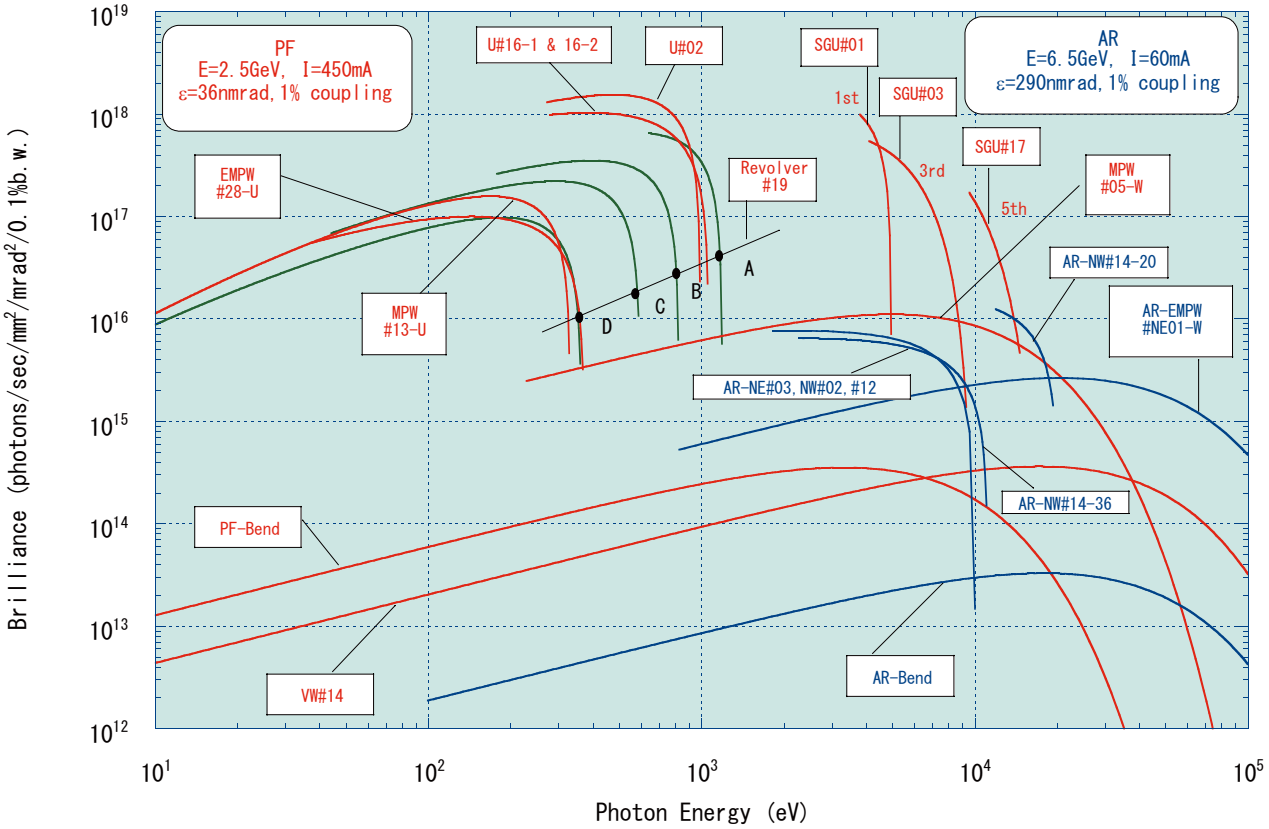

Figure 1: Synchrotron radiation spectra available at the PF Storage Ring (2.5 GeV) and the AF-AR (6.5 GeV). Brilliance of the radiation vs. photon energy are denoted by red curves for the insertion devices, SGU#01, U#02, SGU#03, MPW#05, MPW#13, VW#14, U#16-1 & 16-2, SGU#17, Revolver#19 and EMPW#28, and bending magnets(PF-Bend) at the PF Storage Ring. Blue curves denote those for the insertion devices, EMPW#NE01, U#NE03, U#NW02, U#NW12, U#NW14-36 and U#NW14-20, and the bending magnets (AR-Bend) at the PF-AR. The name of each source is assigned in Table 2. Several insertion devices have both undulator and wiggler modes, which are denoted by u and W, respectively (the undulator mode of MPW#05 and AR-EMPW#NE01 is not shown). The spectral curve of each undulator (or undulator mode of multipole wiggler) is a locus of the peak of the first harmonic within the allowance range of K parameter. For SGU#01, SGU#03 and SGU#17, spectra are shown for the first, third and fifth harmonic regions. Spectra of Revolver#19 are shown for four kinds of period.

2 PF Ring

2-1 Operation Summary

In FY2012, PF ring and PF-AR operated stably following several problems caused by the aftereffects of the Tohoku Earthquake. The timetable of operations at the PF ring and PF-AR in FY2012 is shown in Fig. 1.

The operational statistics for the PF ring are summarized in Table 1. The statistics for each fiscal year since the commencement of operation of the accelerator are shown in Fig. 2. In FY2012, the total operation time and actual user time were 4416.0 hrs and 3752.9 hrs, respectively. The actual user operation time was less than 4000 hrs because it was difficult to preserve the total operation time due to an increase in electricity rates, among other factors. The failure time for this year was 39.1 hrs, which is shown as a percentage of the total operation time in Fig. 3. This failure time includes that caused by the aftereffects of the earthquake, such as problems with the rf high-voltage power supplies and the leakage of cooling water from circulators, as shown in Fig. 4. Both of these problems were resolved during the summer shutdown. In the PF ring, a top-up operation mode with an injection scheme that uses a single pulsed sextupole magnet was established. The beam current was usually maintained at 450.0 ± 0.1 mA, which corresponds to a current accuracy of $\pm 1 \times 10^{-4}$ at an injection repetition frequency of 1.0 Hz. User operation of the hybrid mode was also established using a single-bunch current of 50 mA and a multi-bunch current of 350 mA. In addition, the variably polarized undulator demonstrated smooth operation at a switching frequency of 10 Hz.

Table 1: Operation statistics for PF ring in FY2012.

	Total
Ring operation time (hrs)	4416.0
Actual user time (hrs)	3752.9
Machine adjustment time (hrs)	624.0
Failure time (hrs)	39.1

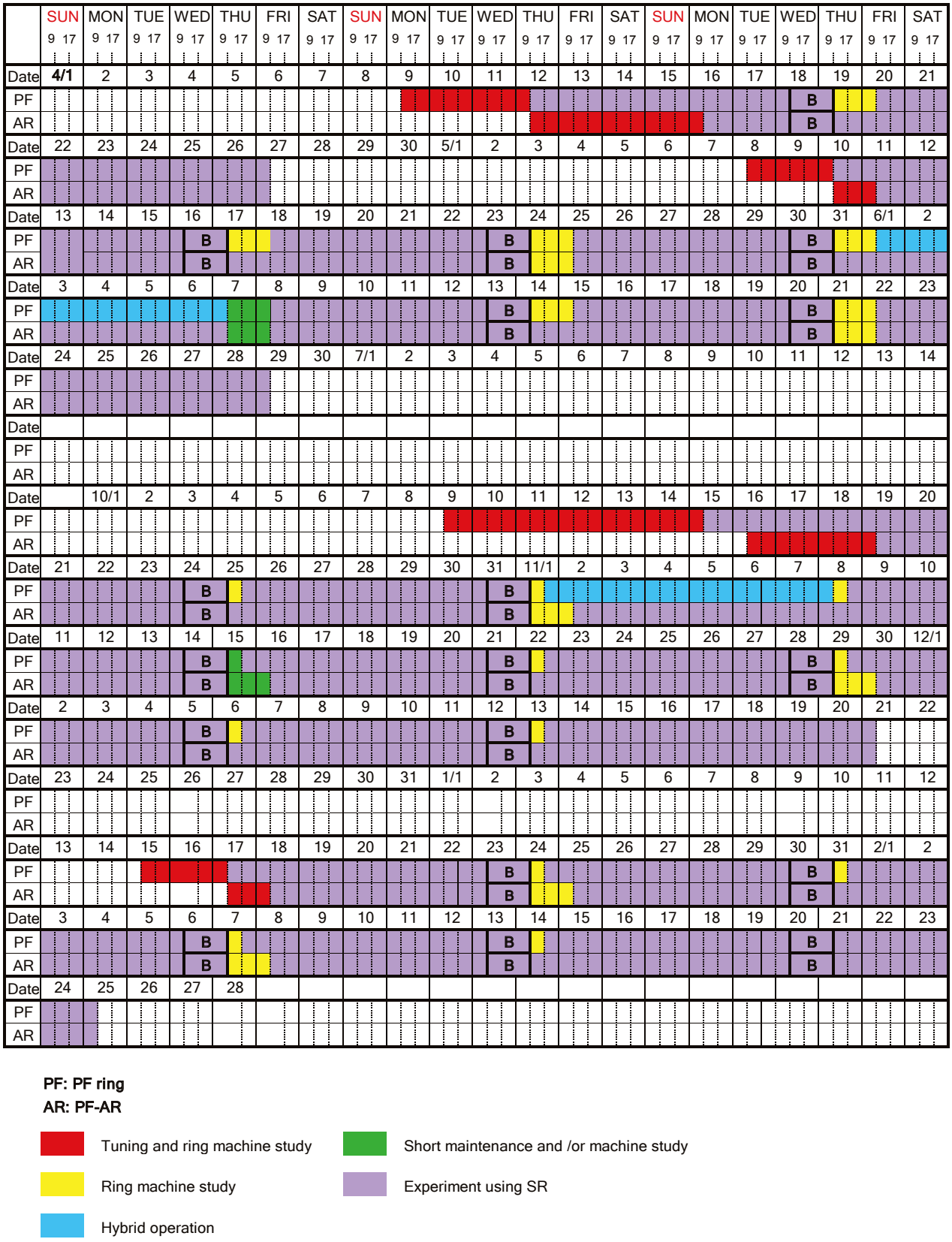

PF: PF ring
AR: PF-AR

Tuning and ring machine study

Short maintenance and /or machine study

Ring machine study

Experiment using SR

Hybrid operation

Figure 1: Timetable of PF ring and PF-AR operation in FY2012.

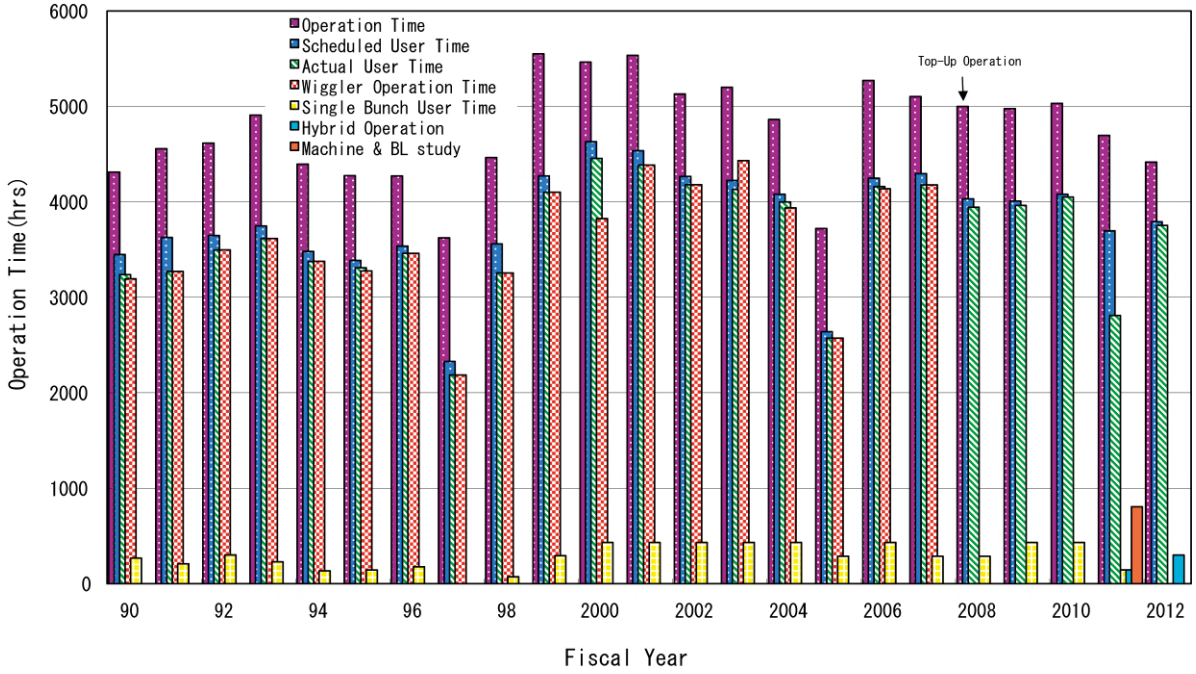

Figure 2: Total operation time, scheduled user time, actual user time, and single-bunch user time for PF ring in each fiscal year since the commencement of accelerator operation.

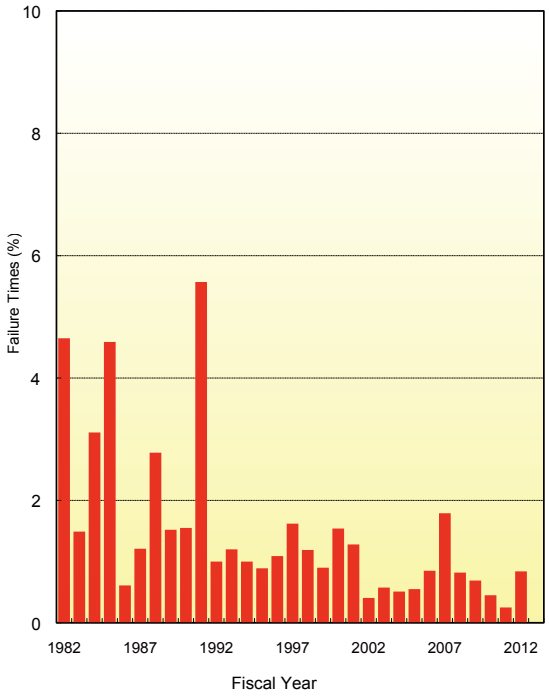

Figure 3: Failure rate for PF ring (percentage of failure time with respect to total operation time).

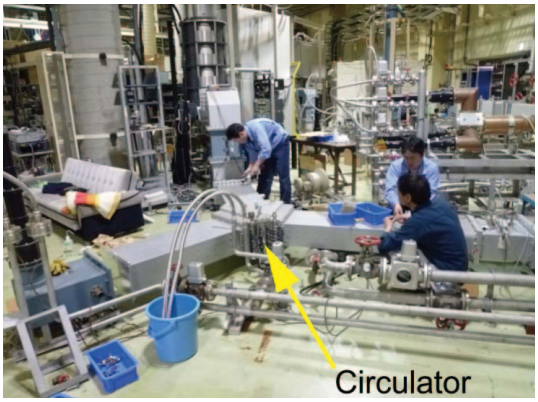

Figure 4: Photograph showing the replacement of the circulator that experienced leakage of cooling water.

2-2 Project to Renew the Insertion Devices at the PF Ring

2-2-1. Construction of a New Short Gap Undulator (SGU#15)

A new short gap undulator (SGU), named SGU#15, is being constructed at the PF ring. This is the fourth SGU and will be installed in the last remaining 1.4 m straight section of the PF ring. SGU#15 is designed as a light source for both small-angle X-ray experiments and XAFS experiments. It has a period length of 17.6 mm and the number of periods is 27. The photon energy region of SGU#15 ranges from 2 keV to 15 keV using the higher harmonics of undulator radiation. One requirement for the magnetic field is that the phase error should be less than 2 degrees in order to use the 9th higher harmonics effectively. To satisfy this requirement, the magnetic field of SGU#15 was carefully adjusted in the autumn of 2012. Figure 5 shows a photograph of SGU#15 during the magnetic measurements, and Fig. 6 summarizes the results of the magnetic field adjustment. The latter figure shows the electron orbits at several typical gaps, which were calculated based on measured magnetic data. The standard deviation of the phase errors was 1.8 degrees at the minimum gap of 4 mm.

We will install SGU#15 in the PF ring in the summer of 2013 after vacuum commissioning, and it will enter operation for user experiments during the autumn operation of the PF ring.

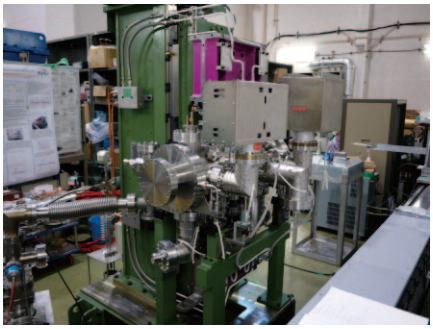

Figure5: SGU#15 during the magnetic measurements.

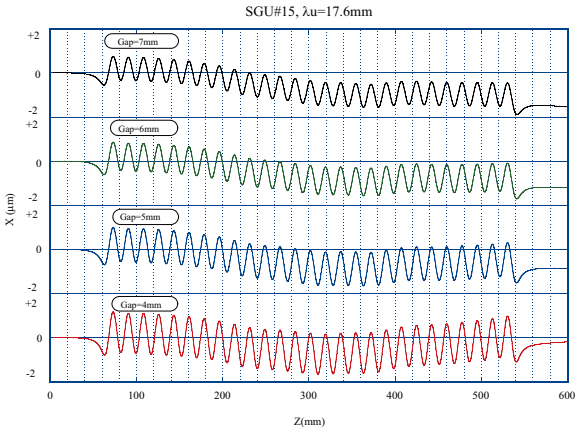

Figure 6: Calculated electron orbits for several typical gaps.

2-2-2. Project to Renew the Undulators for the VUV-SX Beamlines

At the PF ring, we are constructing three new undulators for BL02, BL13 and BL28, which will be called U#02-2, U#13 and U#28, respectively. All these undulators are designed as elliptically polarizing undulators (EPUs) to obtain various polarization states, not only circular (left-handed and right-handed) polarization but also linear (horizontal and vertical) polarization.

The detailed parameters and magnetic configurations of these undulators were determined by the summer of 2012. The mechanical design and construction of the undulators are now progressing steadily. Table 2 summarizes the basic parameters of the new undulators.

For BL02, we plan to move the existing undulator (U#02) to the downstream of the B01-B02 straight section, and install a new undulator (U#02-2) tandem at the upstream of U#02. Figure 7 shows a schematic view of the B01-02 straight section before and after the reconstruction.

We will use U#02 and U#02-2 exclusively to obtain photons over a wide energy region at the single beamline. The photon energy region of U#02 ranges from 400 eV to 2 keV and the target energy region of U#02-2 is from 15 eV to 300 eV with the first harmonic radiation of EPU. The period lengths of U#02 and U#02-2 are 60 mm and 160 mm, respectively.

We renewed the present undulators for BL13 and BL28 to utilize the extended straight section as much as possible. U#13 has a period length of 76 mm and its target photon energy region is from 50 eV to 1.5 keV under various polarization states. U#28 has the same parameters as U#02-2 except the total length.

The magnetic adjustment of U#02-2 is scheduled to be conducted in the winter of 2013 and we will install U#02-2 in the PF ring in March 2014. For U#13 and U#28, we will adjust the magnetic fields continuously in the spring of 2014. The installation of U#13 and U#28 in the PF ring will be carried out at the same time during the summer shutdown of the ring in 2014.

Table 2: Basic parameters of the new undulators in the PF ring.

Name	Period length (mm)	Number of periods	Length (m)	Maximum Bx, By (T)	Target photon energy region (eV)	Type of undulator
U#02-2	160	17	2.72	0.33, 0.33	30-300	EPU
U#13	76	48	3.65	0.68, 0.34	50-1500	EPU
U#28	160	22	3.52	0.33, 0.33	30-300	EPU

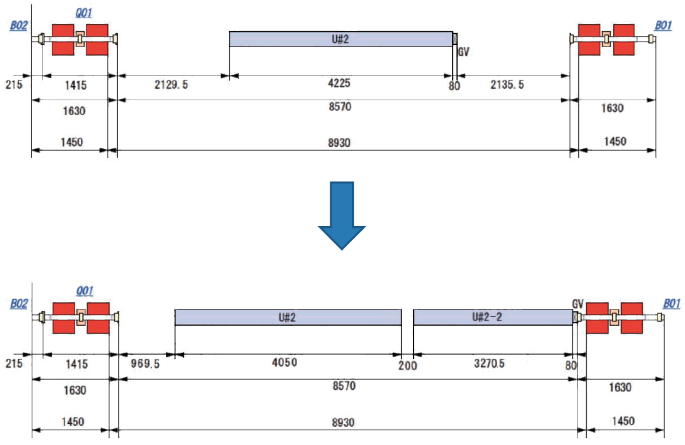

Figure 7: Schematic view of the B01-02 straight section before and after the reconstruction.

3 PF-AR

3-1 Operation Summary

The full history of the total operation time of the PF-AR is shown in Fig. 1, and the operation statistics of recent six years are summarized in table 1. In FY2012, the scheduled user time was recovered to 3672 hrs and its ratio to the total operation time reached 90 % though it decreased temporarily to about 70 % in FY2011 under the influence of the Great East Japan Earthquake. We could operate the PF-AR storage ring without a serious aftereffect of the earthquake in FY 2012. Both the failure rate and the mean time between failures (MTBF) of the user time recorded the best values in these six years.

The sources of troubles are summarized in table 2. In the previous fiscal year, the outstanding faults other than the earthquake were the magnet (power supply) and the dust trapping.

There are a large number of aged magnet power supplies using since 1980s. So renewal of the aged power supplies continues year by year. The power supplies of the sextupoles were updated in FY2011, and most of the aged quadrupole power supplies of will be updated in FY2013. So the operation of the magnet power supplies is expected to be stable.

In FY2012, we continued the operation with a vacuum problem through the year. The heating up was occurred at the stripline kicker of the transverse feedback system. Abnormal pressure rises were frequently observed during the beam injection or at the maximum beam current. As a symptomatic therapy of this problem, we have reduced the stored current from 60 mA to 55 mA. The abnormal pressure rise was almost controlled by reducing the stored current. It was thought that the reduction of the stored current caused a large decrease of the dust trapping which is the most frequent failure of the PF-AR, and the stripline itself might be one of the sources of micro dusts.

Construction of the direct beam transport (BT) line for the PF-AR has been approved and the design of the new BT tunnel was decided as shown in Fig. 2. The construction of the tunnel will be completed by the end of FY2013. The new BT line can pass 6.5-GeV electron, so the full-energy injection is enabled for the PF-AR. By using additional pulse bending magnets installed in the 3rd switch yard of the LINAC, the continuous injection of the PF-AR will be realized simultaneously with the other three storage rings, two KEKB main rings and PF ring. The installation of the accelerator components of the BT line and the reconstruction of the storage ring to make a new injection part will be accomplished in 2015 in parallel with the commissioning of the Super KEK B factory started from January 2015.

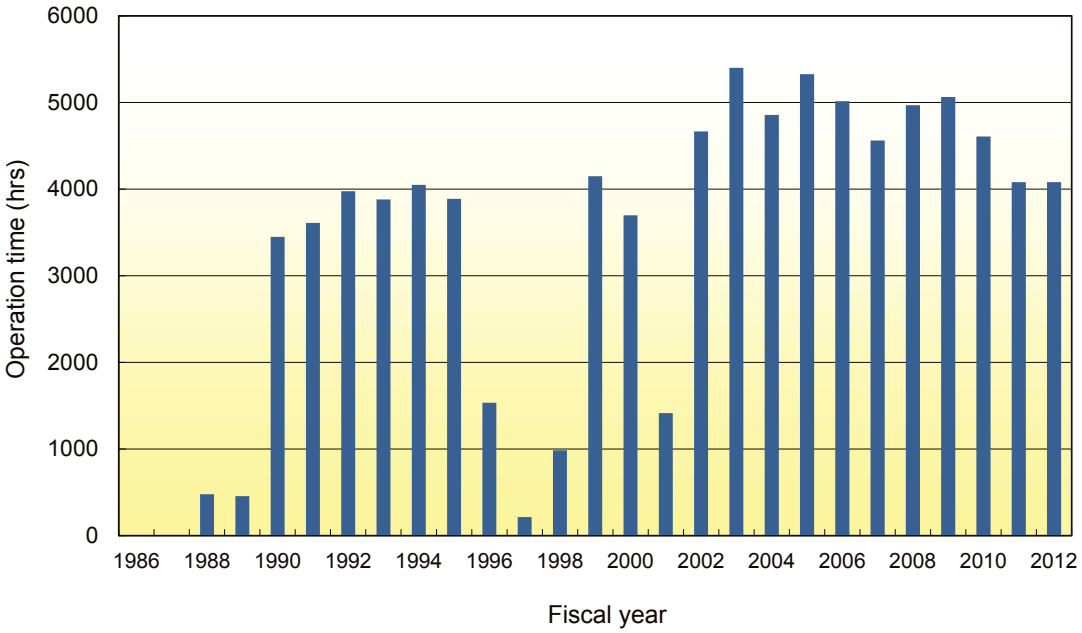

Figure 1: Operation time as a function of fiscal year.

Table 1: Operation statistics and the mean time between failures (MTBF) during FY2005 – FY2012.

Fiscal Year	2005	2006	2007	2008	2009	2010	2011	2012
Total operation time (h)	5313	5016	4561	4969	5063	4608	4080	4080
Scheduled user time (h)	4456	4032	3624	4344	4392	4032	2904	3672
Ratio of the user time (%)	83.9	80.4	79.5	87.4	86.7	87.5	71.2	90.0
No. of failures	79	51	60	40	41	74	49	33
Total down time (h)	69.3	55.1	45.2	41.7	91.0	73.7	38.7	29.7
Failure rate (%)	1.6	1.4	1.2	1.0	2.1	1.8	1.3	0.8
MTBF (h)	56.4	79.1	60.4	108.6	107.1	54.5	59.3	111.3
Mean down time (h)	0.9	1.1	0.8	1.0	2.2	1.0	0.8	0.9

Table 2: Classification of failures based on the source of trouble.

Fiscal Year	2005	2006	2007	2008	2009	2010	2011	2012
RF	12	10	1	4	8	10	5	4
Magnet	4	1	1	2	2	10	8	3
Injection	4	3	8	9	1	6	4	3
Vacuum	2	6	2	0	2	1	0	1
Dust trapping	37	24	39	15	16	24	20	13
Insertion Devices	0	1	0	0	0	0	0	0
Control/ Monitor	4	0	1	1	1	2	1	2
Cooling water	5	1	0	3	4	4	1	0
Safety/ Beamline	9	4	5	5	7	17	3	4
Earthquake	2	0	1	0	0	0	5	3
Electricity	0	1	2	1	0	0	2	0
Total	79	51	60	40	41	74	49	33

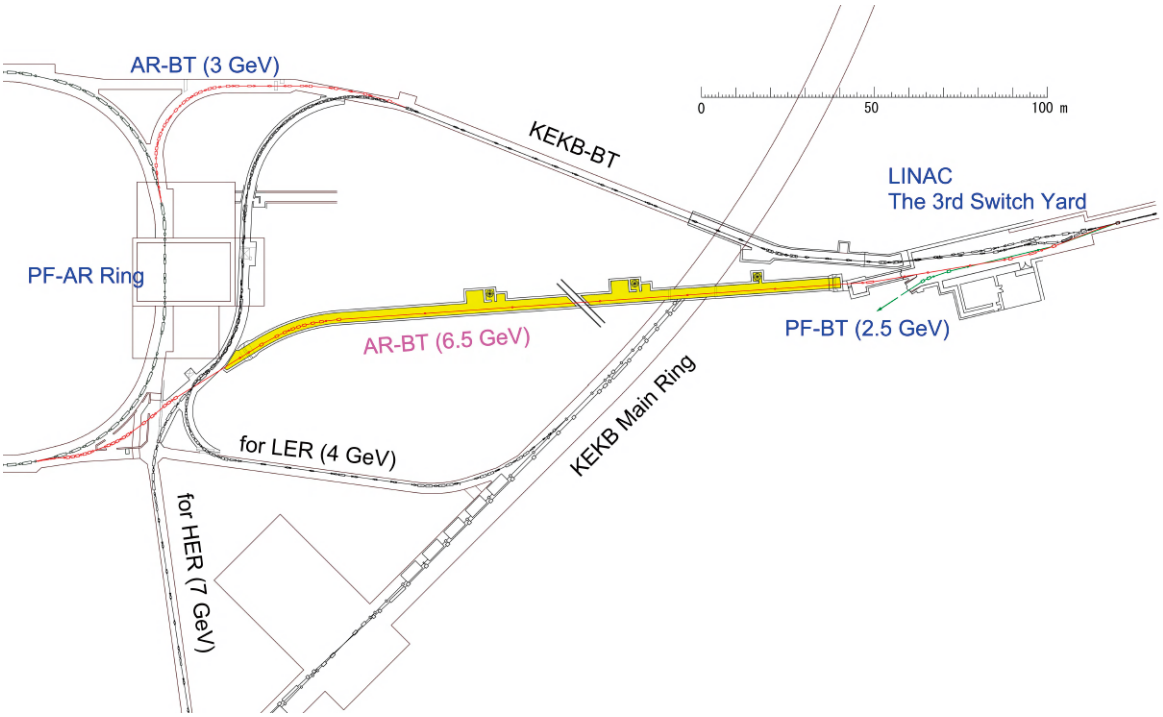

Figure 2: Construction of the 6.5-GeV beam transport line from the LINAC to the PF-AR ring.

Future Light Source

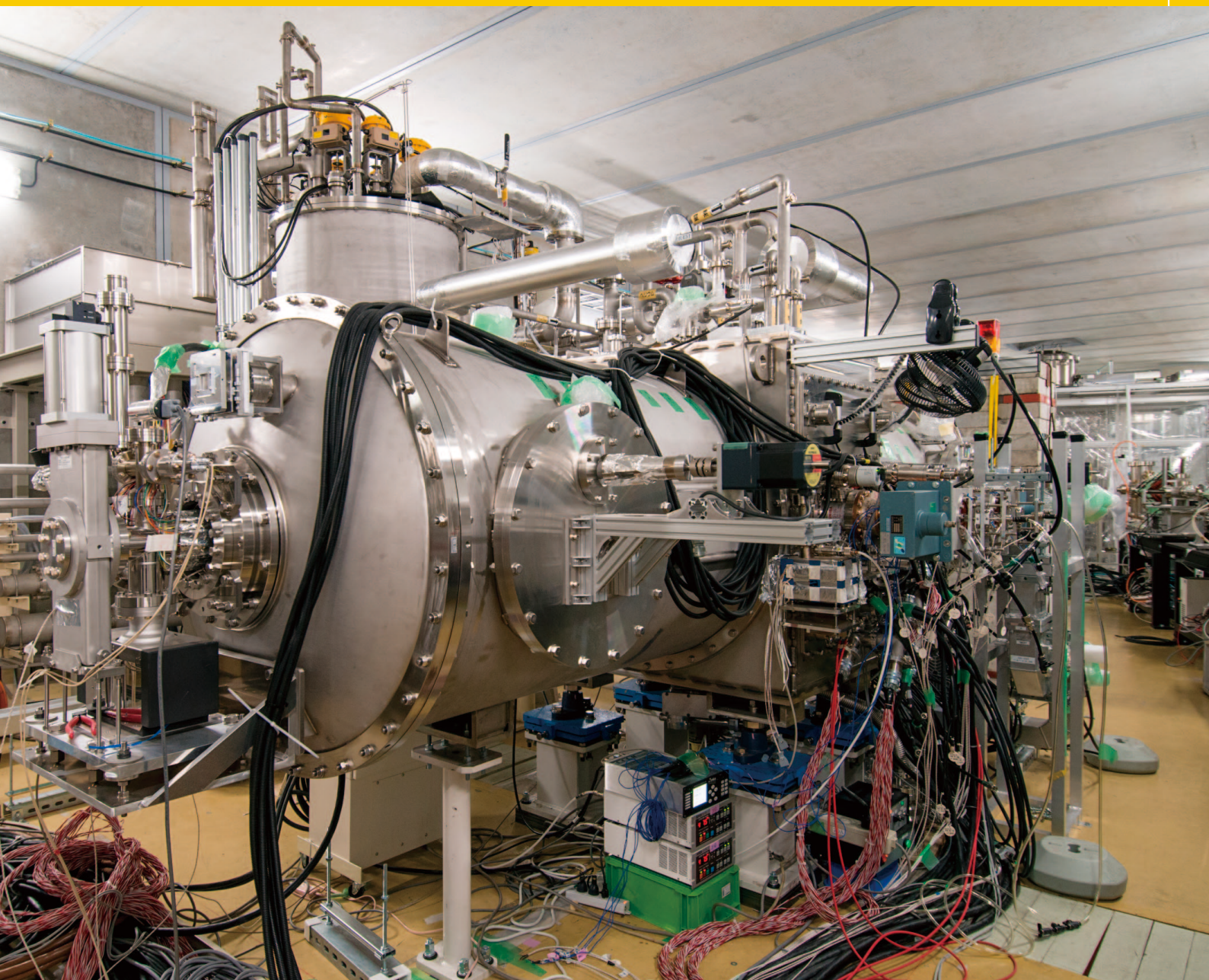

Future Light Source

1 ERL Project Overview

The energy recovery linac (ERL) is a future X-ray light source designed on the basis of state-of-the-art superconducting linear accelerator technology, which will offer significantly better performance than existing storage ring technologies. The high repetition rate, short pulse, high spatial coherence, and high brightness of ERL will enable the filming of ultrafast atomic-scale movies as well as the determination of the structure of nanoscale heterogeneous systems. These unique capabilities of the ERL will drive a distinct paradigm shift in X-ray science, from the study of "static and homogeneous" systems to "dynamic and heterogeneous" systems; in other words, from the study of "time- and space-averaged" analysis to "time- and space-resolved" analysis.

This paradigm shift will make it possible to directly observe the behavior of heterogeneous functional materials in real time and space. It will also enable predictions to be made for the design and innovation of better functional materials. These advances will contribute to solving the grand challenges of society and will support life in the future. Such functional materials will continue to be used in indispensable technological tools such as catalysts, batteries, superconductors, biofuels, random access memories, spintronic devices, and photoswitches. Life itself is an intrinsically heterogeneous and dynamic system; structural biology based on existing storage ring technology has greatly contributed to rational drug design by providing the static atomic coordinates of proteins. The ERL will further contribute to biological science and biotechnology by shedding light on the heterogeneity and complexity of cellular functions.

In short, the ERL will be an unprecedented tool that will bridge critical gaps in our understanding of material science and technology.

In addition, the continuous improvement of linear accelerator technology will result in significant advances in X-ray science in the future. One possibility is the realization of a fully coherent X-ray free-electron laser. Although self-amplified spontaneous emission X-ray free-electron lasers (SASE-XFELs) have been constructed, the X-ray beam from a SASE-XFEL is not fully coherent in the temporal domain. It is proposed that the unprecedented electron beam quality of the ERL will make an X-ray free-electron laser oscillator (XFEL-O) feasible when used with a Bragg diamond cavity configured for lasing in the X-ray region. The construction of an XFEL-O is scheduled to take place during the second phase of the ERL project.

KEK established the ERL Project Office in April 2006. Because a GeV-class ERL machine had not been constructed anywhere in the world, it was necessary to first construct a compact ERL (cERL) with energy of 35 MeV that could be used for the development of several critical accelerator components such as a high-brilliance DC photocathode electron gun and superconducting cavities for the injector and main accelerator. In the 2012 fiscal year, such main accelerator components were successfully installed in an ERL test facility; performance of these could be checked by the end of the 2012 fiscal year.

We published the "Conceptual Design Report for 3-GeV ERL" at the 2nd ERL symposium (http://pfwww.kek.jp/ERLoffice/detabase/ERL%20CDR_0807.pdf). We organized an International Advisory Committee (IAC) to evaluate our 3-GeV ERL project according to the Conceptual Design Report and provide critical comments on the project. The members of the committee were as follows: Ingolf Lindau (Chair) from Stanford Univ., Thomas Tschentscher from Euro XFEL, Kwang-Je Kim from APS, Zhao Zhentang from SSRF, Junichiro Mizuki from Kwansei Gakuin Univ., Masahiro

Figure1: Group photo of the International Advisory committee for 3-GeVERL project.

Kato from UVSOR, and Alfred Baron from Riken. Unfortunately, Dr. Thomas Tschentscher could not attend the IAC. Figure 1 shows a group photo of the committee members, presenters, and directorates of the ERL project. A summary of the IAC meeting is available at the web site [1]. In particular, we asked the IAC members to give us critical comments for the following four questions.

1) Question 1 – Are the scope and strategies of the 3-GeV ERL project including the further upgrade of XFEL-O satisfactory as the future light source in KEK?

2) Question 2 – The Science Case for the 3-GeV ERL project

A. Is the scope of the science case of the 3-GeV ERL reasonable and also satisfactory?

B. Is the effort to brush up the science case enough?

C. Further recommendation for this item

3) Question 3 – Development for accelerator technologies

A. Is the technical development for the accelerator components for the cERL sufficient?

B. Is there anything to check the technical problem in cERL before construction of the 3-GeV ERL?

4) Question 4 – Construction of 3-GeV ERL

A. Is the construction of the 3-GeV ERL feasible under the R&D planning of accelerator development?

B. Further recommendations for this item

For Question 1, the IAC gave us positive comments; for example: *"The ERL, with the XFEL-O, is a logical step in the development of next generation accelerator-based photon sources. It will have unprecedented characteristics, and will be complementary to high-gain FELs and ultimate storage rings. Going far beyond present state-of-the-art, and ERL will open up major new research areas. The ERL is therefore an exceedingly strong and logical candidate as a future light source at KEK."* For Question 2, the IAC mentioned that *"the scientific case for a 3-GeV ERL is mature and is solidly anchored in both the Japanese and the international scientific community. The Preliminary Conceptual Design Report has an impressive expose of the breadth of novel scientific opportunities an ERL source offers."* Also, the IAC recommended that *"PF/ERL-team play an active role in promoting the evolution of the scientific case with workshops, symposia, etc. and also the ERL team should continue to pursue further advanced capabilities, such as sub-femtosecond pulse generation via echo-enhanced harmonic generation, and fold these into the scientific case."* For Question 3, *"the IAC was very impressed by the advanced status and the rapid progress of the cERL project."* The committee also mentioned that *"the strategy to construct the cERL as a precursor to the 3-GeV ERL is critical since the cERL has the main technology components required for the 3-GeV ERL."* For Question 4, we presented that the cERL was expected to be operational and commissioned at the end of 2012 and that the experience from this endeavor would be the basis for a design plan scheduled to be largely finalized in 2014. *"The IAC fully supports this approach".* Also, The IAC stressed the importance that *"this plan must be scrutinized by outside review committees with appropriate technical background."* The IAC also fully supported the fact that *"a continuous R&D effort of the gun/laser is necessary and in parallel with the ERL construction, extending into the commissioning/operational phase."* The IAC mentioned that *"the proposed construction time, with completion of the 3-GeV ERL in 2021, is timely and feasible, given sufficient resources."* The IAC recommended that *"a careful study is done to make sure that the chosen layout is optimal, with particular care that there is enough space for future expansion."* A complete and detailed of the summary of the IAC's comments can be found online at the URL mentioned above.

Figure 2: Logo of ERL project, designed on the basis of the logo of the Photon Factory and the motif of a pearl.

After the IAC meeting, the *"Energy Recovery Linac Conceptual Design Report"* was partially revised and finalized as the KEK report and opened on a website [2].

In March 2013, the nickname and logo of our ERL project were settled and opened at the Photon Factory Symposium. The nickname was PEARL (Photon Factory ERL Advanced Research Laboratory) and the logo is shown in Fig. 2. The nickname PEARL inherits the name of the Photon Factory as well as research centers with a synchrotron radiation facility. In addition, the pearl is a gem popular in the traditional technology of Japan, and it emits the brightness of the seven colors. These features characterize the pearl as a symbol of science and the radiation accelerator technology to be produced by the ERL project. The logo design was developed from the logo of the Photon Factory as well as the motif of a pearl.

REFERENCES

[1] http://pfwww.kek.jp/ERLoffice/detabase/ERL_AC/ERL_iac3gev/index.html

[2] "Energy Recovery Linac Conceptual Design Report", *KEK Report* 2012-**4**, http://ccdb5fs.kek.jp/tiff/2012/1224/1224004.pdf

2 3-GeV ERL Design

The future ERL-based light source consists of a 3-GeV ERL and an XFEL-O. A conceptual view of the project and the target parameters are given in Ref. [1]. The 3-GeV ERL provides super-bright and/or ultra-short synchrotron radiation (SR) in the vacuum ultra-violet (VUV) to hard X-ray range, and the XFEL-O provides fully coherent radiation. In XFEL-O operation, an electron beam is accelerated twice by the superconducting main linac of the ERL without energy recovery and transported to the XFEL-O after acceleration up to 6 – 7 GeV.

Figure 1 shows the preliminary result of the optical functions for the main linac and the return loop of the 3-GeV ERL. In the design, the injection energy is assumed to be 10 MeV. The main linac consists of more than 200 super-conducting (SC) 9-cell cavities, each of which has a moderate accelerating field of less than 15 MV/m to suppress field-emitted electrons causing beam halo and radiation hazards. Quadrupole triplets are placed at every eighth SC cavity for horizontal and vertical focusing. The optics of the main linac is mirror-symmetric for acceleration and deceleration and designed so that the betatron function is well suppressed for achieving a high BBU (beam breakup) threshold current. The return loop of the 3-GeV ERL has 28 TBA (Triple Bend Achromat) cells with 22 × 6-m and 6 × 30-m long straight sections for insertion devices. The bending radius of the bending magnet is sufficiently long and as a result the increase in emittance growth and energy spread due to incoherent SR are negligibly small for both ERL and XFEL-O modes. A bunch compression scheme for generating ultra-short SR pulses and a path-length control system for switching from ERL to X-FELO operational modes should be studied and added. Figure 2 shows the tentative layout of the ERL-based light source on the KEK Tsukuba campus.

Figure 3 shows examples of the calculated spectral brightness for VUV-SX (soft X-ray) and X-ray undulators. As shown in this figure, the 3-GeV ERL can provide undulator radiation with maximum spectral brightness of 10^{22} – 10^{23} phs/s/mm^2/mrad^2/0.1%b.w. The 6-7 GeV XFEL-O generates spatially and temporally coherent X-rays with brightness greater than 10^{26} phs/s/mm^2/mrad^2/0.1%b.w. For future development, a 300-m long straight section is reserved in the middle of the return loop. This section has major potential for (1) EEHG (Echo-Enabled Harmonic Generation) including attosecond pulse generation, (2) 3-GeV XFEL-O using the higher harmonics, and (3) a very long undulator with spectral brightness up to 10^{23} – 10^{24} phs/s/mm2/mrad2/0.1%b.w.

REFERENCE

[1] "Energy Recovery Linac Conceptual Design Report", KEK Report 2012-14, http://ccdb5fs.kek.jp/tiff/2012/1224/1224004.pdf

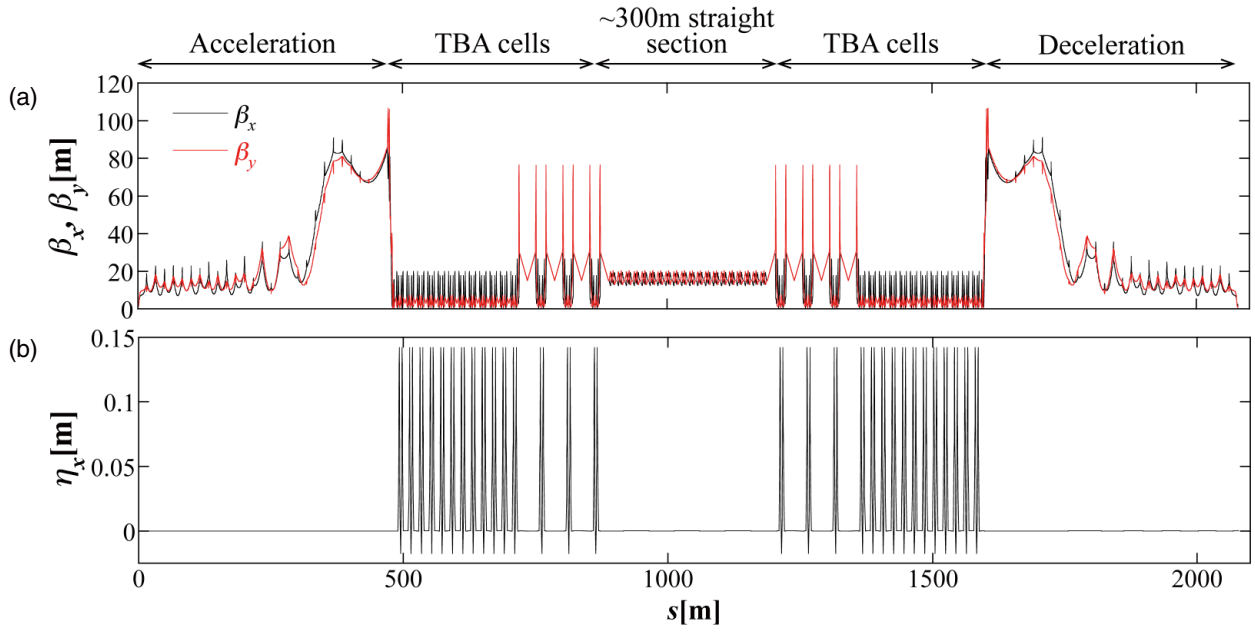

Figure 1: Betatron (a) and dispersion (b) functions of the main linac and the return loop for the 3-GeV ERL.

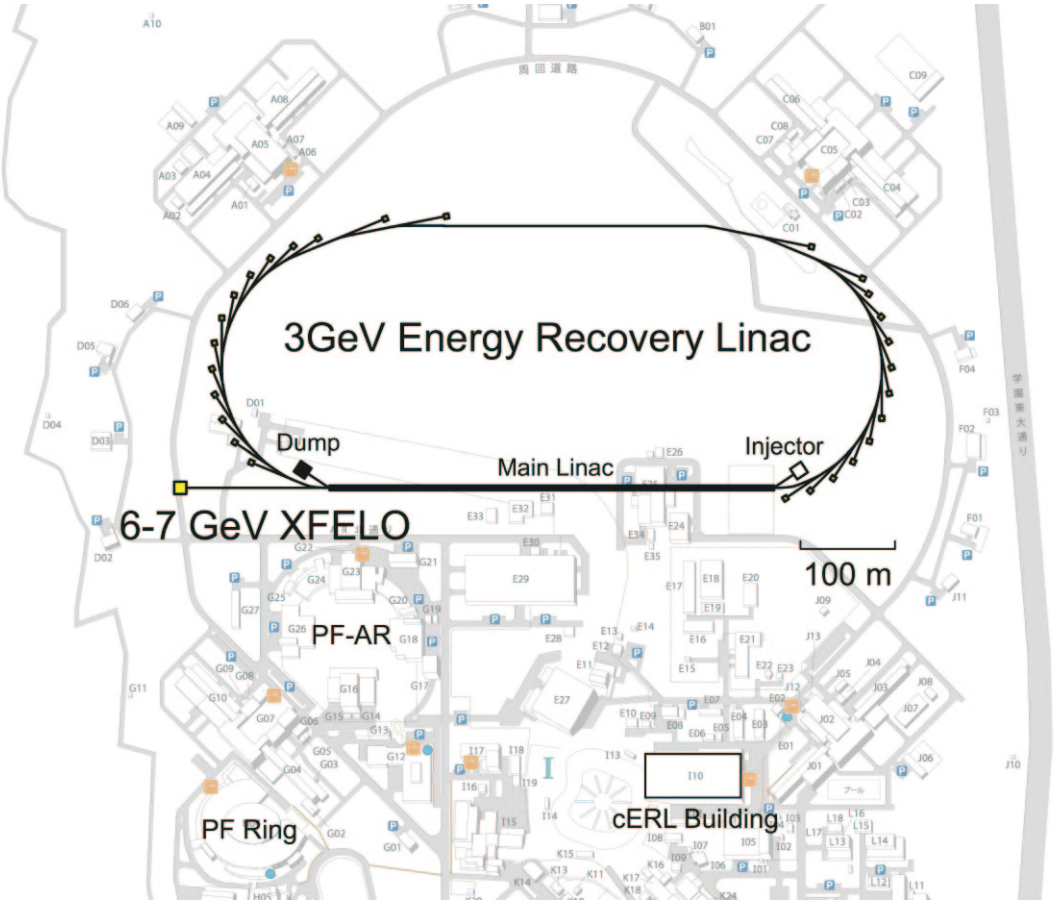

Figure 2: Tentative layout of the ERL-based light source at KEK Tsukuba campus.

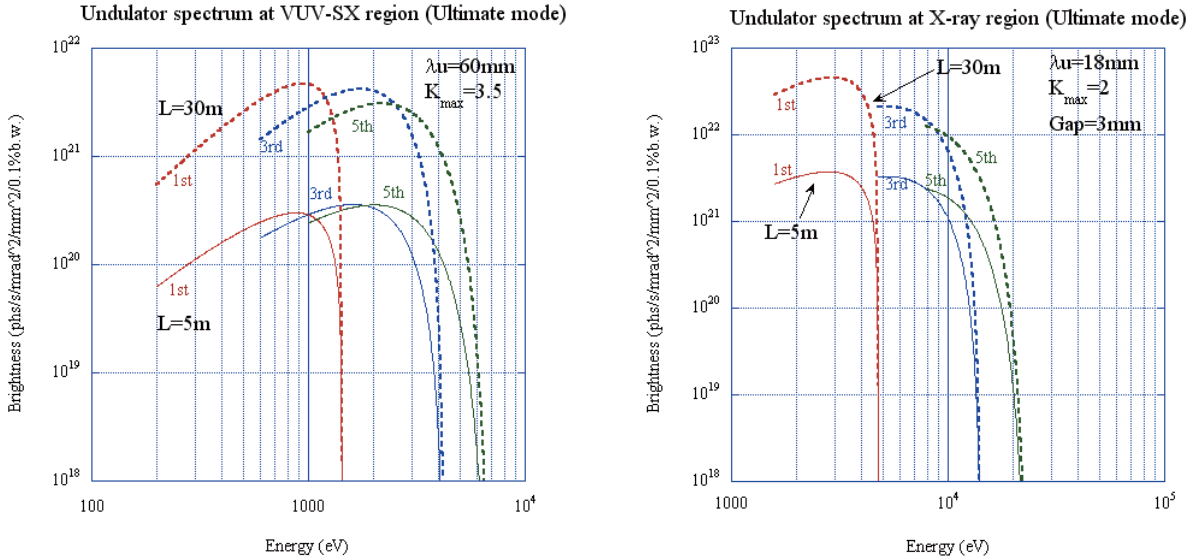

Figure 3: Examples of calculated spectral brightness for VUV-SX and X-ray undulators

3 cERL

3-1 cERL Overview

As described before, the aim of the cERL in the R&D program includes the development of critical components for the ERL, as well as the construction of a test accelerator. The design parameters of the cERL are shown in Table 1. In 2012, we could complete the construction of the radiation shielding to cover accelerator components for the cERL, as shown in Fig. 1. The key accelerator components, such as a photocathode DC electron gun, super conducting cavities for the injector and main linac, and an evaluation beamline for the injector electron beam, were successfully installed in the radiation shielding. An RF power test for each super conducting cavity was also completed by the end of the 2012 fiscal year, and the interlock systems for beam operation at the injector part were also completed. Beam operation of the injector part will start in April 2013.

Table 1: The design parameters of the cERL.

Parameter	Value
Beam energy (injector) (return loop)	5 MeV 35 MeV
Beam current (initial goal) (future goal)	10 mA 100 mA
Normalized beam emittance	< 1 mm·mrad (at 77 pC/bunch)
RMS bunch length (usual) (with compression)	1–3 ps < 150 fs
RF frequency	1.3 GHz

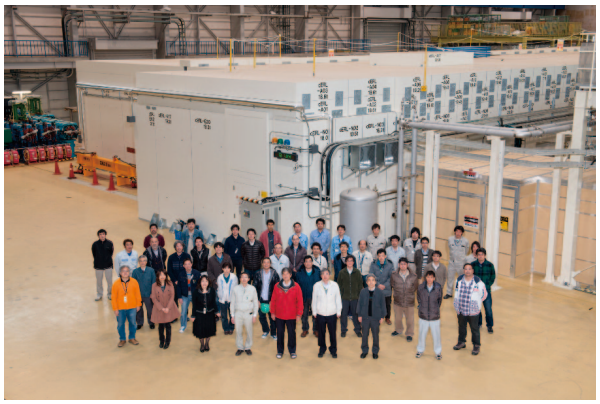

Figure 1: ERL project members in front of radiation shield for cERL.

3-2 High-brightness DC Photocathode Gun and Gun Test Beamline

A collaboration team, including the staff of Japan Atomic Energy Agency (JAEA), KEK, Hiroshima University, and Nagoya University, has developed a 500-kV DC photocathode gun to produce small-emittance electron beams with high average current. Their outstanding achievements included successful application of a high DC voltage up to 510 kV, as well as the production of an electron beam of 1.8 mA with applied voltage of 500 kV as show in Fig. 2 [1]. These achievements were done in the laboratory at the JAEA Tokai site. After confirming these performances, the DC gun has been installed in the cERL and is ready for operation. Beam characterization is important in evaluating the performance of the injector accelerator. Several components for the characterization beamline have been developed at the gun test facility, which is located in the PF-AR south experimental hall. The beamline has also been installed in the cERL by using components from the PF-AR south experimental hall. Figure 8 shows the injector part of the cERL with a 500-kV DC electron gun and super conducting cavity for the injector.

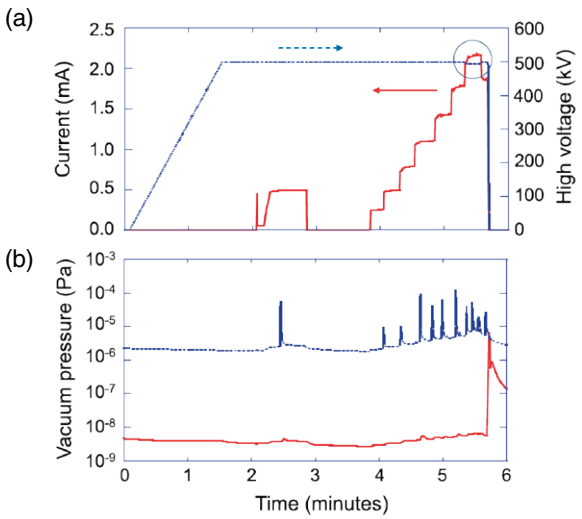

Figure 2: (a) Beam current (red solid line) and gun high voltage (blue dotted line) as a function of time. As shown the figure, 1.8mA with 500kV can be demonstrated.
(b) Vacuum pressures of gun (red solid line and beam dump (blue dotted line), respectively (after ref.[1]).

Figure 3: Photograph of the injector part of the cERL with 500-kV DC electron gun and super conducting cavity for injector.

3-3 SC Cavities for the Injector

An injector for the cERL is required to accelerate continuous-wave (CW) electron beams of 10 mA from 500 keV to 5 MeV of beam energy. The injector cryomodule contains three 2-cell cavities equipped with two input couplers and five HOM couplers. In order to qualify the cavity performance, vertical tests of the three 2-cell cavities were conducted at KEK-STF (Superconducting RF Test Facility). The three 2-cell cavities attached to new types of RF feedthroughs achieved an accelerating gradient higher than 20 MV/m, which exceeds the operating gradient as a cERL injector. After this, the 2-cell cavities were sent back to a company for welding with a He jacket made of titanium. RF conditioning of six input couplers was performed with a high power RF source of CW-300 kW. The conditioning was carefully carried out up to 200 kW in a short pulsed operation with a duty of less than 1 % and 30 – 40 kW in a CW operation.

Assembly of the injector cryomodule began in April 2012. All components, including input couplers, beam tubes, RF feedthroughs, and vacuum parts were carefully rinsed. Six input couplers were mounted at the upper and lower ports of the three 2-cell cavities, and the string assembly was completed in a class-10 cleanroom (Fig. 4). Then, the attachment of a tuner system and the alignment of the three cavities were carried out. After a cold-mass assembly including a cooling pipeline of 2K-He, two reservoir panels of 5K-He, and thermal shields of 80K-N2, the string cavities were inserted into a vacuum vessel. The entire assembly of the injector cryomodule was completed in June 2012. The injector cryomodule was installed in a beamline and was connected to a cold valve box, as shown in Fig. 5.

Figure 4: The assembly of the super conducting cavities for injector in a clean room.

Figure 5: Completed cERL injector cryomodule installed in beam line and connected with cold box.

The first set of cool-down tests for low RF power measurements was carried out in September 2012. The temperature distribution, static heat loads at 2K, and RF-coupling parameters such as the input coupler (Qin), HOM filter (QHOM), and monitor coupler (Qt) were measured. The tuner performance of the motor and piezo tuners was tested, and control of the resonant frequency was successfully confirmed, as shown in Fig. 6. The second set of cool-down tests for high RF power measurements was carried out in February 2013. The conditioning of an accelerating gradient in each individual cavity was initially started in a pulsed operation of 2 ms and 5 Hz (duty of 1%). After an accelerating gradient reached 15 MV/m, the duty factor was increased to 10 % (5 ms and 2 Hz). Finally, stable CW operation at 9 MV/m (7.5 MV/m in the specification) was confirmed. Measurement of Qo values by dynamic heat loads of 2K-He was carried out at 5 – 8 MV/m; however, the obtained Qo values in all three cavities were one order lower than expected (1×10^{10}) due to heat-up at the HOM RF feedthroughs. The improvement of the cooling system of HOM RF feedthroughs will be an important item in the future.

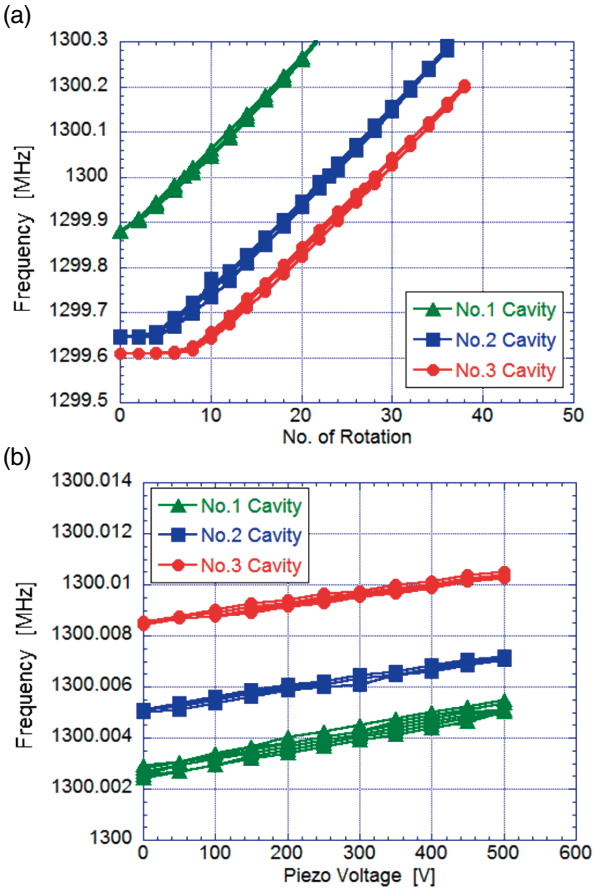

Figure 6: Measurement results of tuner performance in three 2-cell cavities; Coarse tuner by stepping motor (a) and fine tuner by piezo (b).

3-4 SC Cavities for Main Linac

A prototype module of the cERL main linac was assembled and cooled. The module contained two 9-cell cavities of 1.3 GHz. The cavities were connected to each other with three HOM absorbers and fixed in a 5K shield titanium frame. A cross-sectional view is shown in Fig. 7 In October, after assembly, the module was installed in the cERL (Fig. 8). The first 2K cooling test was performed for one month, beginning in the middle of November. The first half of this period was used to determine the fundamental performance of the modules, such as cooling speed, temperature distribution, heat loss, cavity alignment, and low-level RF measurements including frequency tuners. Acceptable results of these tests allowed us to execute the RF high-power test in the second half of the testing period. The accelerating gradient of both cavities reached 16 MV/m; however, strong field emission was observed at the gradient of more than 10 MV/m, which limited the CW to operating below 14 MV/m because of the limitations of the X-ray shield and the cryogenic power capacity.

A beam commissioning of the injector section will be followed by the construction of the return loop, which is scheduled for the summer of 2013. Preparation of a low-level RF and other operation systems of the main linac is in progress, aiming for total beam commissioning of the cERL in December 2013.

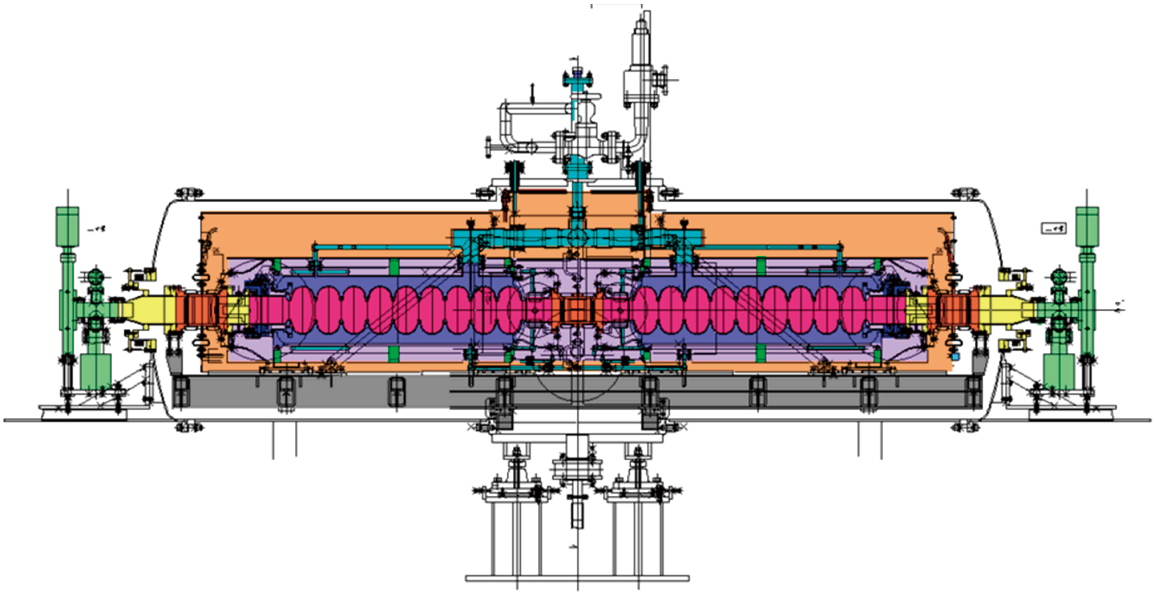

Figure 7: A cross-sectional view of the main linac module. Two 9-cell Nb cavities (red) dressed in the Ti-jacket (blue) are connect each other with HOM absorbers (orange). This structure is supported by the Ti-frame (violet) which has a magnetic shield and work as the 5K shield.

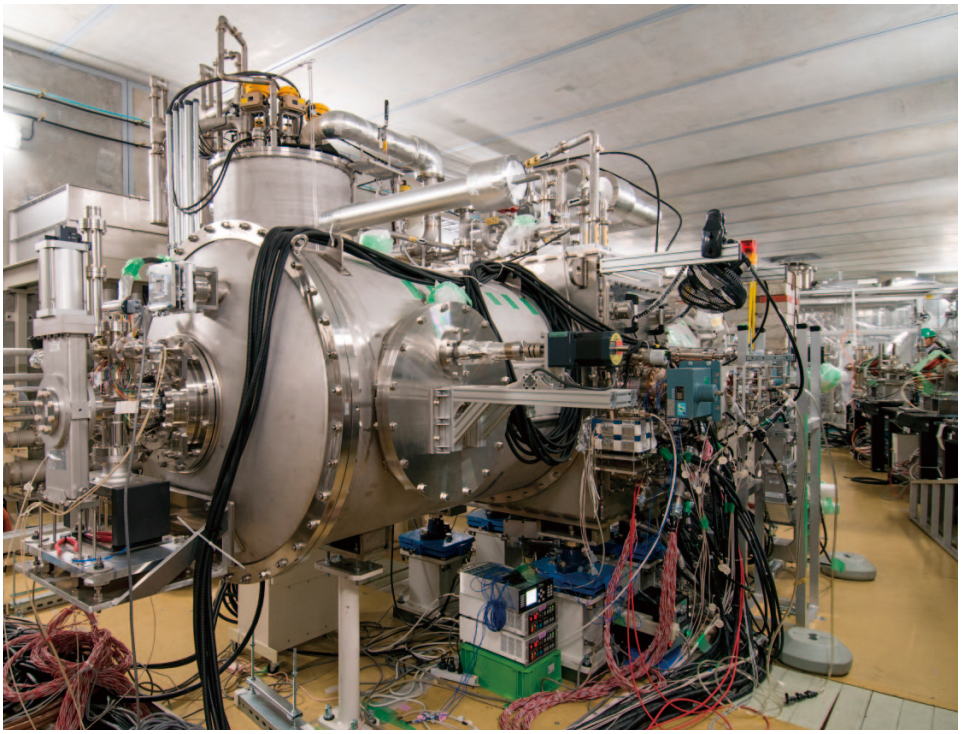

Figure 8: Prototype module of a main linac installed in the cERL shield room.

3-5 RF Sources

RF stabilities of 0.1% in amplitude and 0.1 deg. in phase are required for the cERL. In order to satisfy these requirements, we adopted a digital low-level RF (LLRF) system, which is located inside the temperature-controlled hut in the LLRF control room on the 2nd floor. This hut has been used for the KEKB injector linac and the temperature inside is regulated by controlling the ventilating fans on the roof. The temperature stability of the hut is about 0.2 °C. An RF source (RF; 1.3 GHz), local oscillator (LO;1.31 GHz), and clock generator are installed inside the thermostat chamber, which operates using a Peltier device. Figure 9(a) shows the thermostat chamber and the temperature controlled hut. The phase drift of the cavity probe signal can be the dominant error of the RF stability because no air conditioners are installed in the ERL test hall. In order to realize stable RF signals, RF cables were packed inside the water-cooled cable duct between the LLRF control room and the radiation shield inside, as shown in Fig. 9(b).

(a)

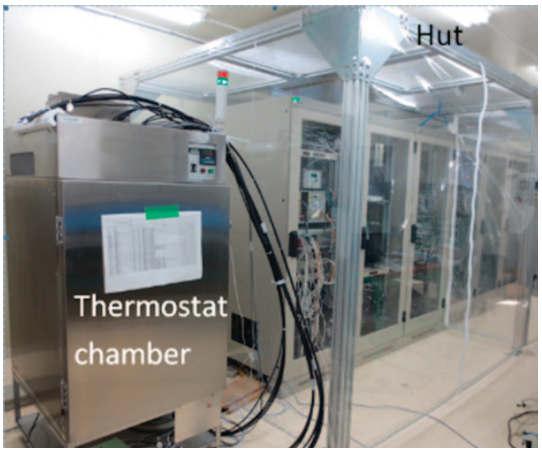

(b)

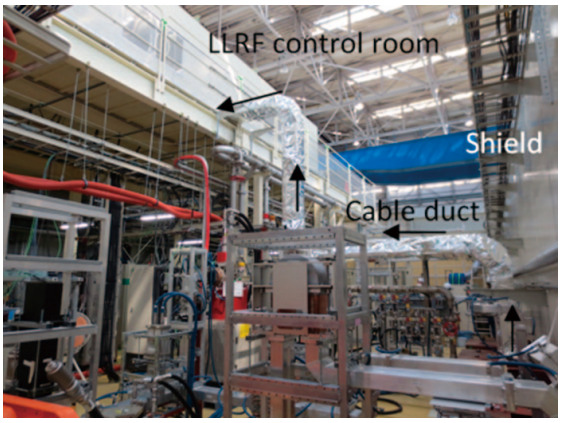

Figure 9: (a) Thermostat chamber and temperature controlled hut. (b) Water cooled rf cable duct.

Figure 10: Variable waveguide phase shifter for adjusting the cavity input phase.

Concerning the high-power RF system (HPRF), a total of 5 RF sources will be installed in the cERL. An IOT (Inductive Output Tube; 20 kW) will drive a normal conducting buncher cavity. An Injector 1 superconducting (SC) cavity will be driven by a 30-kW klystron. Injector 2 and 3 cavities will both be driven by a 300-kW klystron. All the power distribution waveguides (including circulators and power splitters) were installed in the injector linac. Each injector SC cavity has two RF couplers. The RF input phase is adjusted by the waveguide phase shifter located inside the radiation shield, as shown in Fig. 10.

3-6 Cryogenic Systems

In FY2012, both the injector cryomodule and the main linac cryomodule were installed in the cERL and connected to each 2K helium cryogenic system. In June 2012, before the installation of these cryomodules (Fig. 11), the performance of the cryogenic system, including two 2K refrigerator cold boxes and transfer lines for the cryomodules, was measured. We produced 2K superfluid helium in the two 2K refrigerator cold boxes and measured static heat loads to the cryogenic system. The response of the cryogenic system to the heat load variations was also measured using electric heaters in the 2K refrigerator cold boxes to simulate dynamic heat loads from superconducting RF cavity cryomodules.

In July 2012, the injector cryomodule was connected to one of the 2K refrigerator cold boxes as shown in Fig. 12(a). A connection transfer line was specially designed to minimize the ambient heat load to the cryogenic system. The cryogenic system, including the injection cryomodule, was inspected by the Ibaraki prefecture under the High Pressure Gas Safety Act in August 2012 and passed its completion inspection. The injector cryomodule was successfully cooled down to 2K, and performance of the superconducting RF cavities was measured in September 2012. The main linac cryomodule was connected to another 2K refrigerator cold box in October 2012, as shown in Fig. 12(b), following the first cryogenic test of the injector cryomodule, and it passed the completion inspection by the Ibaraki prefecture in early November 2012. The cryogenic test of the main linac cryomodule was carried out with high RF power in November and December 2012. The injector cryomodule was cooled down again in January and February 2013 for cryogenic testing of the cavities with high RF power.

We have conducted cryogenic tests of the cryomodules with 4 sets of rotary oil pumps and mechanical boosters in the helium gas pumping system of the 2K helium cryogenic system. For the injector cryomodule, it was found the current cooling power at 2K of the cryogenic system could sustain all heat loads from the cryogenic system itself and from the cryomodule. On the other hand, for the main linac cryomodule, the cooling power of the cryogenic system was slightly insufficient to sustain the heat loads. Considering the results of the cryogenic tests with high RF power into the cryomodules, we have increased the number of rotary oil pumps and mechanical boosters to 8 sets of pumps in order to increase the cooling power at 2K, since the cooling power at 2K depends directly on the pumping capacity of the helium gas pumping system in the 2K helium cryogenic system.

Figure 11: 2K refrigerator cold boxes and transfer lines for cryomodules.

(a)

(b)

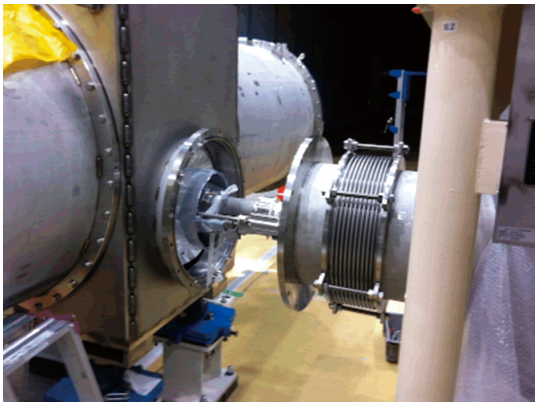

Figure 12: (a) and (b) show the connections of injector (main linac) cryomodules and 2K refrigerator cold boxes, respectively.

3-7 cERL Magnet Systems

Almost all of the magnets and girders required for 35 MeV operation were manufactured until the end of the 2012 fiscal year. In 2013, three of the four girders for the quadrupoles and sextupoles of the arc section, and two girders for the LCS (laser Compton scattering) matching section, will be made. The eight sextuple magnets and four steering magnets will be manufactured in the future as well. In 2012, the 167 bipolar power supplies of 5 A and 60 V for the quadrupole magnets were manufactured. The four power supplies for the injection, extraction, and path length control chicanes will be made in 2013. Figure 13 shows the girders and power supplies, ready for the construction of the recirculation path. The prototype of the quadrupole and sextupole magnet girder of the arc section was manufactured on the basis of the optimized design from the static and dynamic structure analysis shown in Fig. 14.

Figure 13: The girders and power supplies at the ERL Hall.

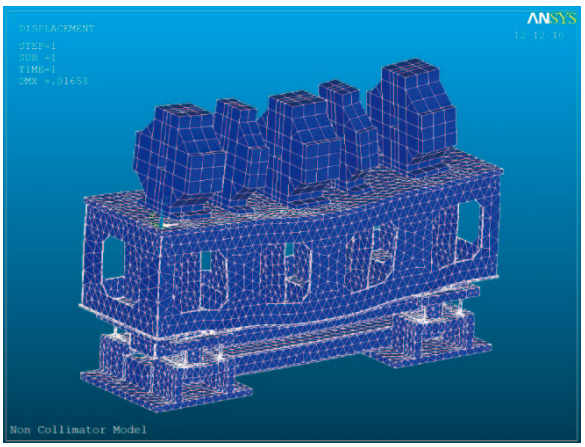

Figure 14: The sample of the distortion analysis of the girder.

3-8 Schedule

Fabrication of the accelerator components such as the injector part, super conducting cavities, RF sources, and He cryogenic systems was completed by the end of the 2012 fiscal year. We will start the beam tests of the injector parts at the beginning of the 2013 fiscal year. These tests will characterize the beam quality at the injector and will be performed until the end of July 2013. Then we will install the recirculation loop from the summer to November 2013 and begin the ERL operation in December 2013. We will carefully increase the beam current to avoid radiation problems from the cERL and will check the beam quality of the cERL in 2014. The target values during the first stage are a beam current of 10 mA and a normalized emittance of 1 mm mrad. Finally, we will check for normalized emittances of 0.3 mm mrad with 7.7 pc/bunch and 1 mm mrad with 77 pc/bunch. The beam test will provide important information on whether further improvement of the components is necessary, as well as information on the drawbacks of the design of the 3-GeV-class ERL.

REFERENCE

[1] N. Nishimori, R. Nagai, S. Matsuba, R. Hajima, M. Yamamoto, T. Miyajima, Y. Honda, H. Iijima, M. Kuriki, M. Kuwahara, *Appl. Phys. Lett.* **102** (2013) 234103.

Users Program & Outreach Activities

Users Program and Outreach Activities

1 Experimental Proposals

1-1 Scientific Proposals

The Photon Factory accepts experimental proposals submitted by researchers mainly at universities and research institutes inside and outside Japan. The proposals are reviewed by the PF Program Advisory Committee (PF-PAC), and those that are favorably recommended are formally approved by the Advisory Committee for the Institute of Materials Structure Science. The number of accepted proposals over the period 2001-2012 is shown in Table 1, where S1/S2, U, G, and P denote Special, Urgent, General and Preliminary proposals, respectively. The number of current G-type proposals each year has exceeded 800 for the past few years. A full list of the proposals effective in FY2012 and their scientific output can be found in Part B of this volume.

S-type proposals are divided into two categories, S1 and S2. S1 proposals are self-contained projects of excellent scientific quality, and include projects such as the construction and improvement of beamlines and experimental stations which will be available for general users after the completion of the project. S2 proposals are superior-grade projects that require the full use of synchrotron radiation or a large amount of beam time. Table 2 lists the S-type projects effective in FY2012.

Table 1: Number of proposals accepted for the period 2001-2012.

Category	FY2001	2002	2003	2004	2005	2006	2007	2008	2009	2010	2011	2012
S1	0	0	1	1	0	1	0	0	0	0	0	0
S2	2	3	2	0	3	6	1	4	6	3	2	4
U	5	3	2	4	0	1	7	3	2	2	0	4
G	346	321	318	382	310	386	403	402	397	407	415	454
P	18	16	9	13	10	22	14	14	14	16	11	18

Table 2: List of S-type proposals effective in FY2012.

Proposal No.	Spokesperson	Title
2009S2-007	J. Yoshinobu Univ. of Tokyo	Electronic states and charge transfer dynamics of organic molecules on surfaces
2009S2-008	H. Nakao KEK-PF	Condensed matter studied by resonant soft/hard X-ray scattering
2010S2-001	K. Amemiya KEK-PF	Exploration of spintronics materials by soft X-ray polarization switching
2010S2-003	Y. Nagashima Tokyo Univ. of Sci.	Laser spectroscopy of positronium negative ions and its applications
2010S2-004	A. Nakao KEK-PF	Structural studies of molecular crystals under extreme conditions
2011S2-003	M. Oshima Univ. of Tokyo	Operando analysis of green nano-device structures by high-resolution electron spectroscopy
2012S2-001	T. Takahashi Tohoku Univ.	Quantum phenomena of Dirac fermion systems studied by high-resolution angle-resolved photoemission spectroscopy
2012S2-004	A. Waseda AIST	Crystal evaluation of silicon crystals for the determination of the Avogadro constant
2012S2-005	H. Nakao KEK-PF	Materials structure science by resonant soft x-ray scattering underexternal field
2012S2-006	J. Yoshinobu Univ. of Tokyo	Physical chemistry at surface and interface of energy-conversionmaterials using VUV/SX SR spectroscopies

The current status and results to date of S1 and S2 proposals must be reported at the PF Symposium held at the end of every Japanese fiscal year. The scientific output of S1 and S2 proposals is presented in the Highlights of Part A and in the Users' Reports of Part B of this volume.

Proposals are categorized into five scientific disciplines, and reviewed by the five subcommittees of PF-PAC: 1) electronic structure, 2) structural science, 3) chemistry and new materials, 4) life science I (protein crystallography), and 5) life science II (including soft matter science). Figure 1 shows the distribution by research field of the proposals accepted by the subcommittees in FY2012.

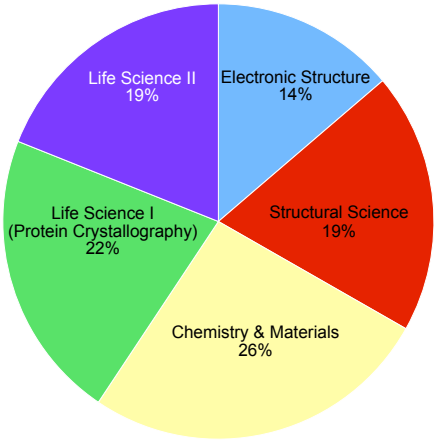

Figure 1: Distribution by scientific field of experimental proposals accepted in FY2012.

1-2 Industrial Proposals

The S, U, G, and P-type proposals are opened for nonproprietary industrial research by limited companies that can apply for the Grant-in-Aid for Scientific Research. Besides these, 29 proprietary industrial projects (Y-type) and 12 nonproprietary collaborative studies with private companies (C-type) were conducted.

Fourteen trial-use programs for industrial applications are carried out with the financial support of a MEXT project, the Open Advanced Research Facilities Initiative. Among these, nine are newly approved, eight are continued from FY2011 and one is an XAFS training course. About a quarter of the companies are continuing Y- or C-type projects after the end of the trial-use program.

1-3 Statistics of the Proposals

The number of users, for all types of proposals, has reached 3,372. Although the number of experimental stations has decreased, the approved academic proposals and number of users have increased annually, as shown in Fig. 2. This indicates a high and increasing demand for synchrotron radiation and can be attributed to continuous improvements in the storage rings, beamlines, and experimental stations. The synchrotron has become one of the most important research tools for carrying out advanced science experiments and developments. About 30% of the proposals are conducted by new spokespersons, which indicates that the Photon

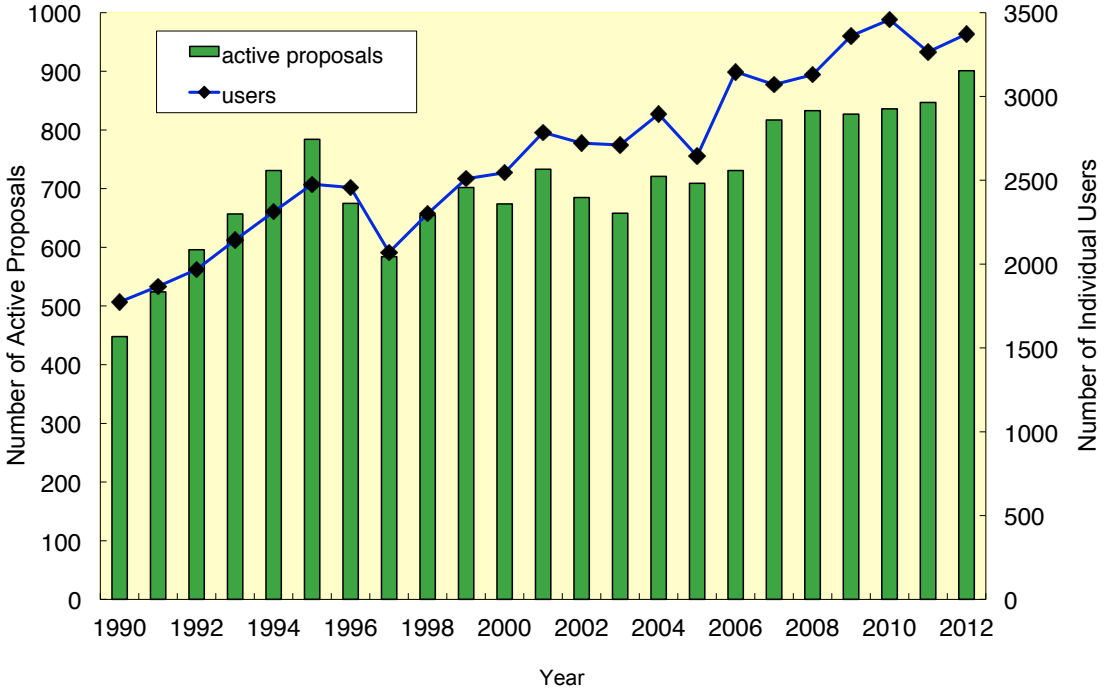

Figure 2: Number of registered PF users and scientific proposals over the period 1990-2012.

Factory is open to public academic scientists. Figure 3 shows the distribution of users by institution and position. Over two-thirds of the users belong to universities, with approximately 75% of the users associated with national universities. Over half of the university users are graduate and undergraduate students; this indicates that the Photon Factory plays an important role in both research and education. The geographical distribution of the Photon Factory users is shown in Fig. 4 and Fig. 5, which also indicates the immense contribution of the Photon Factory to research and education throughout Japan. The registered number of papers published in 2012 based on experiments at the PF was 572 at the time of this writing and is expected to exceed 650. In addition, 31 doctoral and 78 master theses have been presented.

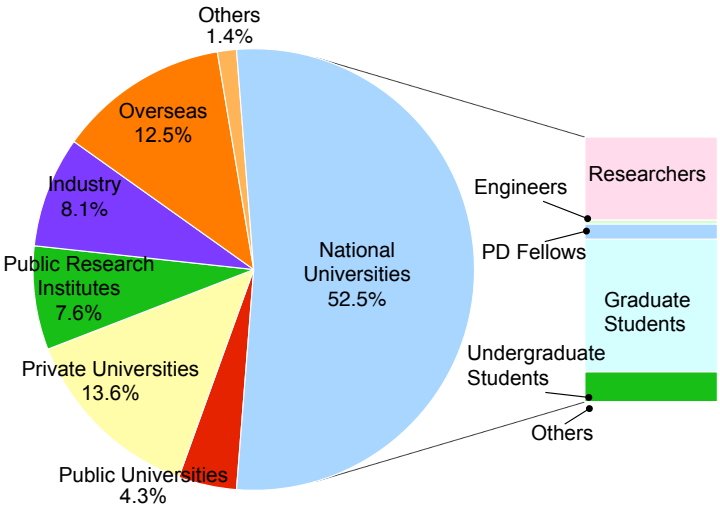

Figure 3: Distribution of users by institution and position.

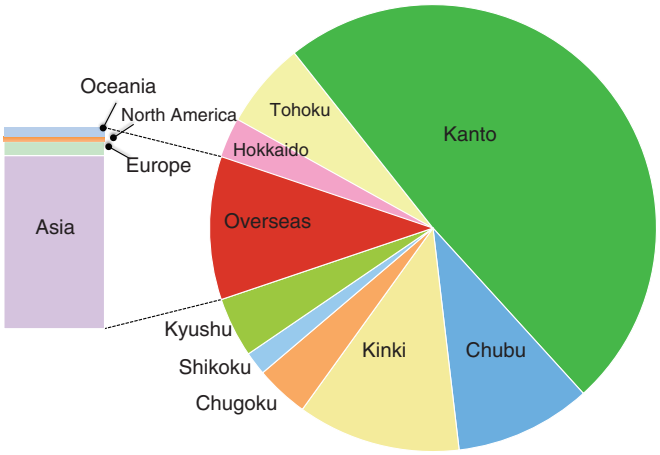

Figure 4: Regional distribution of the spokespersons of proposals accepted in FY2012.

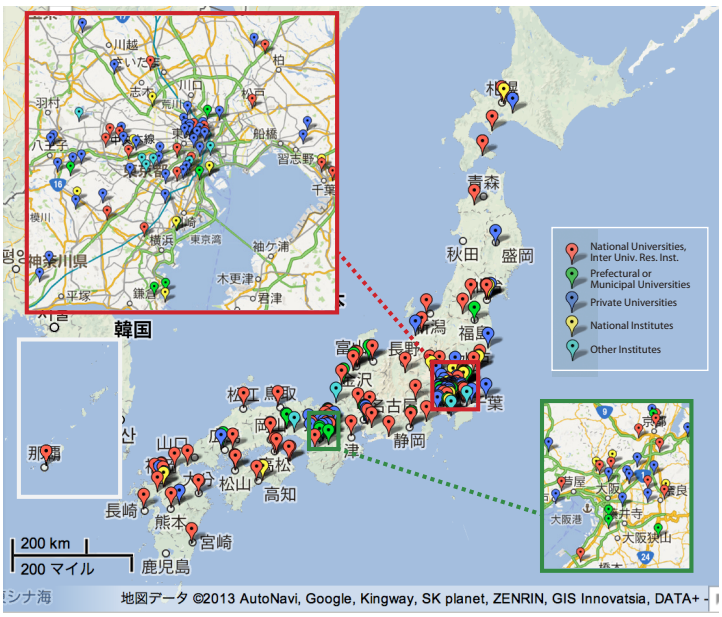

Figure 5: Affiliation of Photon Factory users in FY 2012 (domestic users only).

2 Workshops and Seminars

2-1 IMSS Science Festa

The 1st IMSS (Institute of Materials Structure Science) SCIENCE FESTA was held on March 14-15, 2013 at EPOCHAL Tsukuba with the support of the user community and KEK. Following two Scientific Sessions with invited speakers—one concerning research using multiple types of study probes including synchrotron radiation, neutrons and muons for investigating materials, and the other concerning research on soft matter—a Poster Session was held on the first day. There were 239 user poster presentations, with results presented from 10 S-type and 3 U-type proposals. There were more than 40 presentations from the staff of the Accelerator Laboratory of KEK, Neutron Science Division and Muon Science Division of IMSS and PF staff, resulting in a total of 294 poster presentations. The 30th PF symposium, the annual users' meeting, the 1st KENS (KEK Neutron Science Laboratory) symposium and the 1st MSL (Muon Science Laboratory) symposium were held simultaneously on March 15, the second day. The IMSS SCIENCE FESTA provided an excellent opportunity to exchange a broad range of knowledge in such fields as synchrotron, neutron and muon science, and was attended by more than 500 users and IMSS staff. The main purpose of the PF symposium is to discuss the present status and future projects of the PF, and to encourage networking among users and PF staff through scientific presentations and discussions. At the beginning of the PF symposium, PF staff reported on the recent progress of the facility, including the rearrangement of beamlines. We also had two discussion sessions on future light sources at the PF such as ERL. In addition, a special session, "Closing Ceremony of Australian Beamline", was held. The Australian National Beamline Facility (ANBF) was Australia's first synchrotron beamline; it was installed at BL-20B at the PF in 1992 and officially opened the following year, and has been used for many scientific activities by Australian research groups. Following a presentation on the history of Australia's involvement at the PF by Professor Richard F. Garrett of the Australian Nuclear Science and Technology Organization, and a presentation on bioinorganic chemistry at ANBF by Professor Peter A. Lay of the University of Sydney, the closing ceremony was held. We greatly appreciate their scientific contributions to the PF. Another special session, "India-Japan Collaboration at Photon Factory", was also held, at which Professor Milan K. Sanyal of the Saha Institute of Nuclear Physics presented the recent status of the Indian beamline, BL-18B, at the PF.

2-2 PF Workshops

Six PF workshops were held in FY2012. Anyone can propose such a workshop; free discussion is made on a specific scientific topic in synchrotron-radiation research and related applications. The proceedings of the workshops can be found in the KEK proceedings, which are available at the KEK Library.

(1) "Silicon Single Crystal: Insatiable Pursuit towards Ideal Quality as Crop in Semiconductor Industry and X-ray Optical in Synchrotron Science", May 26-27, 2012. KEK Proceedings 2012-3.
(2) "Buried Interface Sciences with X-rays and Neutrons 2012", June 26-28, 2012.
(3) "Compact ERL Science Workshop II", July 30-31, 2012. KEK Proceedings 2012-10 (in Japanese).
(4) "New Progress of Nanospectroscopy", September 13-14, 2012. KEK Proceedings 2012-5 (in Japanese).
(5) "New Research Developments at KEK-Slow Positron Facility-Positron Diffraction and Ps Beam", October 3-4, 2012. KEK Proceedings 2012-11.
(6) "The 1st Workshop on Advanced Observational Techniques - Local Structural Analysis and Imaging -", December 26, 2012. KEK Proceedings 2012-9 (in Japanese).

2-3 Seminars

The seminars hosted by each scientific project in the Institute of Materials Structure Science (IMSS) were arranged as seminars hosted by IMSS, and are called "IMSS Colloquium" and "IMSS Danwakai". These seminars provide an opportunity to exchange a broad range of knowledge in such fields as synchrotron, neutron and muon science. "IMSS Colloquium" invites leading scientists in each scientific field. "IMSS Colloquium" and "IMSS Danwakai" were held in FY2012.
http://imss.kek.jp/seminar/colloquium/index.html
http://imss.kek.jp/seminar/imss-danwakai/2012/index.html

3 Graduate School Education

KEK is one of the basic organizations of the Graduate University for Advanced Studies (SOKENDAI), and has the School of High Energy Accelerator Science, which consists of three departments: Accelerator Science, Materials Structure Science, and Particle and Nuclear Physics. The majority of the PF staff members are in charge of giving lectures and supervising graduate students of the Department of Materials Structure Science. SOKENDAI offers a five-year PhD course for undergraduate students and a three-year PhD course for master's degree holders. The School of High Energy Accelerator Science held its "open campus day" for young researchers and undergraduate students at the Tsukuba campus on July 5, 2012 and half-day guidance meetings for potential young candidates in early summer 2012 at Hakata, Osaka, and Tokyo.

The PF has also a system for Joint PhD (JPHD) students, who are accepted by the PF to pursue advanced studies under the supervision of PF staff members towards their PhD degrees in collaboration with their home universities. The numbers of graduate students of SOKENDAI and JPHD during the past fifteen years are listed in Table 1.

In addition to the SOKENDAI and JPHD graduate students, a number of doctoral theses were written based on research carried out at the PF. Figure 1 shows the statistics of such graduate students.

Table 1: Number of SOKENDAI and JPHD students at the PF over the period 1998-2012.

FY	SOKENDAI	JPHD
1998	9	14
1999	6	11
2000	8	12
2001	10	8
2002	12	13
2003	12	7
2004	14	5
2005	14	6
2006	9	10
2007	6	13
2008	6	10
2009	6	9
2010	5	10
2011	4	5
2012	6	6

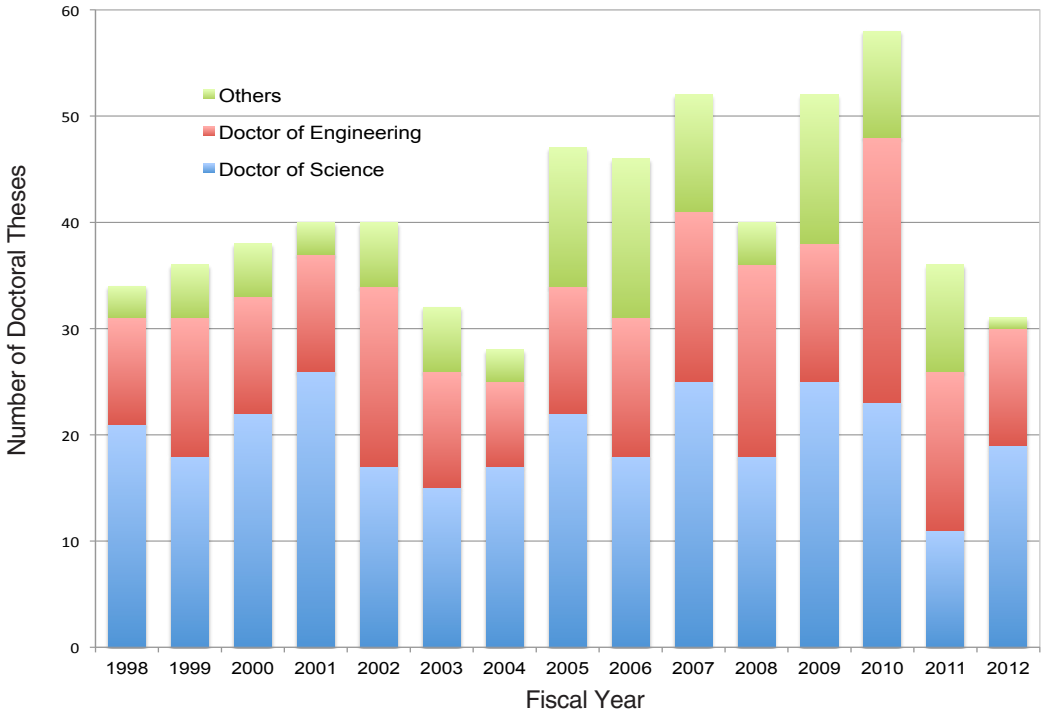

Figure 1: Number of students who obtained doctoral degrees based on scientific activities at the PF.

4 International Collaboration

4-1 Overview

The Photon Factory is collaborating internationally in various aspects. The Australian National beamline BL-20B was constructed by the Australian Nuclear Science and Technology Organization (ANSTO) in 1992, and finally ceased operation in March 2013. The Indian beamline BL-18B started operation in 2009. The Photon Factory is also collaborating with international synchrotron radiation communities through meetings, workshops, and schools.

4-2 Australian Beamline

The Australian beamline BL-20B was constructed by ANSTO in 1992, and finally ceased operation at the end of this fiscal year (March 2013). The beamline has been extremely productive, with more than 1,000 papers published from about 900 experimental projects. In FY2012, 33 experiments were carried out at BL-20B. Many of them used the XAFS technique, especially the fluorescent XAFS technique which is applied to environmental and biological systems. 8 papers based on BL-20B experiments were published in FY2012. The closing ceremony of the Australian beamline BL-20B took place at the PF symposium on March 15, 2013, and Dr. Richard Garrett (ANSTO) gave a memorial lecture at the ceremony (Fig. 1).

Figure 1: Dr. Richard Garret giving a memorial lecture at the PF symposium.

4-3 Indian Beamline

The DST, Government of India and KEK agreed to set up an Indian beamline at the Photon Factory in 2008 with the Saha Institute of Nuclear Physics (SINP) as a nodal institute of India. Beamline 18B is leased to DST, and SINP set up two diffractometers and related detection systems. 24 experiments were carried out at BL-18B, and 1 paper based on BL-18B experiments were published in FY2012. The beamline will be fully operational shortly, and will be open not only for Indian scientists but also general users in the near future.

4-4 Cooperation with the SESAME Project

SESAME (Synchrotron-light for Experimental Science and Applications in the Middle East) is a synchrotron radiation facility under construction in Amman, Jordan as a collaborative project of the countries in the Middle East under the auspices of UNESCO. SESAME is expected to be operational in 2015, and KEK is continuously supporting the construction and potential user community at SESAME in various ways. As one of the activities, SESAME staff and students from SESAME-related countries were invited to Japan for one to two months in FY2012, and learned various synchrotron-related subjects (accelerator, radiation safety, structural biology, etc.) at PF, SPring-8, UVSOR and other universities in Japan. The travel and living expenses of the participants were fully supported by the JSPS Asia-Africa Science Platform Program (Fig. 2).

Figure 2: SESAME staff and students from Jordan, Egypt and Iran joined the SESAME-JSPS Program in FY2012.

5 Science Advisory Committee (PF-SAC)

Meetings of the Photon Factory Science Advisory Committee (PF-SAC) have been held every fiscal year since the first PF-SAC in April 2007, providing ongoing advice on the operation and strategic planning for the Photon Factory. The seventh PF-SAC meeting was held on February 7 and 8, 2013.

Table 1 shows a list of members for the seventh PF-SAC. The Photon Factory distributed presentation files and a list of discussion points (Table 2) in advance on which the Photon Factory wished to receive advice from the PF-SAC. On the first day of the meeting, the Photon Factory staff and users presented the present status and strategy relevant to the discussion points and several recent scientific topics. Following Q&A and discussion for each presentation, PF-SAC met in closed sessions in the evening of the first day and the morning of the second day, and formulated the observations, conclusions and recommendations.

Regarding the sixth discussion point in Table 2, the PF-SAC noted that "the SAC considers the continuous upgrades of beamlines and instrumentation as one of the cornerstones in the roadmap for the next decade. This is a necessity to keep the PF in the frontier of international research. In this context the SAC commends the PF management for its initiative in using recovery funding to upgrade beamlines 2, 13, 28 and 15. The research on these beamlines falls within the areas of excellence and thus is of the highest strategic importance for the PF. Future refurbishing of beamlines should follow the same criteria.", and "an exceedingly important component of the roadmap is the successful construction and operation of the compact ERL. The success of this project is of paramount importance for the next step to secure the 3-GEV ERL. The SAC fully supports the high priority the PF/KEK gives this project and stresses the importance of full attention to this endeavor."

Other itemized questions and the answers from the PF-SAC can be found at:
http://pfwww.kek.jp/SAC12Feb/PF-SACExecutiveSummaryFeb2013.pdf

Table 1: PF-SAC members as of FY2012.

Efim GLUSKIN	Advanced Photon Source
Yasuhiro IWASAWA	University of Electro-Communications Tokyo
Yasuhiro IYE	Institute for Solid State Physics, The University of Tokyo
Ingolf LINDAU	Stanford University, **Chair**
Kunio MIKI	Kyoto University
Junichiro MIZUKI	Kwansei Gakuin University
Fulvio PARMIGIANI	University of Trieste
Moonhor REE	Pohang Accelerator Laboratory/PSTECH
Zhentang ZHAO	Shanghai Synchrotron Radiation Facility

Table 2: List of discussion points.

1	How does the PF-SAC evaluate the PF future plan in the next decade?
2	Is the construction of the direct injection path for PF-AR reasonable in relation with the PF future plan?
3	Is the BL refurbishment program for the new BL-2 and BL-15 effective for the best use of the PF facility?
4	How does PF-SAC evaluate the suggestions of the time-resolved science subcommittee and the response from PF?
5	Is the new PF users' association well organized to promote the activities of the PF users and PF?
6	How does the PF-SAC evaluate the progress of the preparations for the ERL project including the construction of the cERL?

Appendices

1. Site and Organization

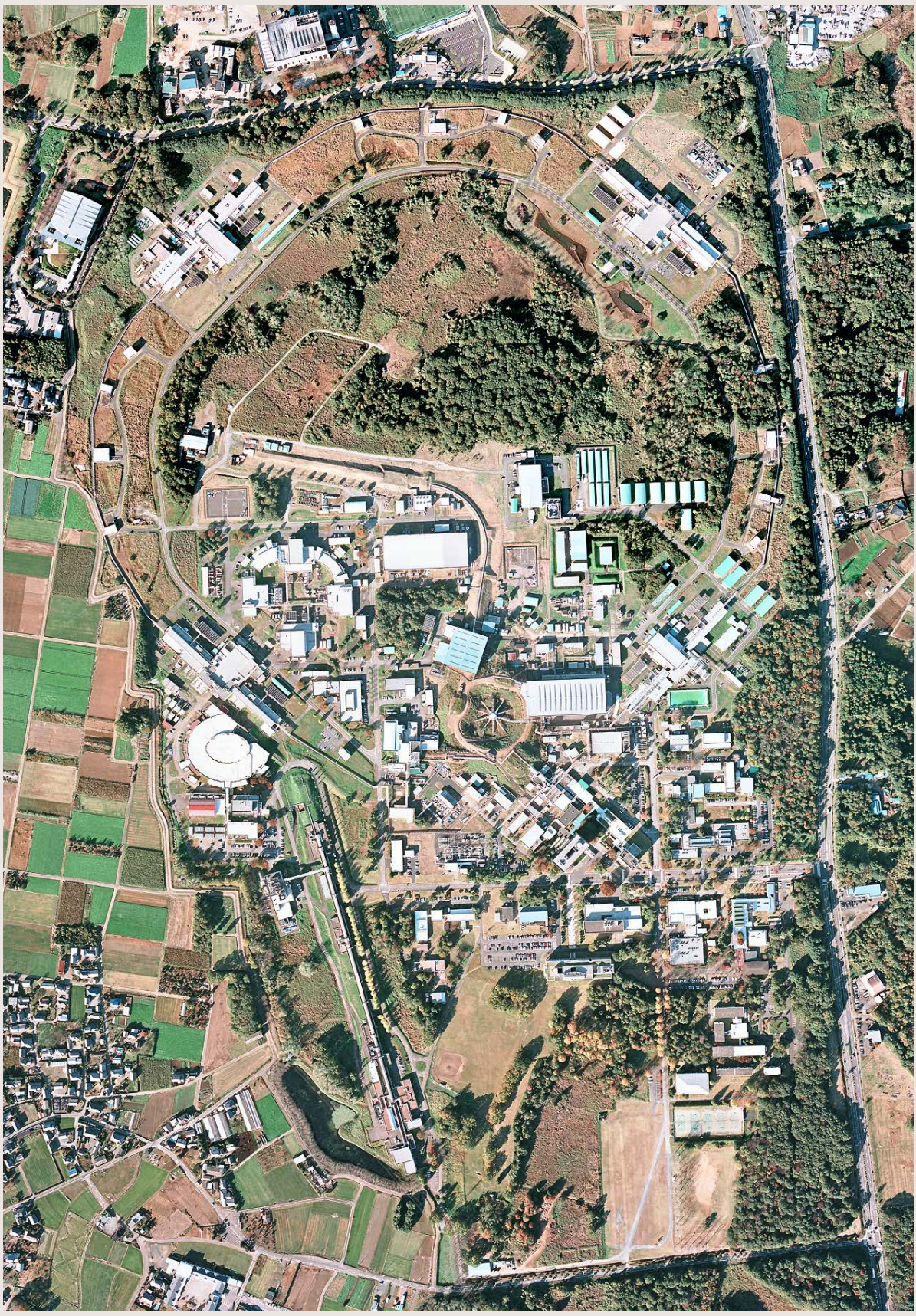

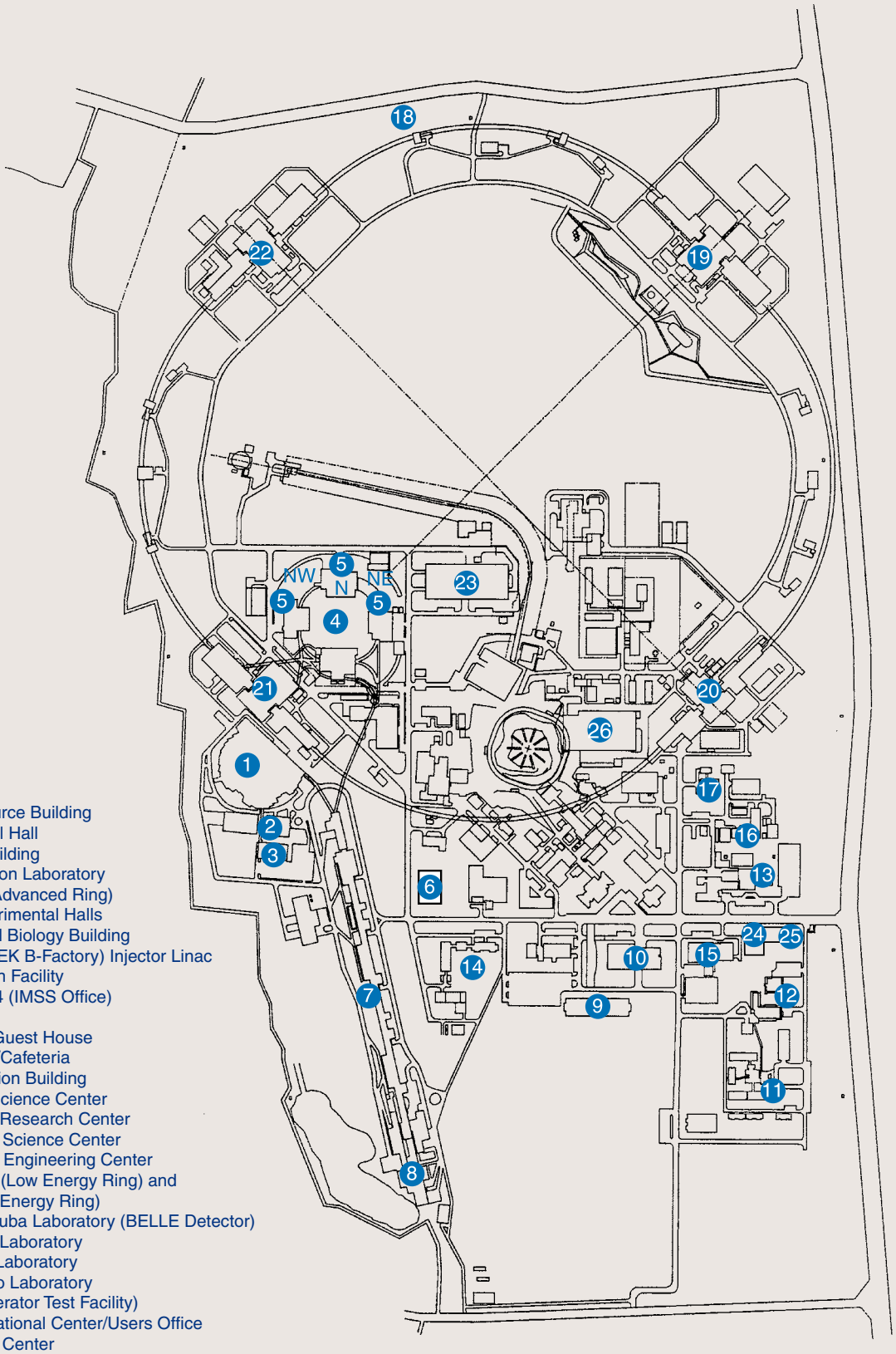

1. PF Light Source Building
   Experimental Hall
2. PF Office Building
3. PF Preparation Laboratory
4. PF-AR (PF Advanced Ring)
5. PF-AR Experimental Halls
6. PF Structural Biology Building
7. PF/KEKB (KEK B-Factory) Injector Linac
8. Slow Positron Facility
9. Building No.4 (IMSS Office)
10. Library
11. Dormitory/Guest House
12. Restaurant/Cafeteria
13. Administration Building
14. Radiation Science Center
15. Computing Research Center
16. Cryogenics Science Center
17. Mechanical Engineering Center
18. KEKB LER (Low Energy Ring) and
    HER (High Energy Ring)
19. KEKB Tsukuba Laboratory (BELLE Detector)
20. KEKB Oho Laboratory
21. KEKB Fuji Laboratory
22. KEKB Nikko Laboratory
23. ATF (Accelerator Test Facility)
24. KEK International Center/Users Office
25. Information Center
26. ERL Test Facility

KEK consists of four research institutions, i.e., the Institute of Materials Structure Science (IMSS), the Institute of Particle and Nuclear Studies (IPNS), the Accelerator Laboratory (AL), and the Applied Research Laboratory. As shown in Fig. 1, the IMSS constitutes the Synchrotron Radiation Divisions I and II, the Neutron Science Division, the Muon Science Division, the Structural Biology Research Center, and the Condensed Matter Research Center. Table I shows a list of the members of the Advisory Committee of the IMSS.

Photon Factory (PF) consists of two divisions of the IMSS (the Synchrotron Radiation Divisions I and II) and the Accelerator Division VII of the AL as shown in the organization chart of Fig. 2. The staff members of the PF list in Table 2. Synchrotron Radiation Science Divisions I and II consist of seven groups such as “Electronic Structure”, “Structural Material Science”, “Materials Chemistry”, “Life Sciences”, “Beamline Engineering, Technical Services & Safety”, “User Support and Dissemination”. The Accelerator Division VII has six groups, which are named Light Source Group I to VI. The missions of each group are as follows: Group I is in charge of orbits, magnets, and insertion devices, Group II of RF, SC cavities and so on, Group III mainly of vacuum, Group IV mainly of beam diagnostics and accelerator control, Group V of front-end, safety and so on, and Group VI mainly of electron guns.

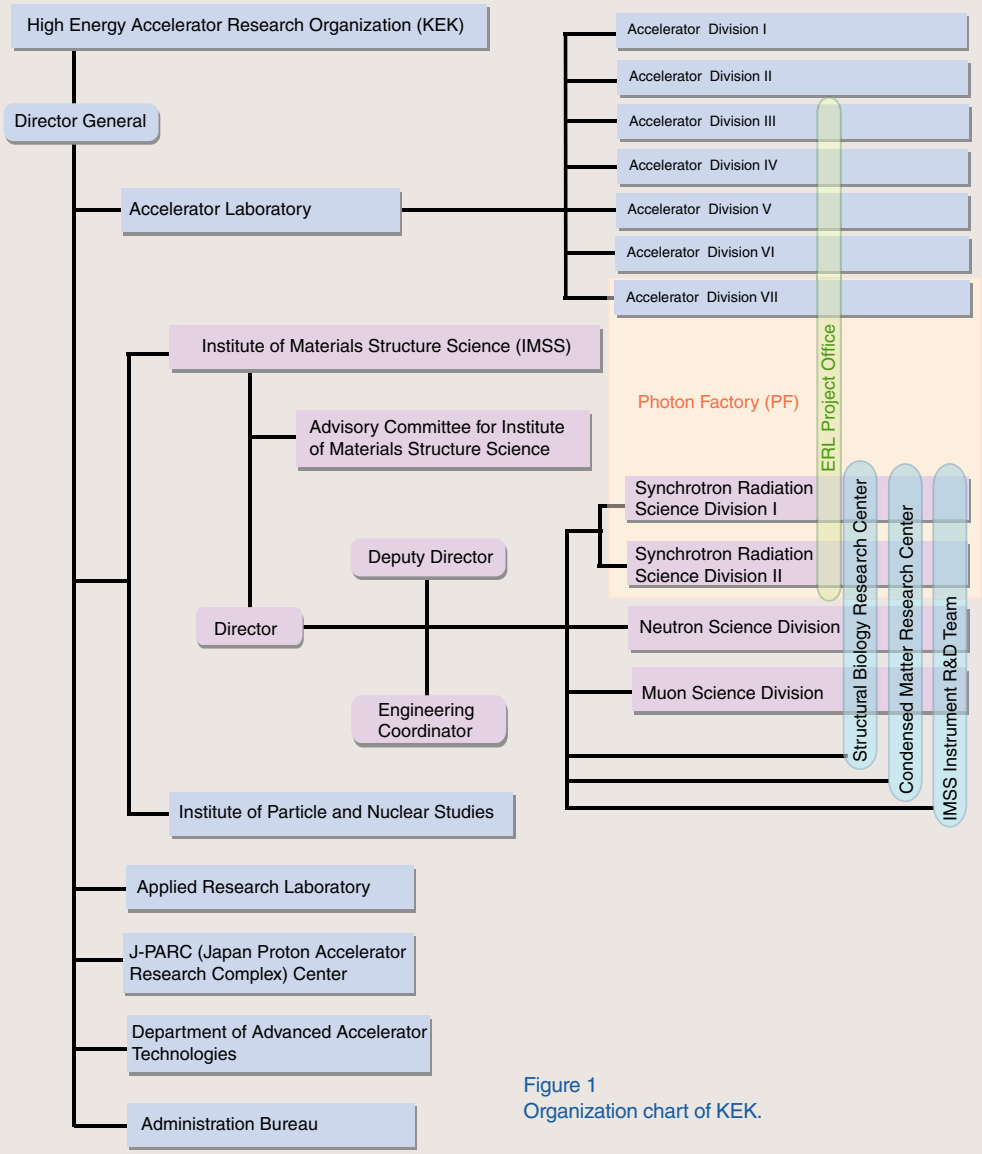

Figure 1
Organization chart of KEK.

Table 1 The members of the Advisory Committee for Institute of Materials Structure Science.

ADACHI, Shin-ichi	Photon Factory, IMSS, KEK
AKIMITSU, Jun	Aoyama Gakuin University
AMEMIYA, Yoshiyuki**	The University of Tokyo
FUJII, Yasuhiko	Comprehensive Research Organization for Science and Society
ITO, Kenji	Photon Factory, IMSS, KEK
KADONO, Ryosuke	Muon Science Division, IMSS, KEK
KANAYA, Toshiji	Kyoto University
KATAOKA, Mikio	Nara Institute of Science and Technology
KAWATA, Hiroshi	Photon Factory, IMSS, KEK
KOBAYASHI, Yukinori	Photon Factory, Accelerator Laboratory, KEK
KUMIGASHIRA, Hiroshi	Photon Factory, IMSS, KEK
MIYAKE, Yasuhiro	Muon Science Division, IMSS, KEK
MIZUKI, Jun'ichiro	Kwansei Gakuin University
MURAKAMI, Youichi	Photon Factory, IMSS, KEK
OSHIMA, Masaharu	The University of Tokyo
OTOMO, Toshiya	Neutron Science Division, IMSS, KEK
SAITO, Naohito	Institute of Particle and Nuclear Studies, KEK
SASAKI, Shinichi	Applied Research Laboratory, KEK
SATO, Mamoru	Yokohama City University
SETO, Hideki*	Neutron Science Division, IMSS, KEK
TAKATA, Masaki	RIKEN/SPring-8
TORIKAI, Eiko	University of Yamanashi
WAKATSUKI, Soichi	Photon Factory, IMSS, KEK
YAMAGUCHI, Seiya	Accelerator Laboratory, KEK

* Chairperson ** Vice-Chairperson

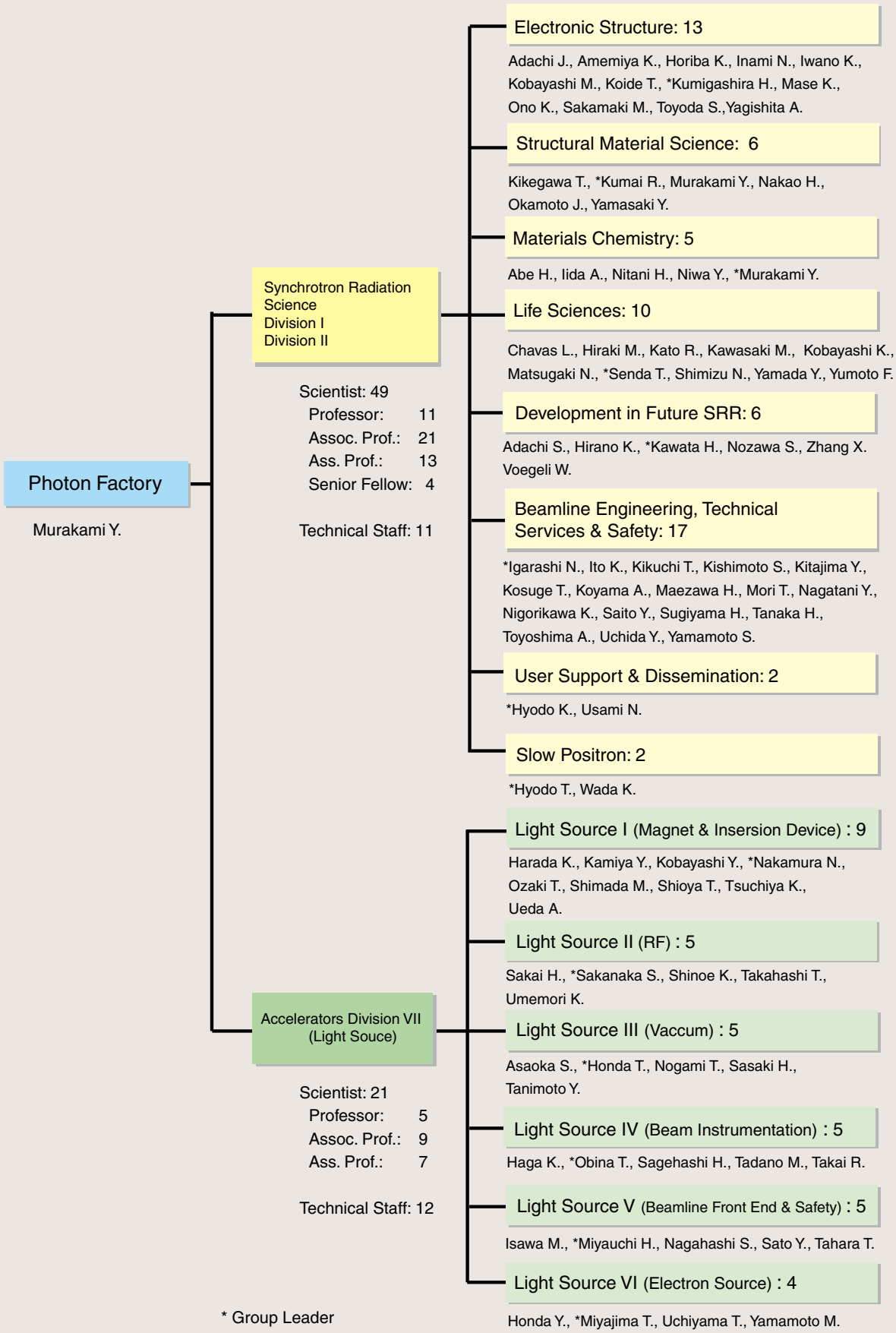

Figure 2
Organization chart of PF (as of March 31, 2013) .

Table 2 Staff members of the Photon Factory.

Name	Group*
Research Staff	
Director	
MURAKAMI, Youichi	SMS/MC
Synchrotron Radiation Science Division I & II	
ABE, Hitoshi	MC
ADACHI, Jun-ichi	ES
ADACHI, Shinichi	DF (*SMS*)
AMEMIYA, Kenta	ES (*BETSS*)
CHAVAS, Leonard	LS
HIRAKI, Masahiko	LS (*BETSS*)
HIRANO, Keiichi	DF
HORIBA, Koji	ES
HYODO, Kazuyuki	USD (*BETSS)*
HYODO, Toshio	SPF
IGARASHI, Noriyuki	BETSS (*LS*)
IIDA, Atsuo	MC
INAMI, Nobuhito	ES
ITO, Kenji	BETSS (*ES*)
IWANO, Kaoru	ES (*DF*)
KATO, Ryuichi	LS
KAWASAKI, Masato	LS
KAWATA, Hiroshi	DF
KIKEGAWA, Takumi	SMS
KIKUCHI, Takashi	BETSS
KISHIMOTO, Shunji	BETSS (*DF*)
KITAJIMA, Yoshinori	BETSS (*ES*)
KOBAYASHI, Katsumi	LS
KOBAYASHI, Masaki	ES
KOIDE, Tsuneharu	ES
KOSUGE, Takashi	BETSS
KOYAMA, Atsushi	BETSS
KUMAI, Reiji	SMS
KUMIGASHIRA, Hiroshi	ES
MAEZAWA, Hideki	BETSS
MASE, Kazuhiko	ES
MATSUGAKI, Naohiro	LS
MORI, Takeharu	BETSS
NAGATANI, Yasuko	BETSS
NAKAO, Hironori	SMS
NIGORIKAWA, Kazuyuki	BETSS
NITANI, Hiroaki	MC
NIWA, Yasuhiro	MC (*BETSS*)
NOZAWA, Shunsuke	DF
OKAMOTO, Jun	SMS
ONO, Kanta	ES
SAITO, Yuuki	BETSS
SAKAMAKI, Masako	ES

Name	Group*
SENDA, Toshiya	LS
SHIMIZU, Nobutaka	LS
SUGIYAMA, Hiroshi	BETSS (*DF*)
TANAKA, Hirokazu	BETSS
TOYODA, Satoshi	ES
TOYOSHIMA, Akio	BETSS
UCHIDA, Yoshinori	BETSS
USAMI, Noriko	USD (*LS*)
VOEGELI, Wolfgang	DF
WADA, Ken	SPF
YAGISHITA, Akira	ES
YAMADA, Yusuke	LS
YAMAMOTO, Shigeru	BETSS
YAMASAKI, Yuichi	SMS
YUMOTO, Fumiaki	LS
ZHANG, Xiaowei	DF
Accelerator Division VII	
ASAOKA, Seiji	Light Source III
HAGA, Kaiichi	Light Source IV
HARADA, Kentaro	Light Source I
HONDA, Tohru	Light Source III
HONDA, Yosuke	Light Source VI
ISAWA, Masaaki	Light Source II
KAMIYA, Yukihide	Light Source I
KOBAYASHI, Yukinori	Light Source I
MIYAJIMA, Tsukasa	Light Source VI
MIYAUCHI, Hiroshi	Light Source V
NAGAHASHI, Shinya	Light Source V
NAKAMURA, Norio	Light Source I
NOGAMI, Takashi	Light Source III
OBINA, Takashi	Light Source IV
OZAKI, Toshiyuki	Light Source I
SAGEHASHI, Hidenori	Light Source IV
SAKAI, Hiroshi	Light Source III
SAKANAKA, Shogo	Light Source II
SATO, Yoshihiro	Light Source V
SHIMADA, Miho	Light Source I
SHINOE, Kenji	Light Source II
SHIOYA, Tatsuro	Light Source I
TADANO, Mikito	Light Source IV
TAHARA, Toshihiro	Light Source III
TAKAHASHI, Takeshi	Light Source II
TAKAI, Ryota	Light Source IV
TANIMOTO, Yasunori	Light Source III
TSUCHIYA, Kimichika	Light Source I
UCHIYAMA, Takashi	Light Source VI
UEDA, Akira	Light Source I
UMEMORI, Kensei	Light Source II

Name	Group*
YAMAMOTO, Masahiro	Light Source VI

Guest Professor

ASAKURA, Kiyotaka	(Hokkaido Univ.)
HAJIMA, Ryoichi	(JAEA)
ISHIHARA, Sumio	(Tohoku Univ.)
KAMIKUBO, Hironari	(NAIST)
KATO, Masahiro	(IMS)
KIMURA, Masao	(NIPPON STEEL & SUMITOMO METAL)
KOSHIHARA, Shinya	(Tokyo Inst. Tech.)
MORITOMO, Yutaka	(Tsukuba Univ.)
OHKUMA, Haruo	(JASRI/SPring-8)
TAKAHASHI, Yoshio	(Hiroshima Univ.)
YAO, Min	(Hokkaido Univ.)

Postdoctoral Fellow

SAKAI, Enju
SUDAYAMA, Takaaki
TAKEICHI, Yasuo
YONEMURA, Hiroki

The Graduate University for Advanced Studies

INOUE, Keisuke
WU, Yanlin

* Synchrotron Radiation Science Division

ES	Electronic Strucuture
SMS	Structural Material Science
MC	Materials Chemistry
LS	Life Sciences
DF	Development in Future SRR
BETSS	Beamline Engineering, Technical Services and Safety
USD	User Support and Dissemination
SPF	Slow Positron Facility

Italic: the additional post

2. Awards

The Commendation for Science and Technology by the Minister of Education, Culture, Sports, Science and Technology, Prizes for Science and Technology
NISHIKAWA, Keiko (Chiba Univ.)
“Studies on Fluctuations of Condensed Materials”

The Commendation for Science and Technology by the Minister of Education, Culture, Sports, Science and Technology, Prizes for Science and Technology
YAMAMOTO, Kimihisa (Tokyo Inst. of Tech.)
“Study on Fine Controlled Metal-Hybrid Materials”

The Commendation for Science and Technology by the Minister of Education, Culture, Sports, Science and Technology, The Young Scientists’ Prize
KIGUCHI, Manabu (Tokyo Inst. of Tech.)
“Novel Properties Appeared at Well Defined Low-Dimensional Nano Material”

The Chemical Society of Japan (CSJ) Award, 2012
FUJITA, Makoto (The Univ. of Tokyo)
“Self-Assembly Control of the Structure of Matter on the Nanoscale”

The Crystallographic Society of Japan, The CrSJ Award
UEKUSA, Hidehiro (Tokyo Inst. of Tech.)
“Investigation of Dynamic Phenomena in Molecular Crystals by ab Initio Structure Determination from Powder Diffraction Data”

Particle Accelerator Society of Japan, PASJ Award for Young Scientists
TAKAKI, Hiroyuki (The Univ. of Tokyo)
“Development of Beam Injection System with a Pulsed Sextupole Magnet”

Japan Association of Mineralogical Sciences Award
YOSHIASA, Akira (Kumamoto Univ.)
“Precise Structure Analyses of the Earth and Planetary Materials by Both Diffraction and XAFS Methods”

The Japan Society for Analytical Chemistry Award, 2012
NAKAI, Izumi (Tokyo Univ. of Sci.)
“Development of Innovative X-Ray Analytical Techniques and their Application to the Decoding of Material History”

The Foundation for High Energy Accelerator Science, Nishikawa Prize, 2012
WADA, Ken (KEK-PF)
“Intensification of the Slow-Positron Beam at KEK Slow Positron Facility and its Application”

Volkswagen and BASF, Science Award Electrochemistry
YABUUCHI, Naoaki (Tokyo Univ. of Sci.)
“Toward Development of Novel High-Capacity Sodium Insertion Materials”

The Japan Academy, Japan Academy Medal
NOJIRI, Hideaki (The Univ. of Tokyo)
“Molecular Bases of Xenobiotic-Degrading Capacity of Environmental Bacteria”

Japan Society for the Promotion of Science, JSPS Prize
NOJIRI, Hideaki (The Univ. of Tokyo)
“Molecular Bases of Xenobiotic-Degrading Capacity of Environmental Bacteria”

The Chemical Society of Japan Award for Outstanding Woman Chemists, 2012
TADA, Mizuki (IMS)
“Molecular-Level Design and Visualization of Structures and Catalytic Functions on Solid Surfaces”

Young Scientist Award of the Physical Society of Japan
YAMAZAKI, Masakazu (Tohoku Univ.)
“Study on Molecular Orbitals by Multidimensional Electron Spectroscopy”

Young Scientist Awards of the Japan Society for Molecular Science
YOSHIKAWA, Hirofumi (Nagoya Univ.)
“Functional Properties of Molecular Clusters Based on Solid-State Electrochemistry”

The Society of Chemical Engineers, Japan, The SCEJ Young Investigator Researcher Award
NAKAGAWA, Keizo (The Univ. of Tokushima)
“Improvement of Catalytic Functionality of Metal Nanoparticles by Surface Coating”

“Sano Award, 2013” (Young Researcher Award of Electrochemical Society in Japan)
YABUUCHI, Naoaki (Tokyo Univ. of Sci.)
“Studies of Solid State Electrochemistry on Functional Insertion Materials for Advanced Rechargeable Batteries”

The Japanese Society for Extremophiles, Research Award for Young Scientists
GODA, Shuichiro (Nagasaki Univ.)
“Elucidation of the Heat Activation Mechanism of the Glutamate Dehydrogenase from Hyperthermophiles”

15th The Japanese Society of Carbohydrate Research Encouragement Award
SATOH, Tadashi (Nagoya City Univ.)
“Structural Biology Study of Intracellular Lectin Involved in Gycoprotein Transport and Degradation”

The 66th CerSJ Awards for Advancements in Ceramics Science and Technology
MASUBUCHI, Yuji (Hokkaido Univ.)
“Synthesis, Structure and Properties of New Functional Oxynitride Ceramics”

The Atomic Collision Society of Japan, Incentive Award for Young Scientist
TOMOYA, Mizuno (KEK-PF)
“Molecular Fragmentation by Charge-Changing Collisions of Fast Heavy Ions”

Japanese Society for Synchrotron Radiation Research, 17th JSSRR Scientific Awards
WADATI, Hiroki (The Univ. of Tokyo)
“Resonant Soft X-Ray Scattering Studies of Thin Films of Transition-Metal Oxides”

Chemical Society of Japan, Encouragement Award from Division of Colloid and Interface Science
OHKUBO, Takahiro (Okayama Univ.)
“Peculiar Structure of Aqueous Solution Confined in Nanospace”

The FY2012 (the 3rd) The Graduate University for Advanced Studies, Sokendai President’s Award
WU, Yanlin (Soken Univ.)
“The Development and Application of High Sensitivity X-Ray Phase Contrast Imaging System by using Multiple-Diffraction”

3. Theses

Lists of doctoral theses, which were written based on the PF experiments.

Doctor of Science
AHMED, Naveed (Chiba Univ.)
“Photocatalytic Conversion of Carbon Dioxide into Methanol over Layered Double Hydroxide Catalysts” (7C, 9A and 9C)

Doctor of Science
TORIGOE, Hiroe (Okayama Univ.)
“Preparation of New Type of Xe-Compounds and Activation of Small Molecules by Utilizing Zeolite as A Specific Reaction Field” (NW10A and 9C)

Doctor of Science
TANG, Qun (CAS)
“RecOR Complex Including RecR N-N Dimer and RecO Monomer Displays a High Affinity for ssDNA. Nucleic Acid Research” (NW10A and 9C)

Doctor of Engineering
YAMAMOTO, Takafumi (Kyoto Univ.)
“Synthesis, Structure, and Physical Properties of Novel Iron Oxides Prepared by Topotactic Reactions” (NE1A)

Doctor of Science
OHTSUBO, Yoshiyuki (Kyoto Univ.)
“Spin-Polarized Electronic States on Ge(111)” (18A and 19A)

Doctor of Science
KOITAYA, Takanori (The Univ. of Tokyo)
“Adsorbed Cyclohexane on Rh(111): Two-Dimensional Superstructure, Energy Level Alignment, and Kinetic and Geometric Isotope Effects” (13A)

Doctor of Engineering
NIWA, Hideharu (The Univ. of Tokyo)
“Electronic Structure of Carbon-Based Oxygen Reduction Catalysts Studied by Soft X-Ray Spectroscopy” (2C)

Doctor of Engineering
SEKI, Kazuaki (Nagoya Univ.)
“Polytype Control and Twin Suppression in Solution Growth of 3C-SiC” (15C)

Doctor of Engineering
ITO, Eri (Nagoya Inst. of Tech.)
“Structure Analysis of Poly(dimethyl siloxane)-Based Amphiphilic Hydrogel for Medical Device Applications” (6A, 9C, and 15A)

Doctor of Engineering
JEONG, Ji-Hoon (Kyoto Univ.)
“Recovery of Heavy Metals from Wastes using Environmentally Friendly Hydrometallurgical Process” (3A)

Doctor of Engineering
HINOKUMA, Satoshi (Kumamoto Univ.)
“Development of Support Material Stabilizing Precious Metal Nanoparticles and Their Preparation Method” (NW10A)

Doctor of Philosophy
VELAGA, Srihari (Univ. of Madras, INDIA)
“Investigation on CdO CaO Solid Solution with Wide band Gap Tunability: Macroscopic Structure, Vibrational and Local Structural Studies at Atomic Scale” (NW10A)

Doctor of Science
ISOHAMA, Yoichi (Hiroshima Univ.)
“Study of Local Ti Off-Centering of $BaTiO_3$ Probed by Resonant X-Ray Emission Spectroscopy” (15B1)

Doctor of Science
MICHISHIO, KOJI (Tokyo Univ. of Sci.)
“Production of an Energy-Tunable Positronium Beam using the Photodetachment of Positronium Negative Ions” (SPF)

Doctor of Science
HIRAO, Norie (Ibaraki Univ.)
“Development of Micro-XAFS using Synchrotron Soft X-Rays and its Application to Surface State Analyses” (27A)

Doctor of Engineering
HARAGUCHI, Daisuke (Waseda Univ.)
“Investigation of Removal Mechanisms and Modeling for Hydroxide Co-Precipitation Treatment in Wastewater Containing Fluorine and Arsenic” (9A and 12C)

Doctor of Agriculture
NISHIOKA, Taiki (Hokkaido Univ.)
“Structure-Guided Design for Improvement of Enzymes and Their Application” (17A, NE3A, NW12A and 5A)

Doctor of Engineering
MATSUI, Kazuki (MURORAN Inst. of Tech.)
“Pressure-Induced Structural Change of Unfilled Skutterudite Compounds” (NE5C and 18C)

Doctor of Science
EINAGA, Mari (Niigata Univ.)
“Study of Pressure-Induced Superconductivity and Structural Phase Transition in Bismuth Compounds” (NE1A and 18C)

Doctor of Science
OKADA, Akitoshi (The Univ. of Tokyo)
“Crystal Structure Analysis of DnaB-DnaC Complex Involved in DNA Replication in E. Coli” (NW12A)

Doctor of Agriculture
HORITA, Shoichiro (The Univ. of Tokyo)
“Structural Basis of the Different Substrate Preferences of Two Old Yellow Enzymes from Yeasts in Asymmetric Reduction of Enone Compounds” (NW12A)

Doctor of Science
KIYOTANI, Tamiko (Kitasato Univ.)
“Crystal Structure and Powder X-Ray Analysis of Structural Transition Depended on Temperature and Humidity of Peptide Hydrate” (4B2)

Doctor of Science
ISHIGURO, Nozomu (The Univ. of Tokyo)
“Advanced Characterization of Practical Heterogeneous Catalysts using Time-Resolved/Space-Resolved XAFS” (9A, 9C and12C)

Doctor of Science
NISHIDA, Keisuke (Tohoku Univ.)
“Density and Sound Velocity Measurements of Liquid Fe-S at High Pressure: Implications for the Earth’s and the lunar Cores” (14C2 and NE7A)

4. Publication List

1A

D.-H.Im, K.Kimura, F.Hayasaka, T.Tanaka, M.Noguchi, A.Kobayashi, S.Shoda, K.Miyazaki, T.Wakagi and S.Fushinobu
Crystal Structures of Glycoside Hydrolase Family 51 α-L-Arabinofuranosidase from *Thermotoga maritima*
Biosci. Biotechnol. Biochem., **76** (2012) 423.

E.H.Lee, Y.W.Cho and K.Y.Hwang
Crystal Structure of LeuD from *Methanococcus jannaschii*
Biochem. Biophys. Res. Commun., **419** (2012) 160.

S.Kikuchi, K.Hara, T.Shimizu, M.Sato and H.Hashimoto
Structural Basis of Recruitment of DNA Polymerase ζ by Interaction between REV1 and REV7 Proteins
J. Biol. Chem., **287** (2012) 33847.

U.Ohto, K.Fukase, K.Miyake and T.Shimizu
Structural Basis of Species-Specific Endotoxin Sensing by Innate Immune Receptor TLR4/MD-2
Proc. Natl. Acad. Sci. USA, **109** (2012) 7421.

B.G.Han, K.H.Kim, S.J.Lee, K.C.Jeong, J.W.Cho, K. H.Noh, T.W.Kim, S.J.Kim, H.J.Yoon, S.W.Suh, S.Lee and B.I.Lee
Helical Repeat Structure of Apoptosis Inhibitor 5 Reveals Protein-Protein Interaction Modules
J. Biol. Chem., **287** (2012) 10727.

S.Kikuchi, K.Hara, T.Shimizu, M.Sato and H.Hashimoto
Crystallization and X-Ray Diffraction Analysis of the Ternary Complex of the C-Terminal Domain of Human REV1 in Complex with REV7 Bound to a REV3 Fragment Involved in Translesion DNA Synthesis
Acta Cryst. F, **68** (2012) 962.

H.Matsumura, E.Mizohata, H.Ishida, A.Kogami, T.Ueno, A.Makino, T.Inoue, A.Yokota, T.Mae and Y.Kai
Crystal Structure of Rice Rubisco and Implications for Activation Induced by Positive Effectors NADPH and 6-Phosphogluconate
J. Mol. Biol., **422** (2012) 75.

H.Matsumura, N.Kusaka, T.Nakamura, N.Tanaka, K.Sagegami, K.Uegaki, T.Inoue and Y.Mukai
Crystal Structure of the N-Terminal Domain of the Yeast General Corepressor Tup1p and Its Functional Implications
J. Biol. Chem., **287** (2012) 26528.

S.Sugiyama, M.Maruyama, G.Sazaki, M.Hirose, H.Adachi, K.Takano, S.Murakami, T.Inoue, Y.Mori and H. Matsumura
Growth of Protein Crystals in Hydrogels Prevents Osmotic Shock
J. Am. Chem. Soc., **134** (2012) 5786.

A.R.Han, H.S.Kim, G.Y.Cho, H.S.Ki, H-Y.Kim and K.Y.Hwang
Crystallization and Preliminary X-Ray Crystallographic Analysis of the Methionine Sulfoxide Reductase A Domain of MsrAB from *Haemophilus Influenzae*
Acta Cryst. F, **68** (2012) 557.

M.Englert, S.Xia, C.Okada, A.Nakamura, V.Tanavde, M.Yao, S.H.Eom, W.H.Konigsberg D.Soll and J.Wang
Structural and Mechanistic Insights into Guanylylation of RNA-Splicing Ligase RtcB Joining RNA between 3'-Terminal Phosphate and 5'-OH
Proc. Natl. Acad. Sci. USA, **38** (2012) 15235.

Y.Ashikawa, Z.Fujimoto, Y.Usami, K.Inoue, H.Noguchi, H.Yamane and H.Nojiri
Structural Insight into the Substrate- and Dioxygen-Binding Manner in the Catalytic Cycle of Rieske Nonheme Iron Oxygenase System, Carbazole 1,9a-Dioxygenase
BMC Struct. Biol., **12** (2012) 15.

M.Unno, K.Kizawa, M.Ishihara and H.Takahara
Crystallization and Preliminary X-Ray Crystallographic Analysis of Human Peptidylarginine Deiminase Type III
Acta Cryst. F, **68** (2012) 668.

H Ru, LX Zhao, W Ding, LY Jiao, N Shaw, WG Liang, LG Zhang, LW Hung, N Matsugaki, S Wakatsuki and ZJ Liu
S-SAD Phasing Study of Death Receptor 6 and Its Solution Conformation Revealed by SAXS
Acta Cryst. D, **68** (2012) 521.

M.Fujihashi, M.Hiraki, G.Ueno, S.Baba, H.Murakami, M.Suzuki, N.Watanabe, I.Tanaka, A.Nakagawa, S.Wakatsuki, M.Yamamoto and K.Miki
Crystal Sample Pins and a Storage Cassette System Compatible with the Protein Crystallography Beamlines at both the Photon Factory and SPring-8
J. Appl. Cryst., **45** (2012) 1156.

T.Hayashi, M.Senda, H.Morohashi, H.Higashi, M.Horio, Y.Kashiba, L.Nagase, D.Sasaya, T.Shimizu, N.Venugopalan, H.Kumeta, N.Noda, F.Inagaki, T.Senda and M.Hatakeyama
Tertiary Structure-Function Analysis Reveals the Pathogenic Signaling Potentiation Mechanism of *Helicobacter pylori* Oncogenic Effector CagA
Cell Host & Microbe, **12** (2012) 20.

Former 1B

T.Aree and H.-B.Bürgi
Dynamics and Thermodynamics of Crystalline Polymorphs: α-Glycine, Analysis of Variable-Temperature Atomic Displacement Parameters
J. Phys. Chem. A, **116** (2012) 8092.

T.Kambe, X.He, Y.Takahashi, Y.Yamanari, K.Teranishi, H.Mitamura, S.Shibasaki, K.Tomita, R.Eguchi, H.Goto, Y.Takabayashi, T.Kato, A.Fujiwara, T.Kariyado, H.Aoki and Y.Kubozono
Synthesis and Physical Properties of Metal-Doped Picene Solids
Phys. Rev. B, **86** (2012) 214507.

R.I.Thomson, C.M.Pask, G.O.Lloyd, M.Mito and J.M.Rawson
Pressure-Induced Enhancement of Magnetic-Ordering Temperature in an Organic Radical to 70 K: A Magneto-structural Correlation
Chem. Eur. J., **18** (2012) 8629.

2A

T.Miyamoto, T.Wada, H.Niimi, S.Suzuki, M.Kato, M.Kudo and K.Asakura
A New Collinear-Type Energy-Filtered X-Ray Photoemission Electron Microscope Equipped with a Multi-Pole Aberration-Corrected Air-Core Coil Wien Filter
Jpn. J. Appl. Phys., **51** (2012) 046701.

2C

A.Chikamatsu, T.Matsuyama, Y.Hirose, H.Kumigashira, M.Oshima and T.Hasegawa
Investigation of Electronic States of Infinite-Layer $SrFeO_2$ Epitaxial Thin Films by X-Ray Photoemission and Absorption Spectroscopies
J. Elec. Spec. Relat. Phenom., **184** (2012) 547.

Y.Ishiwata, T.Shiraishi, N.Ito, S.Suehiro, T.Kida, H.Ishii, Y.Tezuka, Y.Inagaki, T.Kawae, H.Oosato, E.Watanabe, D.Tsuya, M.Nantoh and K.Ishibashi
Metal-Insulator Transition Sustained by Cr-Doping in V_2O_3 Nanocrystals
Appl. Phys. Lett., **100** (2012) 043103.

M.Minohara, K.Horiba, H.Kumigashira, E.Ikenaga and M.Oshima
Potential Profiling in Depth for Perovskite Oxide Heterojunctions using Photoemission Spectroscopy
Phys. Rev. B, **16** (2012) 165108.

S.Toyoda, H.Kumigashira, M.Oshima, H.Sugaya and H.Morita
Determining Factor of Effective Work Function in Metal/bi-Layer High-k Gate Stack Structure Studied by Photoemission Spectroscopy
Appl. Phys. Lett., **100** (2012) 112906.

J.Adachi
Development and Use of Novel Soft X-Ray Spectroscopic Methods for Gaseous Molecules
Mol. Sci., **6** (2012) A0048. (*in Japanese*).

Y.Ishiwata, S.Suehiro, T.Kida, H.Ishii, Y.Tezuka, H.Oosato, E.Watanabe, D.Tsuya, Y.Inagaki, T.Kawae, M.Nantoh and K.Ishibashi
Spontaneous Uniaxial Strain and Disappearance of the Metal-Insulator Transition in Monodisperse V_2O_3 Nanocrystals
Phys. Rev. B, **86** (2012) 035449.

T.Okumura, T.Inoue, Y.Tasaki, E.Sakai, H.Kumigashira and T.Higuchi
Electronic Structure of $SrTi_{0:99}Sc_{0:01}O_3$ Thin Film Studied by High-Resolution Soft-X-Ray Spectroscopy
J. Phys. Soc. Jpn., **81** (2012) 094705.

S.Aizaki, T.Yoshida, K.Yoshimatsu, M.Takizawa, M.Minohara, S.Ideta, A.Fujimori, K.Gupta, P.Mahadevan, K.Horiba, H.Kumigashira and M.Oshima
Self-Energy on the Low- to High-Energy Electronic Structure of Correlated Metal $SrVO_3$
Phys. Rev. Lett., **109** (2012) 056401.

J.Adachi, M.Kazama, T.Teramoto, N.Miyauchi, T.Mizuno, M.Yamazaki, T.Fujikawa and A.Yagishita
C 1s Photoelectron Angular Distributions from Fixed-in-Space CO Molecules in the High-Energy Continuum ≥ 50 eV
J. Phys. B, **45** (2012) 194007.

E.B.Guedes, M.Abbate, K.Ishigami, A.Fujimori, K.Yoshimatsu, H.Kumigashira, M.Oshima, F.C.Vicentin, P.T.Fonseca and R.J.O.Mossanek
Core Level and Valence Band Spectroscopy of $SrRuO_3$: Electron Correlation and Covalence Effects
Phys. Rev. B, **86** (2012) 235127.

S.Toyoda, T.Shinohara, H.Kumigashira, M.Oshima and Y.Kato
Significant Increase in Conduction Band Discontinuity Due to Solid Phase Epitaxy of Al_2O_3 Gate Insulator Films on GaN Semiconductor
Appl. Phys. Lett., **101** (2012) 231607.

T.Mizuno, J.Adachi, N.Miyauchi, M.Kazama, M.Stener, P.Decleva and A.Yagishita
Recoil Frame Photoelectron Angular Distributions of BF3: A Sensitive Probe of the Shape Resonance in the F 1s Continuum
J. Chem. Phys., **136** (2012) 074305.

M.Stener, P.Decleva, J.Adachi, N.Miyauchi, M.Yamazaki and A.Yagishita
Recoil Frame Photoelectron Angular Distributions in Core O 1s Ionization of H_2CO
J. Phys. B, **45** (2012) 194004.

M.Kazama, H.Shinotsuka, T.Fujikawa, M.Stener, P.Decleva, J.Adachi, T.Mizuno and A.Yagishita
Multiple-Scattering Calculations for 1s Photoelectron Angular Distributions from Single Oriented Molecules in the Energy Region above 50eV
J. Elec. Spec. Relat. Phenom., **185** (2012) 535.

Y.Kozuka, H.Seki, T.C.Fujita, S.Chakraverty, K.Yoshimatsu, H.Kumigashira, M.Oshima, M.S.Bahramy, R.Arita and M.Kawasaki
Epitaxially Stabilized $EuMoO_3$: A New Itinerant Ferromagnet
Chem. Mater., **24** (2012) 3746.

3A

H.Wadati, J.Okamoto, M.Garganourakis, V.Scagnoli, U.Staub, Y.Yamasaki, H.Nakao, Y.Murakami, M.Mochizuki, M.Nakamura, M.Kawasaki and Y.Tokura
Origin of the Large Polarization in Multiferroic $YMnO_3$ Thin Films Revealed by Soft- and Hard-X-Ray Diffraction
Phys. Rev. Lett., **108** (2012) 047203.

D.Bizen, H.Nakao, K.Iwasa, Y.Murakami, T.Osakabe, J.Fujioka, T.Yasue, S.Miyasaka and Y.Tokura
Magnetic Phase Diagrams of YVO_3 and $TbVO_3$ under High Pressure
J. Phys. Soc. Jpn., **81** (2012) 024715.

T.Matsumura, T.Yonemura, K.Kunimori, M.Sera, F.Iga, T.Nagao and J.Igarashi
Antiferroquadrupole Order and Magnetic Field Induced Octupole in CeB_6
Phys. Rev. B, **85** (2012) 174417.

M.Uchida, Y.Yamasaki, Y.Kaneko, K.Ishizaka, J.Okamoto, H.Nakao, Y.Murakami and Y.Tokura
Pseudogap-Related Charge Dynamics in the Layered Nickelate $R_{2-x}Sr_xNiO_4$ ($x \sim 1$)
Phys. Rev. B, **86** (2012) 165126.

3B

T.Hasegawa, S.Munakata, S.Imanishi, Y.Kakefuda, K.Edamoto and K.Ozawa
Oxidation of Ultra-Thin Ti Films on Mo(100): Soft X-Ray Photoelectron Spectroscopy Study
Surf. Sci., **606** (2012) 414.

K.Ozawa
Metallization of Oxide Semiconductor Surfaces by Chemical Modification
Chemical Industry, **63** (2012) 207. (*in Japanese*).

S.Imanishi, S.Munakata, Y.Kakefuda, K.Edamoto and K.Ozawa
Characterization of Ni2P(10-10): Soft X-Ray Photoelectron Spectroscopy Study
e-J. Surf. Sci. Nanotech., **10** (2012) 45.

M.EMORI, M.Sugita, K.Ozawa and H.Sakama
Electronic Structure of Epitaxial Anatase TiO_2 Films: Angle-Resolved Photoelectron Spectroscopy Study
Phys. Rev. B, **85** (2012) 035129.

K.Edamoto, T.Hasegawa, S.Munakata, Y.Kakefuda and K. Ozawa
Electronic Structure of the Ultra-Thin TiO_2 Film on Ag(100): Resonant Photoemission Spectroscopy Study
e-J. Surf. Sci. Nanotech., **10** (2012) 286.

S.Wang, T.Sakurai, R.Kuroda and K.Akimoto
Energy Band Bending Induced Charge Accumulation at Fullerene/Bathocuproine Heterojunction Interface
Appl. Phys. Lett., **100** (2012) 243301.

T.Odagiri, M.Nakano, T.Tanabe, Y.Kumagai, I.H.Suzuki, M.Kitajima and N.Kouchi
Three-Body Neutral Dissociations of a Multiply Excited Water Molecule around the Double Ionization Potential
J. Phys. B, **45** (2012) 215204.

T.Osawa, K.Kawajiri, N.Suzuki, T.Nagata, Y.Azuma and F.Koike
Photoion-Yield Study of the 3p-3d Giant Resonance Excitation Region of Isolated Cr, Mn and Fe Atoms
J. Phys. B, **45** (2012) 225204.

S.Wang, T.Sakurai, R.Kuroda and K.Akimoto
Energy Level Alignment of C_{60}/Ca Interface with Bathocuproine as an Interlayer Studied by Ultraviolet Photoelectron Spectroscopy
Jpn. J. Appl. Phys., **51** (2012) 10NE32.

T.Isao
Electronic Resonance and Photoemission Study of Nitrogen Doped TiO_2 Rutile (110) Single Crystals
Appl. Surf. Sci., **259** (2012) 320.

3C

M.Ito, R.Nagayasu, T.Tadenuma, K.Suzuki, A.Sato, H.Adachi, Y.Sakurai and Y.Onuki
A Study of Spin and Orbital Magnetic Form Factors of $CeRh_3B_2$ by X-ray Magnetic Diffraction
Key Engineering Materials, **497** (2012) 3.

4A

Y.Shinohara, K.Yamazoe, T.Sakurai, S.Kimata, T.Maruyama and Y.Amemiya
Effect of Structural Inhomogeneity on Mechanical Behavior of Injection Molded Polypropylene Investigated with Microbeam X-Ray Scattering
Macromolecules, **45** (2012) 1398.

Y.Sumino, H.Kitahata, Y.Shinohara, N.L.Yamada and H.Seto
Formation of a Multiscale Aggregate Structure through Spontaneous Blebbing of an Interface
Langmuir, **28** (2012) 3378.

S.Mitsunobu, F.Shiraishi, H.Makita, B.N.Orcutt, S.Kikuchi, B.B.Jorgensen and Y.Takahashi
Bacteriogenic Fe(III) (oxyhydr)oxides Characterized by Synchrotron Microprobe Coupled with Spatially-Resolved Phylogenetic Analysis
Environ. Sci. Technol., **64** (2012) 3304.

C.Muramatsu, M.Sakata and S.Mitsunobu
Immobilization of arsenic(V) during the Transformation of Ferrihydrite: A Direct Speciation Study using Synchrotron-Based XAFS Spectroscopy
Chem. Lett., **41** (2012) 270.

W.Satake, P.C.Buchanan, T.Mikouchi and M.Miyamoto
Redox States of Some HED Meteorites as Inferred from Micro-XANES Analyses of Plagioclase
43rd Lunar and Planetary Science Conference, **XLIII** (2012) 1725.

T.Mikouchi, M.Zolensky, W.Satake and L.Le
The Valence of Iron in CM Chondrite Serpentine as Measured by Synchrotron XANES
43rd Lunar and Planetary Science Conference, **XLIII** (2012) 1496.

A.Ito, T.Inoue, K.Takehara, Y.Taki and K.Shinohara
Mapping of Ca and Cysteic Acid, an Oxidation Product of Cystine, in Human Hair at Submicron Resolution
Ad. X-Ray Chem. Anal. Jpn., **43** (2012) 161. (*in Japanese*).

J.Watanabe, Y.Tani, N.Miyata, H.Seyama, S.Mitsunobu and H.Naitoh
Concurrent Sorption of As(V) and Mn(II) during Biogenic Manganese Oxide Formation
Chemical Geology, **306-307** (2012) 123.

Y.Nozue, S.Seno, T.Nagamatsu, S.Hosoda, Y.Shinohara, Y.Amemiya, E.B.Berda, G.Rojas, K.B.Wagener
Cross Nucleation in Polyethylene with Precisely Spaced Ethyl Branches
ACS Macro Lett., **1** (2012) 772.

A.Iida and Y.Takanishi
Synchrotron X-Ray Microbeam Characterization of Smectic A Liquid Crystals under Electric Field
Adv. X-ray Anal., **55** (2012) 73.

S.Asaoka, Y.Takahashi, Y.Araki and M.Tanimizu
Comparison of Antimony and Arsenic Behavior in an Ichinokawa River Water-Sediment System
Chemical Geology, **334** (2012) 1.

Y.Yokoyama, K.Tanaka and Y.Takahashi
Differences in the Immobilization of Arsenite and Arsenate into Calcite
Geochim. Cosmochim. Acta, **91** (2012) 202.

Y.Nagai, Y.Kawabata and T.Kato
Microscopic Investigation on Morphologies of Bilayer Gel Structure in the Mixed Polyoxyethylene-Type Nonionic Surfactant Systems
J. Phys. Chem. B, **116** (2012) 12558.

M.Lei, X.-M.Wan, Z.-C.Huang, T.-B.Chen, X.-W.Li and Y.-R.Liu
First Evidence on Different Transportation Modes of Arsenic and Phosphorus in Arsenic Hyperaccumulator *Pteris vittata*
Environ. Pollut., **161** (2012) 1.

K.Okamoto, T.Noma, A.Komoto, W.Kubo, M.Takahashi, A.Iida and H.Miyata
X-Ray Waveguide Mode in Resonance with a Periodic Structure
Phys. Rev. Lett., **109** (2012) 233907.

P.Wassell, A.Okamura, N.W.G.Young, G.Bonwick, C.Smith, K.Sato and S Ueno
Synchrotron Radiation Macrobeam and Microbeam X-Ray Diffraction Studies of Interfacial Crystallization of Fats in Water-in-Oil Emulsions
Langmuir, **28** (2012) 5539.

4B2

Y.Yang, M.Hirayama, M.Yonemura and R.Kanno
Synthesis, Crystal Structure and Electrode Characteristics of $LiMnPO_4(OH)$ Cathode for Lithium Batteries
J. Solid State Chem., **187** (2012) 124.

Y.-C.Chen, M.Yashima, T.Ohta, K.Ohoyama and S.Yamamoto
Crystal Structure, Oxygen Deficiency, and Oxygen Diffusion Path of Perovskite-Type Lanthanum Cobaltites $La_{0.4}Ba_{0.6}CoO_{3-\delta}$ and $La_{0.6}Sr_{0.4}CoO_{3-\delta}$
J. Phys. Chem. C, **116** (2012) 5246.

K.Fujii, H.Uekusa, N.Itoda, E.Yonemochi and K.Terada
Mechanism of Dehydration-Hydration Processes of Lisinopril Dihydrate Investigated by ab Initio Powder X-Ray Diffraction Analysis
Crystal Growth and Design, **12** (2012) 6165.

J.M.Clark, S.Nishimura, A.Yamada and M.S.Islam
High-Voltage Pyrophosphate Cathode: Insights into Local Structure and Lithium-Diffusion Pathways
Angew. Chem. Int. Ed., **124** (2012) 13326.

K.Kakimoto, T.Hotta and I.Kagomiya
Fine Structural Analysis and Phase Transition Behavior for Li-Modified $Na_{0.5}K_{0.5}NbO_3$ Lead-Free Piezoelectric Ceramics
Ceramics International, **38** (2012) S319.

K.Kakimoto, R.Kaneko and I.Kagomiya
Grain-Size-Controlled (Li,Na,K)NbO_3 Ceramics using Powder Source Classified by Centrifugal Separator
Jpn. J. Appl. Phys., **51** (2012) 09LD06.

M.Yashima, H.Yamada, S.Nuansaeng and T.Ishihara
Role of Ga^{3+} and Cu^{2+} in the High Interstitial Oxide-Ion Diffusivity of Pr_2NiO_4-Based Oxides: Design Concept of Interstitial Ion Conductors through the Higher-Valence d^{10} Dopant and Jahn-Teller Effect
Chem. Mater., **24** (2012) 4100.

M.Tamaru, P.Barpanda, Y.Yamada, S.Nishimura and A.Yamada
Observation of the Highest Mn^{3+}/Mn^{2+} Redox Potential of 4.45 V in a $Li_2MnP_2O_7$ Pyrophosphate Cathode
J. Mater. Chem., **22** (2012) 24526.

4C

H.Wadati, J.Okamoto, M.Garganourakis, V.Scagnoli, U.Staub, Y.Yamasaki, H.Nakao, Y.Murakami, M.Mochizuki, M.Nakamura, M.Kawasaki and Y.Tokura
Origin of the Large Polarization in Multiferroic $YMnO_3$ Thin Films Revealed by Soft- and Hard-X-Ray Diffraction
Phys. Rev. Lett., **108** (2012) 047203.

D.Bizen, H.Nakao, K.Iwasa, Y.Murakami, T.Osakabe, J.Fujioka, T.Yasue, S.Miyasaka and Y.Tokura
Magnetic Phase Diagrams of YVO_3 and $TbVO_3$ under High Pressure
J. Phys. Soc. Jpn., **81** (2012) 024715.

K.Ohwada, T.Yamauchi, Y.Fujii and Y.Ueda
Two-Dimensional Charge Fluctuation in β-$Na_{0.33}V_2O_5$
Phys. Rev. B, **85** (2012) 134102.

M.Nakamura, R.Imai, N.Hoshi and O.Sakata
Interfacial Structure of Co Porphyrins on Au(111) Electrode: Interaction of Porphyrin Molecules with Substrate
Surf. Sci., **606** (2012) 1560.

H.Sakuma, H.Nakao, Y.Yamasaki and K.Kawamura
Structure of Electrical Double Layer at Mica/KI Solution Interface
J. Appl. Sol. Chem. Model., **1** (2012) 1.

H.Sakuma
A Mechanism and Stability of Water Lubrication between Mineral Surfaces: The Physics of Creeping Faults
J. Jpn. Soc. Synchrotron Rad. Res., **25** (2012) 213. (*in Japanese*).

T.Honda, Y.Ishiguro, H.Nakamura, Y.Wakabayashi and T.Kimura
Structure and Magnetic Phase Diagrams of Multiferroic Mn_2GeO_4
J. Phys. Soc. Jpn., **81** (2012) 103703.

M.Shibata, N.Hayashi, T.Sakurai, A.Kurokawa, H.Fukumitsu, T.Masuda, K.Uosaki and T.Kondo
Electrochemical Layer-by-Layer Deposition of Pseudomorphic Pt Layers on Au(111) Electrode Surface Confirmed by Electrochemical and In Situ Resonance Surface X-Ray Scattering Measurements
J. Phys. Chem. C, **116** (2012) 26464.

K.Takubo, T.Kanzaki, Y.Yamasaki, H.Nakao, Y.Murakami, T.Oguchi and T.Katsufuji
Orbital States of V Trimers in $BaV_{10}O_{15}$ Detected by Resonant X-Ray Scattering
Phys. Rev. B, **86** (2012) 085141.

M.Uchida, Y.Yamasaki, Y.Kaneko, K.Ishizaka, J.Okamoto, H.Nakao, Y.Murakami and Y.Tokura
Pseudogap-Related Charge Dynamics in the Layered Nickelate $R_{2-x}Sr_xNiO_4$ ($x \sim 1$)
Phys. Rev. B, **86** (2012) 165126.

5A

T.Tsuda, T.Suzuki and S.Kojima
Crystallization and Preliminary X-Ray Diffraction Analysis of *Bacillus subtilis* YwfE, an L-Amino-Acid Ligase
Acta Cryst. F, **68** (2012) 203.

J.Kondo
A Structural Basis for the Antibiotic Resistance Conferred by an A1408G Mutation in 16S rRNA and for the Antiprotozoal Activity of Aminoglycosides
Angew. Chem. Int. Ed., **51** (2012) 465.

S.Okazaki, R.Kato, Y.Uchida, T.Taguchi, H.Arai and S.Wakatsuki
Structural Basis of the Strict Phospholipid Binding Specificity of the Pleckstrin Homology Domain of Human Evectin-2
Acta Cryst. D, **68** (2012) 117.

A.Rohaim, M.Kawasaki, R.Kato, I.Dikic and S.Wakatsuki
Structure of a Compact Conformation of Linear Diubiquitin
Acta Cryst. D, **68** (2012) 102.

N.Kuwabara, T.Oyama, D.Tomioka, M.Ohashi, J.Yanagisawa, T.Shimizu and H.Miyachi
Peroxisome Proliferator-Activatedreceptors (PPARs) Have Multiple Binding Points That Accommodate Ligands Invarious Conformations: Phenypropanoic Acid-Type PPAR Ligands Bind to PPAR Indifferent Conformations, Depending on the Subtype
J. Med. Chem., **55** (2012) 893.

O.Tsuruta, H.Yokoyama and S.Fujii
A New Crystal Lattice Structure of *Helicobacter pylori* Neutrophil-Activating Protein (HP-NAP)
Acta Cryst. F, **68** (2012) 134.

D.-H.Im, K.Kimura, F.Hayasaka, T.Tanaka, M.Noguchi, A.Kobayashi, S.Shoda, K.Miyazaki, T.Wakagi and S.Fushinobu
Crystal Structures of Glycoside Hydrolase Family 51 α-L-Arabinofuranosidase from *Thermotoga maritima*
Biosci. Biotechnol. Biochem., **76** (2012) 423.

J.Wachino, Y.Yamaguchi, S.Mori, Y.Yamagata, Y.Arakawa and K.Shibayama
Crystallization and Preliminary X-Ray Analysis of the Subclass B3 Metallo-β-Lactamase SMB-1 that Confers Carbapenem Resistance
Acta Cryst. F, **68** (2012) 343.

K.Hanaya, M.Suetsugu, S.Saijo, I.Yamato and S.Aoki
Potent Inhibition of dinuclear zinc(II) Peptidase, an Aminopeptidase from *Aeromonas proteolytica*, by 8-Quinolinol Derivatives: Inhibitor Design Based on Zn^{2+} Fluorophores, Kinetic, and X-Ray Crystallographic Study
J. Biol. Inorg. Chem., **17** (2012) 517.

H.Nojiri
Structural and Molecular Genetic Analyses of the Bacterial Carbazole Degradation System
Biosci. Biotechnol. Biochem., **76** (2012) 1.

K.Yoneda, H.Sakuraba, T.Araki and T.Ohshima
Crystal Structure of Binary and Ternary Complexes of Archaeal UDP-Galactose 4-Epimerase-like L-Threonine Dehydrogenase from *Thermoplasma volcanium*
J. Biol. Chem., **287** (2012) 12966.

S.Nakano, M.Sugihara, R.Yamada, K.Katayanagi and S.Tate
Structural Implication for the Impaired Binding of W150A Mutant LOX-1 to Oxidized Low Density Lipoprotein, OxLDL
Biochim. Biophys. Acta, **1824** (2012) 739.

Z.Zhang, L.Chen, L.Gao, K.Lin, L.Zhu, Y.Lu, X.Shi, Y.Gao, J.Zhou, P.Xu, J.Zhang and G.Wu
Structural Basis for the Recognition of Asef by Adenomatous Polyposis Coli
Cell Res., **22** (2012) 372.

Q.Cao, X.-J.Wang, C.-W.Liu, D.-F.Liu, L.-F.Li, Y.-Q.Gao and X.-D.Su
Inhibitory Mechanism of Caspase-6 Phosphorylation Revealed by Crystal Structures, Molecular Dynamics (MD) Simulations and Biochemical Assays
J. Biol. Chem., **287** (2012) 15371.

M.Nagae, S.Re, E.Mihara, T.Nogi, Y.Sugita and J.Takagi
Crystal Structure of $\alpha 5\beta 1$ Integrin Ectodomain: Atomic Details of the Fibronectin Receptor
J. Cell Biol., **197** (2012) 131.

R.Kawakami, T.Satomura, H.Sakuraba and T.Ohshima
L-Proline Dehydrogenases in Hyperthermophilic Archaea: Distribution, Function, Structure, and Application
Appl. Microbiol. Biotech., **93** (2012) 83.

T.Satomura, A.Hiraki, T.Kawai, R.Kawakami, T.Ohshima and H.Sakuraba
Expression, Purification, Crystallization and Preliminary X-Ray Diffraction Analysis of a Galactose 1-Phosphate Uridylyltransferase from the Hyperthermophilic Archaeon *Pyrobaculum Aerophilum*
Acta Cryst. F, **68** (2012) 330.

D.Pan and Y.Matsuura
Structures of the Pleckstrin Homology Domain of *Saccharomyces cerevisiae* Avo1 and its human orthologue Sin1, an Essential Subunit of TOR Complex 2
Acta Cryst. F, **68** (2012) 386.

T.Nagae, C.Kato and N.Watanabe
Structural Analysis of 3-Isopropylmalate Dehydrogenase from the Obligate Piezophile *Shewanella Benthica* DB21MT-2 and the Nonpiezophile *Shewanella Oneidensis* MR-1
Acta Cryst. F, **68** (2012) 265.

M.Oda, M.Takahashi, H.Tsuge, M.Nagahama and J.Sakurai
Role of Side-Edge Site of Sphingomyelinase from *Bacillus Cereus*
Biochem. Biophys. Res. Commun., **422** (2012) 128.

R.Arai, N.Kobayashi, A.Kimura, T.Sato, K.Matsuo, A.F.Wang, J.M.Platt, L.H.Bradley and M.H.Hecht
Domain-Swapped Dimeric Structure of a Stable and Functional *De Novo* Four-Helix Bundle Protein, WA20
J. Phys. Chem. B, **116** (2012) 6789.

T.Matsumoto, T.Kinoshita, H.Matsuzaka, R.Nakai, Y.Kirii, K.Yokota and T.Tada
Crystal Structure of Non-Phosphorylated MAP2K6 in a Putative Auto-Inhibition State
J. Biochem., **151** (2012) 541.

H.Sakurama, S.Fushinobu, M.Hidaka, E.Yoshida, Y.Honda, H.Ashida, M.Kitaoka, H.Kumagai, K.Yamamoto and T.Katayama
1,3-1,4-α-L-Fucosynthase that Specifically Introduces Lewis a/x Antigens into Type-1/2 Chains
J. Biol. Chem., **287** (2012) 16709.

H.Shoun, S.Fushinobu, L.Jiang, S.-W.Kim and T.Wakagi
Fungal Denitrification and Nitric Oxide Reductase Cytochrome P450nor
Phil. Trans. R. Soc. B, **367** (2012) 1186.

T.Wakagi
A Special Enzyme Acting in a Primordial Metabolism; Discovery of One-Enzyme with Two Reactions
Kagaku, **67** (2012) 72. (*in Japanese*).

H.Nishimasu, S.Fushinobu and T.Wakagi
Molecular Mechanism by which One Enzyme Catalyzes Two Reactions
J. Cryst. Soc. Jpn., **54** (2012) 113. (*in Japanese*).

T.-O.Kim, D.-W.Im, H.Y.Jung, S.J.Kwon and Y.-S.Heo
Purification, Crystallization and Preliminary X-Ray Diffraction Analysis of Enoyl-Acyl Carrier Protein Reductase (FabK) from *Streptococcus mutans* Strain UA159
Acta Cryst. F, **68** (2012) 292.

M.M.Islam, M.A.Khan and Y.Kuroda
Analysis of Amino Acid Contributions to Protein Solubility using Short Peptide Tags Fused to a Simplified BPTI Variant
Biochim. Biophys. Acta, **1824** (2012) 1144.

X.Zhang, J.Zhang, G.Guo, X.Mao, Y.Hu and Q.Zou
Crystal Structure of a Flavin-dependent Thymidylate Synthase from *Helicobacter pylori* strain 26695
Protein & Peptide Letters, **19** (2012) 1225.

U.Ohto, K.Fukase, K.Miyake and T.Shimizu
Structural Basis of Species-Specific Endotoxin Sensing by Innate Immune Receptor TLR4/MD-2
Proc. Natl. Acad. Sci. USA, **109** (2012) 7421.

B.G.Han, K.C.Jeong, J.W.Cho, B.C.Jeong, H.K.Song, J.Y.Lee, D.H.Shin, S.Lee and B.I.Lee
Crystal Structure of *Pyrococcus Furiosus* PF2050, a Member of the DUF2666 Protein Family
FEBS Lett., **586** (2012) 1384.

N.Suzuki, Y.-M.Kim, Z.Fujimoto, M.Momma, M.Okuyama, H.Mori, K.Funane and A.Kimura
Structural Elucidation of Dextran Degradation Mechanism by *Streptococcus mutans* Dextranase Belonging to Glycoside Hydrolase Family 66
J. Biol. Chem., **287** (2012) 19916.

M.Michikawa, H.Ichinose, M.Momma, P.Biely, S.Jongkees, M.Yoshida, T.Kotake, Y.Tsumuraya, S.Withers, Z.Fujimoto and S.Kaneko
Structural and Biochemical Characterization of Glycoside Hydrolase family 79 β-Glucuronidase from *Acidobacterium capsulatum*
J. Biol. Chem., **287** (2012) 14069.

H.Sakuraba, T.Satomura, R.Kawakami, K.Kim, Y.Hara, K.Yoneda and T.Ohshima
Crystal Structure of Novel Dye-Linked L-Proline Dehydrogenase from Hyperthermophilic Archaeon *Aeropyrum Pernix*
J. Biol. Chem., **287** (2012) 20070.

S.Matsumoto, M.Igura, J.Nyirenda, M.Matsumoto, S.Yuzawa, N.Noda, F.Inagaki and D.Kohda
Crystal Structure of the C-Terminal Globular Domain of Oligosaccharyltransferase from *Archaeoglobus Fulgidus* at 1.75 ÅResolution
Biochemistry, **51** (2012) 4157.

M.Nishikiori, S.Sugiyama, H.Xiang, M.Niiyama, K.Ishibashi, T.Inoue, M.Ishikawa, H.Matsumura and E.Katoh.
Crystal Structure of the Superfamily 1 Helicase from Tomato Mosaic Virus
J. Virology, **86** (2012) 7565.

H.Kondo, Y.Hanada, H.Sugimoto, T.Hoshino, C.P.Garnham, P.L.Davies and S.Tsuda
Ice-Binding Site of Snow Mold Fungus Antifreeze Protein Deviates from Structural Regularity and High Conservation
Proc. Natl. Acad. Sci. USA, **109** (2012) 9360.

Q.Tang, P.Gao, Y.-P.Liu, A.Gao, X.-M.An, S.Liu, X.-X.Yan and D.-C.Liang
RecOR Complex Including RecR N-N Dimer and RecO Monomer Displays a High Affinity for ssDNA
Nucleic Acids Res., **40** (2012) 11115.

T.Shirouzono, M.Chirifu, C.Nakamura, Y.Yamagata and S.Ikemizu
Preparation, Crystallization and Preliminary X-Ray Diffraction Studies of the Glycosylated Form of Human Interleukin-23
Acta Cryst. F, **68** (2012) 432.

A.Nakamura, M.Fujihashi, R.Aono, T.Sato, Y.Nishiba, S.Yoshida, A.Yano, H.Atomi, T.Imanaka and K.Miki
Dynamic, Ligand-Dependent Conformational Change Triggers Reaction of Ribose-1,5-Bisphosphate Isomerase from *Thermococcus Kodakarensis* KOD1
J. Biol. Chem., **287** (2012) 20784.

H.Makyio, M.Ohgi, T.Takei, S.Takahashi, H.Takatsu, Y.Katoh, A.Hanai, T.Ueda, Y.Kanaho, Y.Xie, HW.Shin, H.Kamikubo, M.Kataoka, M.Kawasaki, R.Kato, S.Wakatsuki and K.Nakayama
Structural Basis for Arf6-MKLP1 Complex Formation on the Flemming Body Responsible for Cytokinesis
EMBO J., **31** (2012) 2590.

N.N.Noda, T.Kobayashi, W.Adachi, Y.Fujioka, Y.Ohsumi and F.Inagaki
Structure of the Novel C-Terminal Domain of Vacuolar Protein Sorting 30/Autophagy-Related Protein 6 and Its Specific Role in Autophagy
J. Biol. Chem., **287** (2012) 16256.

N.N.Noda
Structure of Atg7 Alone and Its Atg8-Bound Forms
J. Cryst. Soc. Jpn., **54** (2012) 166.

T.Nishioka, Y.Yasutake, Y.Nishiya and T.Tamura
Structure-Guided Mutagenesis for the Improvement of Substrate Specificity of *Bacillus Megaterium* Glucose 1-Dehydrogenase IV
FEBS J., **279** (2012) 3264.

H.Nakano, A.Hosokawa, R.Tagawa, K.Inaka, K.Ohta,T.Nakatsu, H.Kato and K.Watanabe
Crystallization and Preliminary X-Ray Crystallographic Analysis of Pz Peptidase B from *Geobacillus Collagenovorans* MO-1
Acta Cryst. F, **68** (2012) 757.

H.Sakuraba, T.Kawai, K.Yoneda and T.Ohshima
Structure of a UDP-Glucose Dehydrogenase from the Hyperthermophilic Archaeon *Pyrobaculum Islandicum*
Acta Cryst. F, **68** (2012) 1003.

Y.Kezuka, Y.Yoshida and T.Nonaka
Structural Insights into Catalysis by βC-S lyase from *Streptococcus Anginosus*
Proteins, **80** (2012) 2447.

K.Yoneda
Structural and Functional Analyses of Novel NAD(P) Dependent Amino Acid Dehydrogenases from Archaea
vitamins (Japan), **86** (2012) 74. (*in Japanese*).

Y.Shoyama, T.Tamada, K.Kurihara, A.Takeuchi, F.Taura, S.Arai, M.Blaber, Y.Shoyama, S.Morimoto and R.Kuroki
Structure and Function of Δ1-Tetrahydrocannabinolic Acid (THCA) Synthase, the Enzyme Controlling the Psychoactivity of *Cannabis sativa*
J. Mol. Biol., **423** (2012) 96.

M.Momma and Z.Fujimoto
Interdomain Disulfide Bridge in the Rice Granule Bound Starch Synthase I Catalytic Domain as Elucidated by X-Ray Structure Analysis
Biosci. Biotechnol. Biochem., **76** (2012) 1591.

W-Y.Jeng, N-C.Wang, C-T.Lin, W-J.Chang, C-I.Liu and A.H-J.Wang
High-Resolution Structures of *Neotermes Koshunensis* β-Glucosidase Mutants Provide Insights into the Catalytic Mechanism and the Synthesis of Glucoconjugates
Acta Cryst. D, **68** (2012) 829.

S.J.Lee, S-J.Lee, S.K.Lee, H-J.Yoon, H.H.Lee, K.K.Kim, B.J.Lee, B.I.Lee and S.W.Suh
Structures of *Staphylococcus aureus* Peptide Deformylase in Complex with Two Classes of New Inhibitors
Acta Cryst. D, **68** (2012) 784.

H.Yoshida, S.Yamashita, M.Teraoka, A.Itoh, S.Nakakita, N.Nishi and S.Kamitori
X-Ray Structure of a Protease-Resistant Mutant Form of Human Galectin-8 with Two Carbohydrate Recognition Domains
FEBS J., **279** (2012) 3937.

K.Nakamura, Z.Man, Y.Xie, A.Hanai, H.Makyio, M.Kawasaki, R.Kato, H-W.Shin, K.Nakayama and S.Wakatsuki
Structural Basis for Membrane Binding Specificity of the Bin/Amphiphysin/Rvs (BAR) Domain of Arfaptin-2 Determined by Arl1 GTPase
J. Biol. Chem., **287** (2012) 25478.

K.Suzuki, N.Ohbayashi, J.Jiang, X.Zhang, M.M.Hoque, M.Tsunoda, K.Murayama, H.Tanaka and A.Takenaka
Crystallographic Study of the Interaction of the Anti-HIV Lectin Actinohivin with α(1-2)mannobiose Moiety of gp120 HMTG
Acta Cryst. F, **68** (2012) 1060.

M.M.Hoque, K.Suzuki, M.Tsunoda, J.Jiang, F.Zhang, A.Takahashi, N.Ohbayashi, X.Zhang, H.Tanaka, S.Omura and A.Takenaka
Structural Insights into the Specific Anti-HIV Property of Actinohivin: Structure of its Complex with the α(1-2)mannobiose Moiety of gp120
Acta Cryst. D, **68** (2012) 1671.

M.Koyama and Y.Matsuura
Mechanistic Insights from the Recent Structures of the CRM1 Nuclear Export Complex and its Disassembly Intermediate
Biophysics, **8** (2012) 145.

Y.Kezuka, N.Abe, Y.Yoshida and T.Nonaka
Purification, Crystallization and Preliminary X-Ray Analysis of Two Hydrogen Sulfide-Producing Enzymes from *Fusobacterium nucleatum*
Acta Cryst. F, **68** (2012) 1507.

T.Matsui, J.Yamane, N.Mogi, H.Yamaguchi, H.Takemoto, M.Yao and I.Tanaka
Structural Reorganization of the Bacterial Cell -Division Protein FtsZ from *Staphylococcus aureus*
Acta Cryst. D, **68** (2012) 1175.

Y.Itoh, S.Sekine and S.Yokoyama
Crystallization and Preliminary X-Ray Crystallographic Analysis of *Aquifex aeolicus* SelA, a Bacterial Selenocysteine Synthase
Acta Cryst. F, **68** (2012) 1128.

Y.Itoh, S.Sekine and S.Yokoyama
Crystallization and Preliminary X-Ray Crystallographic Analysis of Bacterial $tRNA^{Sec}$ in Complex with Seryl-tRNA Synthetase
Acta Cryst. F, **68** (2012) 678.

P.Zhang, A.Reichardt, H.Liang, R.Aliyari, D.Cheng, Y.Wang, F.Xu, G.Cheng and Y.Liu
Single Amino Acid Substitutions Confer the Antiviral Activity of the TRAF3 Adaptor Protein onto TRAF5
Science Signaling, **5** (2012) 1.

F.Hou, T.Miyakawa, D.Takeshita, M.Kataoka, A.Uzura, K.Nagata, S.Shimizu and M.Tanokura
Expression, Purification, Crystallization and X-Ray Analysis of 3-Quinuclidinone Reductase from *Agrobacterium tumefaciens*.
Acta Cryst. F, **68** (2012) 1237.

L.Guo, M.Okai, T.Mase, F.L.Imai, T.Miyakawa, K.Nagata, H.Yamanaka, H.Fujii, M.Hibi, J.Ogawa and M.Tanokura
Expression, Purification, Crystallization and Preliminary X-Ray Analysis of 4-Hydroxy-3-Methyl-2-Keto-Pentanoate Aldolase, (asHPAL) from *Arthrobacter simplex* Strain AKU 626
Acta Cryst. F, **68** (2012) 958.

Z.Yang, H.Liang, Q.Zhou, Y.Li, H.Chen, W.Ye, D.Chen, J.Fleming, H.Shu and Y.Liu
Crystal Structure of ISG54 Reveals a Novel RNA Binding Structure and Potential Functional Mechanisms
Cell Res., **9** (2012) 1328.

M.Yamaguchi, K.Matoba, R.Sawada, Y.Fujioka, H.Nakatogawa, H.Yamamoto, Y.Kobashigawa, H.Hoshida, R.Akada, Y.Ohsumi, N.N.Noda and F.Inagaki
Noncanonical Recognition and UBL Loading of Distinct E2s by Autophagy-Essential Atg7
Nature Structural Molecular Biology, **19** (2012) 1250.

Y.Ashikawa, Z.Fujimoto, Y.Usami, K.Inoue, H.Noguchi, H.Yamane and H.Nojiri
Structural Insight into the Substrate- and Dioxygen-Binding Manner in the Catalytic Cycle of Rieske Nonheme Iron Oxygenase System, Carbazole 1,9a-Dioxygenase
BMC Struct. Biol., **12** (2012) 15.

M.Unno, K.Kizawa, M.Ishihara and H.Takahara
Crystallization and Preliminary X-Ray Crystallographic Analysis of Human Peptidylarginine Deiminase Type III
Acta Cryst. F, **68** (2012) 668.

K.Arita, S.Isogai, T.Oda, M.Unoki, K.Sugita, N.Sekiyama, K.Kuwata, R.Hamamoto, H.Tochio, M.Sato, M.Ariyoshi and M.Shirakawa
Recognition of Modification Status on a Histone H3 Tail by Linked Histone Reader Modules of the Epigenetic Regulator UHRF1
Proc. Natl. Acad. Sci. USA, **109** (2012) 12950.

K.Kubota, A.Yamagata, Y.Sato, S.Goto-Ito and S.Fukai
Get1 Stabilizes an Open Dimer Conformation of Get3 ATPase by Binding Two Distinct Interfaces
J. Mol. Biol., **422** (2012) 366.

N.Yoshimoto, Y.Sakamaki, M.Haeta, A.Kato, Y.Inaba, T.Itoh, M.Nakabayashi, N.Ito and K.Yamamoto
Butyl Pocket Formation in the Vitamin D Receptor Strongly Affects the Agonistic or Antagonistic behavior of Ligands
J. Med. Chem., **55** (2012) 4373.

Y.Sato, A.Yamagata, S.Goto-Ito, K.Kubota, R.Miyamoto, S Nakada and S.Fukai
Molecular Basis of Lys-63-linked Polyubiquitination Inhibition by the Interaction between Human Deubiquitinating Enzyme OTUB1 and Ubiquitin-Conjugating Enzyme UBC13
J. Biol. Chem., **287** (2012) 25860.

T.Kubota, A.Kumagai, H.Ito, S.Furukawa, Y.Someya, N.Takeda, K.Ishii, T.Wakita, H.Narimatsu and H.Shirato
Structural Basis for the Recognition of Lewis Antigens by Genogroup I Norovirus
J. Virol., **86** (2012) 11138.

F.Akita, A.Higashiura, T.Shimizu, Y.Pu, M.Suzuki, T.Uehara-Ichiki, T.Sasaya, S.Kanamaru, F Arisaka, T.Tsukihara, A.Nakagawa and T.Omura
Crystallographic Analysis Reveals Octamerization of Viroplasm Matrix Protein P9-1 of *Rice Black Streaked Dwarf Virus*
J. Virology, **86** (2012) 746.

R.Arai, S.Fukui, N.Kobayashi and J.Sekiguchi
Solution Structure of IseA, an Inhibitor Protein of DL-Endopeptidases from *Bacillus Subtilis*, Reveals a Novel Fold with a Characteristic Inhibitory Loop
J. Biol. Chem., **287** (2012) 44736.

Y.-H.Huang, X.-Y.Liu, X.-X.Du, Z.-F.Jiang and X.-D.Su
The Structural Basis for the Sensing and Binding of Cyclic di-GMP by STING
Nature Structural Molecular Biology, **19** (2012) 728.

X.-X.Fan, Y.-F.Zhou, X.Liu, L.-F.Li and X.-D.Su
Ellman's Reagent in Promoting Crystallization and Structure Determination of *Anabaena* CcbP
Acta Cryst. F, **68** (2012) 1409.

H.Tanaka, N.Miyazaki, K.Matoba, T.Nogi, K.Iwakasaki and J.Takagi
Higher-Order Architecture of Cell Adhesion Mediated by Polymorphic Synaptic Adhesion Molecules Neurexin and Neuroligin
Cell Reports, **2** (2012) 101.

M.Fujihashi, M.Hiraki, G.Ueno, S.Baba, H.Murakami, M.Suzuki, N.Watanabe, I.Tanaka, A.Nakagawa, S.Wakatsuki, M.Yamamoto and K.Miki
Crystal Sample Pins and a Storage Cassette System Compatible with the Protein Crystallography Beamlines at both the Photon Factory and SPring-8
J. Appl. Cryst., **45** (2012) 1156.

Y.W.Park, H.K.Yeo and J.Y.Lee
Crystallization and Preliminary X-Ray Diffraction Analysis of a Fatty-Acid Metabolism Regulatory Protein, FadR, from *Bacillus halodurans*
Acta Cryst. F, **68** (2012) 975.

T.Miyafusa, J.M.M.Caaveiro, Y.Tanaka and K.Tsumoto
Crystal Structure of the Enzyme CapF of *Staphylococcus aureus* Reveals a Unique Architecture Composed of Two Functional Domains
Biochem. J., **443** (2012) 671.

A.Matsuura, J.Y.Yoon, H.J.Yoon, H.H.Lee and S.W.Suh
Crystal Structure of Pyridoxal Biosynthesis Lyase PdxS from *Pyrococcus Horikoshii*
Mol. Cells, **34** (2012) 407.

K.H.Kim, D.R.An, J.Song, J.Y.Yoon, H.S.Kim, H.J.Yoon, H.N.Im, J.Kim, D.J.Kim, S.J.Lee, K-H.Kim, H-M.Lee, H-J.Kim, E-K.Jo, J.Y.Lee and S.W.Suh
Mycobacterium Tuberculosis Eis Protein Initiates Suppression of Host Immune Responses by Acetylation of DUSP16/MKP-7
Proc. Natl. Acad. Sci. USA, **109** (2012) 7729.

S.Watanabe, D.Sasaki, T.Tominaga and K.Miki
Structural Basis of [NiFe] Hydrogenase Maturation by Hyp Proteins
Biol. Chem., **393** (2012) 1089.

K.Ito, R.Murakami, M.Mochizuki, H.Qi, Y.Shimizu, K.Miura, T.Ueda and T.Uchiumi
Structural Basis for the Substrate Recognition and Catalysis of Peptidyl-tRNA Hydrolase
Nucl. Acids Res., **40** (2012) 10521.

T.Hayashi, M.Senda, H.Morohashi, H.Higashi, M.Horio, Y.Kashiba, L.Nagase, D.Sasaya, T.Shimizu, N.Venugopalan, H.Kumeta, N.Noda, F.Inagaki, T.Senda and M.Hatakeyama
Tertiary Structure-Function Analysis Reveals the Pathogenic Signaling Potentiation Mechanism of *Helicobacter pylori* Oncogenic Effector CagA
Cell Host & Microbe, **12** (2012) 20.

6A

T.Shinkai, M.Ito, K.Sugiyama, K.Ito and H.Yokoyama
Ordered and Foam Structures of Semifluorinated Block Copolymers in Supercritical Carbon Dioxide
Soft Matter, **8** (2012) 5811.

Y.Zhao, G.Matsuba and H.Ito
Shear-Induced Crystallization and Rheological Behavior of Syndiotactic Polystyrene
Journal of Materials Research, **27** (2012) 1372.

Y.Tozuka, K.Higashi, T.Morita, M.Nishikawa, H.Uchiyama, J.Zhang, K.Moribe, K.Nishikawa, H.Takeuchi and K.Yamamoto
Transglycosylated Rutin-Specific Non-Surface-Active Nanostructure Affects Absorption Enhancement of Flurbiprofen
European Journal of Pharmaceutics and Biopharmaceutics, **82** (2012) 120.

T.Morita, M.Ushio, K.Kanoh, E.Tanaka and K.Nishikawa
Small-Angle X-Ray Scattering Measurements of Ionic Liquids Pressurized with Carbon Dioxide using Titanium Sample Holder: 1-Butyl-3-methylimidazolium Bis(trifluoromethylsulfonyl) Amide Mixtures up to 22MPa
Jpn. J. Appl. Phys., **51** (2012) 076703.

Y.Takenaka, Y.Kawabata, H.Kitahata and T.Ohzono
Control of the Long-Axis Length of Gold Nanorods through Temperature Variation
Chem. Lett., **41** (2012) 1173.

S.Takemori and M.Kimura
Structure and Function of Skeletal Muscle and Locomotive Systems: Involvement of Water-State Transitions
J Physical Fitness Sports Med., **1** (2012) 95.

K.Nishikawa and T.Morita
Solution Chemistry Based on the Concept of Fluctuations
Mol. Sci., **6** (2012) A0054. (*in Japanese*).

A.Noro, K.Higuchi, Y.Sageshima and Y.Matsushita
Preparation and Morphology of Hybrids Composed of a Block Copolymer and Semiconductor Nanoparticles via Hydrogen Bonding
Macromolecules, **45** (2012) 8013.

Y.Sageshima, S.Arai, A.Noro and Y.Matsushita
Fabrication and Modification of Ordered Nanoporous Structures from Nanophase-Separated Block Copolymer/Metal Salt Hybrids
Langmuir, **28** (2012) 17524.

R.Hori, D.Furukawa, K.Yamamoto and S.Kutsumizu
Light-Driven Phase Transition in a Cubic Phase-Forming Binary System Composed of 4'-*n*-Docosyloxy-3'-nitrobiphenyl-4-carboxylic Acid and an Azobenzene Derivative
Chem. Eur. J., **18** (2012) 7346.

Former 6A

D.-H.Im, K.Kimura, F.Hayasaka, T.Tanaka, M.Noguchi, A.Kobayashi, S.Shoda, K.Miyazaki, T.Wakagi and S.Fushinobu
Crystal Structures of Glycoside Hydrolase Family 51 α-L-Arabinofuranosidase from *Thermotoga maritima*
Biosci. Biotechnol. Biochem., **76** (2012) 423.

H.Nojiri
Structural and Molecular Genetic Analyses of the Bacterial Carbazole Degradation System
Biosci. Biotechnol. Biochem., **76** (2012) 1.

S.Arai, Y.Yonezawa, N.Okazaki, F.Matsumoto, T.Tamada, H.Tokunaga, M.Ishibashi, M.Blaber, M.Tokunaga and R.Kuroki
A Structural Mechanism for Dimeric to Tetrameric Oligomer Conversion in *Halomonas* sp. Nucleoside Diphosphate Kinase
Protein Science, **21** (2012) 498.

R.Arai, N.Kobayashi, A.Kimura, T.Sato, K.Matsuo, A.F.Wang, J.M.Platt, L.H.Bradley and M.H.Hecht
Domain-Swapped Dimeric Structure of a Stable and Functional *De Novo* Four-Helix Bundle Protein, WA20
J. Phys. Chem. B, **116** (2012) 6789.

L.Wang,K.Zhang, L.Wu, S.Liu, H.Zhang, Q.Zhou, L.Tong, F.Sun and Z.Fan
Structural Insights into the Substrate Specificity of Human Granzyme H: The Functional Roles of a Novel RKR Motif
The Journal of Immunology, **188** (2012) 765.

H.Shoun, S.Fushinobu, L.Jiang, S.-W.Kim and T.Wakagi
Fungal Denitrification and Nitric Oxide Reductase Cytochrome P450nor
Phil. Trans. R. Soc. B, **367** (2012) 1186.

T.Wakagi
A Special Enzyme Acting in a Primordial Metabolism; Discovery of One-Enzyme with Two Reactions
Kagaku, **67** (2012) 72. (*in Japanese*).

H.Nishimasu, S.Fushinobu and T.Wakagi
Molecular Mechanism by which One Enzyme Catalyzes Two Reactions
J. Cryst. Soc. Jpn., **54** (2012) 113. (*in Japanese*).

T.Tonozuka, A.Tamaki, G.Yokoi, T.Miyazaki, M.Ichikawa, A.Nishikawa, Y.Ohta, Y.Hidaka, K.Katayama, Y.Hatada, T.Ito and K.Fujita
Crystal Structure of a Lactosucrose-Producing Enzyme, Arthrobacter sp. K-1 β-Fructofuranosidase
Enzyme and Microbial Technology, **51** (2012) 359.

H.Yokoyama, O.Tsuruta, N.Akao and S.Fujii
Crystal Structure of *Helicobacter Pylori* Neutrophil-Activating Protein with a Di-Nuclear Ferroxidase Center in a Zinc or Cadmium-Bound Form
Biochem. Biophys. Res. Commun., **422** (2012) 745.

M.Zha, C.Zhong, Y.Ou, L.Han, J.Wang and J.Ding
Crystal Structures of Human CaMKIα Reveal Insights into the Regulation Mechanism of CaMKI
PLoS One, **7** (2012) e44828.

N.Yoshimoto, Y.Sakamaki, M.Haeta, A.Kato, Y.Inaba, T.Itoh, M.Nakabayashi, N.Ito and K.Yamamoto
Butyl Pocket Formation in the Vitamin D Receptor Strongly Affects the Agonistic or Antagonistic behavior of Ligands
J. Med. Chem., **55** (2012) 4373.

R.Arai, S.Fukui, N.Kobayashi and J.Sekiguchi
Solution Structure of IseA, an Inhibitor Protein of DL-Endopeptidases from *Bacillus Subtilis*, Reveals a Novel Fold with a Characteristic Inhibitory Loop
J. Biol. Chem., **287** (2012) 44736.

N.Okazaki, M.Adachi, T.Tamada, K.Kurihara, T.Ooga, N.Kamiya, S.Kuramitsu and R.Kuroki
Crystallization and Preliminary Neutron Diffraction Studies of ADP-ribose Pyrophosphatase-I from *Thermus thermophilus* HB8
Acta Cryst. F, **68** (2012) 49.

6C

K.Hayashi, N.Happo, S.Hosokawa, W.Hu and T.Matsushita
X-Ray Fluorescence Holography
J. Phys.: Condens. Matter, **24** (2012) 093201.

H.Ishibashi and Y.Kitadai
Structural and Magnetic Properties in Spinel Type $Fe_{1-x}Zn_xV_2O_4$
J. Phys.: Conf. Ser., **391** (2012) 012092.

M.Okube, T.Yasue and S.Sasaki
Residual-Density Mapping and Site-Selective Determination of Anomalous Scattering Factors to Examine the Origin of the Fe *K* Pre-Edge Peak of Magnetite
J. Synchrotron Rad., **19** (2012) 759.

Y.Ebina, K.Akatsuka, K.Fukuda and T.Sasaki
Synthesis and In-situ X-Ray Diffraction Characterization of Two-dimensional Perovskite-type Oxide Colloids with a Controlled Molecular Thickness
Chem. Mater., **24** (2012) 4201.

7A

J.Okabayashi, K.Nomura, S.Kono and Y.Yamada
Magnetization Enhancement in Room-Temperature Ferromagnetic Fe-Mn Co-Doped SnO_2
Jpn. J. Appl. Phys., **51** (2012) 023003.

M.Sakamaki and K.Amemiya
In Situ Observation of Magnetic Anisotropy Energy of Alternately Layered FeNi Thin Films
e-J. Surf. Sci. Nanotech., **10** (2012) 97.

T.Maruyama,Y.Ishiguro, S.Naritsuka, W.Norimatsu, M.Kusunoki, K.Amemiya, H.Ishii and T.Ohta
Near-Edge X-Ray Absorption Fine Structure Study of Vertically Aligned Carbon Nanotubes Grown by the Surface Decomposition of SiC
Jpn. J. Appl. Phys., **51** (2012) 055102.

S.Tsunegi, Y.Sakuraba, K.Amemiya, M.Sakamaki, E.Ozawa, A.Sakuma, K.Takanashi and Y.Ando
Observation of Magnetic Moments at the Interface Region in Magnetic Tunnel Junctions using Depth-resolved X-Ray Magnetic Circular Dichroism
Phys. Rev. B, **85** (2012) 180408(R).

K.Amemiya
Sub-nm Resolution Depth Profiling of the Chemical State and Magnetic Structure of Thin Films by a Depth-Resolved X-Ray Absorption Spectroscopy Technique
Phys. Chem. Chem. Phys., **14** (2012) 10477.

O.Endo, M.Nakamura, R.Sumii and K.Amemiya
1D Hydrogen Bond Chain on Pt(211) Stepped Surface Observed by O K-NEXAFS Spectroscopy
J. Phys. Chem. C, **116** (2012) 13980.

K.Amemiya and M.Sakamaki
XAFS and XMCD Spectra at the Surface and Interface of Ultrathin Films Observed by the Depth-Resolved XAFS/XMCD Technique
e-J. Surf. Sci. Nanotech., **10** (2012) 521.

K.Amemiya
Recent Developments of the Wavelength-Dispersive XAFS Technique in the Soft X-Ray Region
Houshakou, **25** (2012) 269. (*in Japanese*).

J.Okabayashi, S.Kono, Y.Yamada and K.Nomura
Magnetic and Electronic Properties of Fe and Ni Codoped SnO2
J. Appl. Phys., **112** (2012) 073917.

S.Kono, K.Nomura, Y.Yamada and J.Okabayashi
Magnetic and Mössbauer Studies of Fe and Co Co-Doped SnO_2
Hyperfine Interact., **205** (2012) 105.

Y.Nanba, D.Asakura, M.Okubo, Y.Mizuno, T.Kudo, H.S.Zhou, K.Amemiya, J.-H.Guo and K.Okada
Configuration-Interaction Full-Multiplet Calculation to Analyze the Electronic Structure of a Cyano-Bridged Coordination Polymer Electrode
J. Phys. Chem. C, **116** (2012) 24896.

7C

K.Nakagawa, T.Okayama, Y.Tanimoto, K.Sotowa, S.Sugiyama, T.Moriga, S.Takenaka and M.Kishida
Preparation of Carbon-Supported Pt Catalysts Covered with Microporous Silica Layers using Organosilanes: Sintering Resistance and Superior Catalytic Performance for Cyclohexane Dehydrogenation
Appl. Catal. A, **419-420** (2012) 13.

Y.Yoshida, Y.Mitani, T.Itoi and Y.Izumi
Preferential Oxidation of Carbon Monoxide in Hydrogen using Zinc Oxide Photocatalysts Promoted and Tuned by Adsorbed Copper Ions
J. Catal., **287** (2012) 190.

K.K.Bando, T.Wada, T.Miyamoto, K.Miyazaki, S.Takakusagi, Y.Koike, Y.Inada, M.Nomura, A.Yamaguchi, T.Gott, S.Ted Oyama and K.Asakura
Combined in situ QXAFS and FTIR Analysis of a Ni Phosphide Catalyst under Hydrodesulfurization Conditions
J. Catal., **286** (2012) 165.

M.Morikawa, N.Ahmed, Y.Ogura and Y.Izumi
Polymer Electrolyte Fuel Cell Supplied with Carbon Dioxide. Can Be the Reductant Water Instead of Hydrogen?
Appl. Catal. B, **117** (2012) 317.

M.Harada, Y.Tasaki, H.Qua and T.Okada
Hydration of Ions and Salt Crystallization in Liquid Phase Coexistent with Ice at Temperature Below Eutectic Point
RSC Adv., **2** (2012) 461.

N.Furuta, S.Nishimura, P.Barpanda and A.Yamada
Fe^{3+}/Fe^{2+} Redox Couple Approaching 4 V in $Li_{2-x}(Fe_{1-y}Mn_y)P_2O_7$ Pyrophosphate Cathode
Chem. Mater., **24** (2012) 1055.

K.Asakura
Polarization-Dependent Total Reflection Fluorescence Extended X-Ray Absorption Fine Structure and its Application to Supported Catalysis
RCS Catalysis Book Series, **24** (2012) 281.

T.Ohkubo, Y.Takehara and Y.Kuroda
Water-Initiated Ordering Around a Copper Ion of Copper Acetate Confined in Slit-Shaped Carbon Micropores
Micropor. Mesopor. Mater., **154** (2012) 82.

N.Naveed, M.Morikawa and Y.Izumi
Photocatalytic Conversion of Carbon Dioxide into Methanol using Optimized Layered Double Hydroxide Catalysts
Catal. Today, **185** (2012) 263.

M.J.Hossain, H.Tsunoyama, M.Yamauchi, N.Ichikuni and T.Tsukuda
High-Yield Synthesis of PVP-Stabilized Small Pt Clusters by Microfluidic Method
Catalysis Today, **183** (2012) 101.

S.T.Oyama, H.Zhao, H.J.Freund, K.Asakura, R.Wlodarczyk and M.Sierka
Unprecedented Selectivity to the Direct Desulfurization (DDS) Pathway in a Highly Active FeNi Bimetallic Phosphide Catalyst
J. Catal., **285** (2012) 1-5.

Y.Moritomo, M.Takachi, Y.Kurihara and T.Matsuda
Thin Film Electrodes of Prussian Blue Analogues with Rapid Li+ Intercalation
Appl. Phys. Express, **5** (2012) 041801.

T.Matsuda and Y.Moritomo
Two-Electron Reaction without Structural Phase Transition in Nanoporous Cathode Material
J. Nanotechnology, **2012** (2012) 568147.

T.Shishido, K.Shimamura, K.Teramura and T.Tanaka
Role of CO_2 in Dehydrogenation of Propane over Cr-Based Catalysts
Catal. Today, **185** (2012) 151.

P.Maity, T.Wakabayashi, N.Ichikuni, H.Tsunoyama, S.Xie, M.Yamauchi and T.Tsukuda
Selective Synthesis of Organogold Magic Clusters $Au_{54}(CCPh)_{26}$
Chem. Comm., **48** (2012) 6085.

B.Sarkar, P.Prajapati, R.Tiwari, R.Tiwari, S Ghosh, S.S.Acharyya, C.Pendem, R.K.Singha, L.N.S.Konathala, J.Kumar, T.Sasaki and R.Bal
Room Temperature Selective Oxidation of Cyclohexane over Cu-Nanoclusters Supported on Nanocrystalline Cr_2O_3
Green Chemistry, **14** (2012) 2600.

C.Zhang, F.Liu, Y.Zhai, H.Ariga, N.Yi, Y.Liu, K.Asakura, M.Flytzani-Stephanopoulos and H.He
Alkali-Metal-Promoted Pt/TiO_2 Opens a More Efficient Pathway to Formaldehyde Oxidation at Ambient Temperatures
Angew. Chem. Int. Ed., **51** (2012) 9628.

T.Wada, K.K.Bando, S.T.Oyama, T.Miyamoto, S.Takakusagi and K.Asakura
Operando Observation of Ni_2P Structural Changes during Catalytic Reaction: Effect of H_2S Pretreatment
Chem. Lett., **41** (2012) 1238.

H.Kobayashi, Y.Takenaka, Y.Arachi, H.Nitani, T.Okumura, M.Shikano, H.Kageyama and K.Tatsumi
Study on Li De-Intercalation/Intercalation Mechanism for a High Capacity Layered $Li_{1.20}Ni_{0.17}Co_{0.10}Mn_{0.53}O_2$ Material
Solid State Ionics, **225** (2012) 580.

K.Kakimoto, T.Hotta and I.Kagomiya
Fine Structural Analysis and Phase Transition Behavior for Li-Modified $Na_{0.5}K_{0.5}NbO_3$ Lead-Free Piezoelectric Ceramics
Ceramics International, **38** (2012) S319.

K.Kakimoto, R.Kaneko and I.Kagomiya
Grain-Size-Controlled (Li,Na,K)NbO_3 Ceramics using Powder Source Classified by Centrifugal Separator
Jpn. J. Appl. Phys., **51** (2012) 09LD06.

C.Pendem, P.Gupta, N.Chaudhary, S.Singh, J.Kumar, T.Sasaki, A.Datta and R.Bal
Aqueous Phase Reforming of Glycerol to 1,2-Propanediol over Pt-Nanoparticles Supported on Hydrotalcite in the Absence of Hydrogen
Green Chemistry, **14** (2012) 3107.

K.Layek, M.L.Kantam, M.Shirai, D.Nishio-Hamane, T.Sasaki and H.Maheswaran
Gold Nanoparticles Stabilized on Nanocrystalline Magnesium Oxide as an Active Catalyst for Reduction of Nitroarenes in Aqueous Medium at Room Temperature
Green Chemistry, **14** (2012) 3164.

S.Ganorkar , K.R.Priolkar , P.R.Sarode, A.Banerjee, R.Rawat and S.Emura
Influence of Local Structure on Magnetic Properties of Layered Cobaltites $PrBaCo_2O_{5+\delta}$, δ ¿ 0.5
J. Phys.: Condens. Matter, **24** (2012) 476003.

N.Nakajima, M.Oki, Y.Isohama, H.Maruyama, Y.Tezuka, K.Ishiji, T.Iwazumi and K.Okada
Enhancement of Dielectric Constant of $BaTiO_3$ Nanoparticles Studied by Resonant X-Ray Emission Spectroscopy
Phys. Rev. B, **86** (2012) 224114.

K.Mori, K.Watanabe, Y.Terai, Y.Fujiwara and H.Yamashita
Hybrid Mesoporous-Silica Materials Functionalized by Pt^{II} Complexes: Correlation between Spatial Distribution of the Active Center, Photoluminescence Emission, and Photocatalytic Activity
Chem. Eur. J., **18** (2012) 11371.

K.Fuku, S.Takakura, T.Kamegawa, K.Mori and H.Yamashita
Preparation of Size-Controlled Copper Nanoparticles Supported Catalyst using Rapid and Uniform Heating Under Microwave Irradiation
Chem. Lett., **41** (2012) 614.

K.Fuku, T.Sakano, T.Kamegawa, K.Mori and H.Yamashita
Enhanced Hydrogenation Activity of Nano-sized Pd-Ni Bimetal Particles on Ti-containing Mesoporous Silica Prepared by Photo-Assisted Deposition Method
J. Mater. Chem., **22** (2012) 16243.

S.Okada, S.Ikurumi, T.Kamegawa, K.Mori and H.Yamashita
Structural Design of Pd/SiO_2@Ti-Containing Mesoporous Silica Core-Shell Catalyst for Efficient One-Pot Oxidation using in Situ Produced H_2O_2
J. Phys. Chem. C, **116** (2012) 14360.

K.Fuku, T.Kamegawa, K.Mori and H.Yamashita
Highly Dispersed Platinum Nanoparticles on TiO_2 Prepared by using the Microwave-Assisted Deposition Method: An Efficient Photocatalyst for the Formations of H_2 and N_2 from Aqueous NH_3
Chem. Asian J., **7** (2012) 1366.

Y.Imai, H.H.Li, H.Takumi, H.Tanida, I.Watanabe, T.Takiue, H.Matsubara and M.Aratono
Study on the Distribution of Binary Mixed Counterions in Surfactant Adsorbed Films by Total Reflection XAFS Measurements
J. Colloid Interface Sci., **388** (2012) 219.

E.Ohtomi, N.Ikeda, Y.Tokiwa, I.Watanabe, H.Tanida, T.Takiue, M.Aratono and H.Matsubara
Thin-Thick Transition of Foam Film Driven by Phase Transition of Surfactant-Alkane Mixed Adsorbed Film
Chem. Lett., **41** (2012) 1300.

T.Kamegawa, Y.Shimizu and H.Yamashita
Superhydrophobic Surfaces with Photocatalytic Self-Cleaning Properties by Nanocomposite Coating of TiO_2 and Polytetrafluoroethylene
Adv. Mater., **24** (2012) 3697.

Y.Kuwahara, D.Y.Kang, J.R.Copeland, P.Bollini, C.Sievers, T.Kamegawa, H.Yamashita and C.W.Jones
Enhanced CO_2 Adsorption over Polymeric Amines Supported on Heteroatom-Incorporated SBA-15 Silica: Impact of Heteroatom Type and Loading on Sorbent Structure and Adsorption Performance
Chem. Eur. J., **18** (2012) 16649.

J.Kugai, R.Kitagawa, S.Seino, T.Nakagawa, Y.Ohkubo, H.Nitani, H.Daimon and T.A.Yamamoto
CeO_2-Supported Pt-Cu Alloy Nanoparticles Synthesized by Radiolytic Process for Highly Selective CO Oxidation
Itn. J. Hydrogen Energy, **37** (2012) 4787.

N.Ichikuni, O.Tsuchida, J.Naganuma, T.Hara, H.Tsunoyama, T.Tsukuda and S.Shimazu
Preparation and Catalysis of Supported NiO Nanocluster for Oxidative Coupling of Thiophenol
Trans. Mater. Res. Soc. Jpn., **37** (2012) 177.

8A

T.Kawamoto, T.Mori, A.Nakao, Y.Murakami and J.A.Schlueter
T_c of 11 K Identified for the Third Polymorph of the $(BEDT\text{-}TTF)_2Ag(CF_3)_4(TCE)$ Organic Superconductor
J. Phys. Soc. Jpn., **81** (2012) 023705.

R.Kumai, S.Horiuchi, J.Fujioka and Y.Tokura
Ferroelectricity and Pressure-Induced Phenomena Driven by Neutral Ionic Valence Instability of Acid-Base Supramolecules
J. Am. Chem. Soc., **134** (2012) 1036.

Y.Moritomo, M.Takachi, Y.Kurihara and T.Matsuda
Thin Film Electrodes of Prussian Blue Analogues with Rapid Li+ Intercalation
Appl. Phys. Express, **5** (2012) 041801.

T.Matsuda and Y.Moritomo
Two-Electron Reaction without Structural Phase Transition in Nanoporous Cathode Material
J. Nanotechnology, **2012** (2012) 568147.

K.Kobayashi, S.Horiuchi, R.Kumai, F.Kagawa, Y.Murakami and Y.Tokura
Electronic Ferroelectricity in a Molecular Crystal with Large Polarization Directing Antiparallel to Ionic Displacement
Phys. Rev. Lett., **108** (2012) 237601.

T.Kakiuchi, N.Fujita, K.Mase and M.Tanaka
Study of Local Valence Electronic States of SiO_2 Ultrathin Films Grown on Si(111) by using Auger Photoelectron Coincidence Spectroscopy: Upward Shift of Valence-Band Maximum Depending on the Interface Structure
J. Phys. Soc. Jpn., **81** (2012) 074706.

Y.Moritomo, XH.Zhu, M.Takachi and T.Matsuda
Fast Discharge Process of Thin Film Electrode of Prussian Blue Analogue
Jpn. J. Appl. Phys., **51** (2012) 107301.

S.Ishibashi, S.Horiuchi, R.Kumai and K.Terakura
First-Principles Calculations of Spontaneous Polarization for TTF-$QBrCl_3$
Phys. Status Solidi B, **249** (2012) 1008.

K.Hemmi, R.Fukuta, E.Uykur, S.Miyasaka, S.Tajima, A.Nakao, H.Nakao, R.Kumai and Y.Murakami
Cr- and Mo-Doping Effects on Structural and Orbital Order Phase Transition in Spinel-Type MnV_2O_4
J. Phys. Soc. Jpn., **81** (2012) SB030.

A.Takemori, S.Saijo, S.Suzuki, S.Miyasaka, S.Tajima, A.Nakao, H.Nakao, R.Kumai and Y.Murakami
Correlation between T_c and Transport Properties in $PrFeP_{1-x}$ $As_xO_{0.9}F_{0.1}$
J. Phys. Soc. Jpn., **81** (2012) SB043.

S.Horiuchi, F.Kagawa, K.Hatahara, K.Kobayashi, R.Kumai, Y.Murakami and Y.Tokura
Above-Room-Temperature Ferroelectricity and Antiferroelectricity in Benzimidazoles
Nature Communications, **3** (2012) 1308.

T.Honda, Y.Ishiguro, H.Nakamura, Y.Wakabayashi and T.Kimura
Structure and Magnetic Phase Diagrams of Multiferroic Mn_2GeO_4
J. Phys. Soc. Jpn., **81** (2012) 103703.

N.Hoshino, F.Iijima, G.N.Newton, N.Yoshida, T.Shiga, H.Nojiri, A.Nakao, R.Kumai, Y.Murakami and H.Oshio
Three-Way Switching in a Cyanide-Bridged [CoFe] Chain
Nature Chemistry, **4** (2012) 921.

M.Takachi, Y.Kurihara and Y.Moritomo
Channel Size Dependence of Li^+ Insertion/Extraction in Nanoporous Hexacyanoferrates
J. Mater. Sci. Eng., **2** (2012) 452.

8B

A.Nakao, Y.Yamaki, H.Nakao, Y.Murakami, K.Hasegawa, M.Isobe and Y.Ueda
Observation of Structural Change in the Novel Ferromagnetic Metal-Insulator Transition of $K_2Cr_8O_{16}$
J. Phys. Soc. Jpn., **81** (2012) 054710.

M.Mito, M.Ogawa, H.Deguchi, M.Yamashita and H.Miyasaka
Effects of Pressure on Two-Dimensional Networked Single-Molecule Magnets Exhibiting AC-Field-Switchable Magnetic Properties
J. Phys. Soc. Jpn., **81** (2012) 064716.

I.Doi, K.Goshome, E.Miyazaki and K.Takimiya
A Soluble α-Dithienotetrathiafulvalene Derivative for Organic Field-Effect Transistors
Chem. Lett., **41** (2012) 435.

N.Ishimatsu, T.Shichijo, Y.Matsushima, H.Maruyama, Y.Matsuura, T.Tsumuraya, T.Shishidou, T.Oguchi, N.Kawamura, M.Mizumaki, T.Matsuoka and K.Takemura
Hydrogen-Induced Modification of the Electronic Structure and Magnetic States in Fe, Co, and Ni Monohydrides
Phys. Rev. B, **86** (2012) 104430.

M.Ikawa, T.Yamada, H.Matsui, H.Minemawari, J.Tsutsumi, Y.Horii, M.Chikamatsu, R.Azumi, R.Kumai and T.Hasegawa
Simple Push Coating of Polymer Thin-Film Transistors
Nature Communications, **3** (2012) 1176.

S.Horiuchi, F.Kagawa, K.Hatahara, K.Kobayashi, R.Kumai, Y.Murakami and Y.Tokura
Above-Room-Temperature Ferroelectricity and Antiferroelectricity in Benzimidazoles
Nature Communications, **3** (2012) 1308.

T.Honda, Y.Ishiguro, H.Nakamura, Y.Wakabayashi and T.Kimura
Structure and Magnetic Phase Diagrams of Multiferroic Mn_2GeO_4
J. Phys. Soc. Jpn., **81** (2012) 103703.

J.Tsutsumi, H.Matsui, T.Yamada, R.Kumai and T.Hasegawa
Generation and Diffusion of Photocarriers in Molecular Donor-Acceptor Systems: Dependence on Charge-Transfer Gap Energy
J. Phys. Chem. C, **116** (2012) 23957.

H.Kurihara, X.Lu, Y.Iiduka, H.Nikawa, M.Hachiya, N.Mizorogi, Z.Slanina, T.Tsuchiya, S.Nagase and T.Akasaka
X-Ray Structures of $Sc_2C_2@C_{2n}$ (n = 40, 41, 42): In-Depth Understanding of the Core-Shell Interplay in Carbide Cluster Metallofullerenes
Inorg. Chem., **51** (2012) 746.

M.Mito, T.Imakyurei, H.Deguchi, K.Matsumoto, T.Tajiri, H.Hara, T.Ozaki, H.Takeya and Y.Takano
Uniaxial Strain Effects on Cuprate Superconductor $YBa_2Cu_4O_8$
J. Phys. Soc. Jpn., **81** (2012) 113709.

R.I.Thomson, C.M.Pask, G.O.Lloyd, M.Mito and J.M.Rawson
Pressure-Induced Enhancement of Magnetic-Ordering Temperature in an Organic Radical to 70 K: A Magneto-structural Correlation
Chem. Eur. J., **18** (2012) 8629.

T.Tajiri, S.Hohdai, K.Hamamoto, H.Deguchi, M.Mito and A.Kohno
Magnetic Properties of $La_{2-x}Sr_xCuO_4$ Nanoparticles in Mesoporous Silica
J. Phys: Conf. Ser., **400** (2012) 032095.

A.Kobayashi, Y.Fukuzawa, H.-C.Chang and M.Kato
Vapor-Controlled Linkage Isomerization of a Vapochromic Bis(thiocyanato)platinum(II) Complex: New External Stimuli To Control Isomerization Behavior
Inorg. Chem., **51** (2012) 7508.

A.Kobayashi, H.Hara, T.Yonemura, H.-C.Chang and M.Kato
Systematic Structural Control of Multichromic Platinum(II)-Diimine Complexes Ranging from Ionic Solid to Coordination Polymer
Dalton Trans., **41** (2012) 1878.

9A

K.Shimizu, T.Oda, Y.Sakamoto, Y.Kamiya, H.Yoshida and A.Satsuma
Quantitative Determination of Average Rhodium Oxidation State by a Simple XANES Analysis
Appl. Catal. B, **111** (2012) 509.

Y.Yoshida, Y.Mitani, T.Itoi and Y.Izumi
Preferential Oxidation of Carbon Monoxide in Hydrogen using Zinc Oxide Photocatalysts Promoted and Tuned by Adsorbed Copper Ions
J. Catal., **287** (2012) 190.

M.Morikawa, N.Ahmed, Y.Ogura and Y.Izumi
Polymer Electrolyte Fuel Cell Supplied with Carbon Dioxide. Can Be the Reductant Water Instead of Hydrogen?
Appl. Catal. B, **117** (2012) 317.

K.Asakura
Polarization-Dependent Total Reflection Fluorescence Extended X-Ray Absorption Fine Structure and its Application to Supported Catalysis
RCS Catalysis Book Series, **24** (2012) 281.

S.Emura, M.-T.Siti-Nooraya, D.Krishnamurthy and H.Asahi
An Approach to Temperature - Insensitive Band Gap - The InGaGdN Case
Phys. Status. Solidi B, **249** (2012) 489.

K.Shimizu, Y.Kamiya, K.Osaki, H.Yoshda and A.Satsuma
The Average Pd Oxidation State in Pd/SiO_2 Quantified by L_3-Edge XANES Analysis and its Effects on Catalytic Activity for CO Oxidation
Catal. Sci. Technol., **2** (2012) 767.

N.Naveed, M.Morikawa and Y.Izumi
Photocatalytic Conversion of Carbon Dioxide into Methanol using Optimized Layered Double Hydroxide Catalysts
Catal. Today, **185** (2012) 263.

T.Itai, D.Hayase, Y.Hyobu, S.H.Hirata M.Kumagai and S.Tanabe
Hypoxia-Induced Exposure of Isaza Fish to Manganese and Arsenic in the Bottom of Lake Biwa, Japan: Experimental and Geochemical Verification
Environmental Science & Technology, **46** (2012) 5789.

S.T.Oyama, H.Zhao, H.J.Freund, K.Asakura, R.Wlodarczyk and M.Sierka
Unprecedented Selectivity to the Direct Desulfurization (DDS) Pathway in a Highly Active FeNi Bimetallic Phosphide Catalyst
J. Catal., **285** (2012) 1-5.

S.Furukawa, D.Tsukio, T.Shishido, K.Teramura and T.Tanaka
Correlation between the Oxidation State of Copper and the Photocatalytic Activity of Cu/Nb_2O_5
J. Phys. Chem. C, **116** (2012) 12181.

T.Takeguchi, T.Yamanaka, K.Asakura, E.N.Muhamad, K.Uosaki and W.Ueda
Evidence of Nonelectrochemical Shift Reaction on a CO-Tolerant High-Entropy State Pt-Ru Anode Catalyst for Reliable and Efficient Residential Fuel Cell Systems
J. Am. Chem. Soc., **134** (2012) 14508.

M.Tada, S.Zhang, S.Malwadkar, N.Ishiguro, J.Soga, Y.Nagai, K.Tezuka, H.Imoto, S.Otsuka-Yao-Matsuo, S.Ohkoshi and Y.Iwasawa
The Active Phase of Nickel/Ordered $Ce_2Zr_2O_x$ Catalysts with a Discontinuity (x = 7-8) in Methane Steam Reforming
Angew. Chem. Int. Ed., **51** (2012) 9361.

T.Wada, K.K.Bando, S.T.Oyama, T.Miyamoto, S.Takakusagi and K.Asakura
Operando Observation of Ni_2P Structural Changes during Catalytic Reaction: Effect of H_2S Pretreatment
Chem. Lett., **41** (2012) 1238.

S.Asaoka, Y.Takahashi, Y.Araki and M.Tanimizu
Comparison of Antimony and Arsenic Behavior in an Ichinokawa River Water-Sediment System
Chemical Geology, **334** (2012) 1.

Y.Takahashi, K.Kondo, A.Miyaji, M.Umeo, T.Honma and S.Asaoka
Recovery and Separation of Rare Earth Elements using Columns Loaded with DNA-Filter Hybrid
Analytical Sciences, **28** (2012) 985.

H.Qin, Y.Yokoyama, Q.Fan, H.Iwatani, K.Tanaka, A.Sakaguchi, Y.Kanai, J.Zhu, Y.Onda and Y.Takahashi
Investigation of Cesium Adsorption on Soil and Sediment Samples from Fukushima Prefecture by Sequential Extraction and EXAFS Technique
Analytical Sciences, **46** (2012) 297.

Y.Yokoyama, K.Tanaka and Y.Takahashi
Differences in the Immobilization of Arsenite and Arsenate into Calcite
Geochim. Cosmochim. Acta, **91** (2012) 202.

K.Ito, K.Yoshida, S.Kittaka and T.Yamaguchi
Pore Size Dependent Behavior of Hydrated Ag^+ Ions Confined in Mesoporous MCM-41 Materials under Synchrotron X-Ray Irradiation
Anal. Sci., **28** (2012) 639.

K.Fuku, T.Sakano, T.Kamegawa, K.Mori and H.Yamashita
Enhanced Hydrogenation Activity of Nano-sized Pd-Ni Bimetal Particles on Ti-containing Mesoporous Silica Prepared by Photo-Assisted Deposition Method
J. Mater. Chem., **22** (2012) 16243.

F.Gao, S.Yamazoe, T.Maeda, and T.Wada
Structural Study of Cu-Deficient $Cu_{2(1-x)}ZnSnSe_4$ Solar Cell Materials by X-Ray Diffraction and X-ray Absorption Fine Structure
Jpn. J. Appl. Phys., **51** (2012) 10NC28.

S.Yamashita, M.Katayama and Y.Inada
Redox Reactions of Nickel Species Supported on Silica
Memoirs of the SR Center Ritsumeikan University, **14** (2012) 3.

M.Okube, S.Sasaki, A.Yoshiasa, L.Wnag, T.Nakatani, H.Hongu, K.Murai, A.Nakatsuka and R.Miyawaki
Local Structure of Zn in Cretaceous-Tertiary Boundary Clays from Stevns Klint
J. Mineralogical and Petrological Sci., **107** (2012) 192.

A.Koide, T.Fujikawa, D.Abe, and S.Emura
Multiple Scattering Approach to GaN:Gd Gd L_3-Edge XANES
e-J. Surf. Sci. Nanotech, **10** (2012) 661.

Y.Ogawa, D.Ishiyama, N.Shikazono, K.Iwane, M.Kajiwara and N.Tsuchiya
The Role of Hydrous Ferric Oxide Precipitation in the Fractionation of Arsenic, Gallium, and Indium during the Neutralization of Acidic Hot Spring Water by River Water in the Tama River Watershed, Japan
Geochim. Cosmochim. Acta, **86** (2012) 367.

9C

K.Nakagawa, T.Okayama, Y.Tanimoto, K.Sotowa, S.Sugiyama, T.Moriga, S.Takenaka and M.Kishida
Preparation of Carbon-Supported Pt Catalysts Covered with Microporous Silica Layers using Organosilanes: Sintering Resistance and Superior Catalytic Performance for Cyclohexane Dehydrogenation
Appl. Catal. A, **419-420** (2012) 13.

M.Harada and Y.Kamigaito
Nucleation and Aggregative Growth Process of Platinum Nanoparticles Studied by in Situ Quick XAFS Spectroscopy
Langmuir, **28** (2012) 2415.

Y.Yoshida, Y.Mitani, T.Itoi and Y.Izumi
Preferential Oxidation of Carbon Monoxide in Hydrogen using Zinc Oxide Photocatalysts Promoted and Tuned by Adsorbed Copper Ions
J. Catal., **287** (2012) 190.

T.Wada, K.K.Bando, T.Miyamoto, S.Takakusagi, S.T.Oyama and K.Asakura
Operando QEXAFS Studies of Ni_2P during Thiophene Hydrodesulfurization: Direct Observation of Ni-S Bond Formation under Reaction Conditions
J. Synchrotron Rad., **19** (2012) 205.

K.K.Bando, T.Wada, T.Miyamoto, K.Miyazaki, S.Takakusagi, Y.Koike, Y.Inada, M.Nomura, A.Yamaguchi, T.Gott, S.Ted Oyama and K.Asakura
Combined in situ QXAFS and FTIR Analysis of a Ni Phosphide Catalyst under Hydrodesulfurization Conditions
J. Catal., **286** (2012) 165.

M.Morikawa, N.Ahmed, Y.Ogura and Y.Izumi
Polymer Electrolyte Fuel Cell Supplied with Carbon Dioxide. Can Be the Reductant Water Instead of Hydrogen?
Appl. Catal. B, **117** (2012) 317.

S.Kimura, T.Mashino, T.Hiroki, D.Shigeoka, N.Sakai, L.Zhu and Y.Ichiyanagi
Effect of Heat Treatment on Jahn-Teller Distortion and Magnetization in Cu Ferrite Nanoparticles
Thermochimica Acta, **532** (2012) 119.

H.Takahashi, K.Shimada, Y.Yamamoto and H.Uehara
Reconstruction of Calorimetric Curves from X-Ray Diffraction Data during the Melting-Recrystallization Process of Polymers: Simultaneous Calorimetry/Xray Diffraction Measurements of Isotactic Poly(1-butene) in Form III
J. Macromol. Sci. Phys. B, **51** (2012) 338.

T.Ohkubo, Y.Takehara and Y.Kuroda
Water-Initiated Ordering Around a Copper Ion of Copper Acetate Confined in Slit-Shaped Carbon Micropores
Micropor. Mesopor. Mater., **154** (2012) 82.

M.Tanaka, A.Itadani, Y.Kuroda and M.Iwamoto
Effect of Pore Size and Nickel Content of Ni-MCM-41 on Catalytic Activity for Ethene Dimerization and Local Structures of Nickel Ions
J. Phys. Chem. C, **116** (2012) 5664.

N.Naveed, M.Morikawa and Y.Izumi
Photocatalytic Conversion of Carbon Dioxide into Methanol using Optimized Layered Double Hydroxide Catalysts
Catal. Today, **185** (2012) 263.

T.Itai, D.Hayase, Y.Hyobu, S.H.Hirata M.Kumagai and S.Tanabe
Hypoxia-Induced Exposure of Isaza Fish to Manganese and Arsenic in the Bottom of Lake Biwa, Japan: Experimental and Geochemical Verification
Environmental Science & Technology, **46** (2012) 5789.

K.Yamamoto and Y.Miwa
Determination of Glass Transition Temperature at Specific Sites in Polymers by Microwave Power Saturation in Electron Spin Resonance
kobunshi Ronbunshu, **69** (2012) 366. (*in Japanese*).

H.Takahashi and K.Jojiki
Effect of Heavy Water on Nonlamellar Structures of Phospholipid and Monoolein Molecular Assemblies
Chem. Lett., **41** (2012) 1101.

T.Shishido, K.Shimamura, K.Teramura and T.Tanaka
Role of CO_2 in Dehydrogenation of Propane over Cr-Based Catalysts
Catal. Today, **185** (2012) 151.

B.Sarkar, P.Prajapati, R.Tiwari, R.Tiwari, S Ghosh, S.S.Acharyya, C.Pendem, R.K.Singha, L.N.S.Konathala, J.Kumar, T.Sasaki and R.Bal
Room Temperature Selective Oxidation of Cyclohexane over Cu-Nanoclusters Supported on Nanocrystalline Cr_2O_3
Green Chemistry, **14** (2012) 2600.

M.Shibukawa, M.Harada, T.Okada, Y.Ogiyama, T.Shimasaki, Y.Kondo, A.Inoue and S.Saito
X-Ray Absorption Fine Structure Spectroscopy Studies of Thermal Effects on Ion-exchange Equilibria
RSC Adv., **2** (2012) 8985.

T.Wada, K.K.Bando, S.T.Oyama, T.Miyamoto, S.Takakusagi and K.Asakura
Operando Observation of Ni_2P Structural Changes during Catalytic Reaction: Effect of H_2S Pretreatment
Chem. Lett., **41** (2012) 1238.

A.Yamaguchi, N.Hiyoshi, O.Sato and M.Shirai
Gasification of Organosolv-Lignin over Charcoal Supported Noble Metal Salt Catalysts in Supercritical Water
Topics in Catal., **55** (2012) 889.

C.Pendem, P.Gupta, N.Chaudhary, S.Singh, J.Kumar, T.Sasaki, A.Datta and R.Bal
Aqueous Phase Reforming of Glycerol to 1,2-Propanediol over Pt-Nanoparticles Supported on Hydrotalcite in the Absence of Hydrogen
Green Chemistry, **14** (2012) 3107.

K.Layek, M.L.Kantam, M.Shirai, D.Nishio-Hamane, T.Sasaki and H.Maheswaran
Gold Nanoparticles Stabilized on Nanocrystalline Magnesium Oxide as an Active Catalyst for Reduction of Nitroarenes in Aqueous Medium at Room Temperature
Green Chemistry, **14** (2012) 3164.

Y.Nagai, Y.Kawabata and T.Kato
Microscopic Investigation on Morphologies of Bilayer Gel Structure in the Mixed Polyoxyethylene-Type Nonionic Surfactant Systems
J. Phys. Chem. B, **116** (2012) 12558.

S.Muratsugu, Z.Weng, H.Nakai, K.Isobe, Y.Kushida, T.Sasaki and M.Tada
Surface-Assisted Transfer Hydrogenation Catalysis on a γ-Al_2O_3-Supported Ir Dimer
Phys. Chem. Chem. Phys., **14** (2012) 16023.

S.Zhang, S Muratsugu, N.Ishiguro, S.Ohkoshi and M.Tada
Perovskite $NaCeTi_2O_6$-Supported Ni Catalysts for CH_4 Steam Reforming
ChemCatChem, **4** (2012) 1783.

R.Akiyama, N.Matsuki, H.Nomura, H.Yoshida, T.Yoshida and S.Kobayashi
Nontoxic, Nonvolatile, and Highly Efficient Osmium Catalysts for Asymmetric Dihydroxylation of Alkenes and Application to one Mol-Scale Synthesis of an Anticancer Drug, Camptothecin Intermediate
RSC Adv., **2** (2012) 7456.

M.Tamaru, P.Barpanda, Y.Yamada, S.Nishimura and A.Yamada
Observation of the Highest Mn^{3+}/Mn^{2+} Redox Potential of 4.45 V in a $Li_2MnP_2O_7$ Pyrophosphate Cathode
J. Mater. Chem., **22** (2012) 24526.

H.C Moon, D.Bae and J.K.Kim
Self-Assembly of Poly(3-Dodecylthiophene)-*block*-Poly(Methyl Methacrylate) Copolymers Driven by Competition between Microphase Separation and Crystallization
Macromolecules, **45** (2012) 5201.

T.Yokoyama
Path Integral Effective Classical Potential Method Applied to Anharmonicity and Quantum Effects in Thermal Expansion of Invar Alloy
e-J. Surf. Sci. Nanotech., **10** (2012) 486.

A.Oda, H.Torigoe, A.Itadani, T.Ohkubo, T.Yumura, H.Kobayashi and Y.Kuroda
Unprecedented Reversible Redox Process in the ZnMFI-H_2 System Involving Formation of Stable Atomic Zn^0
Angew. Chem. Int. Ed., **51** (2012) 7719.

Y.Nishina, H.Hashimoto, N.Kimura, N.Miyata, T.Fujii, B.Ohtani and J.Takada
Biogenic Manganese Oxide: Effective New Catalyst for Direct Bromination of Hydrocarbons
RSC Adv., **2** (2012) 6420.

H.Okudera, A.Yoshiasa, K.Murai, M.Okube, T.Takeda and S.Kikkawa
Local Structure of Magnetite and Maghemite and Chemical Shift in Fe K-Edge XANES
J. Mineralogical and Petrological Sci., **107** (2012) 127.

M.Okube, S.Sasaki, A.Yoshiasa, L.Wnag, T.Nakatani, H.Hongu, K.Murai, A.Nakatsuka and R.Miyawaki
Local Structure of Zn in Cretaceous-Tertiary Boundary Clays from Stevns Klint
J. Mineralogical and Petrological Sci., **107** (2012) 192.

N.Sakai, L.Zhu, A.Kurokawa, H.Takeuchi, S.Yano, T.Yanoh, N.Wada, S.Taira, Y.Hosokai, Y.Machida, H.Saito and Y.Ichiyanagi
Synthesis of Gd_2O_3 Nanoparticle for MRI Contrast Agents
J. Phys.: Conf. Ser., **352** (2012) 012008.

T.Miyasaka, A.Kurokawa, H.Takeuchi, S.Yano, T.Yanoh, K.Onuma, T.Kondo, K.Miike and Y.Ichiyanagi
Magnetic Properties and X-Ray Absorption Fine-Structure Spectra of $CoMn_2O_4$ Nanoparticles
e-J. Surf. Sci. Nanotech., **10** (2012) 643.

A.Itadani, H.Torigoe, T.Yumura, T.Ohkubo, H.Kobayashi and Y.Kuroda
Dual-Copper Catalytic Site Formed in CuMFI Zeolite Makes Effective Activation of Ethane Possible Even at Room Temperature
J. Phys. Chem. C, **116** (2012) 10680.

R.Hori, D.Furukawa, K.Yamamoto and S.Kutsumizu
Light-Driven Phase Transition in a Cubic Phase-Forming Binary System Composed of 4'-*n*-Docosyloxy-3'-nitrobiphenyl-4-carboxylic Acid and an Azobenzene Derivative
Chem. Eur. J., **18** (2012) 7346.

10A

M.Okube, T.Yasue and S.Sasaki
Residual-Density Mapping and Site-Selective Determination of Anomalous Scattering Factors to Examine the Origin of the Fe *K* Pre-Edge Peak of Magnetite
J. Synchrotron Rad., **19** (2012) 759.

H.Okudera, A.Yoshiasa, K.Murai, M.Okube, T.Takeda and S.Kikkawa
Local Structure of Magnetite and Maghemite and Chemical Shift in Fe K-Edge XANES
J. Mineralogical and Petrological Sci., **107** (2012) 127.

10C

K.Kubota, K.Wakamatsu, N.Nameki and Y.Toyama
Inhibition of Protein Aggregation: SAXS Study on the Role of the αC Region of Fibrinogen in the Fibrin Polymerization
Key Materials Engineering, **497** (2012) 41.

K.Terao, R.Kanenaga, T.Sato, K.Mizuno and H.P.Bächinger
Complex Formation of Collagen Model Peptides with Polyelectrolytes and Stabilization of the Triple Helical Structure
Macromolecules, **45** (2012) 392.

S. Nakagawa, K. Kadena, T. Ishizone, S. Nojima, T. Shimizu, K. Yamaguchi and S. Nakahama
Crystallization Behavior and Crystal Orientation of Poly(ϵ-caprolactone) Homopolymers Confined in Nanocylinders : Effects of Nanocylinder Dimension
Macromolecules, **45** (2012) 1892.

Y.Zhao, G.Matsuba and H.Ito
Shear-Induced Crystallization and Rheological Behavior of Syndiotactic Polystyrene
Journal of Materials Research, **27** (2012) 1372.

F.Arai, H.Takeshita, M.Dobashi, K.Takenaka, M.Miya and T.Shiomi
Effects of Liquid-Liquid Phase Separation on Crystallization of Poly(Ethylene Glycol) in Blends with Isotactic Poly(Methyl Methacrylate)
Polymer, **50** (2012) 851.

S.Fujii, D.Mitsumasu, Y.Isono and W.Richtering
Shear-Induced Onion Formation of Polymer-Grafted Lamellar Phase
Soft Matter, **8** (2012) 5381.

M.Hirai, Y.Hagiwara, K.Takeuchi, R.Kimura, T.Onai, R.K.Hirai, N.Ohta and M.Sugiyama
Thermal Unfolding and Refolding of Protein under Osmotic Pressure Clarified by Wide-Angle X-Ray Scattering
Thermochimica Acta, **532** (2012) 15.

H.Takeno, A.Maehara, M.Kuchiishi, K.Yoshiba, H.Takeshita, S Kondo, T.Dobashi, M.Takenaka and H.Hasegawa
Structural and Thermal Properties of Unpurified and Purified 12-Hydroxystearic Acid Solutions
Sen'i Gakkaishi, **68** (2012) 248.

Y.Watanabe and Y.Inoko
An Assessment Study on Two-Dimensional X-Ray Scattering Data for Protein Solutions
Rep. Nat'l Food Res. Inst, **76** (2012) 39. (*in Japanese*).

K.Terao, F.Maeda, K.Oyamada, T.Ochiai, S.Kitamura and T.Sato
Side-Chain-Dependent Helical Conformation of Amylose Alkylcarbamates: Amylose Tris(ethylcarbamate) and Amylose Tris(*n*-hexylcarbamate)
J. Phys. Chem. B, **116** (2012) 12714.

L.Huang, G.Kiyofuji, J.Matsumoto, Y.Fukagawa, C.Gong and S.Nojima
Isothermal Crystallization of Poly(β-propiolactone) Blocks Starting from Lamellar Microdomain Structures of Double Crystalline Poly(β-propiolactone)-*block*-Polyethylene Copolymers
Polymer, **53** (2012) 5856.

K.Tamada, H.Yamamura, K.Terao and T.Sato
Conformation of Single-Stranded DNA in Aqueous Solution
Kobunshi Ronbunshu, **69** (2012) 399. (*in Japanese*).

H.Makyio, M.Ohgi, T.Takei, S.Takahashi, H.Takatsu, Y.Katoh, A.Hanai, T.Ueda, Y.Kanaho, Y.Xie, HW.Shin, H.Kamikubo, M.Kataoka, M.Kawasaki, R.Kato, S.Wakatsuki and K.Nakayama
Structural Basis for Arf6-MKLP1 Complex Formation on the Flemming Body Responsible for Cytokinesis
EMBO J., **31** (2012) 2590.

M.Koga, K.Sato, R.Ishige, T.Ishii, S.Kang, K.Sakajiri, J.Watanabe and M.Tokita
Well-Ordered Lamellar Microphase-Separated Morphology of an ABA Triblock Copolymer Containing a Main-Chain Liquid Crystalline Polyester as the Middle Segment 2: Influence of the Amorphous Segment Molecular Weight
Macromolecules, **45** (2012) 9391.

A.Narumi, Y.Ohashi, D.Togashi, Y.Saito, Y.Jinbo, Y,Izumi, K.Matsuda, T.Kakuchi and S.Kawaguchi
Star Polymer with Crosslinked Core and Water-Soluble Poly(*N*-hydroxyethylacrylamide)-Arms: Synthesis by Arm-First Method using ATRP and Characterizations by SEC-MALS and SAXS Measurement in Water
J. Polym. Sci. Part-A. Polym. Chem., **50** (2012) 3546.

K.Terao, N.Asano, S. Kitamura and T.Sato
Rigid Cyclic Polymer in Solution: Cycloamylose Tris(phenylcarbamate) in 1,4-Dioxane and 2-Ethoxyethanol
ACS Macro Lett., **1** (2012) 1291.

Z.Gai, Y.Kitagawa, Y.Tanaka, N.Shimizu, K.Komoda, I.Tanaka and M.Yao
The Binding Mechanism of eIF2β with its Partner Proteins, eIF5 and eIF2Bε
Biochem. Biophys. Res. Commun., **423** (2012) 515.

H.C.Moon, J.G.Kim and J.K.Kim
Isomeric Effects on the Phase Behavior of Polystyrene-*block*-Poly(Pentyl Methacrylate) Copolymers
Macromolecules, **45** (2012) 3639.

Y.Sageshima, S.Arai, A.Noro and Y.Matsushita
Fabrication and Modification of Ordered Nanoporous Structures from Nanophase-Separated Block Copolymer/Metal Salt Hybrids
Langmuir, **28** (2012) 17524.

E.Otsuka, S.Komiya, S.Sasaki, J.Xing, Y.Bando Y.Hirashima, M.Sugiyama and A.Suzuki
Effects of Preparation Temperature on Swelling and Mechanical Properties of PVA Cast Gels
Soft Matter, **8** (2012) 8129.

Y.Koide, H.Ikake, Y.Muroga and S.Shimizu
Effect of the Cast-Solvent on the Morphology of Cast Films Formed with a Mixture of Stereoisomeric Poly(Lactic Acids)
Polymer J., **2012** (2012) 1.

S.Kudo, J.M.M.Caaveiro, T.Miyafusa, S.Goda, K.Ishii, T.Matsuura, Y.Sudou, T.Kodama, T.Hamakubo and K.Tsumoto
Structural and Thermodynamic Characterization of the Self-Adhesive Properties of Human P-Cadherin
Mol. BioSyst., **8** (2012) 2050.

K.Okoshi
Liquid Crystal Phases Observed in Rigid-Rod Polymers
Ekisho, **16** (2012) 172. (*in Japanese*).

K.Okoshi, M.Fujiki and J.Watanabe
Asymmetrically Tilted Alignment of Rigid-Rod Helical Polysilanes on a Rubbed Polyimide Surface
Langmuir, **28** (2012) 4811.

H.Nakatani, S.Goda, H.Unno, T.Nagai, T.Yoshimura, and H.Hemmi
Substrate-Induced Change in the Quaternary Structure of Type 2 Isopentenyl Diphosphate Isomerase from *Sulfolobus shibatae*
J. Bacteriol., **194** (2012) 3216.

11A

M.Ukibe, S.Shiki, Y.Kitajima and M.Ohkubo
Soft X-Ray Detection Performance of Superconducting Tunnel Junction Arrays with Asymmetric Tunnel Junction Layer Structure
Jpn. J. Appl. Phys., **51** (2012) 010115.

K.Kawai, T.Kohmura, S.Ikeda, K.Kaneko, T.watanabe, H.Tsunemi, K.Hayashida, N.Anabuki, H.Nakajima, S.Ueda, T.G.Tsuru, T.Dotani, M.Ozaki, K.Matsuta, T.Fujinaga, S.Kitamoto, H.Murakami, J.Hiraga, K.Mori and ASTRO-H SXI Team
Optical, UV and Soft X-Ray Transmission of Optical Blocking Layer for the X-Ray CCD
AIP Conf. Proc., **1427** (2012) 255.

K.Amemiya
Sub-nm Resolution Depth Profiling of the Chemical State and Magnetic Structure of Thin Films by a Depth-Resolved X-Ray Absorption Spectroscopy Technique
Phys. Chem. Chem. Phys., **14** (2012) 10477.

K.Amemiya and M.Sakamaki
XAFS and XMCD Spectra at the Surface and Interface of Ultrathin Films Observed by the Depth-Resolved XAFS/XMCD Technique
e-J. Surf. Sci. Nanotech., **10** (2012) 521.

M.Ohkubo, S.Shiki, M.Ukibe, N.Matsubayashi, Y.Kitajima and S.Nagamachi
X-Ray Absorption Near Edge Spectroscopy with a Superconducting Detector for Nitrogen Dopants in SiC
Scientific Reports, **2** (2012) 831.

T.Okajima, K.Hara, M.Yamamoto and K.Seki
NEXAFS Spectroscopic Study of Surface Modification on Poly(Butylene Terephthalate) Induced by UV Irradiation
Internal J. Polymer Anal. Charact., **17** (2012) 218.

T.Okajima, K.Hara, M.Yamamoto and K.Seki
Near Edge X-Ray Absorption Fine Structure Spectroscopic and Infrared Reflection Absorption Spectroscopic Studies of Surface Modification of Poly(Butylene Terephthalate) Induced by UV Irradiation
Polymer, **53** (2012) 2956.

S.Ikeda, T.Kohmura, K.Kawai, K.Kaneko, T.Watanabe, H.Tsunemi, K.Hayashida, N.Anabuki, H.Nakajima, S.Ueda, T.G.Tsuru, T.Dotani, M.Ozaki, K.Matsuta, T.Fujinaga, S.Kitamoto, H.Murakami, J.Hiraga, K.Mori,ASTRO-H SXI Team
Soft X-Ray Response of the X-Ray CCD Camera Directly Coated with Optical Blocking Layer
AIP Conf. Proc., **1427** (2012) 253.

S.Shiki, N.Zen, N.Matsubayashi, M.Koike, M.Ukibe, Y.Kitajima, S.Nagamachi and M.Ohkubo
Analysis of Wide-Gap Semiconductors with Superconducting XAFS Apparatus
Progress in Superconductivity, **14** (2012) 99.

11B

H.Okuda, K.Takeshita, S.Ochiai, Y.Kitajima, S.Sakurai and H.Ogawa
Contrast Matching of an Si Substrate with Polymer Films by Anomalous Dispersion at the Si *K* Absorption Edge
J. Appl. Cryst., **45** (2012) 119.

T.Miyamoto, T.Wada, H.Niimi, S.Suzuki, M.Kato, M.Kudo and K.Asakura
A New Collinear-Type Energy-Filtered X-Ray Photoemission Electron Microscope Equipped with a Multi-Pole Aberration-Corrected Air-Core Coil Wien Filter
Jpn. J. Appl. Phys., **51** (2012) 046701.

T.Tanaka, M.Kato, T.Kurosawa, Y.Morishita, N.Saito, I.H.Suzuki, M.Krumrey and F.Scholze
First Comparison of Spectral Responsivity in the Soft X-Ray Region
Metrologia, **49** (2012) 501.

A.Ito, T.Inoue, K.Takehara, Y.Taki and K.Shinohara
Mapping of Ca and Cysteic Acid, an Oxidation Product of Cystine, in Human Hair at Submicron Resolution
Ad. X-Ray Chem. Anal. Jpn., **43** (2012) 161. (*in Japanese*).

T.Imazono, M.Koike, M.Koeda, T.Nagano, H.Sasai, Y.Oue, Z.Yonezawa, S.Kuramoto, M.Terauchi, H.Takahashi, N.Handa and T.Murano
A Multilayer Grating with a Novel Layer Structure for a Flat-Field Spectrograph Attached to Transmission Electron Microscopes in Energy Region of 2-4 keV
AIP Conf. Proc., **1437** (2012) 24.

R.Takahashi, R.Okazaki, Y.Yasui, I.Terasaki, T.Sudayama, H.Nakao, Y.Yamasaki, J.Okamoto, Y.Murakami and Y.Kitajima
High-Temperature Thermoelectric Properties of the Double-Perovskite Ruthenium Oxide $(Sr_{1-x}La_x)_2ErRuO_6$
J. Appl. Phys., **112** (2012) 073714.

S.Sugita, A.Furuzawa, K.Ishibashi, K.Tamura, T.Okajima, Y.Maeda, T.Sato, K.Ichihara, K.Tomikawa, R.Iizuka, T.Awaya and K.Okada
Measurement of Reflectivity of X-Ray Mirror for Soft X-Ray Telescope Onboard ASTRO-H
SPIE proc., **8443** (2012) 844358.

11D

K.Ozawa
Metallization of Oxide Semiconductor Surfaces by Chemical Modification
Chemical Industry, **63** (2012) 207. (*in Japanese*).

S.Arae, T.Yamazaki, K.Yanase, K.Ochi, A.Ishii, M.Okusawa, K.Mase and M.Tanaka
Simple Low-Outgassing Atomic Hydrogen Source
J. Vac. Soc. Jpn., **55** (2012) 403.

12C

M.Harada and Y.Kamigaito
Nucleation and Aggregative Growth Process of Platinum Nanoparticles Studied by in Situ Quick XAFS Spectroscopy
Langmuir, **28** (2012) 2415.

T.Masuda, H.Fukumitsu, S.Takakusagi, W.-J.Chun, T.Kondo, K.Asakura and K.Uosaki
Molecular Catalysts Confined on and Within Molecular Layers Formed on a Si(111) Surface with Direct Si-C Bonds
Adv. Mater., **24** (2012) 268.

Y.Yoshida, Y.Mitani, T.Itoi and Y.Izumi
Preferential Oxidation of Carbon Monoxide in Hydrogen using Zinc Oxide Photocatalysts Promoted and Tuned by Adsorbed Copper Ions
J. Catal., **287** (2012) 190.

T.Wada, K.K.Bando, T.Miyamoto, S.Takakusagi, S.T.Oyama and K.Asakura
Operando QEXAFS Studies of Ni_2P during Thiophene Hydrodesulfurization: Direct Observation of Ni-S Bond Formation under Reaction Conditions
J. Synchrotron Rad., **19** (2012) 205.

K.K.Bando, T.Wada, T.Miyamoto, K.Miyazaki, S.Takakusagi, Y.Koike, Y.Inada, M.Nomura, A.Yamaguchi, T.Gott, S.Ted Oyama and K.Asakura
Combined in situ QXAFS and FTIR Analysis of a Ni Phosphide Catalyst under Hydrodesulfurization Conditions
J. Catal., **286** (2012) 165.

T.Kamegawa, M.Saito, T.Sakai, M.Matsuoka and M.Anpo
Characterization of Phenylene-Bridged Hybrid Mesoporous Materials Incorporating Arenetricarbonyl Complexes and their Catalytic Activities
Catalysis Today, **181** (2012) 14.

M.Morikawa, N.Ahmed, Y.Ogura and Y.Izumi
Polymer Electrolyte Fuel Cell Supplied with Carbon Dioxide. Can Be the Reductant Water Instead of Hydrogen?
Appl. Catal. B, **117** (2012) 317.

M.Harada, Y.Tasaki, H.Qua and T.Okada
Hydration of Ions and Salt Crystallization in Liquid Phase Coexistent with Ice at Temperature Below Eutectic Point
RSC Adv., **2** (2012) 461.

Y.Zong, K.Fujita, H.Akamatsu, S.Nakashima, S.Murai and K.Tanaka
Local Structure of Amorphous EuO-TiO_2 Thin Films Probed by X-Ray Absorption Fine Structure
J. Am. Ceram. Soc., **95** (2012) 716.

K.Asakura
Polarization-Dependent Total Reflection Fluorescence Extended X-Ray Absorption Fine Structure and its Application to Supported Catalysis
RCS Catalysis Book Series, **24** (2012) 281.

N.Naveed, M.Morikawa and Y.Izumi
Photocatalytic Conversion of Carbon Dioxide into Methanol using Optimized Layered Double Hydroxide Catalysts
Catal. Today, **185** (2012) 263.

L.Zhu, N.Sakai, A.Kurokawa, H.Takeuchi, S.Yano, T Yanoh, N.Wada, S.Taira, Y.Hosokai, Y.Machida, H.Saito and Y.Ichiyanagi
Synthesis of Multiferroic $DyFeO_3$ Nanoparticle and Study of their Magnetic Properties
J. Phys. Conf. Ser., **352** (2012) 012021.

J.Watanabe, Y.Tani, N.Miyata, H.Seyama, S.Mitsunobu and H.Naitoh
Concurrent Sorption of As(V) and Mn(II) during Biogenic Manganese Oxide Formation
Chemical Geology, **306-307** (2012) 123.

S.T.Oyama, H.Zhao, H.J.Freund, K.Asakura, R.Wlodarczyk and M.Sierka
Unprecedented Selectivity to the Direct Desulfurization (DDS) Pathway in a Highly Active FeNi Bimetallic Phosphide Catalyst
J. Catal., **285** (2012) 1-5.

N.Yabuuchi, M.Kajiyama, J.Iwatate, H.Nishikawa, S.Hitomi, R.Okuyama, R.Usui, Y.Yamada and S.Komaba
P2-Type $Na_x[Fe_{1/2}Mn_{1/2}]O_2$ made from Earth-Abundant Elements for Rechargeable Na Batteries
Nature Materials, **11** (2012) 512.

S.Komaba, N.Yabuuchi, T.Nakayama, A.Ogata, T.Ishikawa and I.Nakai
Study on the Reversible Electrode Reaction of $Na_{1-x}Ni_{0.5}Mn_{0.5}O_2$ for a Rechargeable Sodium-Ion Battery
Inorganic Chem., **51** (2012) 6211.

S.Furukawa, D.Tsukio, T.Shishido, K.Teramura and T.Tanaka
Correlation between the Oxidation State of Copper and the Photocatalytic Activity of Cu/Nb_2O_5
J. Phys. Chem. C, **116** (2012) 12181.

M.Sakamaki, K.Amemiya, M.O.Liedke, J.Fassbender, P.Mazalski, I.Sveklo and A.Maziewski
Perpendicular Magnetic Anisotropy in a Pt/Co/Pt Ultrathin Film Arising from a Lattice Distortion Induced by Ion Irradiation
Phys. Rev. B, **86** (2012) 024418.

T.Takeguchi, T.Yamanaka, K.Asakura, E.N.Muhamad, K.Uosaki and W.Ueda
Evidence of Nonelectrochemical Shift Reaction on a CO-Tolerant High-Entropy State Pt-Ru Anode Catalyst for Reliable and Efficient Residential Fuel Cell Systems
J. Am. Chem. Soc., **134** (2012) 14508.

C.Zhang, F.Liu, Y.Zhai, H.Ariga, N.Yi, Y.Liu, K.Asakura, M.Flytzani-Stephanopoulos and H.He
Alkali-Metal-Promoted Pt/TiO_2 Opens a More Efficient Pathway to Formaldehyde Oxidation at Ambient Temperatures
Angew. Chem. Int. Ed., **51** (2012) 9628.

M.Shibukawa, M.Harada, T.Okada, Y.Ogiyama, T.Shimasaki, Y.Kondo, A.Inoue and S.Saito
X-Ray Absorption Fine Structure Spectroscopy Studies of Thermal Effects on Ion-exchange Equilibria
RSC Adv., **2** (2012) 8985.

M.Tada, S.Zhang, S.Malwadkar, N.Ishiguro, J.Soga, Y.Nagai, K.Tezuka, H.Imoto, S.Otsuka-Yao-Matsuo, S.Ohkoshi and Y.Iwasawa
The Active Phase of Nickel/Ordered $Ce_2Zr_2O_x$ Catalysts with a Discontinuity (x = 7-8) in Methane Steam Reforming
Angew. Chem. Int. Ed., **51** (2012) 9361.

T.Wada, K.K.Bando, S.T.Oyama, T.Miyamoto, S.Takakusagi and K.Asakura
Operando Observation of Ni_2P Structural Changes during Catalytic Reaction: Effect of H_2S Pretreatment
Chem. Lett., **41** (2012) 1238.

S.Asaoka, Y.Takahashi, Y.Araki and M.Tanimizu
Comparison of Antimony and Arsenic Behavior in an Ichinokawa River Water-Sediment System
Chemical Geology, **334** (2012) 1.

Y.Takahashi, K.Kondo, A.Miyaji, M.Umeo, T.Honma and S.Asaoka
Recovery and Separation of Rare Earth Elements using Columns Loaded with DNA-Filter Hybrid
Analytical Sciences, **28** (2012) 985.

H.Qin, Y.Yokoyama, Q.Fan, H.Iwatani, K.Tanaka, A.Sakaguchi, Y.Kanai, J.Zhu, Y.Onda and Y.Takahashi
Investigation of Cesium Adsorption on Soil and Sediment Samples from Fukushima Prefecture by Sequential Extraction and EXAFS Technique
Analytical Sciences, **46** (2012) 297.

Y.Yokoyama, K.Tanaka and Y.Takahashi
Differences in the Immobilization of Arsenite and Arsenate into Calcite
Geochim. Cosmochim. Acta, **91** (2012) 202.

A.Ohta, H.Kagi, H.Tsuno, M.Nomura and T.Okai
Speciation Study of Cr(VI/III) Reacting with Humic Substances and Determination of Local Structure of Cr Binding Humic Substances using XAFS Spectroscopy
Geochemical Journal, **46** (2012) 409.

K.Kakimoto, T.Hotta and I.Kagomiya
Fine Structural Analysis and Phase Transition Behavior for Li-Modified $Na_{0.5}K_{0.5}NbO_3$ Lead-Free Piezoelectric Ceramics
Ceramics International, **38** (2012) S319.

K.Kakimoto, R.Kaneko and I.Kagomiya
Grain-Size-Controlled (Li,Na,K)NbO_3 Ceramics using Powder Source Classified by Centrifugal Separator
Jpn. J. Appl. Phys., **51** (2012) 09LD06.

Q.Yu, K.Sasaki, K.Tanaka, T.Ohnuki and T.Hirajima
Structural Factors of Biogenic Birnessite Produced by Fungus *Paraconiothyrium* sp. WL-2 Strain Affecting Sorption of Co^{2+}
Chemical Geology, **310-311** (2012) 106.

K.Ito, K.Yoshida, S.Kittaka and T.Yamaguchi
Pore Size Dependent Behavior of Hydrated Ag^+ Ions Confined in Mesoporous MCM-41 Materials under Synchrotron X-Ray Irradiation
Anal. Sci., **28** (2012) 639.

Z.Pan, F.Hu, S.He, Q.Liu, Z.Sun, T.Yao, Y.Xie, H.Oyanagi, Z.Xie, Y.Jiang, W.Yan and S.Wei
Co Cluster Formation Induced by Cu Codoping in Co:ZnO Semiconductor Thin Films
J. Phys. Chem. C, **116** (2012) 4855.

S.Muratsugu, Z.Weng, H.Nakai, K.Isobe, Y.Kushida, T.Sasaki and M.Tada
Surface-Assisted Transfer Hydrogenation Catalysis on a γ-Al_2O_3-Supported Ir Dimer
Phys. Chem. Chem. Phys., **14** (2012) 16023.

S.Zhang, S Muratsugu, N.Ishiguro, S.Ohkoshi and M.Tada
Perovskite $NaCeTi_2O_6$-Supported Ni Catalysts for CH_4 Steam Reforming
ChemCatChem, **4** (2012) 1783.

S.Yamashita, M.Katayama and Y.Inada
Redox Reactions of Nickel Species Supported on Silica
Memoirs of the SR Center Ritsumeikan University, **14** (2012) 3.

V.Mah and F.Jalilehvand
Lead(II) Complex Formation with Glutathione
Inorg. Chem., **51** (2012) 6285.

Y.Sotome, W.S.K Bong and I.Nakai
Characterization of Black/Brown Pigments on Iron Age Pottery Excavated from Central Anatolia using X-Ray Analyses
Advances in X-Ray Chemical Analysis, **43** (2012) 331. (*in Japanese*).

13A

K.Ozawa
Metallization of Oxide Semiconductor Surfaces by Chemical Modification
Chemical Industry, **63** (2012) 207. (*in Japanese*).

Md.Z.Hossain, J.E.Johns, K.H.Bevan, H.J.Karmel, Y.T.Liang, S.Yoshimoto, K.Mukai, T.Koitaya, J.Yoshinobu, M.Kawai, A.M.Lear, L.L.Kesmodel, S.L.Tait and M.C.Hersam
Chemically Homogeneous and Thermally Reversible Oxidation of Epitaxial Graphene
Nature Chemistry, **4** (2012) 305.

H.Nakazawa, S.Miura, R.Kamata, S.Okuno, Y.Enta, M.Suemitsu, and T.Abe
Characteristics of Silicon/Nitrogen-Incorporated Diamond-Like Carbon Films Prepared by Plasma-Enhanced Chemical Vapor Deposition
Jpn. J. Appl. Phys., **51** (2012) 015603.

T.Koitaya, S.Shimizu, K.Mukai, S.Yoshimoto and J.Yoshinobu
Kinetic and Geometric Isotope Effects Originating from Different Adsorption Potential Energy Surfaces: Cyclohexane on Rh(111)
J. Chem. Phys., **136** (2012) 214705.

R.Toyoshima, M.Yoshida, Y.Monya, Y.Kousa, K.Suzuki, H.Abe, B.S.Mun, K.Mase, K.Amemiya and H.Kondoh
In Situ Ambient Pressure XPS Study of CO Oxidation Reaction on Pd(111) Surfaces
J. Phys. Chem. C, **116** (2012) 18691.

R.Toyoshima, M.Yoshida, Y.Monya, K.Suzuki, B.S.Mun, K.Amemiya, K.Mase and H.Kondoh
Active Surface Oxygen for Catalytic CO Oxidation on Pd(100) Proceeding under Near Ambient Pressure Conditions
J. Phys. Chem. Lett., **3** (2012) 3182.

S.Wang, T.Sakurai, R.Kuroda and K.Akimoto
Energy Band Bending Induced Charge Accumulation at Fullerene/Bathocuproine Heterojunction Interface
Appl. Phys. Lett., **100** (2012) 243301.

S.Kawasaki, K.Nakatsuji, J.Yoshinobu, F.Komori, R.Takahashi, M.Lippmaa, K.Mase and A.Kudo
Epitaxial Rh-Doped $SrTiO_3$ Thin Film Photocathode for Water Splitting under Visible Light Irradiation
Appl. Phys. Lett., **101** (2012) 033910.

A.Toyoshima, T.Kikuchi, H.Tanaka, J.Adachi, K.Mase and K.Amemiya
In Situ Removal of Carbon Contamination from Optics in a Vacuum Ultraviolet and Soft X-Ray Undulator Beamline using Oxygen Activated by Zeroth-Order Synchrotron Radiation
J. Synchrotron Rad., **19** (2012) 722.

T.Kikuchi, K.Mase and F.Watanabe
Construction of Simple Non-Evaporable Getter Assemblies using St 707 Strips or St 172 Modules
J. Vac. Soc. Jpn., **55** (2012) 21.

A.Sano-Furukawa, T.Yagi, T.Okada, H.Gotou and T.Kikegawa
Compression Behaviors of Distorted Rutile-Type Hydrous Phases, MOOH (M = Ga, In, Cr) and CrOOD
Phys. Chem. Minerals, **39** (2012) 375.

S.Wang, T.Sakurai, R.Kuroda and K.Akimoto
Energy Level Alignment of C_{60}/Ca Interface with Bathocuproine as an Interlayer Studied by Ultraviolet Photoelectron Spectroscopy
Jpn. J. Appl. Phys., **51** (2012) 10NE32.

Y.Nakayama, Y.Uragami, S.Machida, K.R.Koswattage, D.Yoshimura, H.Setoyama, T.Okajima, K.Mase and H.Ishii
Full Picture of Valence Band Structure of Rubrene Single Crystals Probed by Angle-Resolved and Excitation-Energy-Dependent Photoelectron Spectroscopy
Appl. Phys. Express, **5** (2012) 111601.

T.Isao
Electronic Resonance and Photoemission Study of Nitrogen Doped TiO_2 Rutile (110) Single Crystals
Appl. Surf. Sci., **259** (2012) 320.

Former 13C

T.Omiya, H.Yokohara and M.Shimomura
Well-Oriented Pyrazine Lines and Arrays on Si(001) Formed by Thermal Activation of Substrate
J. Phys. Chem. C, **116** (2012) 9980.

14A

M.Koshimizu, K.Onodera, F.Nishikido, R.Haruki, K.Shibuya, S.Kishimoto and K.Asai
X-Ray Detection Capability of a $BaCl_2$ Single Crystal Scintillator
J. Appl. Phys., **111** (2012) 024906.

K.Asakura
Polarization-Dependent Total Reflection Fluorescence Extended X-Ray Absorption Fine Structure and its Application to Supported Catalysis
RCS Catalysis Book Series, **24** (2012) 281.

S.Kishimoto, F.Nishikido, R.Haruki, K.Shibuya and M.Koshimizu
Fast Scintillation Detectors for High-Energy X-Ray Region
Hyperfine Interact., **204** (2012) 101.

S.Kishimoto
X-Ray Detection with an Avalanche Photodiode and its Application
HOSHASEN, **38** (2012) 13. (*in Japanese*).

S.Kishimoto, S.Shimazaki, M.Ikeno, M.Saito, T.Taniguchi and M.Tanaka
A Frontend ASIC for a Silicon Avalanche Photodiode Linear Array Detector for Synchrotron X-Ray Experiments
2011 IEEE Nuclear Science Symposium Conference Record, (2012) 1674.

D.Yonetoku, T.Murakami, S.Gunji, T.Mihara, K.Toma, Y.Morihara, T.Takahashi, Y.Wakashima, H.Yonemochi, T.Sakashita and N.Toukairin
Magnetic Structures in Gamma-Ray Burst Jets Probed by Gamma-Ray Polarization
The Astrophysical J. Lett., **758** (2012) 1.

T.Miyoshi, Y.Arai, Y.Fujita, K.Hara, R.Ichimiya, Y.Ikegami, Y.Ikemoto, H.Kasai, H.Katsurayama, T.Kohriki, M.Okihara, Y.Ono, Y.Onuki, K.Shinsho, A.Takeda, K.Tauchi, T.Tsuboyama and Y.Unno
Recent Progress of Pixel Detector R&D based on SOI Technology
Phys. Procedia, **37** (2012) 1039.

14B

K.Mizuno, T.Kanai, K.Hirano and H.Okamoto
Determination of Hydrogen Diffusivity Depending on the Hydride Concentration in Titanium-Hydride by means of the Diffraction-Enhanced X-Ray Imaging Method
Trans. Mat. Res. Soc. Jpn., **37** (2012) 319.

T.Miyoshi, Y.Arai, Y.Fujita, K.Hara, R.Ichimiya, Y.Ikegami, Y.Ikemoto, H.Kasai, H.Katsurayama, T.Kohriki, M.Okihara, Y.Ono, Y.Onuki, K.Shinsho, A.Takeda, K.Tauchi, T.Tsuboyama and Y.Unno
Recent Progress of Pixel Detector R&D based on SOI Technology
Phys. Procedia, **37** (2012) 1039.

H.Okamoto
Potential of the X-Ray Phase-Contrast Imaging
MII online, **29** (2012) 43. (*in Japanese*).

14C

S.-J.Seo, N.Sunaguchi, T.Yuasa, Q.Huo, M.Ando, G.-H.Choi, H.-T.Kim, K.-H.Kim, E.-J.Jeong, W.-S.Chang and J.-K.Kim
Visualization of Microvascular Proliferation as a Tumor Infiltration Structure in Rat Glioma Specimens using the Diffraction-Enhanced Imaging in-Plane CT Technique
Phys. Med. Biol., **57** (2012) 1251.

S.Takeya, K.Honda, Y Gotoh, A.Yoneyama, K.Ueda, A.Miyamoto, T.Hondoh, A.Hori, D.Sun, R.Ohmura, K.Hyodo and T.Takeda
Diffraction-Enhanced X-Ray Imaging under Low-Temperature Conditions: Non-Destructive Observations of Clathrate Gas Hydrates
J. Synchrotron Rad., **19** (2012) 1038.

S.Takeya, A.Yoneyama, K.Ueda, H.Mimachi, M.Takahashi, K.Sano, K.Hyodo, T.Takeda and Y.Gotoh
Anomalously Preserved Clathrate Hydrate of Natural Gas in Pellet Form at 253 K
J. Phys. Chem. C, **116** (2012) 13842.

A.Momose, W.Yashiro, M.P.Olbinado and S.Harasse
X-Ray Phase Imaging: From Static Observation to Dynamic Observation
AIP Conf. Proc., **1466** (2012) 67.

S.Kibayashi, S.Harasse, W.Yashiro and A.Momose
High-Speed X-Ray Phase Tomography with Talbot Interferometer and Fringe Scanning Method
AIP Conf. Proc., **1466** (2012) 261.

M.P.Olbinado, S.Harasse, W.Yashiro and A.Momose
X-Ray Talbot-Lau Interferometer for High-Speed Phase Imaging and Tomography using White Synchrotron Radiation
AIP Conf. Proc., **1466** (2012) 266.

T.Miyoshi, Y.Arai, Y.Fujita, K.Hara, R.Ichimiya, Y.Ikegami, Y.Ikemoto, H.Kasai, H.Katsurayama, T.Kohriki, M.Okihara, Y.Ono, Y.Onuki, K.Shinsho, A.Takeda, K.Tauchi, T.Tsuboyama and Y.Unno
Recent Progress of Pixel Detector R&D based on SOI Technology
Phys. Procedia, **37** (2012) 1039.

K.Sasaki, S.Matsushita, F.Sato, C.Tokunaga, K.Hyodo and Y.Sakakibara
Cardiac Sympathetic Activity Assessed by Heart Rate Variability Indicates Myocardial Ischemia on Cold Exposure in Diabetes.
J. Jpn. College of Angiology, **52** (2012) 295. (*in Japanese*).

15A

H.Okuda, K.Takeshita, S.Ochiai, Y.Kitajima, S.Sakurai and H.Ogawa
Contrast Matching of an Si Substrate with Polymer Films by Anomalous Dispersion at the Si *K* Absorption Edge
J. Appl. Cryst., **45** (2012) 119.

S.Miisako, S.Kutsumizu and K.Sakajiri
A Partially Crosslinked Bicontinuous Cubic Phase Exhibiting A Temperature Range of More Than 100 °C
Chem. Comm., **48** (2012) 2225.

Y.Takenaka, H.Kitahata, N.L.Yamada, H.Seto and M.Hara
Gelation Effect on the Synthesis of High-Aspect-Ratio Gold Nanorods
J. Nanosci. Nanotechnol., **12** (2012) 714.

L.S.K.Dessanayake, D.Kodali, S.Ueno and K.Sato
Crystallization Kinetics of Organogels Prepared by Rice Bran Wax and Vegetable Oils
J. Oleo Sci., **61** (2012) 1.

Y.Sugimoto, M.Shioya, K.Yamamoto and S.Sakurai
Relationship between Axial Compression Strength and Longitudinal Microvoid Size for PAN-Based Carbon Fibers
Carbon, **50** (2012) 2860.

T.Shinkai, M.Ito, K.Sugiyama, K.Ito and H.Yokoyama
Ordered and Foam Structures of Semifluorinated Block Copolymers in Supercritical Carbon Dioxide
Soft Matter, **8** (2012) 5811.

S.Nagano, Y.Koizuka, T.Murase, M.Sano, Y.Shinohara, Y.Amemiya and T.Seki
Synergy Effect on Morphology Switching: Real-Time Observation of Photo-Orientation of Microphase Separation in a Block Copolymer
Angew. Chem. Int. Ed., **51** (2012) 5884.

Y.Zhao, G.Matsuba and H.Ito
Shear-Induced Crystallization and Rheological Behavior of Syndiotactic Polystyrene
Journal of Materials Research, **27** (2012) 1372.

H.Takeno, A.Maehara, M.Kuchiishi, K.Yoshiba, H.Takeshita, S Kondo, T.Dobashi, M.Takenaka and H.Hasegawa
Structural and Thermal Properties of Unpurified and Purified 12-Hydroxystearic Acid Solutions
Sen'i Gakkaishi, **68** (2012) 248.

Y.Tozuka, K.Higashi, T.Morita, M.Nishikawa, H.Uchiyama, J.Zhang, K.Moribe, K.Nishikawa, H.Takeuchi and K.Yamamoto
Transglycosylated Rutin-Specific Non-Surface-Active Nanostructure Affects Absorption Enhancement of Flurbiprofen
European Journal of Pharmaceutics and Biopharmaceutics, **82** (2012) 120.

H.Takahashi and K.Jojiki
Effect of Heavy Water on Nonlamellar Structures of Phospholipid and Monoolein Molecular Assemblies
Chem. Lett., **41** (2012) 1101.

Y.Nozue, S.Seno, T.Nagamatsu, S.Hosoda, Y.Shinohara, Y.Amemiya, E.B.Berda, G.Rojas, K.B.Wagener
Cross Nucleation in Polyethylene with Precisely Spaced Ethyl Branches
ACS Macro Lett., **1** (2012) 772.

M.Hishida and K.Tanaka
Transition of the Hydration State of a Surfactant Accompanying Structural Transitions of Self-Assembled Aggregates
J. Phys.: Condens. Matter, **24** (2012) 284113.

H.Takeno, A.Maehara, D.Yamaguchi and S.Koizumi
A Structural Study of an Organogel Investigated by Small-Angle Neutron Scattering and Synchrotron Small-Angle X-Ray Scattering
J. Phys. Chem. B, **116** (2012) 7739.

T.Morita, H.Murai, S.Kase and K.Nishikawa
Small-Angle X-Ray Scattering Study on the Fluctuations of Supercritical Aqueous Solution of *N*-Pentane along the Critical Isotherm of Water
Chem. Phys. Lett., **543** (2012) 68.

T.Morita, M.Ushio, K.Kanoh, E.Tanaka and K.Nishikawa
Small-Angle X-Ray Scattering Measurements of Ionic Liquids Pressurized with Carbon Dioxide using Titanium Sample Holder: 1-Butyl-3-methylimidazolium Bis(trifluoromethylsulfonyl) Amide Mixtures up to 22MPa
Jpn. J. Appl. Phys., **51** (2012) 076703.

N.Katina, A.Timchenko, H.Kihara, V.Balobanov, V.Vasiliev, I.Kashparov and V.Bychkova
Kinetics of Mutant Apomyoglobin Association
Macromol. Symp., **317/318** (2012) 215.

S.Takemori and M.Kimura
Structure and Function of Skeletal Muscle and Locomotive Systems: Involvement of Water-State Transitions
J Physical Fitness Sports Med., **1** (2012) 95.

M.Yoshino, H.Takahashi, T.Takagi, T.Baba, K.Morita, H.Amii, T.Kanamori and M.Sonoyama
Effect of Partial Fluorination in the Myristoyl Groups on Thermal and Interfacial Properties of Dimyristoylphosphatidylcholine
Chem. Lett., **41** (2012) 1495.

K.Oshima, Y.Sugimoto, T.C.Irving and K.Wakabayashi
Head-Head Interactions of Resting Myosin Crossbridges in Intact Frog Skeletal Muscles, Revealed by Synchrotron X-Ray Fiber Diffraction
PLoS One, **7** (2012) e52421.

Y.Nagai, Y.Kawabata and T.Kato
Microscopic Investigation on Morphologies of Bilayer Gel Structure in the Mixed Polyoxyethylene-Type Nonionic Surfactant Systems
J. Phys. Chem. B, **116** (2012) 12558.

K.Nishikawa and T.Morita
Solution Chemistry Based on the Concept of Fluctuations
Mol. Sci., **6** (2012) A0054. (*in Japanese*).

A.Noro, K.Higuchi, Y.Sageshima and Y.Matsushita
Preparation and Morphology of Hybrids Composed of a Block Copolymer and Semiconductor Nanoparticles via Hydrogen Bonding
Macromolecules, **45** (2012) 8013.

15B1

K.Wako, K.Kimura, Y.Yamamoto, T.Sawaura, M.Shen, M.Tachibana and K.Kojima
Digital Topography with an X-Ray CCD Camera for Characterizing Perfection in Protein Crystals
J. Appl. Cryst., **45** (2012) 1009.

M.Terabe, H.Okamoto and K.Koshida
Iterative Estimation of Coherent-Scattering Profiles from Given Positions by Use of a Single-Direction Beam
Radiol Phys Technol, **5** (2012) 237.

T.Nakano , D.Terada , Y.Kashiwa , M.Toyonaga , J.Nakamura and K.Abe
Observation of Domain Structures Near the α-INC-β Phase Boundary in Quartz using X-Ray Topography
Ferroelectrics, **441** (2012) 351.

15C

Y.Kato, H.Umezawa, S.Shikata and T.Teraji
Local Stress Distribution of Dislocations in Homoepitaxial Chemical Vapor Deposite Single-Crystal Diamond
Diamond & Related Materials, **23** (2012) 109.

K.Mizuno and H.Okamoto
Characterization of Semiconductor Thin Films by Grazing Incident X-Ray Topography
J. Cryst. Soc. Jpn., **54** (2012) 24. (*in Japanese*).

H.Yamaguchi and H.Matsuhata
Dislocation Analysis in SiC by Means of X-Ray Topography using Collimated Beam
J. Cryst. Soc. Jpn., **54** (2012) 18. (*in Japanese*).

H.Yamaguchi and H.Matsuhata
Threading Dislocations in 4H-SiC Observed by Double-Crystal X-Ray Topography
Materials Science Forum, **725** (2012) 7.

Y.Kato, H.Umezawa, H.Yamaguchi and S.Shikata
Structural Analysis of Dislocations in Type-IIa Single-Crystal Diamond
Diamond and Related Materials, **29** (2012) 37.

Y.Kato, H.Umezawa, H.Yamaguchi and S.Shikata
X-Ray Topography Used to Observe Dislocations in Epitaxially Grown Diamond Film
Jpn. J. Appl. Phys., **51** (2012) 090103.

Y.Yamamoto, S.Harada, K.Seki, A.Horio, T.Mitsuhashi and T.Ujihara
High-Efficiency Conversion of Threading Screw Dislocations in 4H-SiC by Solution Growth
Appl. Phys. Express, **5** (2012) 115501.

T.Ujihara, S.Kozawa, K.Seki, Alexander, Y.Yamamoto and S.Harada
Conversion Mechanism of Threading Screw Dislocation during SiC Solution Growth
Mater. Sci. Forum, **717-720** (2012) 351.

T.Shimura, D.Shimokawa, T.Matsumiya, N.Morimoto, A.Ogura, S.Iida, T.Hosoi and H.Watanabe
Synchrotron X-Ray Topography of Supercritical-Thickness Strained Silicon-on-Insulator Wafers for Crystalline Quality Evaluation and Electrical Characterization using Back-Gate Transistors
Current Appl. Phys., **12** (2012) S69.

T.Shimura, T.Matsumiya, N.Morimoto, T.Hosoi, K.Kajiwara, J.Chen, T.Sekiguchi and H.Watanabe
Analysis of Lattice Distortion in Multicrystalline Silicon for Photovoltaic Cells by Synchrotron White X-Ray Microbeam Diffraction
Mater. Sci. Forum, **725** (2012) 153.

H.Okamoto
Potential of the X-Ray Phase-Contrast Imaging
MII online, **29** (2012) 43. (*in Japanese*).

16A

M.Nakano, Y.Hikosaka, P.Lablanquie, F.Penent, S.-M.Huttula, I.H.Suzuki, K.Soejima, N.Kouchi and K.Ito
Auger Decay of Ar $2p$ Satellite States Studied with a Multielectron Coincidence Method
Phys. Rev. A, **85** (2012) 043405.

M.Sakamaki and K.Amemiya
In Situ Observation of Magnetic Anisotropy Energy of Alternately Layered FeNi Thin Films
e-J. Surf. Sci. Nanotech., **10** (2012) 97.

S.Tsunegi, Y.Sakuraba, K.Amemiya, M.Sakamaki, E.Ozawa, A.Sakuma, K.Takanashi and Y.Ando
Observation of Magnetic Moments at the Interface Region in Magnetic Tunnel Junctions using Depth-resolved X-Ray Magnetic Circular Dichroism
Phys. Rev. B, **85** (2012) 180408(R).

K.Amemiya, M.Sakamaki, S.Nakamoto, M.Yoshida, K.Suzuki, H.Kondoh, T.Koide, K.Ito, K.Tsuchiya, K.Harada, H.Sasaki, T.Aoto, T.Shioya, T.Obina, S.Yamamoto and Y.Kobayashi
Molecular Orientation Change during Adsorption of NO and N_2O on Ir(111) Observed by Real-Time Wavelength-Dispersive X-Ray Absorption Spectroscopy with Polarization Switching
Appl. Phys. Lett., **101** (2012) 161601.

K.Amemiya
Sub-nm Resolution Depth Profiling of the Chemical State and Magnetic Structure of Thin Films by a Depth-Resolved X-Ray Absorption Spectroscopy Technique
Phys. Chem. Chem. Phys., **14** (2012) 10477.

M.Sakamaki, K.Amemiya, M.O.Liedke, J.Fassbender, P.Mazalski, I.Sveklo and A.Maziewski
Perpendicular Magnetic Anisotropy in a Pt/Co/Pt Ultrathin Film Arising from a Lattice Distortion Induced by Ion Irradiation
Phys. Rev. B, **86** (2012) 024418.

K.Amemiya and M.Sakamaki
XAFS and XMCD Spectra at the Surface and Interface of Ultrathin Films Observed by the Depth-Resolved XAFS/XMCD Technique
e-J. Surf. Sci. Nanotech., **10** (2012) 521.

K.Amemiya
Recent Developments of the Wavelength-Dispersive XAFS Technique in the Soft X-Ray Region
Houshakou, **25** (2012) 269. (*in Japanese*).

V.R.Singh, V.K.Verma, K.Ishigami, G.Shibata, T.Kadono, A.Fujimori, D.Asakura, T.Koide, Y.Miura, M.Shirai, G.-f.Li, T.Taira and M.Yamamoto
Effects of Off-Stoichiometry on the Spin Polarization at the $Co_2Mn_\beta Ge_{0.38}$/MgO Interfaces: X-Ray magnetic Circular Dichroism Study
Phys. Rev. B, **86** (2012) 144412.

M.Tashiro, M.nakano, M.Ehara, F.Penent, L.Andric, J.Palaudoux, K.Ito, Y.Hikosaka, N.Kouchi and P.Lablanquie
Auger Decay of Molecular Double Core-Hole and its Satellite States: Comparison of Experiment and Calculation
J. Chem. Phys., **137** (2012) 224306.

Y.Hikosaka, K.Yamamoto, M.Nakano, T.Odagiri, K.Soejima, I.H.Suzuki, P.Lablanquie, F.Penent and K.Ito
Formation of Slow Electrons in the Auger Decay of Core-Ionized Water Molecules
J. Chem. Phys., **137** (2012) 191101.

P.Lablanquie, S.Sheinerman, L.Andric, J.Palaudoux, Y.Hikosaka, K.Ito and F.Penent
Post Collision Interaction Probed by Multi-Electron Coincidences: Application to the Ar 2s Inner-Shell Photoionization
J. Elec. Spec. Relat. Phenom., **185** (2012) 198.

M.Uchida, Y.Yamasaki, Y.Kaneko, K.Ishizaka, J.Okamoto, H.Nakao, Y.Murakami and Y.Tokura
Pseudogap-Related Charge Dynamics in the Layered Nickelate $R_{2-x}Sr_xNiO_4$ ($x \sim 1$)
Phys. Rev. B, **86** (2012) 165126.

T.Kataoka, Y.Yamazaki, V.R.Singh, Y.Sakamoto, K.Ishigami, V.K.Verma, A.Fujimori, F.-H.Chang, H.-J.Lin, D.J.Huang, C.T.Chen, D.Asakura, T.Koide, A.Tanaka, D.Karmakar, S.K.Mandal, T.K.Nath and I.Dagupta
X-Ray Absorption Spectroscopy and X-Ray Magnetic Circular Dichroism Studies of Transition-Metal-Codoped ZnO Nano-Particles
e-J. Surf. Sci. Nanotech., **10** (2012) 594.

17A

T.Tsuda, T.Suzuki and S.Kojima
Crystallization and Preliminary X-Ray Diffraction Analysis of *Bacillus subtilis* YwfE, an L-Amino-Acid Ligase
Acta Cryst. F, **68** (2012) 203.

J.Kondo
A Structural Basis for the Antibiotic Resistance Conferred by an A1408G Mutation in 16S rRNA and for the Antiprotozoal Activity of Aminoglycosides
Angew. Chem. Int. Ed., **51** (2012) 465.

S.Nakano, M.Takahashi, A.Sakamoto, H.Morikawa and K.Katayanagi
Structure-Function Relationship of Assimilatory Nitrite Reductases from the Leaf and Root of Tobacco Based on the High Resolution Structure
Protein Science, **21** (2012) 383.

N.Kuwabara, T.Oyama, D.Tomioka, M.Ohashi, J.Yanagisawa, T.Shimizu and H.Miyachi
Peroxisome Proliferator-Activatedreceptors (PPARs) Have Multiple Binding Points That Accommodate Ligands Invarious Conformations: Phenypropanoic Acid-Type PPAR Ligands Bind to PPAR Indifferent Conformations, Depending on the Subtype
J. Med. Chem., **55** (2012) 893.

D.Takeshita and K.Tomita
Molecular Basis for RNA Polymerization by Qβ Replicase
Nature Structural Molecular Biology, **19** (2012) 229.

D.-H.Im, K.Kimura, F.Hayasaka, T.Tanaka, M.Noguchi, A.Kobayashi, S.Shoda, K.Miyazaki, T.Wakagi and S.Fushinobu
Crystal Structures of Glycoside Hydrolase Family 51 α-L-Arabinofuranosidase from *Thermotoga maritima*
Biosci. Biotechnol. Biochem., **76** (2012) 423.

S.Chen, Y.Xu, K.Zhang, X.Wang, J.Sun, G.Gao and Y.Liu
Structure of N-Terminal Domain of ZAP Indicates How a Zinc-Finger Protein Recognizes Complex RNA
Nature Structural Molecular Biology, **19** (2012) 430.

H.Nojiri
Structural and Molecular Genetic Analyses of the Bacterial Carbazole Degradation System
Biosci. Biotechnol. Biochem., **76** (2012) 1.

K.Yoneda, H.Sakuraba, T.Araki and T.Ohshima
Crystal Structure of Binary and Ternary Complexes of Archaeal UDP-Galactose 4-Epimerase-like L-Threonine Dehydrogenase from *Thermoplasma volcanium*
J. Biol. Chem., **287** (2012) 12966.

S.Nakano, M.Sugihara, R.Yamada, K.Katayanagi and S.Tate
Structural Implication for the Impaired Binding of W150A Mutant LOX-1 to Oxidized Low Density Lipoprotein, OxLDL
Biochim. Biophys. Acta, **1824** (2012) 739.

J.Bunzen, J.Iwasa, P.Bonakdarzadeh, E.Numata, K.Rissanen, S.Sato and M.Fujita
Self-Assembly of $M_{24}L_{48}$ Polyhedra Based on Empirical Prediction
Angew. Chem. Int. Ed., **51** (2012) 3161.

Z.Zhang, L.Chen, L.Gao, K.Lin, L.Zhu, Y.Lu, X.Shi, Y.Gao, J.Zhou, P.Xu, J.Zhang and G.Wu
Structural Basis for the Recognition of Asef by Adenomatous Polyposis Coli
Cell Res., **22** (2012) 372.

K.-T.Wang, B.Desmolaize, J.Nan, X.-W.Zhang, L.-F.Li, S.Douthwaite and X.-D.Su
Structure of the Bifunctional Methyltransferase YcbY (RlmKL) That Adds the M^7G2069 and M^2G2445 Modifications in *Escherichia Coli* 23S rRNA
Nucleic Acids Res., **40** (2012) 5138.

N.Kuwabara,Y.Murayama, H.Hashimoto, Y.Kokabu, M.Ikeguchi, M.Sato, K.Mayanagi, Y.Tsutsui, H.Iwasaki and T.Shimizu
Mechanistic Insights into the Activation of Rad51-Mediated Strand Exchange from the Structure of a Recombination Activator, the Swi5-Sfr1 Complex
Structure, **20** (2012) 440.

M.Nagae, S.Re, E.Mihara, T.Nogi, Y.Sugita and J.Takagi
Crystal Structure of $\alpha5\beta1$ Integrin Ectodomain: Atomic Details of the Fibronectin Receptor
J. Cell Biol., **197** (2012) 131.

A.Nakamura, J.Ohtsuka, K.Miyazono, A.Yamamura, K.Kubota, R.Hirose, N.Hirota, M.Ataka, Y.Sawano and M.Tanokura
Improvement in Quality of Protein Crystals Grown in a High Magnetic Field Gradient
Crystal Growth and Design, **12** (2012) 1141.

S.Nakano, M.Takahashi, A.Sakamoto, H.Morikawa and K.Katayanagi
The Reductive Reaction Mechanism of Tobacco Nitrite Reductase Derived from a Combination of Crystal Structures and Ultraviolet-Visible Microspectroscopy
Proteins, **80** (2012) 2035.

J.S.Park, W.C.Lee, K.J.Yeo, K.S.Ryu, M.Kumarasiri, D.Hesek, M.Lee, S Mobashery, J.H.Song, S.I.Kim, J.C.Lee, C.Cheong, Y.H.Jeon and H.Y.Kim
Mechanism of Anchoring of OmpA Protein to the Cell Wall Peptidoglycan of the Gram-Negative Bacterial Outer Membrane
FASEB J., **26** (2012) 219.

L.Wang,K.Zhang, L.Wu, S.Liu, H.Zhang, Q.Zhou, L.Tong, F.Sun and Z.Fan
Structural Insights into the Substrate Specificity of Human Granzyme H: The Functional Roles of a Novel RKR Motif
The Journal of Immunology, **188** (2012) 765.

X.Wang, L.Wang, X.Wang, F.Sun and C.Wang
Structural Insights into the Peroxidase Activity and Inactivation of Human Peroxiredoxin 4
Biochem. J., **441** (2012) 113.

H.Sakurama, S.Fushinobu, M.Hidaka, E.Yoshida, Y.Honda, H.Ashida, M.Kitaoka, H.Kumagai, K.Yamamoto and T.Katayama
1,3-1,4-α-L-Fucosynthase that Specifically Introduces Lewis a/x Antigens into Type-1/2 Chains
J. Biol. Chem., **287** (2012) 16709.

H.Shoun, S.Fushinobu, L.Jiang, S.-W.Kim and T.Wakagi
Fungal Denitrification and Nitric Oxide Reductase Cytochrome P450nor
Phil. Trans. R. Soc. B, **367** (2012) 1186.

T.Wakagi
A Special Enzyme Acting in a Primordial Metabolism; Discovery of One-Enzyme with Two Reactions
Kagaku, **67** (2012) 72. (*in Japanese*).

H.Nishimasu, S.Fushinobu and T.Wakagi
Molecular Mechanism by which One Enzyme Catalyzes Two Reactions
J. Cryst. Soc. Jpn., **54** (2012) 113. (*in Japanese*).

M.M.Islam, M.A.Khan and Y.Kuroda
Analysis of Amino Acid Contributions to Protein Solubility using Short Peptide Tags Fused to a Simplified BPTI Variant
Biochim. Biophys. Acta, **1824** (2012) 1144.

K.Yu, Z.Ming, Y.Li, C.Chen, Z.Bao, Z.Ren, B.Liu, W.Tao, Z.Rao and Z.Lou
Purification, Crystallization and Preliminary X-Ray Analysis of Nonstructural Protein 2 (nsp2) from Avian Infectious Bronchitis Virus
Acta Cryst. F, **68** (2012) 716.

M.Gao, D.Li, Y.Hu, Y.Zhang, Q.Zou and D.-C.Wang
Crystal Structure of TNF-α-Inducing Protein from *Helicobacter Pylori* in Active Form Reveals the Intrinsic Molecular Flexibility for Unique DNA-Binding
PLoS One, **7** (2012) e41871.

J.Ding, W.Wang, H.Feng, Y.Zhang and D.-C.Wang
Structural Insights into the *Pseudomonas aeruginosa* Type VI Virulence Effector Tse1 Bacteriolysis and Self-protection Mechanisms
J. Biol. Chem., **287** (2012) 26911.

S.Kikuchi, K.Hara, T.Shimizu, M.Sato and H.Hashimoto
Structural Basis of Recruitment of DNA Polymerase ζ by Interaction between REV1 and REV7 Proteins
J. Biol. Chem., **287** (2012) 33847.

U.Ohto, K.Fukase, K.Miyake and T.Shimizu
Structural Basis of Species-Specific Endotoxin Sensing by Innate Immune Receptor TLR4/MD-2
Proc. Natl. Acad. Sci. USA, **109** (2012) 7421.

N.Suzuki, Y.-M.Kim, Z.Fujimoto, M.Momma, M.Okuyama, H.Mori, K.Funane and A.Kimura
Structural Elucidation of Dextran Degradation Mechanism by *Streptococcus mutans* Dextranase Belonging to Glycoside Hydrolase Family 66
J. Biol. Chem., **287** (2012) 19916.

X.Wang, W.Peng, J.Ren, Z.Hu, J.Xu, Z.Lou, X.Li, W.Yin, X.Shen, C.Porta, T.S.Walter, G.Evans, D.Axford, R.Owen, D.J.Rowlands, J.Wang, D.I.Stuart, E.E.Fry and Z.Rao
A Sensor-Adaptor Mechanism for Enterovirus Uncoating from Structures of EV71
Nature Structural Molecular Biology, **19** (2012) 424.

M.Nishikiori, S.Sugiyama, H.Xiang, M.Niiyama, K.Ishibashi, T.Inoue, M.Ishikawa, H.Matsumura and E.Katoh.
Crystal Structure of the Superfamily 1 Helicase from Tomato Mosaic Virus
J. Virology, **86** (2012) 7565.

H.Kondo, Y.Hanada, H.Sugimoto, T.Hoshino, C.P.Garnham, P.L.Davies and S.Tsuda
Ice-Binding Site of Snow Mold Fungus Antifreeze Protein Deviates from Structural Regularity and High Conservation
Proc. Natl. Acad. Sci. USA, **109** (2012) 9360.

Q.Tang, P.Gao, Y.-P.Liu, A.Gao, X.-M.An, S.Liu, X.-X.Yan and D.-C.Liang
RecOR Complex Including RecR N-N Dimer and RecO Monomer Displays a High Affinity for ssDNA
Nucleic Acids Res., **40** (2012) 11115.

A.Nakamura, M.Fujihashi, R.Aono, T.Sato, Y.Nishiba, S.Yoshida, A.Yano, H.Atomi, T.Imanaka and K.Miki
Dynamic, Ligand-Dependent Conformational Change Triggers Reaction of Ribose-1,5-Bisphosphate Isomerase from *Thermococcus Kodakarensis* KOD1
J. Biol. Chem., **287** (2012) 20784.

M.Fukumoto, D.Kudou, S.Murano, T.Shiba, D.Sato, T.Tamura, S.Harada and K.Inagaki
The Role of Amino Acid Residues in the Active Site of L-Methionine γ-lyase from *Pseudomonas putida*
Biosci. Biotechnol. Biochem., **76** (2012) 1275.

D.Fujita, K.Suzuki, S.Sato, M.Yagi-Utsumi, Y.Yamaguchi, N.Mizuno, T.Kumasaka, M.Takata, M.Noda, S.Uchiyama, K.Kato and M.Fujita
Protein Encapsulation within Synthetic Molecular Hosts
Nature Communications, **3** (2012) 1093.

H.Matsumura, E.Mizohata, H.Ishida, A.Kogami, T.Ueno, A.Makino, T.Inoue, A.Yokota, T.Mae and Y.Kai
Crystal Structure of Rice Rubisco and Implications for Activation Induced by Positive Effectors NADPH and 6-Phosphogluconate
J. Mol. Biol., **422** (2012) 75.

H.Matsumura, N.Kusaka, T.Nakamura, N.Tanaka, K.Sagegami, K.Uegaki, T.Inoue and Y.Mukai
Crystal Structure of the N-Terminal Domain of the Yeast General Corepressor Tup1p and Its Functional Implications
J. Biol. Chem., **287** (2012) 26528.

S.Sugiyama, M.Maruyama, G.Sazaki, M.Hirose, H.Adachi, K.Takano, S.Murakami, T.Inoue, Y.Mori and H. Matsumura
Growth of Protein Crystals in Hydrogels Prevents Osmotic Shock
J. Am. Chem. Soc., **134** (2012) 5786.

K.Suzuki, N.Ohbayashi, J.Jiang, X.Zhang, M.M.Hoque, M.Tsunoda, K.Murayama, H.Tanaka and A.Takenaka
Crystallographic Study of the Interaction of the Anti-HIV Lectin Actinohivin with α(1-2)mannobiose Moiety of gp120 HMTG
Acta Cryst. F, **68** (2012) 1060.

M.M.Hoque, K.Suzuki, M.Tsunoda, J.Jiang, F.Zhang, A.Takahashi, N.Ohbayashi, X.Zhang, H.Tanaka, S.Omura and A.Takenaka
Structural Insights into the Specific Anti-HIV Property of Actinohivin: Structure of its Complex with the α(1-2)mannobiose Moiety of gp120
Acta Cryst. D, **68** (2012) 1671.

M.Koyama and Y.Matsuura
Mechanistic Insights from the Recent Structures of the CRM1 Nuclear Export Complex and its Disassembly Intermediate
Biophysics, **8** (2012) 145.

K.Miyazono, N.Tabei, S.Morita, Y.Ohnishi, S.Horinouchi and M.Tanokura
Substrate Recognition Mechanism and Substrate-Dependent Conformational Changes of an ROK Family Glucokinase from *Streptomyces Griseus*
J. Bacteriol., **194** (2012) 607.

D.Sen, N.H.Heo and K.Seff
Using InCl Vapor to Ion Exchange Indium into Zeolite Na-X. Single Crystal Structure of —$In_{34}Na_{50}$—$[Si_{100}Al_{92}O_{384}]$-FAU Containing In_5^{7+} and In^+
J. Phys. Chem. C, **116** (2012) 14445.

T.Matsui, J.Yamane, N.Mogi, H.Yamaguchi, H.Takemoto, M.Yao and I.Tanaka
Structural Reorganization of the Bacterial Cell -Division Protein FtsZ from *Staphylococcus aureus*
Acta Cryst. D, **68** (2012) 1175.

Y.Itoh, S.Sekine and S.Yokoyama
Crystallization and Preliminary X-Ray Crystallographic Analysis of *Aquifex aeolicus* SelA, a Bacterial Selenocysteine Synthase
Acta Cryst. F, **68** (2012) 1128.

Y.Itoh, S.Sekine and S.Yokoyama
Crystallization and Preliminary X-Ray Crystallographic Analysis of Bacterial $tRNA^{Sec}$ in Complex with Seryl-tRNA Synthetase
Acta Cryst. F, **68** (2012) 678.

Y.Hirano, Y.Kimura, H.Suzuki, K.Miki and Z.-Y.Wang
Structure Analysis and Comparative Characterization of the Cytochrome *c'* and Flavocytochrome *c* from Thermophilic Purple Photosynthetic Bacterium *Thermochromatium tepidum*
Biochemistry, **51** (2012) 6556.

J.Han, H.J.Kim, S.-C.Lee, S.Hong, K.Park, Y.H.Jeon, D.Kim, H.-K.Cheong and H.-S.Kim
Structure-Based Rational Design of a Toll-like Receptor 4 (TLR4) Decoy Receptor with High Binding Affinity for a Target Protein
PLoS One, **7** (2012) e30929.

H.M.Qin, T.Miyakawa, A.Nakamura, Y.L.Xue, T.Kawashima, T.Kasahara, M.Hibi, J.Ogawa and M.Tanokura
Expression, Purification, Crystallization and Preliminary X-Ray Analysis of a Novel N-Substituted Branched-Chain L-Amino-Acid Dioxygenase from *Burkholderia ambifaria* AMMD
Acta Cryst. F, **68** (2012) 1067.

D.Takeshita, S.Yamashita and K.Tomita
Mechanism for Template-Independent Terminal Adenylation Activity of Qβ Replicase
Structure, **20** (2012) 1661.

S.-S.Cha, Y.J.An, C.-S.Jeong, M.-K.Kim, S.-G.Lee, K.-H.Lee and B.-H.Oh
Experimental Phasing using Zinc Anomalous Scattering
Acta Cryst. D, **68** (2012) 1253.

M.Unno, K.Kizawa, M.Ishihara and H.Takahara
Crystallization and Preliminary X-Ray Crystallographic Analysis of Human Peptidylarginine Deiminase Type III
Acta Cryst. F, **68** (2012) 668.

K.Arita, S.Isogai, T.Oda, M.Unoki, K.Sugita, N.Sekiyama, K.Kuwata, R.Hamamoto, H.Tochio, M.Sato, M.Ariyoshi and M.Shirakawa
Recognition of Modification Status on a Histone H3 Tail by Linked Histone Reader Modules of the Epigenetic Regulator UHRF1
Proc. Natl. Acad. Sci. USA, **109** (2012) 12950.

N.Maita, H.Taniguchi and H.Sakuraba
Crystallization, X-Ray Diffraction Analysis and SIRAS Phasing of Human α-L-Iduronidase
Acta Cryst. F, **68** (2012) 1363.

L.Yan, Y.Ma Y, D.Liu, X.Wei, Y.Sun, X.Chen, H.Zhao, J.Zhou, Z.Wang, W.Shui and Z.Lou
Structural Basis for the Impact of Phosphorylation on the Activation of Plant Receptor-Like Kinase BAK1
Cell Res., **22** (2012) 1304.

K.Kubota, A.Yamagata, Y.Sato, S.Goto-Ito and S.Fukai
Get1 Stabilizes an Open Dimer Conformation of Get3 ATPase by Binding Two Distinct Interfaces
J. Mol. Biol., **422** (2012) 366.

J.Gao, Y.Ma, Y.Sun, H.Zhao, D.Hong, L.Yan and Z.Lou
Crystallization and Preliminary Crystallographic Analysis of *Arabidopsis thaliana* BRI1-Associated Kinase 1 (BAK1) Cytoplasmic Domain
Acta Cryst. F, **68** (2012) 340.

J.Park, M.I.Kim, Y.D.Park, I.Shin, J.Cha, C.H.Kim and S.Rhee
Structural and Functional Basis for Substrate Specificity and Catalysis of Levan Fructotransferase
J. Biol. Chem., **287** (2012) 31233.

Y.Sato, A.Yamagata, S.Goto-Ito, K.Kubota, R.Miyamoto, S Nakada and S.Fukai
Molecular Basis of Lys-63-linked Polyubiquitination Inhibition by the Interaction between Human Deubiquitinating Enzyme OTUB1 and Ubiquitin-Conjugating Enzyme UBC13
J. Biol. Chem., **287** (2012) 25860.

T.Ohnuma, T.Numata, T.Osawa, H.Inanaga, Y.Okazaki, S.Shinya, K.Kondo, T.Fukuda and T.Fukamizo
Crystal Structure and Chitin Oligosaccharide-Binding Mode of a 'Loopful' Family GH19 Chitinase from Rye, *Secale Cereale, Seeds*
FEBS J., **279** (2012) 3639.

Y.Guo, W.Wang, W.Ji, M.Deng, Y.Sun, H.Zhou, C.Yang, F.Deng, H.Wang, Z.Hu, Z.Lou and Z.Rao
Crimean-Congo Hemorrhagic Fever Virus Nucleoprotein Reveals Endonuclease Activity in Bunyaviruses
Proc. Natl. Acad. Sci. USA, **109** (2012) 5046.

H Ru, LX Zhao, W Ding, LY Jiao, N Shaw, WG Liang, LG Zhang, LW Hung, N Matsugaki, S Wakatsuki and ZJ Liu
S-SAD Phasing Study of Death Receptor 6 and Its Solution Conformation Revealed by SAXS
Acta Cryst. D, **68** (2012) 521.

R.Arai, S.Fukui, N.Kobayashi and J.Sekiguchi
Solution Structure of IseA, an Inhibitor Protein of DL-Endopeptidases from *Bacillus Subtilis*, Reveals a Novel Fold with a Characteristic Inhibitory Loop
J. Biol. Chem., **287** (2012) 44736.

Y.-H.Huang, X.-Y.Liu, X.-X.Du, Z.-F.Jiang and X.-D.Su
The Structural Basis for the Sensing and Binding of Cyclic di-GMP by STING
Nature Structural Molecular Biology, **19** (2012) 728.

H.Tanaka, N.Miyazaki, K.Matoba, T.Nogi, K.Iwakasaki and J.Takagi
Higher-Order Architecture of Cell Adhesion Mediated by Polymorphic Synaptic Adhesion Molecules Neurexin and Neuroligin
Cell Reports, **2** (2012) 101.

M.Fujihashi, M.Hiraki, G.Ueno, S.Baba, H.Murakami, M.Suzuki, N.Watanabe, I.Tanaka, A.Nakagawa, S.Wakatsuki, M.Yamamoto and K.Miki
Crystal Sample Pins and a Storage Cassette System Compatible with the Protein Crystallography Beamlines at both the Photon Factory and SPring-8
J. Appl. Cryst., **45** (2012) 1156.

B.-G.Lee, M.K.Kim, B.-W.Kim, S.W.Suh and H.K.Song
Structures of the Ribosome-Inactivating Protein from Barley Seeds Reveal a Unique Activation Mechanism
Acta Cryst. D, **68** (2012) 1488.

T.Miyafusa, J.M.M.Caaveiro, Y.Tanaka and K.Tsumoto
Crystal Structure of the Enzyme CapF of *Staphylococcus aureus* Reveals a Unique Architecture Composed of Two Functional Domains
Biochem. J., **443** (2012) 671.

K.H.Kim, D.R.An, J.Song, J.Y.Yoon, H.S.Kim, H.J.Yoon, H.N.Im, J.Kim, D.J.Kim, S.J.Lee, K-H.Kim, H-M.Lee, H-J.Kim, E-K.Jo, J.Y.Lee and S.W.Suh
Mycobacterium Tuberculosis Eis Protein Initiates Suppression of Host Immune Responses by Acetylation of DUSP16/MKP-7
Proc. Natl. Acad. Sci. USA, **109** (2012) 7729.

H.Yoshida, A.Yoshihara, M.Teraoka, S.Yamashita, K.Izumori and S.Kamitori
Structure of L-Rhamnose Isomerase in Complex with L-Rhamnopyranose Demonstrates the Sugar-Ring Opening Mechanism and the Role of a Substrate Sub-Binding Site
FEBS Open Bio, **3** (2012) 35.

S.Hoshino, T.Maki and I.Hayashi
Crystallization and Preliminary X-Ray Data Analysis of the pXO1 Plasmid-Partitioning Factor TubZ from *Bacillus cereus*
Acta Cryst. F, **68** (2012) 1550.

S.Watanabe, D.Sasaki, T.Tominaga and K.Miki
Structural Basis of [NiFe] Hydrogenase Maturation by Hyp Proteins
Biol. Chem., **393** (2012) 1089.

S.Watanabe, R.Matsumi, H.Atomi, T.Imanaka and K.Miki
Crystal Structures of the HypCD Complex and the HypCDE Ternary Complex: Transient Intermediate Complexes during [NiFe] Hydrogenase Maturation
Structure, **20** (2012) 2124.

B.Ku, K.-H.Lee, W.S.Park, C.-S.Yang, J.Ge, S.-G.Lee, S.-S.Cha, F.Shao, W.D.Heo, J.U.Jung and B.-H.Oh
VipD of *Legionella pneumophila* Targets Activated Rab5 and Rab22 to Interfere with Endosomal Trafficking in Macrophages
PLoS Pathogens, **8** (2012) e1003082.

K.Ito, R.Murakami, M.Mochizuki, H.Qi, Y.Shimizu, K.Miura, T.Ueda and T.Uchiumi
Structural Basis for the Substrate Recognition and Catalysis of Peptidyl-tRNA Hydrolase
Nucl. Acids Res., **40** (2012) 10521.

M.Bai, X.Pang, J.Lou, Q.Zhou, K.Zhang, J.Ma, J.Li, F.Sun and V.W.Hsu
Mechanistic Insights into Regulated Cargo Binding by ACAP1 Protein
J. Biol. Chem., **287** (2012) 28675.

X.Wang, L.Wang, X.Wang, F.Sun and C.-C.Wang
Structural Insights into the Peroxidase Activity and Inactivation of Human Peroxiredoxin 4
Biochem. J., **441** (2012) 113.

Y.Takashima, E.Mizohata, K.Tokuoka, S.R.Krungkrai, Y.Kusakari, S.Konishi, A.Satoh, H.Matsumura, J.Kurngkrai, T.Horii and T.Inoue
Crystallization and Preliminary X-Ray Diffraction Analysis of Orotate Phosphoribosyltransferase from the Human Malaria Parasite *Plasmodium falciparum*
Acta Cryst. F, **68** (2012) 244.

T.Hayashi, M.Senda, H.Morohashi, H.Higashi, M.Horio, Y.Kashiba, L.Nagase, D.Sasaya, T.Shimizu, N.Venugopalan, H.Kumeta, N.Noda, F.Inagaki, T.Senda and M.Hatakeyama
Tertiary Structure-Function Analysis Reveals the Pathogenic Signaling Potentiation Mechanism of *Helicobacter pylori* Oncogenic Effector CagA
Cell Host & Microbe, **12** (2012) 20.

18A

K.Yaji, S.Hatta, T.Aruga and H.Okuyama
Structural and Electronic Properties of the Pb/Ge(111)-$\beta(\sqrt{3}\times\sqrt{3})R30°$ Surface Studied by Photoelectron Spectroscopy and First-Principles Calculations
Phys. Rev. B, **86** (2012) 235317.

A.Fleurence, R.Friedlein, T.Ozaki, H.Kawai, Y.Wang and Y.Yamada-Takamura
Experimental Evidence for Epitaxial Silicene on Diboride Thin Films
Phys. Rev. Lett., **108** (2012) 245501.

18B

B.Saha, P.Chakraborty, H.Gnaser, M.Sharma and M.K.Sanyal
Exact Compositional Analysis of SiGe Alloys by Matrix Effect Compensated MCs SIMS
Appl. Phys. A, **108** (2012) 671.

Former 18B

H.Shoun, S.Fushinobu, L.Jiang, S.-W.Kim and T.Wakagi
Fungal Denitrification and Nitric Oxide Reductase Cytochrome P450nor
Phil. Trans. R. Soc. B, **367** (2012) 1186.

H.-S.Youn, M.-K.Kim, G.B.Kang, T.G.Kim, J.Y.An, J.-G.Lee, K.R.Park, Y.L, S.Fukuoka and S.H.Eom
Crystallization and Preliminary X-Ray Crystallographic Analysis of Quinolinate Phosphoribosyltransferase from Porcine Kidney in Complex with Nicotinate Mononucleotide.
Acta Cryst. F, **68** (2012) 1488.

18C

S.Nakano
Effect of Helium Quasi-Hydrostatic Pressure on High-Pressure Behavior of Some Materials with Nano Spaced
The Review of High Pressure Science & Technology, **22** (2012) 26. (*in Japanese*).

A.Shinozaki, H.Hirai, H.Kagi, T.Kondo, T.Okada, D.Nishio-Hamane, S.Machida, T.Irifune, T.Kikegawa and T.Yagi
Reaction of Forsterite with Hydrogen Molecules at High Pressure and Temperature
Phys. Chem. Minerals, **39** (2012) 123.

Y.Ishii, K.Okamura, T.Matsushita and S.Kawasaki
Origin of High Power Performance of Mesoporous Carbon-TiO_2(B) Nanocomposite Electrodes: An *In Situ* Synchrotron X-Ray Diffraction Study of TiO_2(B) Electrode upon Lithium Insertion
Mater. Express, **2** (2012) 23.

A.Al-zubaidi, T.Inoue, T.Matsushita, Y.Ishii, T.Hashimoto and S.Kawasaki
Cyclic Voltammogram Profile of Single-Walled Carbon Nanotube Electric Double-Layer Capacitor Electrode Reveals Dumbbell Shape
J. Phys. Chem. C, **116** (2012) 7681.

K.Matsui, K.Yamamoto, T.Kawaai, Y.Kawamura, J.Hayashi, K.Takeda and C.Sekine
Structural Instability of Unfilled Skutterudite Compounds MX_3 (M = Co, Rh, and Ir; X = As and Sb) under High Pressure
J. Phys. Soc. Jpn., **81** (2012) 104604.

D.Y.Tan, W.S.Xiao, W.Zhou, M.Chen, W.G.Zhou, X.D.Li, Y.C.Li and J.Liu
High Pressure X-Ray Diffraction Study on $BaWO_4$-II
High Pressure Res., **32** (2012) 262.

D.Y.Tan, W.S.Xiao, W.Zhou, M.Chen, X.L.Xiong and M.S.Song
First-Order Character of the Displacive Structural Transition in $BaWO_4$
Chin. Phys. B, **21** (2012) 086201.

H.Yamawaki, H.Fujihisa, Y.Gotoh and S.Nakano
Formation of $LiBH_4$ Hydrate with Dihydrogen Bonding
J. Alloys and Compounds, **541** (2012) 111.

H.Hirai, S.Kagawa, T.Tanaka, T.Matsuoka, T.Yagi, Y.Ohishi, S.Nakano, Y.Yamamoto and T.Irifune
Structural Changes of Filled Ice Ic Hydrogen Hydrate under Low Temperatures and High Pressures from 5 to 50 GPa
J. Chem. Phys., **137** (2012) 074505.

19A

K.Yaji, S.Hatta, T.Aruga and H.Okuyama
Structural and Electronic Properties of the Pb/Ge(111)-$\beta(\sqrt{3}\times\sqrt{3})R30^\circ$ Surface Studied by Photoelectron Spectroscopy and First-Principles Calculations
Phys. Rev. B, **86** (2012) 235317.

20A

K.Kawai, T.Kohmura, S.Ikeda, K.Kaneko, T.watanabe, H.Tsunemi, K.Hayashida, N.Anabuki, H.Nakajima, S.Ueda, T.G.Tsuru, T.Dotani, M.Ozaki, K.Matsuta, T.Fujinaga, S.Kitamoto, H.Murakami, J.Hiraga, K.Mori and ASTRO-H SXI Team
Optical, UV and Soft X-Ray Transmission of Optical Blocking Layer for the X-Ray CCD
AIP Conf. Proc., **1427** (2012) 255.

M.Kitajima, M.Kurokawa, T.Kishino, K.Toyoshima, T.Odagiri, H.Kato, K.Anzai, M.Hoshino, H.Tanaka and K.Ito
Ultra-Low-Energy Electron Scattering Cross Section Measurements of Ar, Kr and Xe Employing the Threshold Photoelectron Source
Eur. Phys. J. D, **66** (2012) 130.

S.Ikeda, T.Kohmura, K.Kawai, K.Kaneko, T.Watanabe, H.Tsunemi, K.Hayashida, N.Anabuki, H.Nakajima, S.Ueda, T.G.Tsuru, T.Dotani, M.Ozaki, K.Matsuta, T.Fujinaga, S.Kitamoto, H.Murakami, J.Hiraga, K.Mori,ASTRO-H SXI Team
Soft X-Ray Response of the X-Ray CCD Camera Directly Coated with Optical Blocking Layer
AIP Conf. Proc., **1427** (2012) 253.

20B

D.J.Sprouster and M.C.Ridgway
Ion Beam Formation and Modification of Cobalt Nanoparticles
Applied Science, **2** (2012) 396.

C.C.Scarborough, S.Sproules, C.J.Doonan, K.S.Hagen, T.Weyhermuller and K.Wieghardt
Scrutinizing Low-Spin Cr(II) Complexes
Inorg. Chem., **51** (2012) 6969.

Q.Zhou, P.Blanchard, B.J.Kennedy, E.Reynolds, Z.Zhang, W.Miiller, J.B.Aitken, M.Avdeev, L-Y.Jang and J.A.Kimpton
Synthesis, Structural and Magnetic Studies of the Double Perovskites Ba_2CeMO_6 (M= Ta, Nb)
Am. Chem. Soc., **24** (2012) 2978.

S.G.Johnston, E.D.Burton, A.F.Keene, B.Planer-Friedrich, A.Voegelin, M.G.Blackford and G.R.Lumpkin
Arsenic Mobilization and Iron Transformations during Sulfidization of As(V)-Bearing Jarosite
Chem. Geology, **334** (2012) 9.

R.He, R.K.Hocking and T.Tsuzuki
Local Structure and Photocatalytic Property of Sol-Gel Synthesized ZnO Doped with Transition Metal Oxides
J. Mater. Sci., **47** (2012) 3150.

C.T.Chantler, N.A.Rae, M.T.Islam, S.P.Best, J.Yeo, L.F.Smale, J.Hester, N.Mohammadi and F.Wang
Stereochemical Analysis of Ferrocene and the Uncertainty of Fluorescence XAFS Data
J. Synchrotron Rad., **19** (2012) 145.

W.Liu, S.Borg, B.Etschmann, Y.Mei and J.Brugger
An XAS Study of Speciation and Thermodynamic Properties of Aqueous Zinc Bromide Complexes at 25-150 C°
Chemical Geology, **298** (2012) 57.

E.Donner, C.G.Ryan, D.L.Howard, B.Zarcinas, K.G.Scheckel, S.P.McGrath, M.D.Jonge, D.Paterson, R.Naidu and E.Lombi
A Multi-Technique Investigation of Copper and Zinc Distribution, Speciation and Potential Bioavailability in Biosolids
Environmental Pollution, **166** (2012) 57.

27A

Y.Baba, A.Narita, T.Sekiguchi, I.Shimoyama, N.Hirao, S.Entani and S.Sakai
Structure Determination of Self-Assembled Monolayer on Oxide Surface by Soft-X-Ray Standing Wave
e-J. Surf. Sci. Nanotech., **10** (2012) 69.

A.Narita, Y.Baba, T.Sekiguchia, I.Shimoyama, N.Hirao and T.Yaita
Anchoring of Alkyl Chain Molecules on Oxide Surface using Silicon Alkoxide
Appl. Surf. Sci., **258** (2012) 2034.

A.Narita, Y.Baba, T.Sekiguchi, I.Shimoyama N.Hirao and T.Yaita
Immobilization of Alkyl Chain Molecules on Oxide Surface using Phosphonic Acid as an Anchor
e-J. Surf. Sci. Nanotech., **10** (2012) 367.

M.A.Mannan, Y.Baba, T.Sekiguchi, I.Shimoyama, N.Hirao, M.Nagano and H.Noguchi
Orientation of One-Dimensional Silicon Polymer Films Studied by X-Ray Absorption Spectroscopy
J. Nanomaterials, **2012** (2012) 528256.

S.Ishiyama, Y.Baba, R.Fujii, M.Nakamura and Y.Imahori
Synthesis of Lithium Nitride for Neutron Production Target of BNCT by *in situ* Lithium Deposition and Ion Implantation
Nucl. Instrum. Meth. Phys. Res. B, **293** (2012) 42.

S.Ishiyama, Y.Baba, R.Fujii, M.Nakamura and Y.Imahori
In-situ Vacuum Deposition Technique of Lithium on Neutron Production Target for BNCT
Nucl. Instrum. Meth. Phys. Res. B, **288** (2012) 18.

27B

C.Suzuki, T.Nishi, M.Nakada, M.Akabori, M.Hirata and Y.Kaji
Core-Hole Effect on XANES and Electronic Structure of Minor Actinide Dioxides with Fluorite Structure
J. Phys. Chem. Solids, **73** (2012) 209.

M.Tomita, K.Kobayashi and M.Maeda
Microbeam Studies of Soft X-Ray Induced Bystander Cell Killing using Microbeam X-Ray Cell Irradiation System at CRIEPI
J. Radiat. Res., **53** (2012) 482.

H.Okamura, A.Ikeda-Ohno, T.Saito, N.Aoyagi, H.Naganawa, N.Hirayama, S.Umetani, H.Imura and K.Shimojo
Specific Cooperative Effect of a Macrocyclic Receptor for Metal Ion Transfer into an Ionic Liquid
Anal. Chem., **84** (2012) 9332.

28A

T.Arakane, T.Sato, S.Souma, K.Kosaka, K.Nakayama, M.Komatsu, T.Takahashi, Z.Ren, K.Segawa and Y.Ando
Tunable Dirac Cone in the Topological Insulator $Bi_{2-x}Sb_xTe_{3-y}Se_y$
Nature Communications, **3** (2012) 636.

S.Souma, K.Eto, M.Nomura, K.Nakayama, T.Sato, T.Takahashi, K.Segawa and Y.Ando
Topological Surface States in Lead-Based Ternary Telluride $Pb(Bi_{1-x}Sb_x)_2Te_4$
Phys. Rev. Lett., **108** (2012) 116801.

K.Nakayama, E.Ieki, Y.Tanaka, T.Sato, T.Takahashi, T.Kuroda, H.Mizoguchi, S.W.Kim and H.Hosono
Angle-Resolved Photoemission Spectroscopy of Co-Based Boride Superconductor $LaCo_{1.73}Fe_{0.27}B_2$
Phys. Rev. B, **86** (2012) 014503.

S.Aizaki, T.Yoshida, K.Yoshimatsu, M.Takizawa, M.Minohara, S.Ideta, A.Fujimori, K.Gupta, P.Mahadevan, K.Horiba, H.Kumigashira and M.Oshima
Self-Energy on the Low- to High-Energy Electronic Structure of Correlated Metal $SrVO_3$
Phys. Rev. Lett., **109** (2012) 056401.

Y.Tanaka, Z.Ren, T.Sato, K.Nakayama, S.Souma, T.Takahashi, K.Segawa and Y.Ando
Experimental Realization of a Topological Crystalline Insulator in SnTe
Nature Physics, **8** (2012) 800.

K.Nakayama, K.Eto, Y.Tanaka, T.Sato, S.Souma, T.Takahashi, K.Segawa and Y.Ando
Manipulation of Topological States and the Bulk Band Gap using Natural Heterostructures of a Topological Insulator
Phys. Rev. Lett., **109** (2012) 236804.

28B

T.Osawa, K.Kawajiri, N.Suzuki, T.Nagata, Y.Azuma and F.Koike
Photoion-Yield Study of the 3p-3d Giant Resonance Excitation Region of Isolated Cr, Mn and Fe Atoms
J. Phys. B, **45** (2012) 225204.

G.Purohit, P.Singh, V.Patidar, Y.Azuma, and K.K.Sud
Effects of Target Polarization and Postcollision Interaction on the Electron-Impact Single Ionization of Ne($2p$), Ar($3p$), and Na($3s$) Atoms
Phys. Rev. A, **85** (2012) 022714.

NE1A

S.Nakano
Effect of Helium Quasi-Hydrostatic Pressure on High-Pressure Behavior of Some Materials with Nano Spaced
The Review of High Pressure Science & Technology, **22** (2012) 26. (*in Japanese*).

A.K.Arora, T.Sato, T.Okada and T.Yagi
High-Pressure Amorphous Phase of Vanadium Pentaoxide
Phys. Rev. B, **85** (2012) 094113.

A.Sano-Furukawa, T.Yagi, T.Okada, H.Gotou and T.Kikegawa
Compression Behaviors of Distorted Rutile-Type Hydrous Phases, MOOH (M = Ga, In, Cr) and CrOOD
Phys. Chem. Minerals, **39** (2012) 375.

D.Y.Tan, W.S.Xiao, W.Zhou, M.Chen, W.G.Zhou, X.D.Li, Y.C.Li and J.Liu
High Pressure X-Ray Diffraction Study on $BaWO_4$-II
High Pressure Res., **32** (2012) 262.

H.Yusa, Y.Shirako, M.Akaogi, H.Kojitani, N.Hirao, Y.Ohishi and T.Kikegawa
Perovskite-to-Postperovskite Transitions in $NaNiF_3$ and $NaCoF_3$ and Disproportionation of $NaCoF_3$ Postperovskite under High Pressure and High Temperature
Inorg. Chem., **51** (2012) 6659.

NE3A

T.Tsuda, T.Suzuki and S.Kojima
Crystallization and Preliminary X-Ray Diffraction Analysis of *Bacillus subtilis* YwfE, an L-Amino-Acid Ligase
Acta Cryst. F, **68** (2012) 203.

O.Tsuruta, H.Yokoyama and S.Fujii
A New Crystal Lattice Structure of *Helicobacter pylori* Neutrophil-Activating Protein (HP-NAP)
Acta Cryst. F, **68** (2012) 134.

D.-H.Im, K.Kimura, F.Hayasaka, T.Tanaka, M.Noguchi, A.Kobayashi, S.Shoda, K.Miyazaki, T.Wakagi and S.Fushinobu
Crystal Structures of Glycoside Hydrolase Family 51 α-L-Arabinofuranosidase from *Thermotoga maritima*
Biosci. Biotechnol. Biochem., **76** (2012) 423.

Z.Hou, I.Nakanishi, T.Kinoshita, Y.Takei, M.Yasue, R.Misu, Y.Suzuki, S.Nakamura, T.Kure, H.Ohno, K.Murata, K.Kitaura, A.Hirasawa, G.Tsujimoto, S.Oishi and N.Fujii
Structure-Based Design of Novel Potent Protein Kinase CK2 (CK2) Inhibitors with Phenyl-Azole Scafolds
J. Med. Chem., **55** (2012) 2899.

K.Hanaya, M.Suetsugu, S.Saijo, I.Yamato and S.Aoki
Potent Inhibition of dinuclear zinc(II) Peptidase, an Aminopeptidase from *Aeromonas proteolytica*, by 8-Quinolinol Derivatives: Inhibitor Design Based on Zn^{2+} Fluorophores, Kinetic, and X-Ray Crystallographic Study
J. Biol. Inorg. Chem., **17** (2012) 517.

K.Yoneda, H.Sakuraba, T.Araki and T.Ohshima
Crystal Structure of Binary and Ternary Complexes of Archaeal UDP-Galactose 4-Epimerase-like L-Threonine Dehydrogenase from *Thermoplasma volcanium*
J. Biol. Chem., **287** (2012) 12966.

Q.-F.Sun, S.Sato and M.Fujita
An $M_{18}L_{24}$ Stellated Cuboctahedron through Post-Stellation of an $M_{12}L_{24}$ Core
Nature Chem., **4** (2012) 330.

T.Nagae, C.Kato and N.Watanabe
Structural Analysis of 3-Isopropylmalate Dehydrogenase from the Obligate Piezophile *Shewanella Benthica* DB21MT-2 and the Nonpiezophile *Shewanella Oneidensis* MR-1
Acta Cryst. F, **68** (2012) 265.

J.Wang, M.Xu, K.Zhu, L.Li and X.Liu
The N-Terminus of FILIA Forms an Atypical KH Domain with a Unique Extension Involved in Interaction with RNA
PLoS ONE, **7** (2012) e30209.

X.Zhang, W.Wu and Z.Chen
Crystallization and Preliminary X-Ray Diffraction Studies of the Abscisic Acid Receptor PYL3 and its Complex with Pyrabactin
Acta Cryst. F, **68** (2012) 479.

L.Wang,K.Zhang, L.Wu, S.Liu, H.Zhang, Q.Zhou, L.Tong, F.Sun and Z.Fan
Structural Insights into the Substrate Specificity of Human Granzyme H: The Functional Roles of a Novel RKR Motif
The Journal of Immunology, **188** (2012) 765.

H.Sakurama, S.Fushinobu, M.Hidaka, E.Yoshida, Y.Honda, H.Ashida, M.Kitaoka, H.Kumagai, K.Yamamoto and T.Katayama
1,3-1,4-α-L-Fucosynthase that Specifically Introduces Lewis a/x Antigens into Type-1/2 Chains
J. Biol. Chem., **287** (2012) 16709.

T.Wakagi
A Special Enzyme Acting in a Primordial Metabolism; Discovery of One-Enzyme with Two Reactions
Kagaku, **67** (2012) 72. (*in Japanese*).

H.Nishimasu, S.Fushinobu and T.Wakagi
Molecular Mechanism by which One Enzyme Catalyzes Two Reactions
J. Cryst. Soc. Jpn., **54** (2012) 113. (*in Japanese*).

X.Zhang, Q.Zhang, Q.Xin, L.Yu, Z.Wang, W.Wu, L.Jiang, G.Wang, W.Tian, Z.Deng, Y.Wang, Z.Liu, J. Long, Z.Gong and Z.Chen
Complex Structures of the Abscisic Acid Receptor PYL3/RCAR13 Reveal a Unique Regulatory Mechanism
Structure, **20** (2012) 780.

T.Mase, H.Yabuki, M.Okai, J.Ohtsuka, F.L.Imai, Y.Nagata and M.Tanokura
Crystallization and Preliminary X-Ray Analysis of Haloalkanedehalogenase DatA from *Agrobacterium tumefaciens* C58
Acta Cryst. F, **68** (2012) 652.

U.Ohto, K.Fukase, K.Miyake and T.Shimizu
Structural Basis of Species-Specific Endotoxin Sensing by Innate Immune Receptor TLR4/MD-2
Proc. Natl. Acad. Sci. USA, **109** (2012) 7421.

T.Nakaniwa, H.Fukada, T.Inoue, M.Gouda, R.Nakai, Y.Kirii, M.Adachi, T.Tamada, S.Segawa, R.Kuroki, T.Tada and T.Kinoshita
Seven Cysteine-Deficient Mutants Depict the Interplay between Thermal and Chemical Stabilities of Individual Cysteine Residues in Mitogen-Activated Protein Kinase c-Jun N-Terminal Kinase 1
Biochemistry, **51** (2012) 8410.

N.Suzuki, Y.-M.Kim, Z.Fujimoto, M.Momma, M.Okuyama, H.Mori, K.Funane and A.Kimura
Structural Elucidation of Dextran Degradation Mechanism by *Streptococcus mutans* Dextranase Belonging to Glycoside Hydrolase Family 66
J. Biol. Chem., **287** (2012) 19916.

M.Michikawa, H.Ichinose, M.Momma, P.Biely, S.Jongkees, M.Yoshida, T.Kotake, Y.Tsumuraya, S.Withers, Z.Fujimoto and S.Kaneko
Structural and Biochemical Characterization of Glycoside Hydrolase family 79 β-Glucuronidase from *Acidobacterium capsulatum*
J. Biol. Chem., **287** (2012) 14069.

T.Matsumoto, T.Kinoshita, Y.Kirii, T.Tada and A.Yamano
Crystal and Sulution Structures Disclose a Putative Transient State of Mitogen-Activated Protein Kinase Kinase 4
Biochem. Biophys. Res. Commun., **425** (2012) 195.

T.Nishioka, Y.Yasutake, Y.Nishiya and T.Tamura
Structure-Guided Mutagenesis for the Improvement of Substrate Specificity of *Bacillus Megaterium* Glucose 1-Dehydrogenase IV
FEBS J., **279** (2012) 3264.

S.Nakano, M.Takahashi, A.Sakamoto, H.Morikawa and K.Katayanagi
X-Ray Crystal Structure of a Mutant Assimilatory Nitrite Reductase That Shows Sulfite Reductase-Like Activity
Chemistry and Biodiversity, **9** (2012) 1989.

D.Fujita, K.Suzuki, S.Sato, M.Yagi-Utsumi, Y.Yamaguchi, N.Mizuno, T.Kumasaka, M.Takata, M.Noda, S.Uchiyama, K.Kato and M.Fujita
Protein Encapsulation within Synthetic Molecular Hosts
Nature Communications, **3** (2012) 1093.

M.D.Yao, K.Miyazono, J.Ohtsuka, S.Hirano, K.Nagata, S.Horinouchi, Y.Ohnishi and M.Tanokura
Purification, Crystallization and Preliminary X-Ray Analysis of the DNA-Binding Domain of AdpA, the Central Transcription Factor in the A-Factor Regulatory Cascade in the Filamentous Bacterium *Streptomyces griseus*, in Complex with a Duplex DNA
Acta Cryst. F, **68** (2012) 946.

S.Yamashita, H.Yoshida, N.Uchiyama, Y.Nakakita, S.Nakakita, T.Tonozuka, K.Oguma, A.Nishikawa and S.Kamitori
Carbohydrate Recognition Mechanism of HA70 from *Clostridium Botulinum* Deduced from X-Ray Structures in Complexes with Sialylated Oligosaccharides
FEBS Lett., **586** (2012) 2404.

H.Yoshida, S.Yamashita, M.Teraoka, A.Itoh, S.Nakakita, N.Nishi and S.Kamitori
X-Ray Structure of a Protease-Resistant Mutant Form of Human Galectin-8 with Two Carbohydrate Recognition Domains
FEBS J., **279** (2012) 3937.

K.Suzuki, N.Ohbayashi, J.Jiang, X.Zhang, M.M.Hoque, M.Tsunoda, K.Murayama, H.Tanaka and A.Takenaka
Crystallographic Study of the Interaction of the Anti-HIV Lectin Actinohivin with α(1-2)mannobiose Moiety of gp120 HMTG
Acta Cryst. F, **68** (2012) 1060.

M.M.Hoque, K.Suzuki, M.Tsunoda, J.Jiang, F.Zhang, A.Takahashi, N.Ohbayashi, X.Zhang, H.Tanaka, S.Omura and A.Takenaka
Structural Insights into the Specific Anti-HIV Property of Actinohivin: Structure of its Complex with the α(1-2)mannobiose Moiety of gp120
Acta Cryst. D, **68** (2012) 1671.

K.Yoneda, Y.Fukuda, T.Shibata, T.Araki, T.Nikki, H.Sakuraba and T.Ohshima
Expression, Purification, Crystallization and Preliminary X-Ray Analysis of NAD(P)H-Dependent Carbonyl Reductase Specifically Expressed in Thyroidectomized Chicken Fatty Liver
Acta Cryst. F, **68** (2012) 1568.

Y.Itoh, S.Sekine and S.Yokoyama
Crystallization and Preliminary X-Ray Crystallographic Analysis of *Aquifex aeolicus* SelA, a Bacterial Selenocysteine Synthase
Acta Cryst. F, **68** (2012) 1128.

Y.Itoh, S.Sekine and S.Yokoyama
Crystallization and Preliminary X-Ray Crystallographic Analysis of Bacterial $tRNA^{Sec}$ in Complex with Seryl-tRNA Synthetase
Acta Cryst. F, **68** (2012) 678.

M.Yamaguchi, K.Matoba, R.Sawada, Y.Fujioka, H.Nakatogawa, H.Yamamoto, Y.Kobashigawa, H.Hoshida, R.Akada, Y.Ohsumi, N.N.Noda and F.Inagaki
Noncanonical Recognition and UBL Loading of Distinct E2s by Autophagy-Essential Atg7
Nature Structural Molecular Biology, **19** (2012) 1250.

Y.Ashikawa, Z.Fujimoto, Y.Usami, K.Inoue, H.Noguchi, H.Yamane and H.Nojiri
Structural Insight into the Substrate- and Dioxygen-Binding Manner in the Catalytic Cycle of Rieske Nonheme Iron Oxygenase System, Carbazole 1,9a-Dioxygenase
BMC Struct. Biol., **12** (2012) 15.

Z.Liu, Z.Chen and W.Wu
Crystallization and Preliminary X-Ray Studies of Ferric Uptake Regulator from *Magnetospirillum gryphiswaldense*
Acta Cryst. F, **68** (2012) 902.

T.Kubota, A.Kumagai, H.Ito, S.Furukawa, Y.Someya, N.Takeda, K.Ishii, T.Wakita, H.Narimatsu and H.Shirato
Structural Basis for the Recognition of Lewis Antigens by Genogroup I Norovirus
J. Virol., **86** (2012) 11138.

R.Arai, S.Fukui, N.Kobayashi and J.Sekiguchi
Solution Structure of IseA, an Inhibitor Protein of DL-Endopeptidases from *Bacillus Subtilis*, Reveals a Novel Fold with a Characteristic Inhibitory Loop
J. Biol. Chem., **287** (2012) 44736.

Y.Xu, A.Moeller, S.-Y.Jun, M.Le, B.-Y.Yoon, J.-S.Kim, K.Lee and N.-C.Ha
Assembly and Channel Opening of Outer Membrane Protein in Tripartite Drug Efflux Pumps of Gram-negative Bacteria
J. Biol. Chem., **287** (2012) 11740.

M.Fujihashi, M.Hiraki, G.Ueno, S.Baba, H.Murakami, M.Suzuki, N.Watanabe, I.Tanaka, A.Nakagawa, S.Wakatsuki, M.Yamamoto and K.Miki
Crystal Sample Pins and a Storage Cassette System Compatible with the Protein Crystallography Beamlines at both the Photon Factory and SPring-8
J. Appl. Cryst., **45** (2012) 1156.

T.Miyafusa, J.M.M.Caaveiro, Y.Tanaka and K.Tsumoto
Crystal Structure of the Enzyme CapF of *Staphylococcus aureus* Reveals a Unique Architecture Composed of Two Functional Domains
Biochem. J., **443** (2012) 671.

T.Tominaga, S.Watanabe, R.Matsumi, H.Atomi, T.Imanaka and K.Miki
Structure of the [NiFe]-Hydrogenase Maturation Protein HypF from *Thermococcus kodakaraensis* KOD1
Acta Cryst. F, **68** (2012) 1153.

H.Yoshida, A.Yoshihara, M.Teraoka, S.Yamashita, K.Izumori and S.Kamitori
Structure of L-Rhamnose Isomerase in Complex with L-Rhamnopyranose Demonstrates the Sugar-Ring Opening Mechanism and the Role of a Substrate Sub-Binding Site
FEBS Open Bio, **3** (2012) 35.

S.Watanabe, D.Sasaki, T.Tominaga and K.Miki
Structural Basis of [NiFe] Hydrogenase Maturation by Hyp Proteins
Biol. Chem., **393** (2012) 1089.

T.Hayashi, M.Senda, H.Morohashi, H.Higashi, M.Horio, Y.Kashiba, L.Nagase, D.Sasaya, T.Shimizu, N.Venugopalan, H.Kumeta, N.Noda, F.Inagaki, T.Senda and M.Hatakeyama
Tertiary Structure-Function Analysis Reveals the Pathogenic Signaling Potentiation Mechanism of *Helicobacter pylori* Oncogenic Effector CagA
Cell Host & Microbe, **12** (2012) 20.

NE5C

M.Imai
Structural Phase Transitions of Zintl-Phase Silicide $BaSi_2$ and Formation of Si Clathrate Ba_8Si_{46} at High Pressures and High Temperatures
Rev. High Pressure Sci. Tech., **22** (2012) 17. (*in Japanese*).

K.Matsui, K.Yamamoto, T.Kawaai, Y.Kawamura, J.Hayashi, K.Takeda and C.Sekine
Structural Instability of Unfilled Skutterudite Compounds MX_3 (M = Co, Rh, and Ir; X = As and Sb) under High Pressure
J. Phys. Soc. Jpn., **81** (2012) 104604.

O.Ohtaka, K.Funakoshi and M.Shimono
HIP Production of Diamond-SiC Composite and its Application to High-Pressure in situ X-Ray Experiments
J. Soc. Mater. Sci. Jpn., **61** (2012) 407. (*in Japanese*).

NE7A

T.Ohuchi, Y.Nishihara, T.Kawazoe, D.Spengler, R.Shiraishi, A.Suzuki, T.Kikegawa, E.Ohtani
Superplasticity in Hydrous Melt-Bearing Dunite: Implications for Shear Localization in Earth's Upper Mantle
Earth and Planetary Science Letters, **335-336** (2012) 59.

T.Miyoshi, Y.Arai, Y.Fujita, K.Hara, R.Ichimiya, Y.Ikegami, Y.Ikemoto, H.Kasai, H.Katsurayama, T.Kohriki, M.Okihara, Y.Ono, Y.Onuki, K.Shinsho, A.Takeda, K.Tauchi, T.Tsuboyama and Y.Unno
Recent Progress of Pixel Detector R&D based on SOI Technology
Phys. Procedia, **37** (2012) 1039.

K.Sasaki, S.Matsushita, F.Sato, C.Tokunaga, K.Hyodo and Y.Sakakibara
Cardiac Sympathetic Activity Assessed by Heart Rate Variability Indicates Myocardial Ischemia on Cold Exposure in Diabetes.
J. Jpn. College of Angiology, **52** (2012) 295. (*in Japanese*).

O.Ohtaka, K.Funakoshi and M.Shimono
HIP Production of Diamond-SiC Composite and its Application to High-Pressure in situ X-Ray Experiments
J. Soc. Mater. Sci. Jpn., **61** (2012) 407. (*in Japanese*).

NW2A

Y.Ohgo, S.Neya, D.Hashizume, T.Ozeki and M.Nakamura
Unusual Electronic Structure of Bis-Isocyanide Complexes of Iron(III) Porphyrinoids
Dalton Trans., **41** (2012) 3126.

J.L.Her, Y.H.Matsuda, M.Nakano, Y.Niwa and Y.Inada
Magnetic Field-Induced Spin-Crossover Transition in $[Mn^{III}(taa)]$ Studied by X-Ray Absorption Spectroscopy
J. Appl. Phys., **111** (2012) 053921.

Y.Yakiyama, A.Ueda, Y.Morita and M.Kawano
Crystal Surface Mediated Structure Transformation of a Kinetic Framework Composed of Multi-Interactive Ligand TPHAP and Co(II)
Chem. Comm., **48** (2012) 10651.

M.Saito and T.Ozeki
Crystallization of a Keplerate-Type Polyoxometalate into a Superposed Kagome-Lattice with Huge Channels
Dalton Trans., **41** (2012) 9846.

T.Shishido, K.Shimamura, K.Teramura and T.Tanaka
Role of CO_2 in Dehydrogenation of Propane over Cr-Based Catalysts
Catal. Today, **185** (2012) 151.

T.Shirasawa, E.Arakawa, W.Voegeli, T.Takahashi and T.Matsushita
Development of a Quick Method for Crystal Truncation Rod Scattering Profile Measurement by using a Simultaneous Multi-Wavelength Dispersive Mode
J. Jpn. Soc. Synchrotron Rad. Res., **25** (2012) 229. (*in Japanese*).

K.Sumiwaka, M.Katayama and Y.Inada
Development of 2-Dimentional Imaging XAFS System at BL-4
Memoirs of the SR Center Ritsumeikan University, **14** (2012) 11.

M.Katayama, K.Sumiwaka, K.Hayashi, K.Ozutsumi, T.Ohta and Y.Inada
Development of a Two-Dimensional Imaging System of X-Ray Absorption Fine Structure
J. Synchrotron Rad., **19** (2012) 717.

Y.Kim, S.Das, S.Bhattacharya, S.Hong, M.G.Kim, M.Yoon, S.Natarajan and K.Kim
Metal-Ion Metathesis in Metal-Organic Frameworks: A Synthetic Route to New Metal-Organic Frameworks
Chem. Eur. J., **18** (2012) 16642.

A.Kobayashi, H.Hara, T.Yonemura, H.-C.Chang and M.Kato
Systematic Structural Control of Multichromic Platinum(II)-Diimine Complexes Ranging from Ionic Solid to Coordination Polymer
Dalton Trans., **41** (2012) 1878.

NW10A

K.Shimura and H.Yoshida
Effect of Doped Zinc Species on the Photocatalytic Activity of Gallium Oxide for Hydrogen Production
Phys. Chem. Chem. Phys., **14** (2012) 2678.

T.Wada, K.K.Bando, T.Miyamoto, S.Takakusagi, S.T.Oyama and K.Asakura
Operando QEXAFS Studies of Ni_2P during Thiophene Hydrodesulfurization: Direct Observation of Ni-S Bond Formation under Reaction Conditions
J. Synchrotron Rad., **19** (2012) 205.

K.K.Bando, T.Wada, T.Miyamoto, K.Miyazaki, S.Takakusagi, Y.Koike, Y.Inada, M.Nomura, A.Yamaguchi, T.Gott, S.Ted Oyama and K.Asakura
Combined in situ QXAFS and FTIR Analysis of a Ni Phosphide Catalyst under Hydrodesulfurization Conditions
J. Catal., **286** (2012) 165.

H.Wang, S.Hamanaka, Y.Nishimoto, S.Irle, T.Yokoyama, H.Yoshikawa and K.Awaga
In Operando X-Ray Absorption Fine Structure Studies of Polyoxometalate Molecular Cluster Batteries: Polyoxometalates as Electron Sponges
J. Am. Chem. Soc., **134** (2012) 4918.

T.Ohkubo, Y.Takehara and Y.Kuroda
Water-Initiated Ordering Around a Copper Ion of Copper Acetate Confined in Slit-Shaped Carbon Micropores
Micropor. Mesopor. Mater., **154** (2012) 82.

H.Kobayashi, H.Ohta and A.Fukuoka
Conversion of Lignocellulose into Renewable Chemicals by Heterogeneous Catalysis
Catal. Sci. Technol., **2** (2012) 869.

Y.Yang, Z.Weng, S.Muratsugu, N.Ishiguro, S.Ohkoshi and M.Tada
Preparation and Catalytic Performances of a Molecularly Imprinted Ru-Complex Catalyst with an NH_2 Binding Site on a SiO_2 Surface
Chem. Eur. J., **18** (2012) 1142.

N.Maity, C.Wattanakit, S.Muratsugu, N.Ishiguro, Y.Yang, S.Ohkoshi and M.Tada
Sulfoxidation on a SiO_2-supported Ru Complex using O_2/Aldehyde System
Dalton Trans., **41** (2012) 4558.

V.Srihari, V.Sridharan, M.Nomura, V.S.Sastry and C.S.Sundar
Local Structural Studies of the Cubic $Cd_{1--x}Ca_xO$ System through Cd *K*-Edge Extended X-Ray Absorption Spectroscopic Studies
J. Synchrotron Rad., **19** (2012) 541.

Y.Kubouchi, S.Hayakawa, H.Namatame and T.Hirokawa
Direct Observation of Fractional Change of Niobium Ionic Species in a Solution by Means of X-Ray Absorption Fine Structure Spectroscopy
X-Ray Spectrom., **41** (2012) 259.

H.Wang, N.Kawasaki, T.Yokoyama, H.Yoshikawa and K.Awaga
Molecular Cluster Batteries of Nano-Hybrid Materials between Keggin POMs and SWNTs
J.Chem.Soc., Dalton Trans., **41** (2012) 9863.

Y.Okamoto, M.Nakada, M.Akabori, H.Shiwaku, S.Komamine, T.Fukui, E.Ochi, H.Nitani and M.Nomura
Synchrotron Radiation-Based X-Ray Imaging Study of Ruthenium in Simulated High-Level Waste Glass
Transactions of the Atomic Energy Society of Japan, **11** (2012) 127. (*in Japanese*).

T.Takeguchi, T.Yamanaka, K.Asakura, E.N.Muhamad, K.Uosaki and W.Ueda
Evidence of Nonelectrochemical Shift Reaction on a CO-Tolerant High-Entropy State Pt-Ru Anode Catalyst for Reliable and Efficient Residential Fuel Cell Systems
J. Am. Chem. Soc., **134** (2012) 14508.

M.Shibukawa, M.Harada, T.Okada, Y.Ogiyama, T.Shimasaki, Y.Kondo, A.Inoue and S.Saito
X-Ray Absorption Fine Structure Spectroscopy Studies of Thermal Effects on Ion-exchange Equilibria
RSC Adv., **2** (2012) 8985.

T.Wada, K.K.Bando, S.T.Oyama, T.Miyamoto, S.Takakusagi and K.Asakura
Operando Observation of Ni_2P Structural Changes during Catalytic Reaction: Effect of H_2S Pretreatment
Chem. Lett., **41** (2012) 1238.

A.Yamaguchi, N.Hiyoshi, O.Sato and M.Shirai
Gasification of Organosolv-Lignin over Charcoal Supported Noble Metal Salt Catalysts in Supercritical Water
Topics in Catal., **55** (2012) 889.

K.Ikeue, S.Hinokuma, K.Watanabe, T.Minekishi, T.Sato, Y.Nakahara and M.Machida
Structure and Catalytic Properties of $Pd/10Al_2O_3{\cdot}2B_2O_3$. Effect of Preparation Routes and Additives
Bull. Chem. Soc. Jpn., **85** (2012) 468.

K.Ito, K.Yoshida, S.Kittaka and T.Yamaguchi
Pore Size Dependent Behavior of Hydrated Ag^+ Ions Confined in Mesoporous MCM-41 Materials under Synchrotron X-Ray Irradiation
Anal. Sci., **28** (2012) 639.

K.Shimura, H.Kawai, T.Yoshida and H.Yoshida
Bifunctional Rhodium Cocatalysts for Photocatalytic Steam Reforming of Methane over Alkaline Titanate
ACS Catal., **2** (2012) 2126.

F.Gao, S.Yamazoe, T.Maeda, and T.Wada
Structural Study of Cu-Deficient $Cu_{2(1-x)}ZnSnSe_4$ Solar Cell Materials by X-Ray Diffraction and X-ray Absorption Fine Structure
Jpn. J. Appl. Phys., **51** (2012) 10NC28.

A.Oda, H.Torigoe, A.Itadani, T.Ohkubo, T.Yumura, H.Kobayashi and Y.Kuroda
Unprecedented Reversible Redox Process in the ZnMFI-H_2 System Involving Formation of Stable Atomic Zn^0
Angew. Chem. Int. Ed., **51** (2012) 7719.

J.Kugai, R.Kitagawa, S.Seino, T.Nakagawa, Y.Ohkubo, H.Nitani, H.Daimon and T.A.Yamamoto
CeO_2-Supported Pt-Cu Alloy Nanoparticles Synthesized by Radiolytic Process for Highly Selective CO Oxidation
Itn. J. Hydrogen Energy, **37** (2012) 4787.

S.Kageyama, A.Murakami, S.Ichikawa, S.Seino, T.Nakagawa, H.Daimon, Y.Ohkubo, J Kugai and T.A.Yamamoto
Enhanced Eectrochemical Stability of PtRuAu/C Catalyst Synthesized by Radiolytic Process
J. Mater. Res., **27** (2012) 1037.

J.Kugai, T.Moriya, S.Seino, T.Nakagawa, Y.Ohkubo, H.Nitani, Y.Mizukoshi and T.A.Yamamoto
Effect of Support for Pt-Cu Bimetallic Catalysts Synthesized by Electron Beam Irradiation Method on Preferential CO Oxidation
Appl. Catal. B, **126** (2012) 306.

H.Kitagawa, N.Ichikuni, S.Xie, T.Tsukuda, T.Hara and S.Shimazu
Size Control of Ni Nanocluster by the Carbon Chain Length of Secondary Alkoxide
e-J. Surf. Sci. Nanotech., **10** (2012) 648.

A.Itadani, H.Torigoe, T.Yumura, T.Ohkubo, H.Kobayashi and Y.Kuroda
Dual-Copper Catalytic Site Formed in CuMFI Zeolite Makes Effective Activation of Ethane Possible Even at Room Temperature
J. Phys. Chem. C, **116** (2012) 10680.

NW12A

T.Tsuda, T.Suzuki and S.Kojima
Crystallization and Preliminary X-Ray Diffraction Analysis of *Bacillus subtilis* YwfE, an L-Amino-Acid Ligase
Acta Cryst. F, **68** (2012) 203.

S.Nakano, M.Takahashi, A.Sakamoto, H.Morikawa and K.Katayanagi
Structure-Function Relationship of Assimilatory Nitrite Reductases from the Leaf and Root of Tobacco Based on the High Resolution Structure
Protein Science, **21** (2012) 383.

U.Ohto, K.Usui, T.Ochi, K.Yuki, Y.Satow and T.Shimizu
Crystal Structure of Human β-Galactosidase Structural Basis of G_{M1} Gangliosidosis and Morquio B Diseases
J. Biol. Chem., **287** (2012) 1801.

K.Usui, U.Ohto, T.Ochi, T.Shimizu and Y.Satow
Expression, Purification, Crystallization and Preliminary X-Ray Crystallographic Analysis of Human β-Galactosidase
Acta Cryst. F, **68** (2012) 73.

D.-H.Im, K.Kimura, F.Hayasaka, T.Tanaka, M.Noguchi, A.Kobayashi, S.Shoda, K.Miyazaki, T.Wakagi and S.Fushinobu
Crystal Structures of Glycoside Hydrolase Family 51 α-L-Arabinofuranosidase from *Thermotoga maritima*
Biosci. Biotechnol. Biochem., **76** (2012) 423.

Y.-L.Xue, T.Miyakawa, Y.Sawano and M.Tanokura
Crystallization and Preliminary X-Ray Crystallographic Analysis of Dioscorin from *Dioscorea japonica*
Acta Cryst. F, **68** (2012) 193.

K.Hanaya, M.Suetsugu, S.Saijo, I.Yamato and S.Aoki
Potent Inhibition of dinuclear zinc(II) Peptidase, an Aminopeptidase from *Aeromonas proteolytica*, by 8-Quinolinol Derivatives: Inhibitor Design Based on Zn^{2+} Fluorophores, Kinetic, and X-Ray Crystallographic Study
J. Biol. Inorg. Chem., **17** (2012) 517.

H.Nojiri
Structural and Molecular Genetic Analyses of the Bacterial Carbazole Degradation System
Biosci. Biotechnol. Biochem., **76** (2012) 1.

K.Yoneda, H.Sakuraba, T.Araki and T.Ohshima
Crystal Structure of Binary and Ternary Complexes of Archaeal UDP-Galactose 4-Epimerase-like L-Threonine Dehydrogenase from *Thermoplasma volcanium*
J. Biol. Chem., **287** (2012) 12966.

N.Kuwabara,Y.Murayama, H.Hashimoto, Y.Kokabu, M.Ikeguchi, M.Sato, K.Mayanagi, Y.Tsutsui, H.Iwasaki and T.Shimizu
Mechanistic Insights into the Activation of Rad51-Mediated Strand Exchange from the Structure of a Recombination Activator, the Swi5-Sfr1 Complex
Structure, **20** (2012) 440.

M.Nagae, S.Re, E.Mihara, T.Nogi, Y.Sugita and J.Takagi
Crystal Structure of $\alpha 5\beta 1$ Integrin Ectodomain: Atomic Details of the Fibronectin Receptor
J. Cell Biol., **197** (2012) 131.

A.Nakamura, J.Ohtsuka, K.Miyazono, A.Yamamura, K.Kubota, R.Hirose, N.Hirota, M.Ataka, Y.Sawano and M.Tanokura
Improvement in Quality of Protein Crystals Grown in a High Magnetic Field Gradient
Crystal Growth and Design, **12** (2012) 1141.

T.Nagae, T.Kawamura, L.M.G.Chavas, K.Niwa, M.Hasegawa, C.Kato and N.Watanabe
High-Pressure-Induced Water Penetration into 3-Isopropylmalate Dehydrogenase
Acta Cryst. D, **68** (2012) 300.

J.Wang, M.Xu, K.Zhu, L.Li and X.Liu
The N-Terminus of FILIA Forms an Atypical KH Domain with a Unique Extension Involved in Interaction with RNA
PLoS ONE, **7** (2012) e30209.

M.Oda, M.Takahashi, H.Tsuge, M.Nagahama and J.Sakurai
Role of Side-Edge Site of Sphingomyelinase from *Bacillus Cereus*
Biochem. Biophys. Res. Commun., **422** (2012) 128.

R.Arai, N.Kobayashi, A.Kimura, T.Sato, K.Matsuo, A.F.Wang, J.M.Platt, L.H.Bradley and M.H.Hecht
Domain-Swapped Dimeric Structure of a Stable and Functional *De Novo* Four-Helix Bundle Protein, WA20
J. Phys. Chem. B, **116** (2012) 6789.

X.Zhang, W.Wu and Z.Chen
Crystallization and Preliminary X-Ray Diffraction Studies of the Abscisic Acid Receptor PYL3 and its Complex with Pyrabactin
Acta Cryst. F, **68** (2012) 479.

H.Sakurama, S.Fushinobu, M.Hidaka, E.Yoshida, Y.Honda, H.Ashida, M.Kitaoka, H.Kumagai, K.Yamamoto and T.Katayama
1,3-1,4-α-L-Fucosynthase that Specifically Introduces Lewis a/x Antigens into Type-1/2 Chains
J. Biol. Chem., **287** (2012) 16709.

H.Shoun, S.Fushinobu, L.Jiang, S.-W.Kim and T.Wakagi
Fungal Denitrification and Nitric Oxide Reductase Cytochrome P450nor
Phil. Trans. R. Soc. B, **367** (2012) 1186.

T.Wakagi
A Special Enzyme Acting in a Primordial Metabolism; Discovery of One-Enzyme with Two Reactions
Kagaku, **67** (2012) 72. (*in Japanese*).

H.Nishimasu, S.Fushinobu and T.Wakagi
Molecular Mechanism by which One Enzyme Catalyzes Two Reactions
J. Cryst. Soc. Jpn., **54** (2012) 113. (*in Japanese*).

H.Yokoyama, N.Takizawa, D.Kobayashi, I.Matsui and S.Fujii
Crystal Structure of a Membrane Stomatin-Specific Protease in Complex with a Substrate Peptide
Biochemistry, **51** (2012) 3872.

X.Zhang, Q.Zhang, Q.Xin, L.Yu, Z.Wang, W.Wu, L.Jiang, G.Wang, W.Tian, Z.Deng, Y.Wang, Z.Liu, J. Long, Z.Gong and Z.Chen
Complex Structures of the Abscisic Acid Receptor PYL3/RCAR13 Reveal a Unique Regulatory Mechanism
Structure, **20** (2012) 780.

L.M.G.Chavas, N.Matsugaki, Y.Yamada, M.Hiraki, N.Igarashi, M.Suzuki and S.Wakatsuki
Beamline AR-NW12A: High-Throughput Beamline for Macromolecular Crystallography at the Photon Factory
J. Synchrotron Rad., **19** (2012) 450.

M.Tamura, T.Miyazaki, Y.Tanaka, M.Yoshida, A.Nishikawa and T.Tonozuka
Comparison of the Structural Changes in Two Cellobiohydrolases, CcCel6A and CcCel6C, from *Coprinopsis cinerea* - a Tweezer-Like Motion in the Structure of CcCel6C
FEBS J., **279** (2012) 1871.

K.Miyazono, T.Koura, K.Kubota, T.Yoshida, Y.Fujita, K.Yamaguchi-Shinozaki and M.Tanokura
Purification, Crystallization and Preliminary X-Ray Analysis of OsAREB8 from rice, a member of the AREB/ABF family of bZIP transcription factor, in complex with its congnate DNA
Acta Cryst. F, **68** (2012) 491.

M.Qian, Q.Huang, G.Wu, L.Lai, Y.Tang, J.Pei and M.Kusunoki
Crystal Structure Analysis of a Recombinant Predicted Acetamidase/Formamidase from the Thermophile *Thermoanaerobacter Tengcongensis*
Protein J., **31** (2012) 166.

M.Gao, D.Li, Y.Hu, Y.Zhang, Q.Zou and D.-C.Wang
Crystal Structure of TNF-α-Inducing Protein from *Helicobacter Pylori* in Active Form Reveals the Intrinsic Molecular Flexibility for Unique DNA-Binding
PLoS One, **7** (2012) e41871.

X.Wang, J.Ding and D.Wang
Crystallization and Preliminary X-Ray Analysis of the C-Terminal Domain of CCM2, Part of a Novel Adaptor Protein Involved in Cerebral Cavernous Malformations
Acta Cryst. F, **68** (2012) 683.

T.Tonozuka, A.Tamaki, G.Yokoi, T.Miyazaki, M.Ichikawa, A.Nishikawa, Y.Ohta, Y.Hidaka, K.Katayama, Y.Hatada, T.Ito and K.Fujita
Crystal Structure of a Lactosucrose-Producing Enzyme, Arthrobacter sp. K-1 β-Fructofuranosidase
Enzyme and Microbial Technology, **51** (2012) 359.

U.Ohto, K.Fukase, K.Miyake and T.Shimizu
Structural Basis of Species-Specific Endotoxin Sensing by Innate Immune Receptor TLR4/MD-2
Proc. Natl. Acad. Sci. USA, **109** (2012) 7421.

B.G.Han, K.C.Jeong, J.W.Cho, B.C.Jeong, H.K.Song, J.Y.Lee, D.H.Shin, S.Lee and B.I.Lee
Crystal Structure of *Pyrococcus Furiosus* PF2050, a Member of the DUF2666 Protein Family
FEBS Lett., **586** (2012) 1384.

N.Suzuki, Y.-M.Kim, Z.Fujimoto, M.Momma, M.Okuyama, H.Mori, K.Funane and A.Kimura
Structural Elucidation of Dextran Degradation Mechanism by *Streptococcus mutans* Dextranase Belonging to Glycoside Hydrolase Family 66
J. Biol. Chem., **287** (2012) 19916.

H.Sakuraba, T.Satomura, R.Kawakami, K.Kim, Y.Hara, K.Yoneda and T.Ohshima
Crystal Structure of Novel Dye-Linked L-Proline Dehydrogenase from Hyperthermophilic Archaeon *Aeropyrum Pernix*
J. Biol. Chem., **287** (2012) 20070.

H.Yokoyama, O.Tsuruta, N.Akao and S.Fujii
Crystal Structure of *Helicobacter Pylori* Neutrophil-Activating Protein with a Di-Nuclear Ferroxidase Center in a Zinc or Cadmium-Bound Form
Biochem. Biophys. Res. Commun., **422** (2012) 745.

Y.Koo, D.Jung and E.Bae
Crystal Structure of *Streptococcus pyogenes* Csn2 Reveals Calcium-Dependent Conformational Changes in Its Tertiary and Quaternary Structure
PLoS One, **7** (2012) e33401.

H.Kondo, Y.Hanada, H.Sugimoto, T.Hoshino, C.P.Garnham, P.L.Davies and S.Tsuda
Ice-Binding Site of Snow Mold Fungus Antifreeze Protein Deviates from Structural Regularity and High Conservation
Proc. Natl. Acad. Sci. USA, **109** (2012) 9360.

Q.Tang, P.Gao, Y.-P.Liu, A.Gao, X.-M.An, S.Liu, X.-X.Yan and D.-C.Liang
RecOR Complex Including RecR N-N Dimer and RecO Monomer Displays a High Affinity for ssDNA
Nucleic Acids Res., **40** (2012) 11115.

T.Shirouzono, M.Chirifu, C.Nakamura, Y.Yamagata and S.Ikemizu
Preparation, Crystallization and Preliminary X-Ray Diffraction Studies of the Glycosylated Form of Human Interleukin-23
Acta Cryst. F, **68** (2012) 432.

A.Nakamura, M.Fujihashi, R.Aono, T.Sato, Y.Nishiba, S.Yoshida, A.Yano, H.Atomi, T.Imanaka and K.Miki
Dynamic, Ligand-Dependent Conformational Change Triggers Reaction of Ribose-1,5-Bisphosphate Isomerase from *Thermococcus Kodakarensis* KOD1
J. Biol. Chem., **287** (2012) 20784.

H.Makyio, M.Ohgi, T.Takei, S.Takahashi, H.Takatsu, Y.Katoh, A.Hanai, T.Ueda, Y.Kanaho, Y.Xie, HW.Shin, H.Kamikubo, M.Kataoka, M.Kawasaki, R.Kato, S.Wakatsuki and K.Nakayama
Structural Basis for Arf6-MKLP1 Complex Formation on the Flemming Body Responsible for Cytokinesis
EMBO J., **31** (2012) 2590.

Y.Watanabe, T.Kobayashi, H.Yamamoto, H.Hoshida, R.Akada, F.Inagaki, Y.Ohsumi and N.N.Noda
Structure-Based Analyses Reveal Distinct Binding Sites for Atg2 and Phosphoinositides in Atg18
J. Biol. Chem., **287** (2012) 31681.

T.Nishioka, Y.Yasutake, Y.Nishiya and T.Tamura
Structure-Guided Mutagenesis for the Improvement of Substrate Specificity of *Bacillus Megaterium* Glucose 1-Dehydrogenase IV
FEBS J., **279** (2012) 3264.

H.Nakano, A.Hosokawa, R.Tagawa, K.Inaka, K.Ohta,T.Nakatsu, H.Kato and K.Watanabe
Crystallization and Preliminary X-Ray Crystallographic Analysis of Pz Peptidase B from *Geobacillus Collagenovorans* MO-1
Acta Cryst. F, **68** (2012) 757.

Y.Zhao, T.Wakamatsu, K.Doi, H.Sakuraba and T.Ohshima
A Psychrophilic Leucine Dehydrogenase from *Sporosarcina Psychrophila*: Purification, Characterization, Gene Sequencing and Crystal Structure Analysis
J. Mol. Catal. B, **83** (2012) 65.

H.Shimizu, A.Osanai, K.Sakamoto, D.K.Inaoka, T.Shiba, S.Harada and K.Kita
Crystal Structure of Mitochondrial Quinol-Fumarate Reductase from the Parasitic Nematode *Ascaris Suum*
J. Biochem., **151** (2012) 589.

S.Hoshino and I.Hayashi
Filament Formation of FtsZ/Tubulin-Like Protein TubZ from the *Bacillus cereus* pXO1 Plasmid
J. Biol. Chem., **287** (2012) 32103.

Y.Kezuka, Y.Yoshida and T.Nonaka
Structural Insights into Catalysis by βC-S lyase from *Streptococcus Anginosus*
Proteins, **80** (2012) 2447.

S.Nakano, M.Takahashi, A.Sakamoto, H.Morikawa and K.Katayanagi
X-Ray Crystal Structure of a Mutant Assimilatory Nitrite Reductase That Shows Sulfite Reductase-Like Activity
Chemistry and Biodiversity, **9** (2012) 1989.

S.Inoue-Ito, S.Yajima, S.Fushinobu, S.Nakamura, T.Ogawa, M.Hidaka and H.Masaki
Identification of the Catalytic Residues of Sequence-Specific and Histidine-Free Ribonuclease Colicin E5
J. Biochem., **152** (2012) 365.

K.Yoneda
Structural and Functional Analyses of Novel NAD(P) Dependent Amino Acid Dehydrogenases from Archaea
vitamins (Japan), **86** (2012) 74. (*in Japanese*).

J.Kondo, M.Koganei and T.Kasahara
Crystal Structure and Specific Binding Mode of Sisomicin to the Bacterial Ribosomal Decoding Site
ACS Med. Chem. Lett., **3** (2012) 741.

Y.Shoyama, T.Tamada, K.Kurihara, A.Takeuchi, F.Taura, S.Arai, M.Blaber, Y.Shoyama, S.Morimoto and R.Kuroki
Structure and Function of Δ1-Tetrahydrocannabinolic Acid (THCA) Synthase, the Enzyme Controlling the Psychoactivity of *Cannabis sativa*
J. Mol. Biol., **423** (2012) 96.

M.Momma and Z.Fujimoto
Interdomain Disulfide Bridge in the Rice Granule Bound Starch Synthase I Catalytic Domain as Elucidated by X-Ray Structure Analysis
Biosci. Biotechnol. Biochem., **76** (2012) 1591.

S.Yamashita, H.Yoshida, N.Uchiyama, Y.Nakakita, S.Nakakita, T.Tonozuka, K.Oguma, A.Nishikawa and S.Kamitori
Carbohydrate Recognition Mechanism of HA70 from *Clostridium Botulinum* Deduced from X-Ray Structures in Complexes with Sialylated Oligosaccharides
FEBS Lett., **586** (2012) 2404.

H.Yoshida, S.Yamashita, M.Teraoka, A.Itoh, S.Nakakita, N.Nishi and S.Kamitori
X-Ray Structure of a Protease-Resistant Mutant Form of Human Galectin-8 with Two Carbohydrate Recognition Domains
FEBS J., **279** (2012) 3937.

K.Nakamura, Z.Man, Y.Xie, A.Hanai, H.Makyio, M.Kawasaki, R.Kato, H-W.Shin, K.Nakayama and S.Wakatsuki
Structural Basis for Membrane Binding Specificity of the Bin/Amphiphysin/Rvs (BAR) Domain of Arfaptin-2 Determined by Arl1 GTPase
J. Biol. Chem., **287** (2012) 25478.

K.Suzuki, N.Ohbayashi, J.Jiang, X.Zhang, M.M.Hoque, M.Tsunoda, K.Murayama, H.Tanaka and A.Takenaka
Crystallographic Study of the Interaction of the Anti-HIV Lectin Actinohivin with α(1-2)mannobiose Moiety of gp120 HMTG
Acta Cryst. F, **68** (2012) 1060.

M.M.Hoque, K.Suzuki, M.Tsunoda, J.Jiang, F.Zhang, A.Takahashi, N.Ohbayashi, X.Zhang, H.Tanaka, S.Omura and A.Takenaka
Structural Insights into the Specific Anti-HIV Property of Actinohivin: Structure of its Complex with the α(1-2)mannobiose Moiety of gp120
Acta Cryst. D, **68** (2012) 1671.

Y.Suwa, J.Ohtsuka, T.Miyakawa, F.L.Imai, M.Okai, Y.Sawano, Y.Yasohara, M.Kataoka, S.Shimizu and M.Tanokura
Expression, Purification, Crystallization, and Preliminary X-Ray Analysis of Carbonyl Reductase S1 from *Candida Magnoliae*
Acta Cryst. F, **68** (2012) 540.

Y.Itoh, S.Sekine and S.Yokoyama
Crystallization and Preliminary X-Ray Crystallographic Analysis of *Aquifex aeolicus* SelA, a Bacterial Selenocysteine Synthase
Acta Cryst. F, **68** (2012) 1128.

Y.Itoh, S.Sekine and S.Yokoyama
Crystallization and Preliminary X-Ray Crystallographic Analysis of Bacterial $tRNA^{Sec}$ in Complex with Seryl-tRNA Synthetase
Acta Cryst. F, **68** (2012) 678.

Y.Hirano, Y.Kimura, H.Suzuki, K.Miki and Z.-Y.Wang
Structure Analysis and Comparative Characterization of the Cytochrome *c'* and Flavocytochrome *c* from Thermophilic Purple Photosynthetic Bacterium *Thermochromatium tepidum*
Biochemistry, **51** (2012) 6556.

R.Nomoto, T.Tezuka, K.Miyazono, M.Tanokura, S.Horinouchi and Y.Ohnishi
Purification, Crystallization and Preliminary X-Ray Analysis of SGR6054, a *Streptomyces* Homologue of the Mycobacterial Integration Host Factor mIHF
Acta Cryst. F, **68** (2012) 1085.

M.Yamaguchi, K.Matoba, R.Sawada, Y.Fujioka, H.Nakatogawa, H.Yamamoto, Y.Kobashigawa, H.Hoshida, R.Akada, Y.Ohsumi, N.N.Noda and F.Inagaki
Noncanonical Recognition and UBL Loading of Distinct E2s by Autophagy-Essential Atg7
Nature Structural Molecular Biology, **19** (2012) 1250.

K.Murayama, M.Kato-Murayama, T.Hosaka, A.Sotokawauchi, S.Yokoyama, K.Arima and M.Shirouzu
Crystal Structure of Cucumisin, a Subtilisin-Like Endoprotease from *Cucumis melo* L
J. Mol. Biol., **423** (2012) 386.

Y.Ashikawa, Z.Fujimoto, Y.Usami, K.Inoue, H.Noguchi, H.Yamane and H.Nojiri
Structural Insight into the Substrate- and Dioxygen-Binding Manner in the Catalytic Cycle of Rieske Nonheme Iron Oxygenase System, Carbazole 1,9a-Dioxygenase
BMC Struct. Biol., **12** (2012) 15.

T.Y.Jung, D.Li, J.T.Park, S.M.Yoon, P.L.Tran, B.H.Oh, S.Janecek, S.G.Park, E.J.Woo and K.H.Park
Association of Novel Domain in Active Site of Archaic Hyperthermophilic Maltogenic Amylase from *Staphylothermus marinus*
J. Biol. Chem., **287** (2012) 7979.

M.Unno, K.Kizawa, M.Ishihara and H.Takahara
Crystallization and Preliminary X-Ray Crystallographic Analysis of Human Peptidylarginine Deiminase Type III
Acta Cryst. F, **68** (2012) 668.

N.Maita, H.Taniguchi and H.Sakuraba
Crystallization, X-Ray Diffraction Analysis and SIRAS Phasing of Human α-L-Iduronidase
Acta Cryst. F, **68** (2012) 1363.

K.Kubota, A.Yamagata, Y.Sato, S.Goto-Ito and S.Fukai
Get1 Stabilizes an Open Dimer Conformation of Get3 ATPase by Binding Two Distinct Interfaces
J. Mol. Biol., **422** (2012) 366.

N.Yoshimoto, Y.Sakamaki, M.Haeta, A.Kato, Y.Inaba, T.Itoh, M.Nakabayashi, N.Ito and K.Yamamoto
Butyl Pocket Formation in the Vitamin D Receptor Strongly Affects the Agonistic or Antagonistic behavior of Ligands
J. Med. Chem., **55** (2012) 4373.

Y.Sato, A.Yamagata, S.Goto-Ito, K.Kubota, R.Miyamoto, S Nakada and S.Fukai
Molecular Basis of Lys-63-linked Polyubiquitination Inhibition by the Interaction between Human Deubiquitinating Enzyme OTUB1 and Ubiquitin-Conjugating Enzyme UBC13
J. Biol. Chem., **287** (2012) 25860.

T.Kubota, A.Kumagai, H.Ito, S.Furukawa, Y.Someya, N.Takeda, K.Ishii, T.Wakita, H.Narimatsu and H.Shirato
Structural Basis for the Recognition of Lewis Antigens by Genogroup I Norovirus
J. Virol., **86** (2012) 11138.

F.Akita, A.Higashiura, T.Shimizu, Y.Pu, M.Suzuki, T.Uehara-Ichiki, T.Sasaya, S.Kanamaru, F Arisaka, T.Tsukihara, A.Nakagawa and T.Omura
Crystallographic Analysis Reveals Octamerization of Viroplasm Matrix Protein P9-1 of *Rice Black Streaked Dwarf Virus*
J. Virology, **86** (2012) 746.

J.Tong, H.Yang, S.Ha, Y.Lee, S.H.Eom and Y.J.Im
Crystallization and Preliminary X-Ray Crystallographic Analysis of the Oxysterol-Binding Protein Osh3 from *Saccharomyces cerevisiae*
Acta Cryst. F, **68** (2012) 1498.

R.Arai, S.Fukui, N.Kobayashi and J.Sekiguchi
Solution Structure of IseA, an Inhibitor Protein of DL-Endopeptidases from *Bacillus Subtilis*, Reveals a Novel Fold with a Characteristic Inhibitory Loop
J. Biol. Chem., **287** (2012) 44736.

J.Park, F.Lammers, W.Herr and J.-J.Song
HCF-1 Self-Association via an Interdigitated Fn3 Structure Facilitates Transcriptional Regulatory Complex Formation
Proc. Natl. Acad. Sci. USA, **109** (2012) 17430.

H.Tanaka, N.Miyazaki, K.Matoba, T.Nogi, K.Iwakasaki and J.Takagi
Higher-Order Architecture of Cell Adhesion Mediated by Polymorphic Synaptic Adhesion Molecules Neurexin and Neuroligin
Cell Reports, **2** (2012) 101.

M.Fujihashi, M.Hiraki, G.Ueno, S.Baba, H.Murakami, M.Suzuki, N.Watanabe, I.Tanaka, A.Nakagawa, S.Wakatsuki, M.Yamamoto and K.Miki
Crystal Sample Pins and a Storage Cassette System Compatible with the Protein Crystallography Beamlines at both the Photon Factory and SPring-8
J. Appl. Cryst., **45** (2012) 1156.

S.B.Hong, B.-W.Kim, J.H.Kim and H.K.Song
Structure of the Autophagic E2 Enzyme Atg10
Acta Cryst. D, **68** (2012) 1409.

B.-G.Lee, M.K.Kim, B.-W.Kim, S.W.Suh and H.K.Song
Structures of the Ribosome-Inactivating Protein from Barley Seeds Reveal a Unique Activation Mechanism
Acta Cryst. D, **68** (2012) 1488.

D.F.Li, J.Y.Zhang, Y.Hou, L.Liu, S.J.Liu and W.Liu
Crystallization and Preliminary Crystallographic Analysis of 2-Aminophenol 1,6-Dioxygenase Complexed with Substrate and with an Inhibitor
Acta Cryst. F, **68** (2012) 1337.

T.Miyafusa, J.M.M.Caaveiro, Y.Tanaka and K.Tsumoto
Crystal Structure of the Enzyme CapF of *Staphylococcus aureus* Reveals a Unique Architecture Composed of Two Functional Domains
Biochem. J., **443** (2012) 671.

K.H.Kim, D.R.An, J.Song, J.Y.Yoon, H.S.Kim, H.J.Yoon, H.N.Im, J.Kim, D.J.Kim, S.J.Lee, K-H.Kim, H-M.Lee, H-J.Kim, E-K.Jo, J.Y.Lee and S.W.Suh
Mycobacterium Tuberculosis Eis Protein Initiates Suppression of Host Immune Responses by Acetylation of DUSP16/MKP-7
Proc. Natl. Acad. Sci. USA, **109** (2012) 7729.

H.Yoshida, A.Yoshihara, M.Teraoka, S.Yamashita, K.Izumori and S.Kamitori
Structure of L-Rhamnose Isomerase in Complex with L-Rhamnopyranose Demonstrates the Sugar-Ring Opening Mechanism and the Role of a Substrate Sub-Binding Site
FEBS Open Bio, **3** (2012) 35.

S.Hoshino, T.Maki and I.Hayashi
Crystallization and Preliminary X-Ray Data Analysis of the pXO1 Plasmid-Partitioning Factor TubZ from *Bacillus cereus*
Acta Cryst. F, **68** (2012) 1550.

S.Watanabe, D.Sasaki, T.Tominaga and K.Miki
Structural Basis of [NiFe] Hydrogenase Maturation by Hyp Proteins
Biol. Chem., **393** (2012) 1089.

S.Watanabe, R.Matsumi, H.Atomi, T.Imanaka and K.Miki
Crystal Structures of the HypCD Complex and the HypCDE Ternary Complex: Transient Intermediate Complexes during [NiFe] Hydrogenase Maturation
Structure, **20** (2012) 2124.

K.Ito, R.Murakami, M.Mochizuki, H.Qi, Y.Shimizu, K.Miura, T.Ueda and T.Uchiumi
Structural Basis for the Substrate Recognition and Catalysis of Peptidyl-tRNA Hydrolase
Nucl. Acids Res., **40** (2012) 10521.

T.Hayashi, M.Senda, H.Morohashi, H.Higashi, M.Horio, Y.Kashiba, L.Nagase, D.Sasaya, T.Shimizu, N.Venugopalan, H.Kumeta, N.Noda, F.Inagaki, T.Senda and M.Hatakeyama
Tertiary Structure-Function Analysis Reveals the Pathogenic Signaling Potentiation Mechanism of *Helicobacter pylori* Oncogenic Effector CagA
Cell Host & Microbe, **12** (2012) 20.

NW14A

S.Koshihara, K.Onda, Y.Okimoto and T.Ishikawa
Search for the Photo-Induced Hidden Phase in Inorganic and Organic System
Acta Physica Polonica A, **121** (2012) 328.

M.Hoshino, H.Uekusa, A.Tomita, S.Koshihara, T.Sato, S.Nozawa, S.Adachi, K.Ohkubo, H.Kotani and S.Fukuzumi
Determination of the Structural Features of a Long-Lived Electron-Transfer State of 9-Mesityl-10-methylacridinium Ion
J. Am. Chem. Soc., **134** (2012) 4569.

J.Hu, K.Ichiyanagi, H.Takahashi, H.Koguchi, T.Akasaka, N.Kawai, S.Nozawa, T.Sato, Y.C.Sasaki, S.Adachi and K.G.Nakamura
Reversible Phase Transition in Laser-Shocked 3Y-TPZ Ceramics Observed via Nanosecond Time-Resolved X-Ray Diffraction
J. Appl. Phys., **111** (2012) 053526.

T.Sato, S.Nozawa, A.Tomita, M.Hoshino, S.Koshihara, H.Fujii and S.Adachi
Coordination and Electronic Structure of Ruthenium(II)-*tris*-2,2'-bipyridine in the Triplet Metal-to-Ligand Charge-Transfer Excited State Observed by Picosecond Time-Resolved Ru *K*-Edge XAFS
J. Phys. Chem. C, **116** (2012) 14232.

K.Ichiyanagi, N.Kawai, S.Nozawa, T.Sato, A.Tomita, M.Hoshino, K.G.Nakamura, S.Adachi and Y.C.Sasaski
Shock-Induced Intermediate-Range Structural Change of SiO_2 Glass in the Nonlinear Elastic Region
Appl. Phys. Lett., **101** (2012) 181901.

K.H.Kim, S.Muniyappan, K.Y.Oang, J.G.Kim, S.Nozawa, T.Sato, S.Koshihara, R.Henning, I.Kosheleva, H.K,Y.Kim, T.W.Kim, J.Kim, S.Adachi and H.Ihee
Direct Observation of Cooperative Protein Structural Dynamics of Homodimeric Hemoglobin from 100 Picoseconds to 10 Milliseconds with Pump-Probe X-Ray Solution Scattering
J. Am. Chem. Soc., **134** (2012) 7001.

A.F.Mabied, M.Muller, R.E.Dinnebier, S.Nozawa, M.Hoshino, A.Tomita, T.Sato and S.Adachi
A Time-Resolved Powder Diffraction Study of *in-situ* Photodimerization Kinetics of 9-Methylanthracene using a CCD Area Detector and Parametric Rietveld Refinement
Acta Cryst. B, **68** (2012) 424.

T.Tsuduki, A.Tomita, S.Koshihara, S.Adachi and T.Yamato
Ligand Migration in Myoglobin: A Combined Study of Computer Simulation and X-Ray Crystallography
J. Chem. Phys., **136** (2012) 165101.

SPF

K.Wada, T.Hyodo, A.Yagishita, M.Ikeda, S.Ohsawa, T.Shidara, K.Michishio, T.Tachibana, Y.Nagashima, Y.Fukaya, M.Maekawa and A.Kawasuso
Increase in the Beam Intensity of the Linac-Based Slow Positron Beam and its Application at the Slow Positron Facility, KEK
Eur. Phys. J. D, **66** (2012) 37.

K.Michishio, T.Tachibana, R.H.Suzuki, K.Wada, A.Yagishita, T.Hyodo and Y.Nagashima
An Energy-Tunable Positronium Beam Produced using the Photodetachment of the Positronium Negative Ion
Appl. Phys. Lett., **100** (2012) 254102.

I.Mochizuki, Y.Fukaya, A.Kawasuso, K.Yaji, A.Harasawa, I.Matsuda, K.Wada and T.Hyodo
Atomic Configuration and Phase Transition of Pt-Induced Nanowires on a Ge(001) Surface Studied using Scanning Tunneling Microscopy, Reflection High-Energy Positron Diffraction, and Angle-Resolved Photoemission Spectroscopy
Phys. Rev. B, **85** (2012) 245438.

Y.Nagashima, K.Michishio, T.Tachibana, H.Terabe and R.Suzuki
Positronium Negative Ion Experiments - Formation, Photodetachment and Production of an Energy Tunable Positronium Beam -
J. Phys. Conf. Ser., **388** (2012) 012021.

H.Terabe, K.Michishio, T.Tachibana and Y.Nagashima
Durable Emission of Positronium Negative Ions from Na- and K-Coated W(100) Surfaces
New J. Phys., **14** (2012) 015003.

Synchrotron Radiation Science Division

A.Kotani, K.O.Kvashnina, P.Glatzel, J.C.Parlebas and G.Schmerber
Single Impurity Anderson Model Versus Density Functional Theory for Describing Ce L_3 X-Ray Absorption Spectra of $CeFe_2$: Resolution of a Recent Controversy
Phys. Rev. Lett., **108** (2012) 036403.

T.A.W.Beale, G.Beutier, S.R.Bland, A.Bombardi, L.Bouchenoire, O.Bunau, S.D.Matteo, J.F-Rodriguez, J.E.H-Borrero, J.H-Martin, V.L.R.Jacques, R.D.Johnson, A.Juhin, T.Matsumura, C.Mazzoli, A.M.Mulders, H.Nakao, J.Okamoto, S.Partzsch, A.J.Princep, V.Scagnoli, J.Strempfer, C.Vecchini, Y.Wakabayashi, H.C.Walker, D.Wermeile and Y.Yamasaki
REXS Contribution to Electronic Ordering Investigation in Solids
Eur. Phys. J. Special Topics, **208** (2012) 89.

A.Kotani
Theoretical Analysis of X-Ray Magnetic Circular Dichroism at the Yb $L_{2,3}$ Absorption Edges of $YbInCu_4$ in High Magnetic Fields around the Field-Induced Valence Transition
Eur. Phys. J. B, **83** (2012) 31.

A.Kotani, K.O.Kvashnina, S.M.Butorin and P.Glatzel
Spectator and Participator Processes in the Resonant Photon-In and Photon-Out Spectra at the Ce L_3 Edge of CeO_2
Eur. Phys. J. B, **85** (2012) 257.

T.Nakamura, Y.H.Matsuda, J.-L.Her, K.Kindo, S.Michimura, T.Inami, M.Mizumaki, N.Kawamura, M.Suzuki, B.Chen, H.Ohta, K.Yoshimura and A.Kotani
High-Magnetic-Field X-Ray Absorption and Magnetic Circular Dichroism Spectroscopy in the Mixed-Valent Compound $YbAgCu_4$
J. Phys. Soc. Jpn., **81** (2012) 114702.

T.Nakamura, T.Hirono, T.Kinoshita,Y.Narumi, M.Hayashi, H.Nojiri, A.Mitsuda, H.Wada, K.Kodama, K.Kindo and A.Kotani
Soft-X-Ray Magnetic Circular Dichroism under Pulsed High Magnetic Fields at Eu $M_{4,5}$ Edges of Mixed Valence Compound $EuNi_2(Si_{0.18}Ge_{0.82})_2$
J. Phys. Soc. Jpn., **81** (2012) 103705.

H.Yamaoka, Y.Zekko, A.Kotani, I.Jarrige, N.Tsujii, J.-F.Lin, J.Mizuki, H.Abe, H.Kitazawa, N.Hiraoka, H.Ishii and K.-D.Tsuei
Electronic Transitions in $CePd_2Si_2$ Studied by Resonant X-Ray Emission Spectroscopy at High Pressures and Low Temperatures
Phys. Rev. B, **86** (2012) 235131.

T.Kawauchi, H.Yonemura, S.Kishimoto and K.Fukutani
Hydrogen Redistribution and Performance Improvement of Silicon Avalanche Photodiode by Low-Temperature Annealing
IEEE Electron Device Letters, **33** (2012) 1162.

I.Ascone, K.Asakura, G.N.George and S.Wakatsuki
International Workshop on Improving Data Quality and Quantity for XAFS Experiments (Q2XAFS 2011)
J. Synchrotron Rad., **19** (2012) 849.

Light Source Division

T.Honda and T.Obina
Top-Up Operation of Photon Factory Storage Ring
J. Jpn. Soc. Synchrotron Rad. Res., **25** (2012) 12. (*in Japanese*).

T.Honda, Y.Suetsugu and K.Mase
Damage at KEK B Factory and Photon Factory due to the Great East Japan Earthquake
J. Vacuum Society of Japan, **55** (2012) 7. (*in Japanese*).

The articles of the experiments utilizing multiple beamlines are simultaneously printed here in each section.